UNIVERSITÉ DE SHERBROOKE
Faculté de génie
Département de génie mécanique

Développement de Tourbillon de Bout d'Aile Sous l'Effet du Contrôle Actif

Wing Tip Vortex Development Under the Effect of Active Flow Control

Thèse de doctorat
Specialité: génie mécanique

Marouen DGHIM

Sherbrooke (Québec) Canada

August 2018

JURY MEMBERS

Hachimi FELLOUAH

Supervisor

Mohsen FERCHICHI

Co-supervisor

David RANCOURT

Examiner

Jean LEMAY

Examiner

Jérôme VÉTEL

Examiner

RÉSUMÉ

L'étude des tourbillons de bout d'aile est d'une grande importance scientifique en raison des problèmes pratiques tels que les distances de séparation des aéronefs, les interactions pale / tourbillon dans les hélicoptères, les cavitations des hélices des navires, etc. Récemment, des études extensives ont été conduites pour améliorer la compréhension de la structure du tourbillon, de sa dissipation et de sa persistance par des méthodes analytiques, numériques et expérimentales. Ces études ont principalement porté sur les écoulements à nombres de Reynolds (Re) élevés. Cependant, avec l'émergence de nouveaux drones, les tourbillons de bout d'aile ont des effets extrêmement néfastes sur les performances aérodynamiques des drones pour différentes configurations de vol. Il a également été montré dans la littérature que la dissipation d'un tourbillon de bout d'aile peut être modifiée et accélérée au moyen de jets synthétiques (JS). En effet, les JS exercent un certain contrôle sur un écoulement ce qui modifie spatialement et temporellement son développement. Dans ce travail, plusieurs techniques expérimentales ont été utilisées pour étudier les effets du contrôle actif par jets synthétiques sur le développement, la diffusion et l'errance du tourbillon, y compris l'anémométrie à fils chauds et la vélocimétrie par imagerie de particules stéréoscopique (SPIV). Deux ailes rectangulaires avec un profil NACA 0012 ont été fabriquées pour cette étude et ont été testées pour deux nombres de Reynolds. Dans la première configuration expérimentale, des mesures de pression sur l'intrados de l'aile ont montré que la sélection des fréquences d'actionnement dans la gamme de fréquences des instabilités de courtes et de longues durées diminuait les coefficients de pression pour les cas activés. Des mesures complètes par fils chauds ont ensuite été effectuées dans la région de quasi-sillage pour documenter l'effet de l'actionnement du jet synthétique sur la structure d'un tourbillon de bout d'aile. Les résultats suggèrent que la configuration de contrôle à basse fréquence a permis au JS de pénétrer dans le tourbillon en apportant des structures turbulentes dans son noyau. La même configuration a été utilisée pour l'acquisition des données dans la région du milieu du sillage. Trois configurations de contrôle ont été considérées pour une étude comparative sur un tourbillon auto-similaire. Une technique de correction a été appliquée sur tous les cas étudiés. Le développement du tourbillon actionné a montré que le mélange turbulent a été amélioré au niveau de la région interne, entraînait une diffusion accélérée. L'effet d'errance sur la structure et la diffusion d'un tourbillon de bout d'aile a été étudié en utilisant des mesures de SPIV sur un dispositif expérimental différent et à un nombre de Re différent. La contribution d'errance à la diffusion des tourbillons a été quantifiée en utilisant une décomposition orthogonale (POD). Le mouvement cohérent du tourbillon a été extrait à partir de la triple décomposition du champ de vitesse corrigé. De plus, d'autres observations sur les mécanismes physiques associés à la diffusion des tourbillons ont été identifiées à partir de l'équation de transport d'enstrophie. Il a été démontré que la dissipation de l'enstrophie était principalement attribuable à l'allongement de la vorticité et à la fluctuation du tenseur de déformation causée par le JS.

Mots-clés : Tourbillon de bout d'aile, mesures en soufflerie, contrôle par jet synthétique, errance des tourbillons, POD

ABSTRACT

Wing tip vortex flow is of a great scientific importance because of its effect on practical problems such as landing separation distances for aircrafts, blade/vortex interactions in helicopters, propeller cavitations on ships, etc. Recently, extensive investigations have been conducted to improve the understanding of the tip vortex structure, dissipation and persistence analytically, numerically, and experimentally. Studies on the structure of the wing tip vortex have mainly focused on high Reynolds number flows. However, with the emergence of new unmanned aerial vehicles (UAVs), wing tip vortices have shown to have tremendous detrimental effects on the aerodynamic performance of drones for different flight configurations. It has also been shown in the literature that the dissipation of a wing tip vortex can be altered and accelerated by means of fluidic control schemes. Exhibiting zero net-mass-flux at its exit, synthetic jets (SJ) were shown to exert a certain authority on the structure of the flow which spatially and temporally alters its development. This research used several experimental techniques to study the effects of active control on the development, diffusion and meandering of wing-tip vortices, including hot-wire anemometry and Stereo Particle Image Velocimetry (SPIV). Two rectangular wings with a NACA 0012 profile were fabricated for the use in this research and were tested at two chord based Re_{c_w} numbers, namely 8×10^4 and 2×10^5. In the first experimental setup, spanwise pressure measurements on the suction side of the wing showed that the selection of actuation frequencies in the range of frequencies of the long- and short-wave instabilities resulted in decreased pressure coefficients for the actuated cases compared to the natural vortex. Comprehensive hot-wire measurements were then conducted in the near-wake region to document the effect of SJ actuation on the structure of the vortex. The results suggested that the low frequency control configuration allowed the SJ to penetrate into the vortex bringing turbulent structures within its core. The same setup was used to collect data in the mid-wake region. Three control configurations were considered for a comparative study on a self-similar vortex. A meandering correction technique was applied on all the cases studied. The streamwise development of the actuated vortex showed that the enhanced turbulent mixing at the inner region of the vortex resulted in an accelerated outward diffusion. The effect of the meandering phenomenon on the structure and diffusion of the vortex was investigated using Stereoscopic PIV measurements on a different experimental apparatus and at a different Re number. The contribution of meandering to the vortex decay was quantified using proper orthogonal decomposition (POD). The coherent meandering motion of the vortex was extracted using a triple decomposition of the meandering-corrected velocity field at different downstream positions. In addition, further insight on the physical mechanisms associated with the vortex diffusion were identified from the close examination of the transport equation of the streamwise enstrophy. It was shown that the destruction of enstrophy was mainly attributed to the increased vorticity stretching and the fluctuating strain rate caused by the SJ actuation.

Keywords: Wing tip vortex, wind tunnel measurements, synthetic jet actuation, vortex meandering, POD

ACKNOWLEDGEMENTS

I would like to express my gratitude to my supervisors Prof. Hachimi Fellouah and Prof. Mohsen Ferchichi for their patience and guidance throughout this entire research project. Without their support and encouragement, this thesis would not have been possible.

I would also like to thank the staff members of the Department of Mechanical Engineering at the Université de Sherbrooke and at the Department of Mechanical and Aerospace Engineering at the Royal Military College of Canada who provided constant help and assistance with the manufacturing and installation of the experimental apparatus.

I would not have been able to accomplish this work without the financial support of the Directorate of Technical Airworthiness and Engineering Support (DTAES) office of the Royal Canadian Air Force and the Natural Sciences and Engineering Research Council (NSERC) of Canada.

Special thanks to all of my friends and colleagues with whom I have shared great memories during my time at Kingston and then later at Sherbrooke.

Last but not least, I am greatly indebted to my family and to my dear fiancée, *Ghofrane*, who have inspired me and supported me throughout this wonderful journey. Thank you for never losing faith in me.

TABLE OF CONTENTS

LIST OF FIGURES

LIST OF TABLES

CHAPTER 1

INTRODUCTION

1.1 Background and motivation

The rising pressure for cleaner vehicles driven by the increasing power of the environmental movement has stimulated the need for greener technologies and more efficient designs among aircraft manufactures. In fact, the drag generated by the trailing vortices of an aircraft continues to be a major concern and a topic for extensive aerodynamic research as it substantially contributes to most of the fuel consumption. The behaviour of the strong and coherent wing tip vortex structures constitutes a particular interest in both commercial and military aviation because of their significant contribution toward the overall drag of the aircraft and their hazardous effects on the aircraft flight safety and its limiting factor on today's airports capacity. From a military stand point, there are many issues associated with the effects of wing tip vortex structures on dynamics of towed vehicles, tail buffeting and icing arrays. In rotorcraft applications, the blade tip vortex interaction is a major source of undesirable noise and vibration. When a rotor blade encounters the trailing vortex shed from the preceding blade, the result is a sudden, impulsive loading on the blade which can cause structural deflection and damages as well as an acoustic noise that can limit low-altitude helicopter operations in populated areas.

Figure 1.1 Wing tip vortices at take-off [115]

One of the major challenges in today's aeronautics is the problem of improving flight safety particularly in the vicinity of airports. In fact, the encounter of an airplane during take-off or landing with the trailing vortices generated by a preceding aircraft can present a serious hazard as it occurs near the ground. Imposed roll, loss of altitude and strong structural loads are some of the dangers that preceding aircraft may encounter. To ensure the safety of aircraft with similar flight paths, air-traffic regulations imposed minimum separation distances that depend on the size and weight of the leading as well as following aircraft. These distances are meant to allow sufficient time for the strong trailing vortices to dissipate so that they no longer pose a hazard to the following aircraft [48, 77, 89].

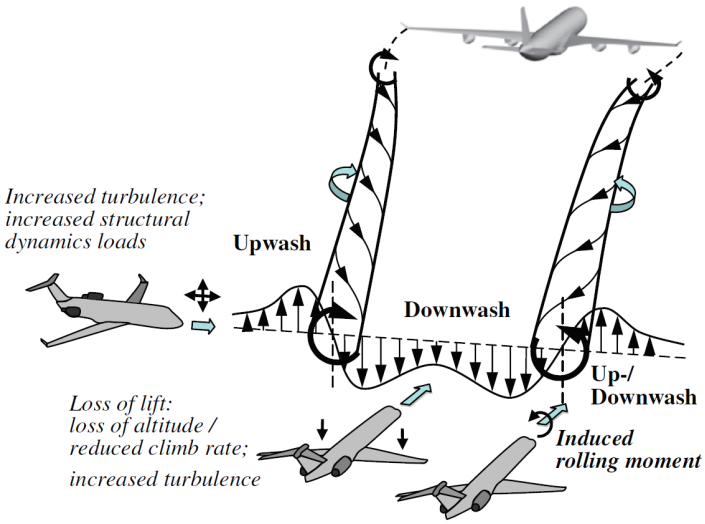

Figure 1.2 Wake vortex hazard [97]

A vortex forms at the tip of any lifting surface as a direct consequence of the pressure difference between the suction and pressure sides. This pressure difference results in a force normal to the free stream and is usually referred to as the lift force. For typical aircraft wings of a finite span, the high pressure fluid on the bottom surface will tend to move towards the wing tip, and leak around to the low pressure side. The spanwise pressure gradient generates a spanwise component of velocity and a corresponding velocity gradient as the pressure difference vanishes out towards the tip. Fed by vorticity from the boundary layer near the tip, the wing tip vortex grows and develops, entrains additional shear layer vorticity and rolls up into an increasing helical structure as it convects downstream. Under the action of viscous and turbulent diffusion, the tip vortex slowly decays with increased downstream distances. This process takes several tens or even several hundreds of chord lengths before the tip vortex completely dissipates [107]. Turbulent and viscous losses responsible for the decay and diffusion of the vortex generally manifest at the external

region of the vortex where the tangential velocity is maximum and the shear stresses are significant. However, the near-solid-body rotation stabilises the core region and makes it less prone to diffusion during the early stage of its development.

Wing tip vortices can be generated in wind tunnel environments, which provides researchers and experts with the advantage of studying the physical phenomenon related to their formation and development in the near, intermediate and far-wake regions. Interestingly, it has been observed that the vortex axis tends to meander side to side as it convects downstream [2, 27, 37, 57, 102]. This introduces additional challenges in the processing and interpreting of the measured data as the vortex velocity field is significantly affected by the vortex meandering. The inherent mechanism responsible of the vortex meandering has always been accepted to be an artifact of wind tunnel imperfections. More recent studies, described the vortex meandering phenomenon to be the result of several independent processes including flow instabilities and free stream turbulence interactions.

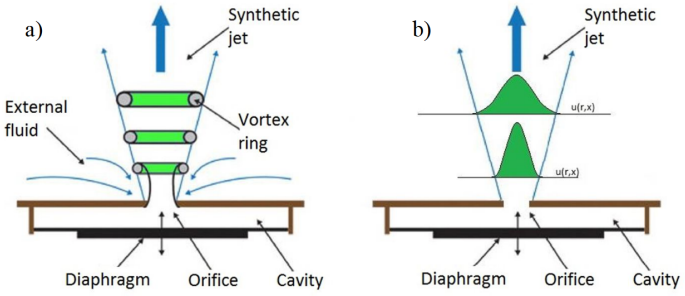

Figure 1.3 Synthetic jet. a)instantaneous and b)time-averaged flow-field [109]

An increased induced drag and a wandering trailing vortex constitute some of the detrimental characteristics of tip vortices on the aerodynamic efficiency of aircraft. Various solutions have been suggested addressing these problems. Some of these remedies suggested reshaping the tip, using of winglets or implementing passive control devices for wake vortex alleviation. Advances in control technology have made the use of active control devices more viable. An important advantage of active means of flow control is their ability to be adapted and optimised for different flight conditions and throughout the flight envelop. A novel approach of implementing active control techniques aiming to alleviate or ultimately suppress trailing vortices employs zero mass-flux fluidic perturbations namely Synthetic Jets (SJ). Such control strategy is believed to outperform the technique of steady blowing and suction as it exhibits less technological challenges and provides more effective forcing. A typical SJ actuator consists of a jet orifice opposed on one side by an enclosed cavity, as illustrated inFigure 1.2. Series of vortices can be generated and ejected from the orifice as a result of time-periodic displacement of the cavity diaphragm yielding

to time-dependent changes in the volume of the cavity. The counter-rotating vortex pair separated from the orifice edges imparts additional momentum to the surrounding flow, although the net mass flux through the orifice is zero.

1.2 Objectives and approach

The effects of active flow control, in particular synthetic jet actuation, on wing tip vortices remain largely understood and undocumented. There is little information available in the literature on the long-time evolution of a wing tip vortex under the effect of fluidic excitation, from genesis to breakdown. The dearth of experimental studies on this topic resulted in a lack of understanding of the underlying mechanisms of vortex dissipation in the presence of turbulent structures injected by a synthetic jet. As a result, the key points that have not been successfully answered by previous studies and that have been thoroughly addressed in the present work.
Therefore, the specific objectives of this thesis can be summarized as follows:

- Document the effect of synthetic jet actuation on the early formation of a wing tip vortex in the near-wake region.
- Identify the mechanisms responsible of the vortex diffusion and breakdown under the effect of fluidic excitation.
- Quantify the contributions of the synthetic jet actuation and the meandering motion on the diffusion and decay of a wing tip vortex.
- Provide further insight into the phenomenon of vortex meandering using POD decomposition

1.3 Thesis outline

The thesis is structured as follows: Details of the first experimental setup, test conditions and measurement techniques were provided in Chapters 2&3. Results of the hot-wire survey on the effect of SJ actuation of the development of a wing tip vortex were presented in Chapter 2 for the near-wake region and in Chapter 3 for the mid-wake region. A detailed description of the second experimental setup along with the SPIV technique were presented in Chapter 4. In this chapter, the determination of the meandering coherent motion of the wing tip vortex via a triple decomposition of the meandering-corrected velocity field is presented. Further insights into the phenomenon of vortex meandering under the effect of SJ actuation are also provided using POD decomposition. A summary of the important conclusions and remarks is then provided in Chapter 5.

CHAPTER 2

Effect of active flow control on the development of a wing tip vortex in the near wake region

2.1 Avant-propos

Auteurs et affiliations:

1. Marouen DGHIM: Étudiant au doctorat[†,*]
2. Mohsen FERCHICHI: Professeur titulaire[*]
3. Ruben E. PEREZ: Professeur agrégé[*]
4. Mahen BEN CHIEKH: Maître de conférences[‡]

[†]Université de Sherbrooke, Faculté de génie, Département de génie mécanique.
[*]Collège Militaire Royal du Canada, Faculté de génie, Département de génie mécanique et aérospatial.
[‡]École Nationale d'Ingénieurs de Monastir, Université de Monastir.

Date d'acceptation: 4 Avril 2016.

État de l'acceptation: version finale publiée.

Revue: Aerospace Science and Technology.

Titre en français:

Effet du contrôle actif sur le développement d'un tourbillon de bout d'aile dans le sillage proche.

Contribution au document:

Cet article contribue à la thèse en mettant en évidence l'effet du contrôle par jet synthétique sur la formation et la genèse d'un tourbillon de bout d'aile dans la région du sillage proche.

Résumé en français:

Une étude expérimentale sur l'efficacité de l'actionnement d'un jet synthétique dans le contrôle d'un tourbillon de bout d'aile NACA 0012 à extrémité carrée rectangulaire à un nombre de Reynolds de corde $Re_c = 8 \times 10^4$ a été rapportée. Des mesures de pression sur la surface d'aspiration de l'aile ont montré que forcer le tourbillon de bout d'aile à une fréquence dans la plage de fréquences des instabilités des ondes longues et courtes, a entraîné une diminution des coefficients de pression par rapport aux mesures de tourbillons naturels. Deux configurations de contrôle ont ensuite été considérées pour les mesures à fils chauds dans le sillage, à savoir une configuration "moins efficace" avec un coefficient d'impulsion $C_\mu = 0.004$ et une fréquence d'activation $F^+ = 0.71$, et une configuration "plus efficace" avec $C_\mu = 0.04$ et $F^+ = 0.213$. Des mesures à $x/c = 1$ ont montré que, dans ce dernier cas, le tourbillon était étiré en une forme ellipsoïdale avec une diminution moyenne de 50% de la vitesse tangentielle maximale et un élargissement de 30% du rayon de noyau de vortex. Plus en aval, le tourbillon semble retrouver sa forme universelle mais avec une résistance réduite. Les résultats suggèrent que la configuration de contrôle avec la fréquence la plus basse a permis au jet synthétique de parcourir de plus grandes distances dans le vortex, amenant des structures turbulentes à l'intérieur de son noyau, entraînant un mélange accru et une diminution de la circulation du tourbillon.

2.2 Near Wake Development of a Wing Tip Vortex Under the Effect of Synthetic Jet Actuation

An experimental investigation on the effectiveness of synthetic jet actuation in controlling a wingtip vortex of a rectangular, square-tipped NACA 0012 wing at a chord Reynolds number $Re_c = 8 \times 10^4$ is reported. Spanwise pressure measurements on the suction surface of the wing showed that forcing the wingtip vortex at a frequency in the range of frequencies of the long and short-wave instabilities, resulted in decreased pressure coefficients as compared to natural vortex measurements. Two control configurations were then considered for hot-wire wake measurements, namely, a "least effective" configuration with momentum coefficient $C_\mu = 0.004$ and actuation frequency $F^+ = 0.71$, and a "most effective" configuration with $C_\mu = 0.04$ and $F^+ = 0.213$. Measurements at $x/c = 1$ showed that, under the latter case, the vortex was stretched into an ellipsoid shape with a 50% average decrease in the peak tangential velocity, and 30% broadening of the effective vortex core radius. Further downstream, the vortex seemed to regain its universal shape but with reduced strength. The results suggested that the lower frequency control configuration allowed the synthetic jet to travel larger distances into the vortex bringing turbulent structures within its core resulting in increased mixing and subsequently decreased vortex strength.

2.2.1 Introduction

Wingtip vortices are of great importance in aerodynamics because of their impact on many practical applications such as airplane drag, wake encounters in congested airports, vortex blade interaction, noise and vibration, and more. For example, induced drag caused by wingtip vortices plays a significant role in its performance as it can amount to up to 40% of the overall aircraft drag [120]. Similarly, the region of strong coherent rotational flow induced by wingtip vortices typically persists for several nautical miles which may pose a potential hazard to the following aircraft both in ground proximity and en-route [48, 89]. Imposed roll (up to 45 degrees has been reported [72]), loss of altitude and stable flight conditions and strong structural dynamic loads are some of the dangers that the following airplane may encounter [77]. Control devices capable of mitigating or weakening the effect of wake vortices to safe levels could enable operational improvements through the reduction in the minimum separation distance between airplanes. Despite the numerous studies on wingtip vortex flows, the state of knowledge is yet to provide a firm base for the design of effective wingtip geometry or control devices. The idea behind developing wingtip devices is to mainly introduce instabilities to initiate wake destruction [107] and there-

fore improve the aerodynamic characteristic of the corresponding lifting surface [1, 67]. Methods of wingtip vortex control can be divided into either passive or active, airborne or ground-based. In the past decade, several methods have been proposed to modify the structure of wingtip vortices on airplane wings, including wing endplates, wingtip sails [108], winglets [47, 116], spiroid winglets [52], wingtip mounted slender half-delta wing [75, 76], oscillating flaps [54], oscillating winglet flaps [18], plasma actuator [55], continuous blowing [59, 80] and pulsed jets [9, 10, 57]. Despite the overall decrease in total drag, winglets have been shown to increase parasitic drag [17]. They may also pose a structural challenge and an inherent limitation to aircraft design as they are generally optimized for part of the flight envelope. Nevertheless, these wingtip devices have been traditionally adopted by aircraft manufacturers. More recently, a patent entitled "Surface Structure on a Ground Surface for Accelerating Decay of Wake Turbulence in the Short Final of an Approach to a Runway" has been suggested in [61], and later tested by the German Aerospace Center (DLR) [62] to reduce the vortex effects encountered in airport runways. The method consisted of placing parallel ground plates near the runway threshold. They found that the introduction of plate lines generate secondary vortices which were drawn and looped around the wing tip vortex. The highly intense interaction of the wingtip vortex and the secondary vortices resulted in a rapid spreading and propagation of disturbances along the wake-vortex direction leading to a fast approaching and early vortex decay in ground proximity [62]. The suggested ground-based method requires relatively little technical effort to be tested and to be installed in airports. However, this method remains passive. The difficulties in parametrically describing all these designs and computationally testing them are continuously driving designers of modern aircraft towards more known, corroborated and simple choices that can be adapted to all flight configurations, specifically landing and take-off. For these reasons, the attention has been recently shifted towards active flow control techniques. As opposed to passive devices, the former can be optimized for a given flight segment of the flight envelope, leading to improved control efficiency of the wingtip vortex. Heyes et al. [57] used pulsed span-wise air jets at the wingtip to perturb a vortex evolving in the near field. They demonstrated that wingtip jets caused a displacement of the vortex with a magnitude proportional to the blowing rate. They also showed that with actuation, a remarkable increase in core radius accompanied with a decrease in peak circumferential velocity and an increase in the core axial velocity deficit were directly related to the added mass of fluid ejected from the wingtip slot. A more elaborate active flow control technique, which uses zero net mass flux fluidic perturbation namely, synthetic jets (SJ) is believed to outperform steady blowing and steady suction as it exhibits less structural challenges and provides more effective

forcing in that no air bleed from the engine is required to operate SJs as they add momentum, turbulence and vorticity to the flow. In addition, SJs introduce variable frequency disturbances that can be tuned to the inherent instabilities of the wingtip vortex. Margaris and Gursul [79] conducted a PIV study on the effect of synthetic jet actuation (SJA) on a wingtip vortex using a wing equipped with several blowing slot geometries placed at different positions at the wingtip proximity. They found that the rate of reduction in the tangential velocity was comparable to that obtained with a continuous blowing. However, no conclusions were drawn on the choice of actuation parameters. Duraisamy and Baeder [41] numerically reproduced the experimental study reported in [57] on the effect of spanwise steady and oscillatory blowing on the wing tip vortex. They achieved a reliable validation of the mean flow field by using a high order accurate scheme with appropriately refined meshes. They concluded that the interaction of the pair of counter-rotating vortices with the vorticity sheet feeding the wing tip vortex resulted in an increased turbulence level in the vortex core; however, no appreciable control effect was achieved by means of SJA as compared to continuous blowing. In a recent study, Greenblatt [50] used a different technique to control the wingtip vortex consisting of deflecting an outboard flap mounted on a wing semi-span and then, modifying the shear layer above the flap by means of SJ perturbations. He showed that a relatively small control momentum coefficient can produce large changes in the shear layer deflection and the flap pressure distribution with relatively small changes in the local aerodynamic loads. However, the deflection of the shear layer was found to move the wing tip vortex outboard considerably, and change the axial velocity in the vortex core from a wake-like to a jet-like flow. A substantial increase in the core axial vorticity and an associated overshoot in circulation were both reported when the actuation was applied. In a more recent study, Dghim et al. [39] used a high aspect ratio curved slot SJ mounted at the tip to control a wing tip vortex at a relatively low Reynolds number. They reported nearly 30% decrease in the core axial vorticity and an increase in the lateral diffusion of the vortex due to turbulence addition. However, the selection of the SJ control parameters was left inconclusive. In their study, only a single actuation frequency and a single momentum coefficient were tested using a curved high aspect ratio jet. Due to the relatively low amplitude of flow velocities generated by SJs, they may not be efficient for cruise flight conditions of commercial aircraft. However, SJs may be effective at low Reynolds number applications such as take-off and landing of commercial aircraft, and also typical of all flight conditions of mini and micro UAVs. For example, take-off and landing of current aircraft are typically performed at velocities in the range of 40 to 90 m/s [107]. At the wing tips, the vortex circumferential velocity component, $\bar{U}_\theta$, would be about 40% that of the freestream, which translates to velocities

of 16 to 36 m/s. These velocities are well within the range for which their ratio with peak actuation velocities achievable by a SJ ($\bar{U}_\theta/\bar{V}_{j,\max}$) provides positive changes to the vortex behavior over large range of low Reynolds numbers [50]. The purpose of this study is to experimentally explore the behavior of the wing tip vortex strength due to activation of a high aspect ratio SJ introduced near the wing tip. A comprehensive set of quantitative results using hot-wire measurements supported by pressure measurements were obtained to highlight the importance of SJA parameters and to provide a physical understanding of the control mechanism leading to the reduction of the wing tip vortex strength.

2.2.2 Experimental Apparatus

The experiments were conducted in a blow-down, low-speed wind tunnel located in the Department of Mechanical and Aerospace Engineering at the Royal Military College of Canada. The wind tunnel has a test section of 0.41×0.41 m^2 cross section. It has a 16:1 contraction upstream of the test section. The mean streamwise velocity in the empty wind tunnel is uniform to within $\pm 1\%$ and a turbulence level of about 0.2%. The model used in the present study was a rectangular planform half-wing with a NACA 0012 airfoil section. The square-tipped half-wing had a chord $c = 154.2$ mm, a semi-span $b/2 = 203.2$ mm (aspect ratio of 2.7), and a dihedral of $\delta = 3°$. The origin of the coordinate system was anchored to the wing tip at the quarter-chord location with x,y and z coordinates aligned respectively with the streamwise, spanwise and transverse directions of the wind tunnel reference frame (Figure 2.1a). The half-wing was manufactured from ABS plastic using a high resolution 3D printer (model: ProJet 3000 HD, 3D Systems, Inc.). It had a hollow rectangular chamber throughout the wingspan for the supply of airflow generated by the loudspeaker as shown in Figure 2.1b. The SJ cavity consisted of a contraction nozzle placed outside the wind tunnel where a loudspeaker (model Visaton GF200) was attached. The loudspeaker was controlled by a function generator connected to a power amplifier (model Hafler PRO5000). The blowing slot at the wing tip was in fluidic communication with the hollow plenum. To counteract the roll-up of the vortex, the SJ slot was designed such that the injected airflow curls down as it passes through a curved nozzle placed inside the half-wing. The slot had a trapezoidal shape of 1 mm height close to the leading edge and 2 mm height near the trailing edge. The total slot length, L_j, was about 114.3 mm. The slot shape was designed such that the SJ velocity is non-uniform along the chord direction to account for changes in the angular velocity of the curling vortex as it evolves towards the trailing edge (Figure 2.1b).

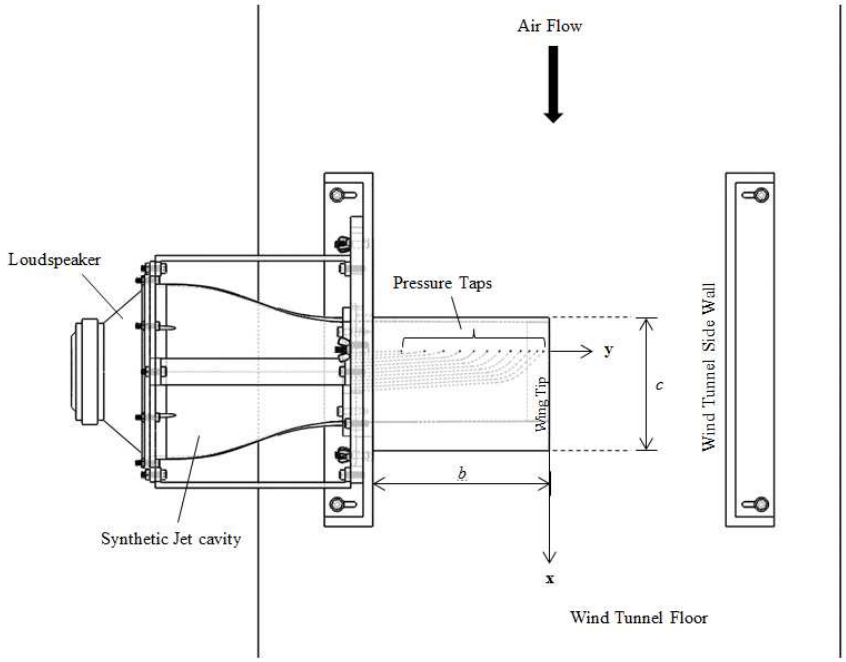

(a)

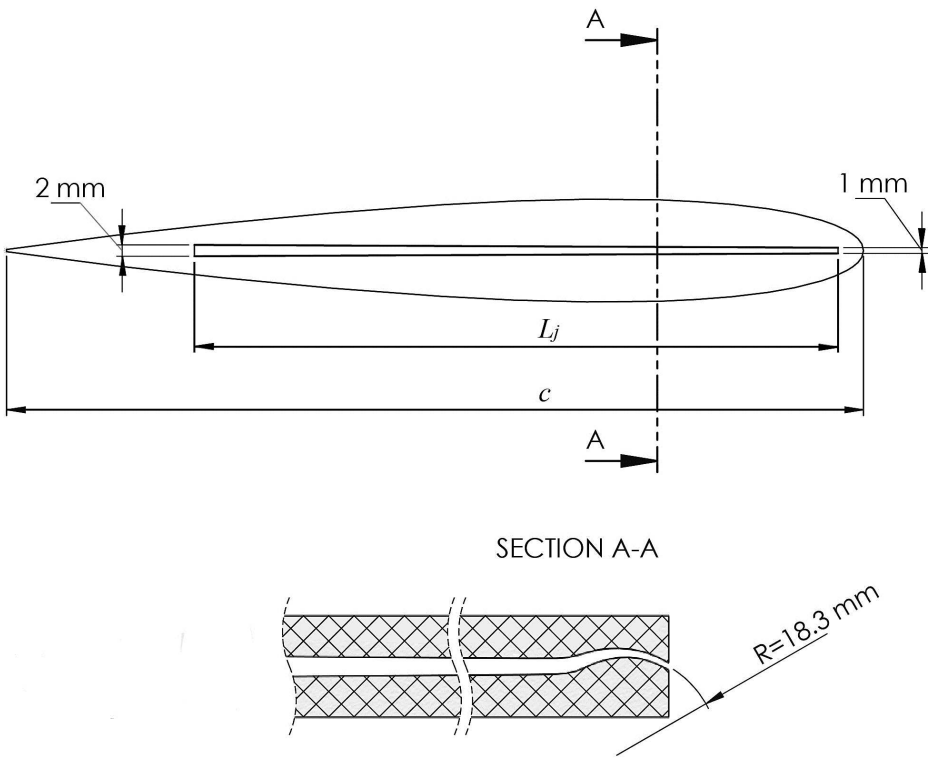

(b)

Figure 2.1 (a) Experimental setup. (b) SJ slot geometry.

The characterization of the generated SJ was performed by means of hot-wire measurements. The SJ momentum coefficient, C_μ, was estimated as:

$$C_\mu = \frac{A_j}{A_w}\frac{\rho_j \bar{V}_j^2}{\rho_\infty \bar{U}_\infty^2} \tag{2.1}$$

where A_j is the slot area and A_w is the half-wing planform area. The SJ time and spatial-averaged velocity scale, $\bar{V}_j$, measured along the slot centerline, is defined by Holman et al [60] as:

$$\bar{V}_j = \frac{2}{T}\frac{1}{A_j}\int_A \int_0^{\frac{T}{2}} \vec{v}_j \cdot d\vec{A}\, dt \tag{2.2}$$

where $\bar{V}_j$ was based only on the blowing phase of actuation to avoid characterization challenges such as the "sink-flow" effect during suction as well as hot-wire rectification. T represents the actuation period. The actuation frequency was non-dimensionalized as:

$$F^+ = \frac{f_a L_j}{\bar{U}_\infty} \tag{2.3}$$

where f_a is the actuation frequency and L_j is the characteristic length of the SJ [51]. Typical profiles of the maximum velocity along the centerline of the SJ slot exit, $\vec{v}_j$, normalized by the maximum SJ velocity at $x/L_j = 0.2$,$\vec{v}_{j_0}$, are shown in Figure 2.2. Clearly the shape of the slot selected resulted in a noticeable velocity gradient along the SJ centerline. Typical time traces of the hot-wire signals at $x/L_j = 0.2$ are plotted in Figure 2.3. The instantaneous jet exit velocity was nearly periodic with the frequencies of the excitation signals but with a prescribed phased lag. Note that for every actuation cycle, the hot-wire signal was corrected for the suction phase. A total number of 12 pressure taps were placed on the suction side of the wing and were logarithmically spaced along the wing span at c/4 and were connected to a Scanivalve (model ZOC 22B) pressure scanner through flexible Tygon tubing. A total number of 25,600 scans were sampled at 500 Hz. A custom-built miniature four-sensor hot-wire probe consisting of two orthogonal X-wire arrays (Auspex Scientific AVOP-4-100) was used in this study to measure the instantaneous three components of the velocity vector field. The tungsten sensors had a diameter of 5μm and a length of 1 mm. The hot-wire probe was mounted on a streamlined automated traversing mechanism that allowed translations in the streamwise, spanwise and transverse directions. The hot-wire probe was powered by a multichannel TSI IFA 300

constant temperature anemometer. All signals were low-pass filtered at a frequency of 2 kHz and simultaneously digitized at a rate of 5 kHz using an IOTECH 16 bit analog-to-digital converter. Time-averaged statistics were calculated from recorded samples with a length of 15 s. All experiments were carried out at an angle of attack of 5 degrees and a free stream velocity, $\bar{U}_\infty$, of 8 m/s, corresponding to a Reynolds number, $Re_c = 8 \times 10^4$. The maximum uncertainties in the experimental measurements according to [70] are as follows; mean velocity 3%, vorticity 9%, and pressure coefficient 0.2%. Throughout this study, qualitative and quantitative data of the controlled cases were all compared to the natural vortex case ($C_\mu = 0$). Table 2.1 summarizes the experimental configurations selected for the wake flow survey.

Table 2.1 Control configurations

	F^+	C_μ
Natural Vortex case (NV)	-	-
Control case 1 (C1)	0.710	0.004
Control case 2 (C2)	0.213	0.040

2.2.3 Preliminary study on the selection of actuation parameters

A comparative study on the SJ control parameters was conducted in order to evaluate the effect of SJA on the time-averaged spanwise pressure distribution, C_p, along the suction side of the wing at the $c/4$ streamwise location. While the jet exit slot geometry was kept unchanged, both the driving frequency, F^+, and the jet momentum coefficient, C_μ, of the SJ were varied. The distribution of the normalized local pressure coefficients, $C_p/C_{p_{nv}}$, where $C_{p_{nv}}$ is the local pressure coefficient for the uncontrolled flow, are shown in Figure 2.4 and Figure 2.5 for different control configurations. A maximum momentum coefficient value of 0.04, which corresponded to a maximum jet velocity at the slot exit, $\bar{V}_j$, of about 21 m/s was imposed in this study. For $C_\mu \geq 0.04$, the effect of the actuation frequency was no longer discernible. The effect of the SJA frequency on the spanwise pressure coefficients is illustrated in Figure 2.4 for C_μ of 0.04. Near the wing tip, at $y/b/2 > 0.8$, a considerable increase in the values of $C_p/C_{p_{nv}}$, which translates into a decrease of pressure on the suction side of the wing, was reported for all the control frequencies tested. The normalized pressure coefficients gradually increased with decreased actuation frequency in particular near the wing tip where they reached a nearly 60% increase at $F^+ = 0.213$ with respect to the natural vortex case. This frequency falls within the wavelength interval corresponding to the inherent instabilities of the wing tip vortex. The latter ranges from the long-wave Crow's instability, λ_L 7.85b, [19, 31, 43, 44] to the shorter-wavelength cooperative Widnall instabilities, λ_S 0.9b, [44, 90, 117]. These wavelengths imply perturbation frequencies,

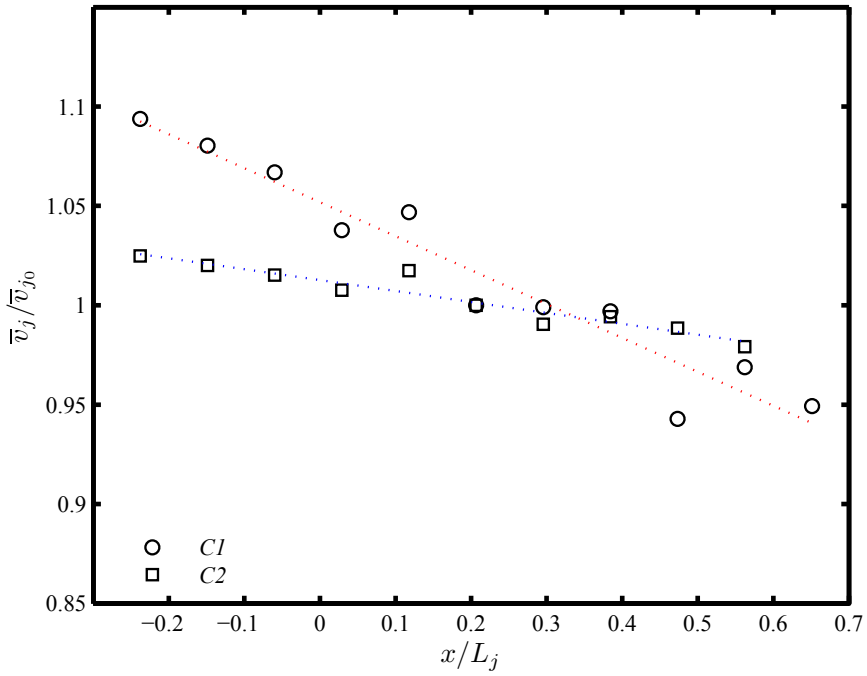

(a)

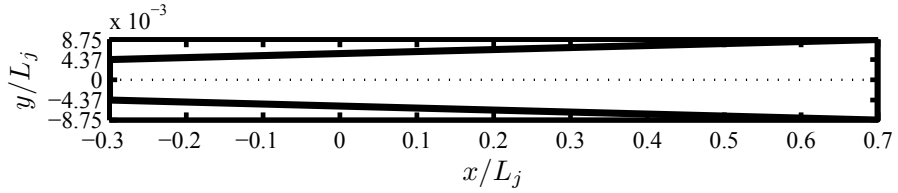

(b)

Figure 2.2 Chordwise variation of the time-averaged maximum velocity along the SJ slot centerline.

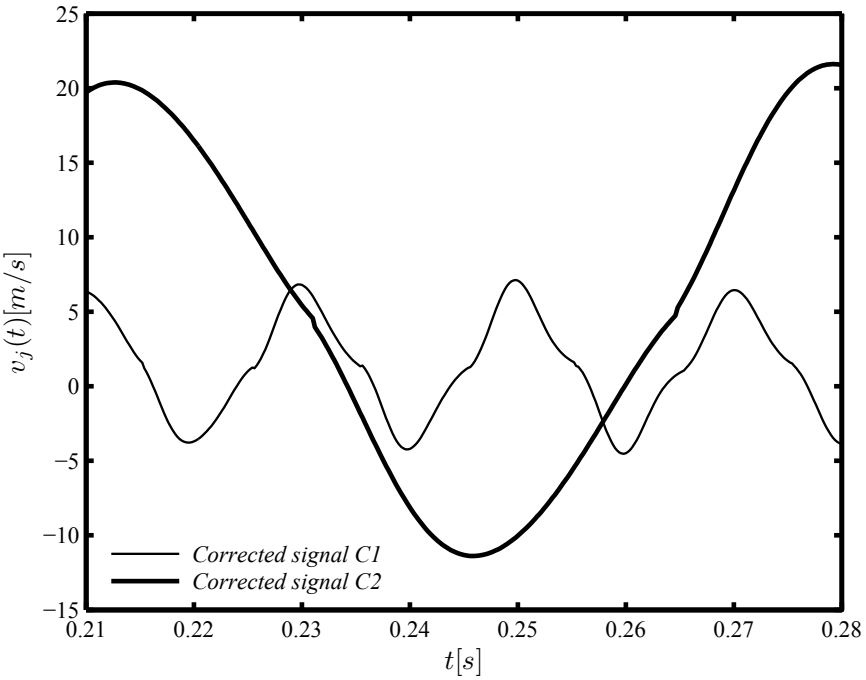

Figure 2.3 Typical time traces of the acquired hot-wire signal at the SJ slot exit.

$F^+ = f_\lambda L_j/\bar{U}_\infty$ where $f_\lambda = \frac{\bar{U}_\infty}{\lambda}$, in the range of 0.035 to 0.3. At $F^+ = 0.213$, a comparative study on the effect of actuation momentum coefficient was also conducted. Figure 2.5 shows the normalized pressure coefficient distributions for various C_μ values. The pressure on the suction side of the wing appeared to decrease with increased C_μ. The control parameters of [39] were selected and used to measure the spanwise pressure distribution which was not provided in their study, and the corresponding $C_p/C_{p_{nv}}$ distributions were plotted in Figure 2.4 and Figure 2.5. Although this case exhibited an overall increase of the normalized pressure coefficients along the wing span, it was considered the least efficient among all tested configurations. It is of interest to show the importance of selecting the appropriate control parameters for this type of flow therefore, the "least-optimal" case was considered for the hot-wire survey which will be discussed in the next section. Comparison between the two selected experimental configurations was deemed appropriate even though their C_μ are different since the normalized pressure coefficients at F^+ of 0.71 are largely insensitive to changes in C_μ.

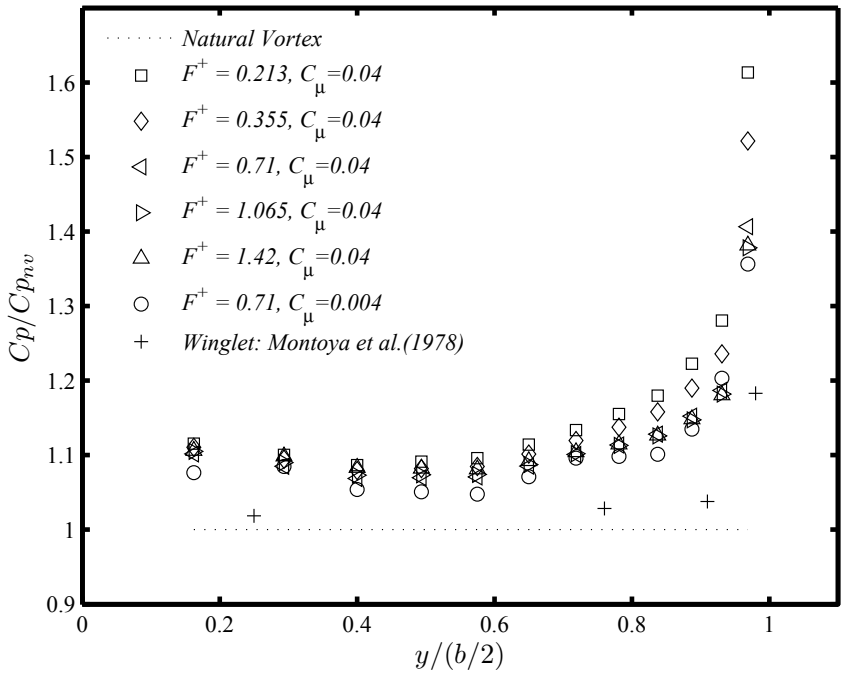

Figure 2.4 Spanwise distribution of the normalized pressure coefficients on the wing upper surface at different actuation frequencies.

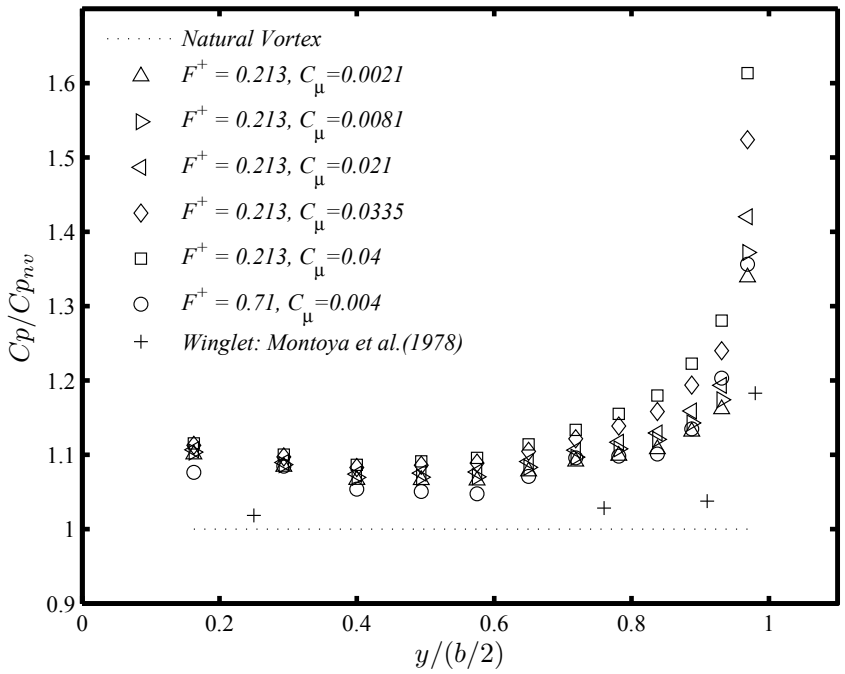

Figure 2.5 Spanwise distribution of the normalized pressure coefficients on the wing upper surface at different actuation momentum coefficients.

2.2.4 Quantitative study

Development of the streamwise velocity

Contour plots of the normalized mean streamwise velocity, $\bar{U}_x/\bar{U}_0$, where $\bar{U}_0$ is the local free-stream velocity which was at worst 3% lower than the undisturbed free-stream $\bar{U}_\infty$, at the measurement planes $x/c = 1$ and $x/c = 2$, are shown in Figure 2.6a and Figure 2.6b for the natural vortex (NV) and Figure 2.6c and Figure 2.6d for the control configuration (C1) and Figure 2.6e and Figure 2.6f for the control configuration (C2), respectively. The dashed line in the figures denotes the position of the trailing edge of the wing. At $x/c = 1$, velocity contours of the NV wake shear layer (Figure 2.6a) showed a nearly straight and horizontal region dominated by a velocity deficit, $\bar{U}_x/\bar{U}_0 \approx 0.85$. The velocity contours of the vortex inner region exhibited a circular and nearly axisymmetric shape where the maximum deficit occurred, but the outer region showed an ovoid shape as the separated shear layer was not entirely drawn by the rolling tip vortex. As the vortex developed downstream to $x/c = 2$, curvature of the contours increased and the wake shear layer appeared to be drawn and fully wrapped around the vortex as a result of the strong velocity deficit near its core (Figure 2.6b). For the C1 case (Figure 2.6c) the vortex core and the wake shear layer at $x/c = 1$ exhibited nearly a 7% lower velocity deficit compared to NV. As the vortex evolved downstream to $x/c = 2$ (Figure 2.6d), it exhibited a wider and more diffuse core region with a 5% decrease in the velocity deficit with respect to NV at the same streamwise location. At this location, the wing tip vortex appeared to have an asymmetric structure similar to that of the NV, but with an increased core size. Outside the vortex core, the rolling shear layer was thickened and its velocity deficit decreased. This is believed to be the result of the diffusion of the vortex structure by the spanwise flow imparted from the SJ. Figure 2.6e shows the vortex velocity contours in case C2 at $x/c = 1$. The tip vortex exhibited a different structure than that of the NV and C1 cases. The subsequent interaction of the SJ with the wing tip vortex appeared to severely affect the rollup process in which the vortex was stretched into an elliptical shape. A 20% decrease in the core velocity deficit compared to NV was achieved as illustrated in Figure 2.6e. It is noteworthy that the vortex rolled up into a nearly well-organized vortex as it evolved to $x/c = 2$ (Figure 2.6f). This reorganization of the vortex to a more axisymmetric coherent shape may be due to the strong rotational effects of the rolling shear layer. The location of the maximum deficit appeared to move further in the inboard direction towards the wing root. Figure 2.6f indicates an increased velocity deficit as the vortex evolved from $x/c = 1$ to $x/c = 2$. However, the resulting deficit was considerably lower than those measured in the NV and C1 cases.

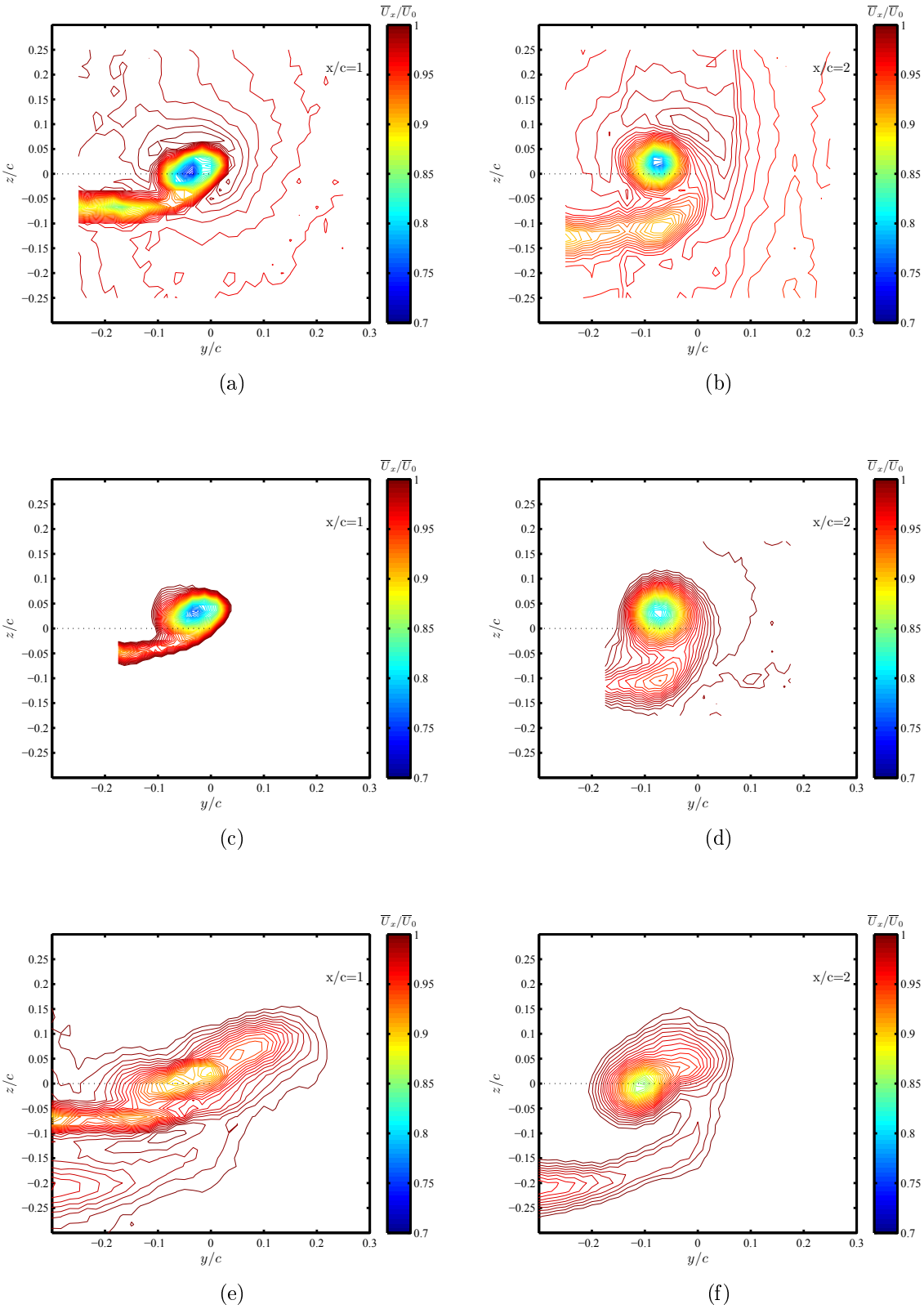

Figure 2.6 Contours of the normalized axial velocity at $x/c = 1$ and $x/c = 2$ locations. (a) and (b): NV, (c) and (d): C1, (e) and (f): C2.

For closer examination of the streamwise velocity development, $\bar{U}_x/\bar{U}_0$ profiles across the wing tip vortex were plotted against the centered coordinates $(y - y_c)/c$, along the axis given by $z = z_c$, where y_c and z_c were the spanwise and transverse positions of the vortex center. The latter was identified as the position where the maximum axial vorticity occurred [76]. Figure 2.7a and Figure 2.7b show the development of $\bar{U}_x/\bar{U}_0$ for the NV, C1 and C2 cases at the locations $x/c = 1$ and $x/c = 2$, respectively. In Figure 2.7a, a large axial velocity deficit in the NV was evidenced by the highly tapered wake-like profiles. This is consistent with the expected velocity deficit resulting from viscous losses suggested by Batchelor [8]. These losses may have been amplified by the effects of the low Reynolds number selected for this study. In Figure 2.7b, as the NV vortex evolved to $x/c = 2$, the maximum velocity deficit decreased by nearly 6% from $x/c = 1$ position, and the wake-like profile appeared wider in the lateral direction which indicated a relative increase in the vortex size. Outside the vortex core, and at both downstream locations, $\bar{U}_x/\bar{U}_0$ profiles reached a nearly asymptotic value that was very close to $\bar{U}_0$. For the C1 case, and at $x/c = 1$, the actuation appeared to affect the axial flow in the vortex core region which resulted in a 5% decrease of its velocity deficit accompanied by a broadening of the velocity profile (Figure 2.7a). The velocity profile, shown in Figure 2.7b, continued to broaden in the outward direction (mostly in the direction of positive $((y - y_c)/c)$ as the vortex evolved to $x/c = 2$. However, at this location, very little change in the maximum deficit was observed with respect to the velocity deficit at $x/c = 1$. In the C2 case, as opposed to the NV and C1 cases, the maximum velocity deficit at $x/c = 1$ was substantially smaller. In fact, at this location, the maximum deficit was reduced by 23% and 17% from those of the NV and C1 cases, respectively. In addition, the higher C_μ of the C2 case appeared to further broaden the velocity profile in the outward direction which indicates an increase in the vortex size. Note that the velocity gradient in the positive $(y - y_c)/c$ is lower than the negative region. This may imply an asymmetry in the vortex shape as it was altered by the higher C_μ selected for case C2. As the vortex moved to $x/c = 2$, the rotational effects of the rolling shear layer were high enough to cause the velocity deficit to increase by nearly 6% from the maximum deficit at $x/c = 1$ position. Although the velocity deficit of the C2 case showed a slight increase at $x/c = 2$, it remained lower than both the NV and C1 cases. Outside the vortex core region and at both measurement positions, $x/c = 1$ and $x/c = 2$, profiles of $\bar{U}_x$ in the C2 case reached an asymptotic value close to $\bar{U}_0$. Interestingly, Heyes and Smith [57] found that increasing C_μ of a pulsed jet blowing from a rectangular slot at the wing tip resulted in an increase of the velocity deficit due to the increased flow blockage caused by the no streamwise velocity component of the pulsed jet.

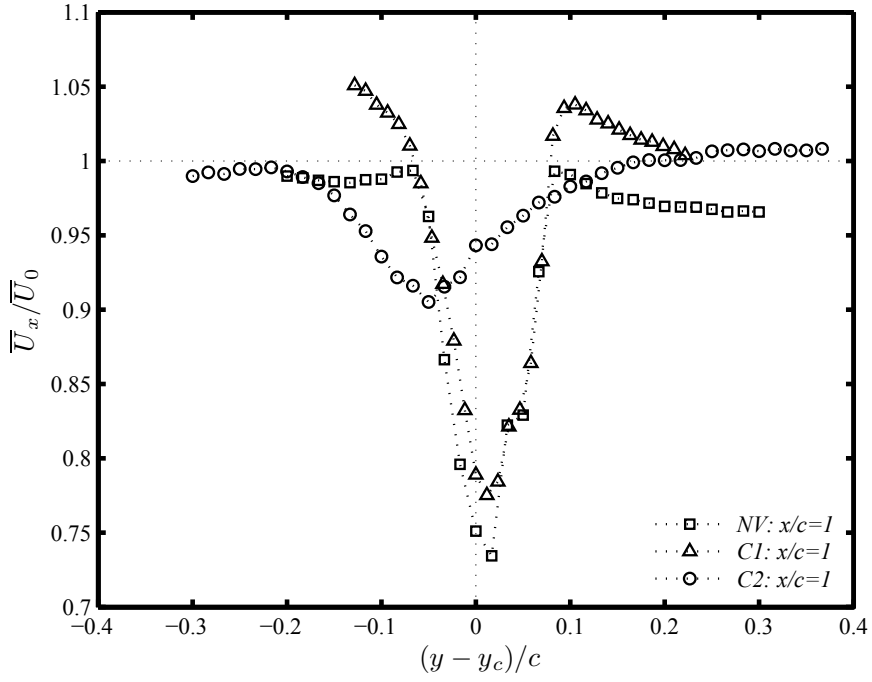

(a)

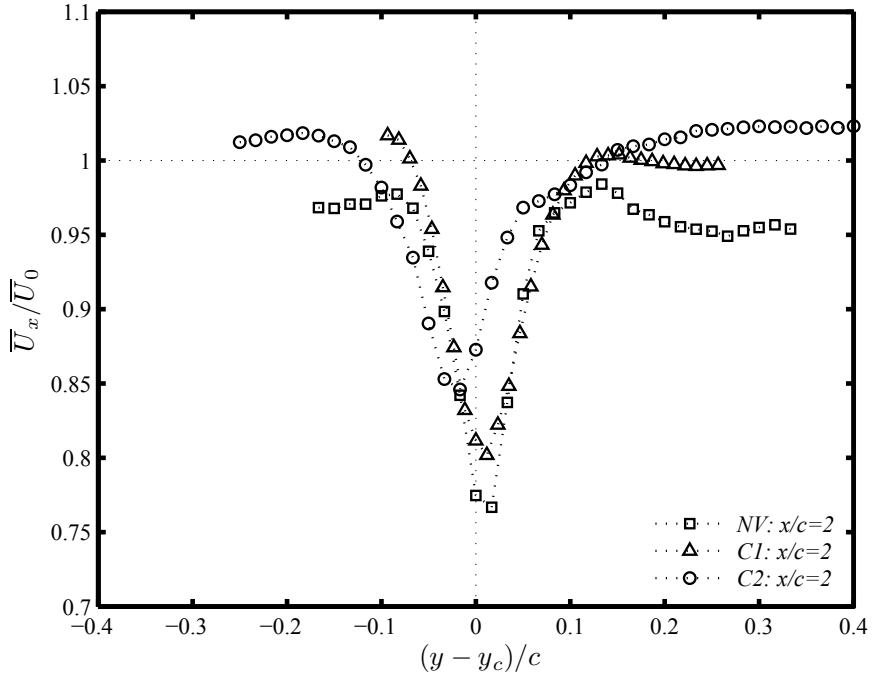

(b)

Figure 2.7 Normalized axial velocity distribution across the vortex center at $(z-z_c)/c=0$. (a) at $x/c=1$ and (b) at $x/c=2$.

Time-averaged circumferential velocity

In order to evaluate the mean circumferential velocity, $\bar{U}_\theta$, the measured spanwise velocity, $\bar{U}_y$, and the transverse velocity, $\bar{U}_z$, were first interpolated in a polar mesh with linearly spaced r/c and θ, where r and θ are the radial and angular positions of the measuring probe in a polar coordinate system centered at the vortex center. The mean circumferential velocity was then calculated as follows:

$$\bar{U}_\theta = \left(\bar{U}_z - \bar{U}_{z_c}\right)\cos\theta - \left(\bar{U}_y - \bar{U}_{y_c}\right)\sin\theta \tag{2.4}$$

where $\bar{U}_{y_c}$ and $\bar{U}_{z_c}$ are the spanwise and transverse velocities of the time-averaged vortex center, respectively. The distribution of the normalized mean circumferential velocity, $\bar{U}_\theta/\bar{U}_0$, against r/c for NV, C1 and C2 cases are shown in Figure 2.8a and Figure 2.8b at $x/c = 1$ and $x/c = 2$, respectively. Interpolated values of $\bar{U}_\theta$ at each measurement plane were divided into two regions: one covering angles between $[270°, 90°]$ where radial positions, r/c, were considered positive, and another region covering angles between $[90°, 270°]$ where radial positions were considered negative. In Figure 2.8a and Figure 2.8b, values of $\bar{U}_\theta$ at a given r/c, were determined by averaging the values of the circumferential velocities, interpolated every 10 degrees, over each region. The vortex radius was defined as the average distance from the vortex center to each of the positive and negative peaks of $\bar{U}_\theta$. Note that at both measurement planes, the circumferential velocity of NV and C1 cases exhibited positive peaks with magnitudes that were nearly 70% and 60% higher than that of the negative peaks. This asymmetry in the distribution of $\bar{U}_\theta$ is believed to be attributed to the wing positive dihedral which may have caused the cross flow to accelerate as it rolls up on to the suction side [74]. In Figure 2.8a and Figure 2.8b, the gradient of $\bar{U}_\theta/\bar{U}_0$ of the NV across the vortex center and within the core region, showed a slight decrease with increased streamwise distance causing the negative peak value of $\bar{U}_\theta/\bar{U}_0$ to increase from a value of -0.15 to a value of -0.13 while the value of the positive peak remained nearly constant. In addition, the normalized vortex radius increased from a value of about $r_{NV}/c = 0.043$ to a value of about $r_{NV}/c = 0.048$. Outside the vortex core, values of $\bar{U}_\theta/\bar{U}_0$ showed a slight increase that may be attributed to the increased roll-up of the shear layer with increased streamwise distance. As opposed to NV, the streamwise change in the peak values of $\bar{U}_\theta/\bar{U}_0$ for the C1 case was more evident; the positive peak value decreased from a value of 0.23 at $x/c = 1$ to a value of 0.20 at $x/c = 2$. However, the negative peak increased from a value of -0.14 to a value of -0.11. The change in the peak values of $\bar{U}_\theta/\bar{U}_0$ was accompanied with an outward displacement

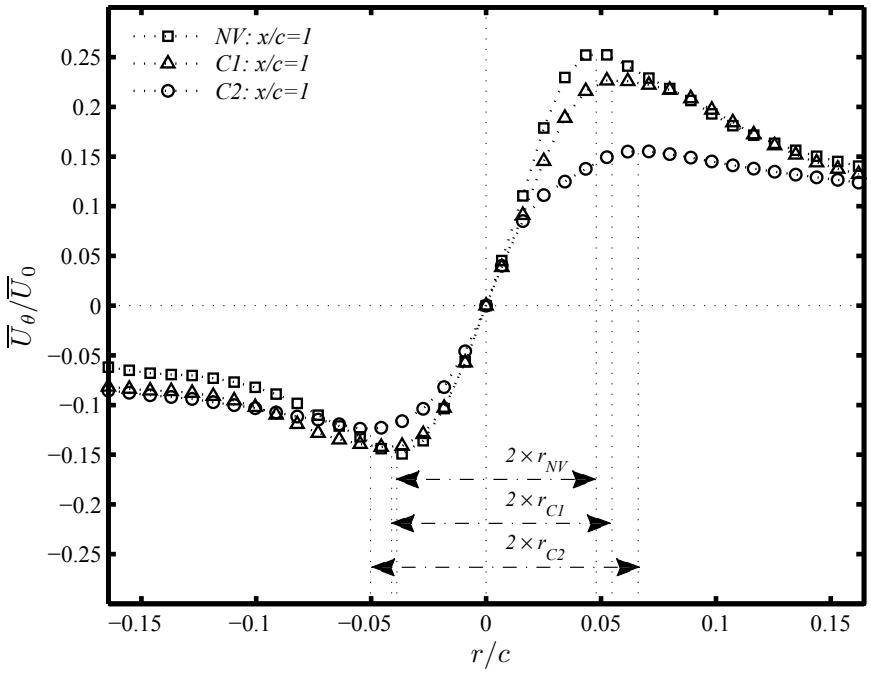

(a)

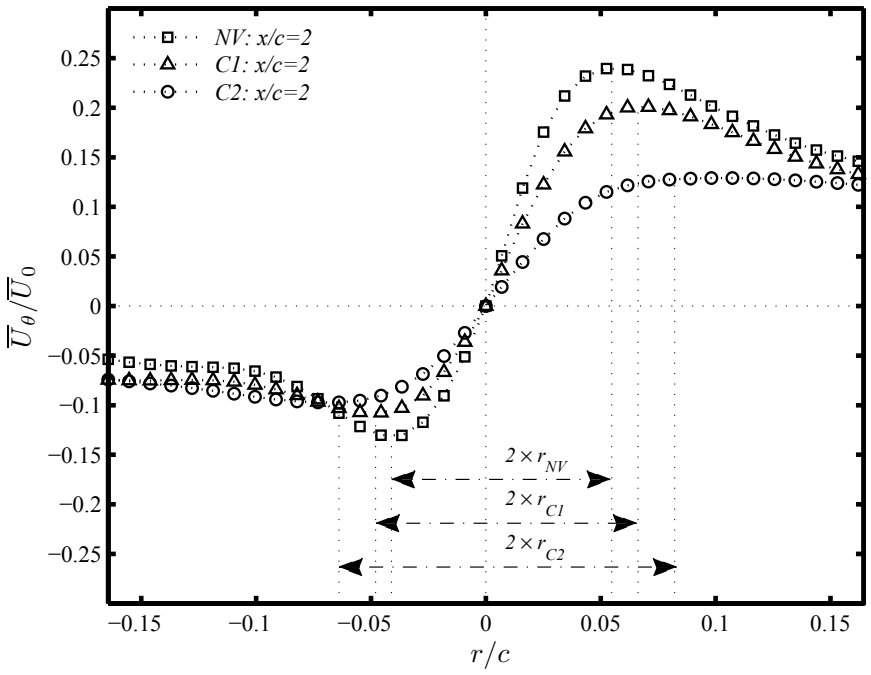

(b)

Figure 2.8 Distribution of the normalized circumferential velocity across the vortex center. (a) at $x/c = 1$ and (b) at $x/c = 2$.

of their positions to larger radial locations, resulting in a relatively large increase of the vortex radius from $r_{C1}/c = 0.048$ at $x/c = 1$ to $r_{C1}/c = 0.057$ at $x/c = 2$. The degree of asymmetry became less pronounced in case C2 at $x/c = 1$, accompanied with a dramatic decrease in circumferential velocity with respect to NV. As the cross flow rolling across the wing tip encountered the relatively high momentum flow imparted from the SJ in case C2, the circumferential velocity at $x/c = 1$ underwent a significant deceleration causing the positive peak values of $\bar{U}_\theta/\bar{U}_0$ to decrease by 60%, the negative peak value to increase by 17% and the core radius, r_{C2}/c, to increase by 30% with respect to NV. With increased downstream distance, and at $(x/c = 2)$, the degree of asymmetry of the circumferential velocity profile in case C2 became less pronounced and the peak values of $\bar{U}_\theta/\bar{U}_0$ were no longer identifiable as the distribution of $\bar{U}_\theta/\bar{U}_0$ increased to nearly asymptotic values with increased r/c. Consequently, it was difficult to identify the vortex radius in the traditional sense. Thus, the vortex "apparent" radius was estimated as the distance separating the radial positions where both positive and negative peak values of $\bar{U}_\theta/\bar{U}_0$ were reached and after which the radial changes in $\bar{U}_\theta/\bar{U}_0$ were no longer significant. Under the effect of C2 case actuation, the positive peak value of $\bar{U}_\theta/\bar{U}_0$ decreased from a value of 0.15 to a value of 0.13; the negative peak value increased from a value of -0.12 to a value of -0.10, and the vortex radius largely increased from $r_{C2}/c = 0.060$ to $r_{C2}/c = 0.074$ as the vortex evolved downstream to $x/c = 2$.

Time-averaged axial vorticity

The hot-wire arrangement used in this study allowed for the estimation of the mean axial vorticity, $\bar{\xi}_x$, estimated as:

$$\bar{\xi}_x = \frac{\partial \bar{U}_z}{\partial y} - \frac{\partial \bar{U}_y}{\partial z} \approx \frac{\Delta \bar{U}_z}{\Delta y} - \frac{\Delta \bar{U}_y}{\Delta z} \tag{2.5}$$

where $\Delta y = 2.54$ mm and $\Delta z = 2.54$ mm were the cross-stream spacing of the measurement grid and $\frac{\Delta \bar{U}_y}{\Delta z}$ and $\frac{\Delta \bar{U}_z}{\Delta y}$ were the velocity gradients across their corresponding grid spacing. A second order central differencing scheme was used to evaluate the gradients. The evolution of the normalized mean axial vorticity contours, $\bar{\xi}_x\ c/\bar{U}_0$, at $x/c = 1$, and its subsequent development downstream at $x/c = 2$ is displayed in Figure 2.9a and Figure 2.9b for NV, in Figure 2.9c and Figure 2.9d for the C1 case and in Figure 2.9e and Figure 2.9f for the C2 case. Contours of the axial vorticity of the NV case at $x/c = 1$, clearly show the roll up of the wake shear layer into a spiraling vortex.

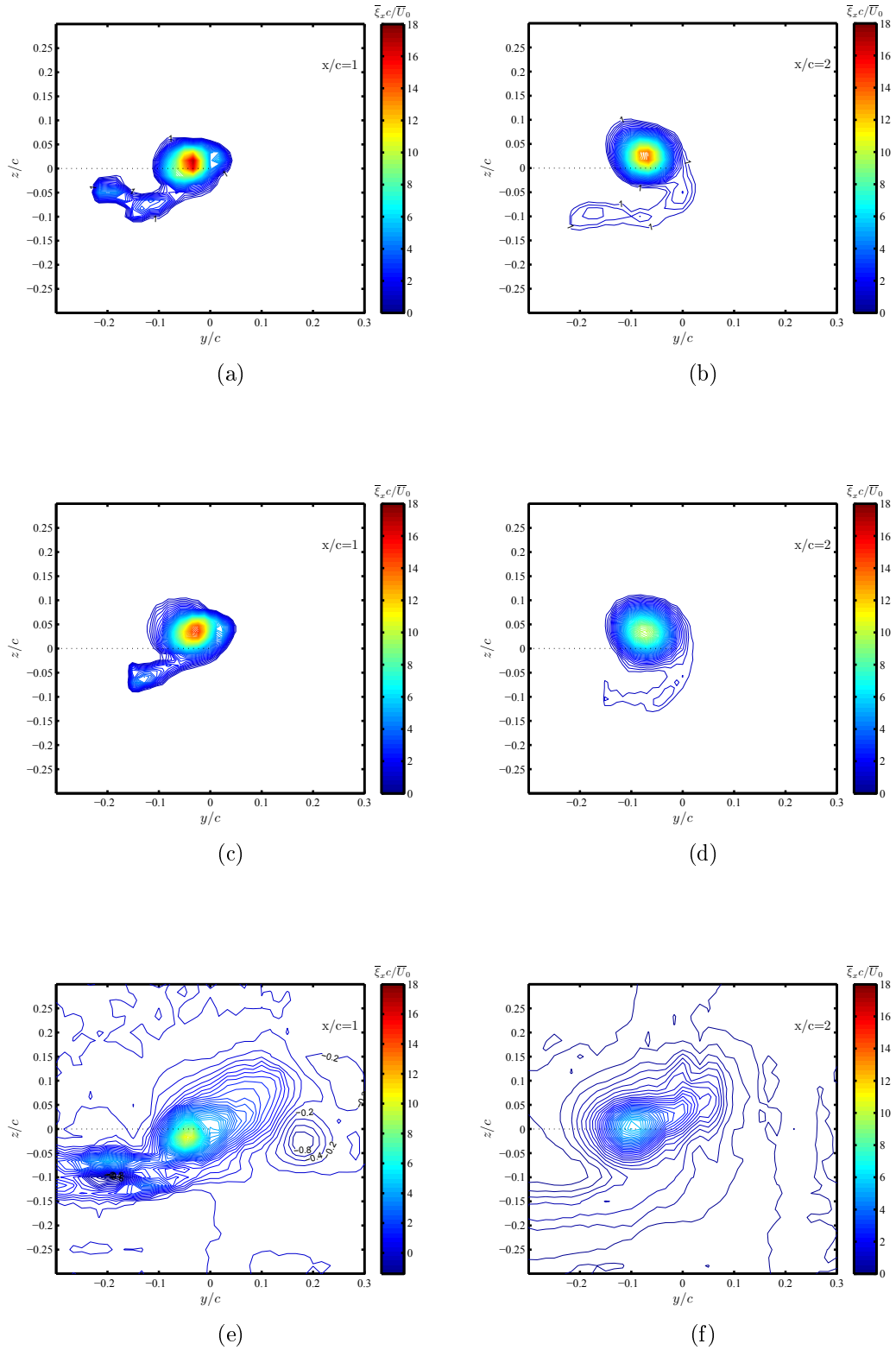

Figure 2.9 Mean axial vorticity contours at $x/c = 1$ and $x/c = 2$. (a) and (b): NV, (c) and (d): C1, (e) and (f): C2.

Most of the vorticity was concentrated in a nearly circular area of a radius of about 0.05c where most of the vortex core is confined. As the NV vortex evolved downstream, the peak value of the normalized mean axial vorticity decreased from a value of about 16.98, at $x/c = 1$, at the vortex center to a value of 13.72, at $x/c = 2$ (Figure 2.9a and Figure 2.9b). This may be attributed to the decreased vorticity of the separated wake shear layer with streamwise distance. In the C1 case and at $x/c = 1$, the actuation achieved a considerable reduction in the normalized vorticity level from a maximum of about 16.98 at the core of the natural vortex to a maximum of about 14.81 at the core of the actuated vortex. The cross flow position of the maximum vorticity, which roughly corresponds to the location of the vortex center, had moved by a distance of 0.02c in the upward direction under the effect of the SJ forcing. The actuation led to a further decrease of about 40% in the maximum normalized vorticity as the vortex evolved to $x/c = 2$. At this downstream plane, vorticity contour on a circle of a diameter of nearly 0.1c exhibited a 30% lower level than that of the natural vortex indicative of an outward diffusion of vorticity. This clearly suggests that the SJA had significantly affected the vorticity level in the wing tip vortex core at its early development, which resulted in a loss of its strength within the near wake region. The C2 control configuration had much larger impact on the wing tip vortex compared to case C1; a considerable initial drop of about 40% in the maximum vorticity level compared to NV was achieved as opposed to the 13% reported in case C1. In Figure 2.9e, the vortex appeared stretched away from the wing tip, and clearly more diffuse than that of the C1 case. A smaller vortex with a low negative vorticity level appeared adjacent to the primary vortex at $x/c = 1$. It is believed that this low vorticity region corresponds to the clockwise rotating vortex ejected from the SJ slot. The former was weakened due to the relatively strong roll-up of the wing tip vortex. The counter-clockwise rotating vortex emanating from the SJ seemed to be merged with the wing tip vortex, leading to a subsequent increase of the vortex size and a diffusion reduction of its maximum core vorticity by nearly 40% with respect to NV. As the vortex evolved downstream, the core vorticity was more diffuse in the outward direction and the vortex appeared larger in size. The normalized maximum vorticity decreased from a value of 10.30 at $x/c = 1$ to a value of 5.81 at $x/c = 2$.

Time-averaged circulation

The mean time-averaged circulation was estimated using the following expression:

$$\bar{\Gamma}(r) = \int_0^{2\pi} \bar{U}_\theta(r)\, r\, d\theta \tag{2.6}$$

In order to study the effect of SJA on the tip vortex circulation, the radial variation of the vortex strength, $\bar{\Gamma}/\bar{U}_0 c$, of the NV, C1 and C2 cases were plotted against r/c at different streamwise locations as displayed in Figure 2.10. Circulation in the core region ($r/c < 0.1$) for the NV showed a little decrease as the vortex developed downstream. It is believed that the circulation of the fully developed vortex remains unchanged in the near wake region as reported in [47] and [15]. With actuation under C1 conditions, the circulation displayed a slight decrease within the inner region at $x/c = 1$ when compared to NV due to the slightly lower vorticity in this region. However, for $r > r_{C1}$, circulation exhibited a noticeable increase and remained greater than that of the NV. At this downstream location, and at $r > r_{C1}$, the increase in circulation was due to the diffusion presence of vorticity over a region larger than that in NV case. Further downstream, at $x/c = 2$, a noticeable decrease in circulation was observed as a result of increased vortex size as seen in Figure 2.9d. With actuation under configuration C2 case, a noticeable reduction in circulation was observed at all radial positions as compared to both NV and C1 cases. This reduction in circulation is due to the considerable decrease of vorticity under the effect of the higher C_μ and the lower actuation frequency, F^+ actuation. As the vortex evolved downstream, circulation across the vortex continued to decrease and showed lower values compared to those of the NV and C1 cases at the same measuring location. To further examine the effect of actuation on the vortex core structure, the vortex core circulation, $\bar{\Gamma}_c$, was defined as follows:

$$\bar{\Gamma}_c = r_c \int_0^{2\pi} \bar{U}_\theta \left(r_c\right) \, d\theta \tag{2.7}$$

where r_c is the vortex radius. In Figure 2.10, the normalized vortex core circulation, $\bar{\Gamma}_c/\bar{U}_0 c$, of NV, showed very little change with streamwise distance from a value of about 0.055 at $x/c = 1$ to a value of about 0.057 at $x/c = 2$. Core circulation of the C1 vortex at $x/c = 1$ had nearly the same order of magnitude as that of NV case, and then, slightly decreased as the vortex developed downstream. As seen in Figure 2.4 the normalized pressure coefficient increased on the upper surface; therefore it would be reasonable to expect the lift to have increased. Accordingly, the vortex core circulation, $\bar{\Gamma}_c$, in this case should have increased as well. However, because r_c could not be identified in this case, $\bar{\Gamma}_c$ could not be determined accurately.

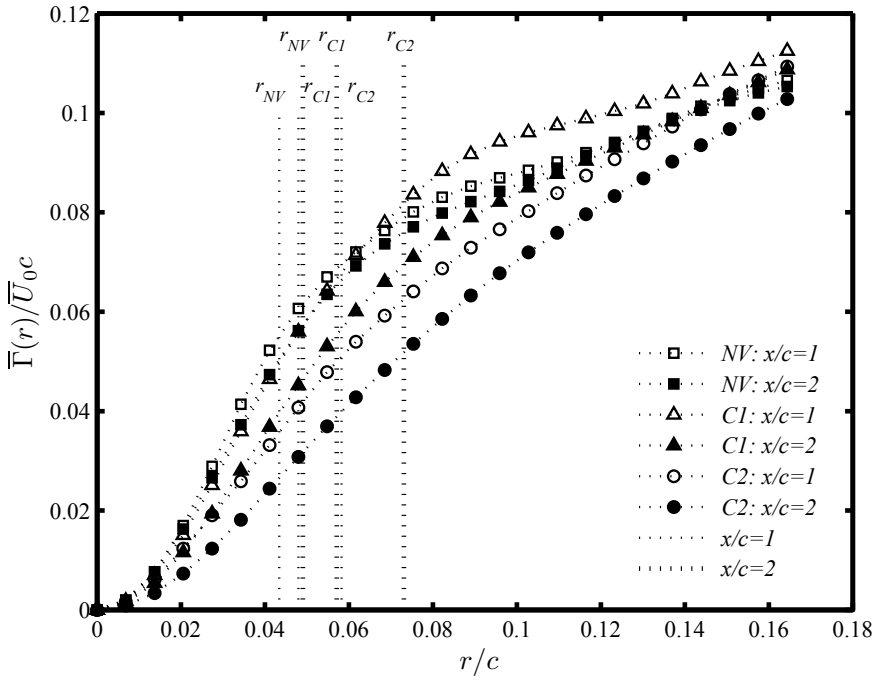

Figure 2.10 Radial distribution of the normalized circulation at $x/c = 1$ and $x/c = 2$. $\bar{\Gamma}_c$ corresponds to the intersection of $\bar{\Gamma}(r)$ with the vertical lines indicating the normalized vortex radius of each case.

Reynolds Stresses

Contour plots of the normalized streamwise, $R_{uu} = \overline{u'u'}/\bar{U}_0^2$, spanwise, $R_{vv} = \overline{v'v'}/\bar{U}_0^2$, and transverse, $R_{ww} = \overline{w'w'}/\bar{U}_0^2$, Reynolds stresses of the NV are shown in Figure 2.11a, 2.11b and 2.11c, respectively, at $x/c = 1$, and in Figure 2.12a, 2.12b and 2.12c, respectively, at $x/c = 2$. u', v' and w' are the fluctuating velocities in the x, y and z directions, respectively and include both a periodic and a turbulent component. At $x/c = 1$, and for the NV flow, turbulent stresses were mostly concentrated in the separated wake shear layer. Contour plots of R_{uu} and R_{vv} in the shear layer depicted peak values of 0.009 and 0.010, respectively, which were largely lower than that of R_{ww} measured to be 0.024, indicative of a wake flow behavior. At $x/c = 1$ and near the vortex core, R_{uu} exhibited a higher maximum stress level of about 0.006 near the vortex core as compared to 0.004 and 0.002 of R_{vv} and R_{ww}, respectively. As the vortex was convected downstream to $x/c = 2$, the contours of R_{uu}, R_{vv} and R_{ww} in the wake shear layer clearly spread out in the transverse direction as a result of the wake thickening with increased streamwise distance. Peak values of R_{vv} in the shear layer decreased by more than two orders of magnitude, and those of R_{uu} and R_{ww} were both reduced by 60% and 20%, respectively. The concentrations of high stresses in the shear layer were drawn into the vortex center as the vortex rolled up. Higher stress

levels were found to be located closer to the vortex center with peak values of R_{uu}, R_{vv} and R_{ww} measured to be 0.0025, 0.0022 and 0.0023, respectively, in agreement with [26]. Under C1 actuation, contour plots of R_{uu}, R_{vv} and R_{ww} are plotted in Figure 2.11d, 2.11e and 2.11f, respectively, at $x/c = 1$, and in Figure 2.12d, 2.12e and 2.12f, respectively, at $x/c = 2$. At $x/c = 1$, peak values of the R_{uu}, R_{vv} and R_{ww} in the shear layer nearly doubled as compared to NV. The increase of the turbulent stress levels in the shear layer was believed to be attributed to the unsteady entrainment of the shear layer by the high frequency flow emanating from the SJ under C1 actuation. Similarly, peak values of R_{uu}, R_{vv} and R_{ww} showed a considerable increase near the vortex core region as compared to NV. Contour plots of R_{uu} showed a region of high stress values concentrated near the vortex core with a peak value of 0.028, being nearly five times higher than that of the NV. The increase in the peak values of R_{uu} in the core region is believed to be attributed to the non-uniform velocity generated by the SJ along the chordwise direction and then entrained near the core region by the rotational motion of the rolling vortex. Contour plots of R_{vv} showed a region of high stress concentrated near the vortex core region with a peak value of 0.017, being more than four times higher than that measured in the vortex core of the NV flow. Contour plots of R_{ww} indicated a significant increase of its peak value in the core region by nearly one order of magnitude that of the NV with a peak value of 0.020. As the vortex evolved to $x/c = 2$, peak stress values in the shear layer decreased to 0.0020, 0.0030 and 0.0025 for R_{uu}, R_{vv} and R_{ww}, respectively, as a result of the wake thickening. Although peak values of R_{uu}, R_{vv} and R_{ww} showed a significant decrease as the vortex was convected to $x/c = 2$, they remained higher (nearly double) than those measured in the NV at the same downstream location. Contour plots of R_{uu} showed that high R_{uu} stresses evolved into a well-organized region as the vortex rolled up to $x/c = 2$. At this location, peak value of R_{uu} decreased to 0.0078 which was three times higher than that of the NV flow. A region of high R_{vv} levels was clearly depicted near the vortex core region with a peak value of 0.0056, being nearly three times higher than that measured in the NV flow. Similarly, a well-organized region of high R_{ww} values was located near the vortex core with a peak value of 0.0050, being nearly twice as much as that of the NV flow. Although peak values near the vortex center decreased as the vortex was convected to $x/c = 2$, they were significantly higher than those found in NV and appeared to cover a larger area of the vortex core region indicative of increased turbulent mixing within the vortex core. When actuated under C2 configuration and at $x/c = 1$, peak stress values in the shear layer were measured to be 0.0012, 0.0010 and 0.0018 for R_{uu}, R_{vv} and R_{ww}, respectively. Peak values of R_{uu}, R_{vv} and R_{ww} were significantly lower than those reported under case C1 and were quite comparable to those of the NV. This

indicated that low frequency actuation under case C2 did not have much of an effect on the wake shear layer. As opposed to both NV and C1 cases, contour plots of R_{uu} showed a more organized region of high stress values concentrated in the top right quadrant of the measurement plane indicating that the average position of the jet spawned by the SJ was rotated by the rolling tip vortex, and had a peak value of 0.040 being nearly 75% higher than that found in the C1 case. The increase of the peak value of R_{uu} was due to the increased turbulence generated by the higher C_μ of the C2 case. Two distinct regions of high R_{vv} values corresponding to the SJ counter-rotating vortices can be identified in the C2 case with peak values of 0.024 and 0.016 where the higher peak is 40% higher than that of the C1 case. The location of the two distinct regions of high stresses clearly moved near the wing tip. The region of the lower R_{vv} peak value, which corresponds to the SJ clockwise vortex, was reduced and diffused by the entrainment of the rolling wake shear layer. Contour plots of R_{ww} showed a concentration of high stress in the region between the two peaks of high R_{vv} stresses indicating the jet nature of the flow field generated by the SJ. In this region, the peak value of R_{ww} was measured to be 0.0050 which was twice as high as that of the C1 case. Note that the behavior of the R_{uu}, R_{vv} and R_{ww} stresses near the core region in case C1 can be loosely compared to those identified in case C2. However, due to the lower C_μ and the higher F^+ of case C1, the SJ vortices remained closer to the wing tip where they seemed to be quickly drawn into the vortex core and merged together over shorter distances downstream. As the vortex evolved to $x/c = 2$, the region of high concentration of R_{uu} at $x/c = 1$ appeared to be rotated by an angle of nearly 180° in the inboard direction and its peak value was reduced to 0.015, but remained twice and six times higher than those of the C1 and the NV cases at the same location, respectively. The two regions of high R_{vv} seen at $x/c = 1$, were also entrained by the rotational motion of the vortex and their locations moved in the inboard direction. Peak values of R_{vv} decreased to 0.0076 and 0.0068 but remained 35% and three times higher than those measured in the C1 and NV cases, respectively. Additionally, at $x/c = 2$, high R_{ww} values were mostly concentrated between the two regions of high R_{vv} values and appeared to cover a larger area of the vortex core region. Peak value of R_{ww} decreased to a value of 0.024 but remained five times and nearly one order of magnitude higher than those measured in the C1 and NV cases, respectively. Based on the above, it was concluded that, at both downstream locations, the regions where higher concentration of R_{uu}, R_{vv} and R_{ww} occurred, appeared to cover a larger area of the vortex core which suggests that the unsteadiness generated by the SJ under C2 actuation was acting on a larger area of the vortex core which led to a higher turbulent mixing and consequently a faster diffusion of the vortex strength.

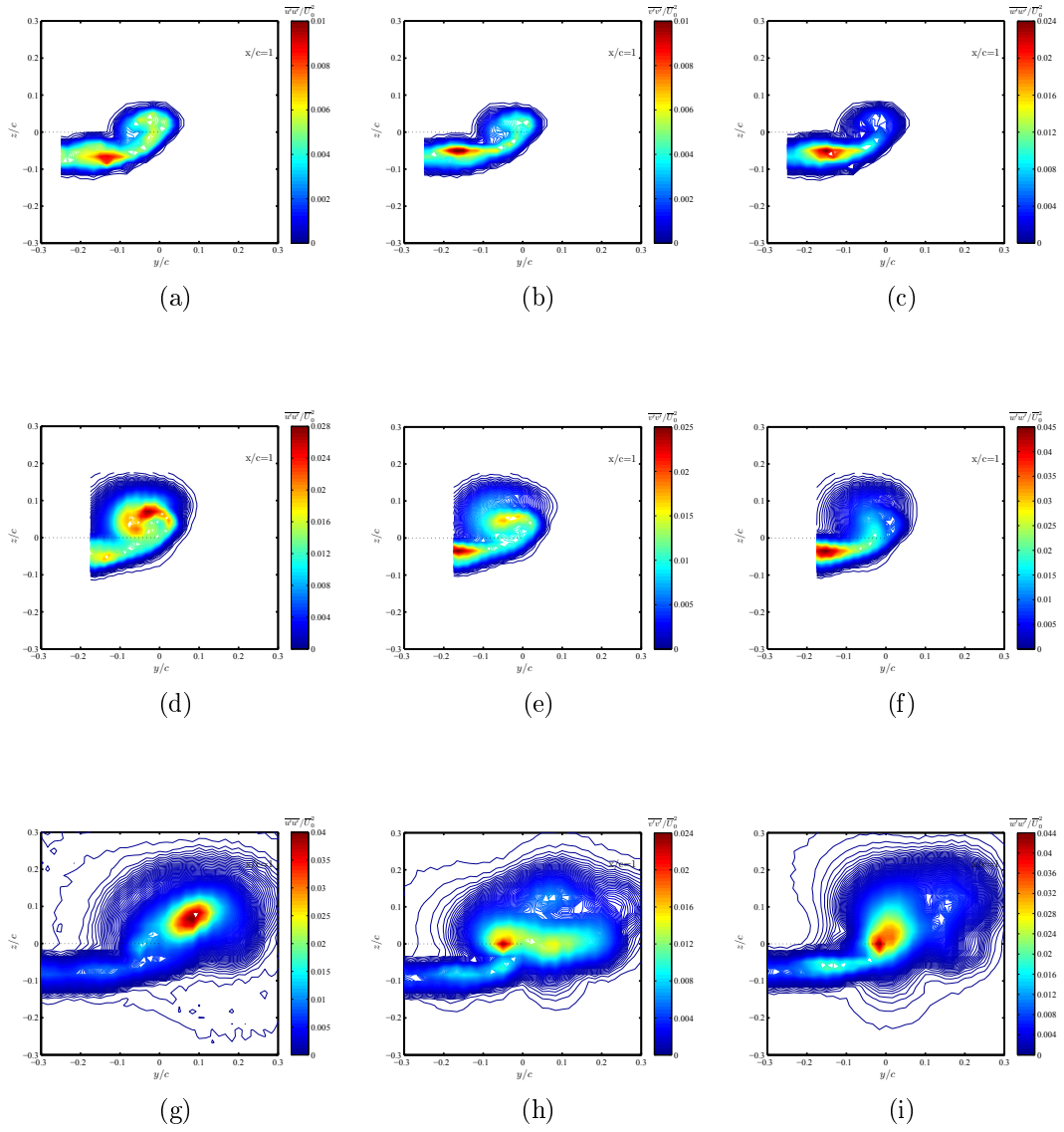

(a) (b) (c)

(d) (e) (f)

(g) (h) (i)

Figure 2.11 Contours of normalized streamwise, transverse and spanwise Reynolds stresses at $x/c = 1$. (a), (b) and (c): NV, (d), (e) and (f): C1, (g), (h) and (i): C2.

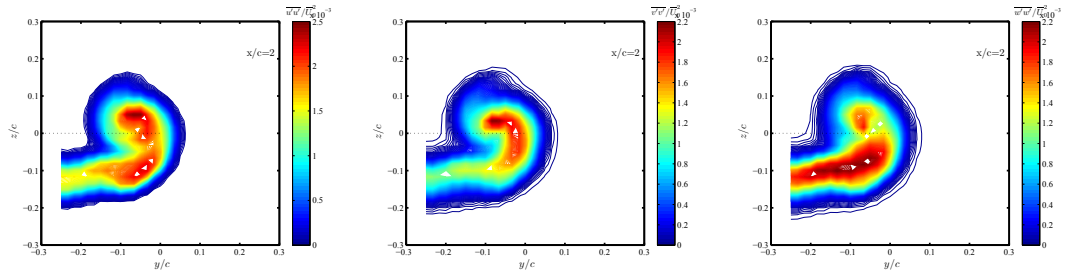

(a) (b) (c)

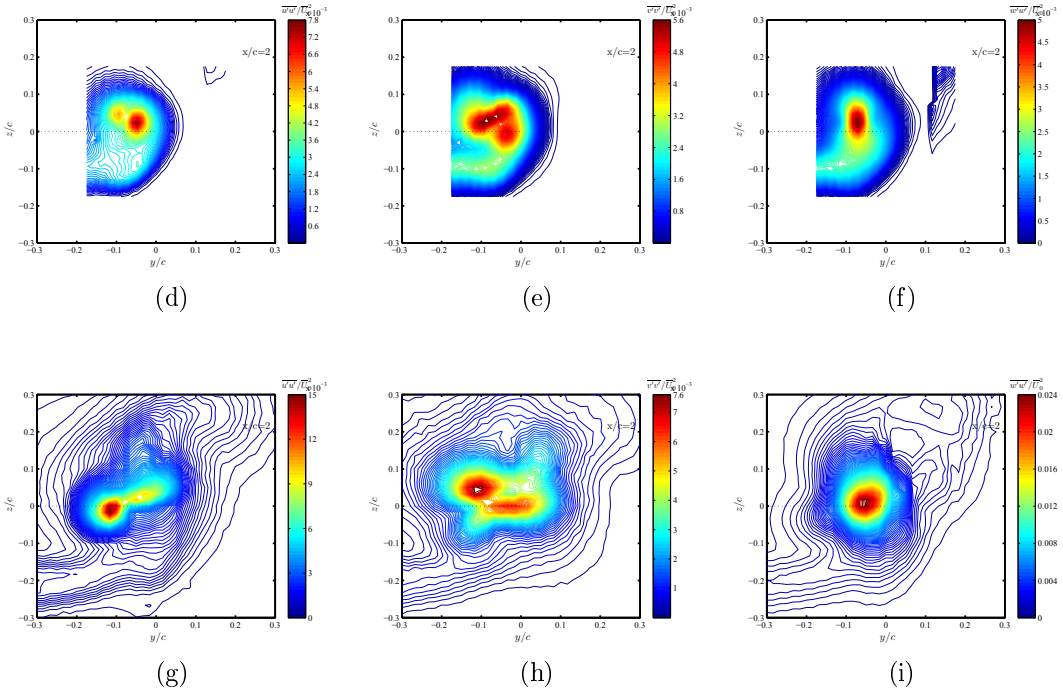

(d) (e) (f)

(g) (h) (i)

Figure 2.12 Contours of normalized streamwise, transverse and spanwise Reynolds stresses at $x/c = 2$. (a), (b) and (c): NV, (d), (e) and (f): C1, (g), (h) and (i): C2.

Spectral analysis

Frequency spectra $S_{yy}(f)$ of $\bar{U}_y$ measured at various locations along a line passing through the vortex centers ($y = y_c$) of the NV, case C1 and case C2, are shown in Figure 2.13 and Figure 2.14 at $x/c = 1$ and $x/c = 2$, respectively. Although the general shape of the frequency spectra $S_{xx}(f)$ of $\bar{U}_x$ and $S_{zz}(f)$ of $\bar{U}_z$ is similar to that of $S_{yy}(f)$, only frequency spectra $S_{yy}(f)$ were examined in this study since the contribution of the large scale motion to the total fluctuation energy happened to be the greatest in the spanwise direction. At $x/c = 1$, power spectra of the NV inside the vortex core region, shown in Figure 2.13a and Figure 2.13b, depict that normalized frequencies, $f^* = fc/\bar{U}_\infty$, lower than 10 contain most of the energy level in the spectra. In this range of frequencies, the spectra of the NV show a relatively flat region which increases in level as the vortex center is approached in agreement with the observations of [2, 11, 34]. At frequencies above 10, the spectra show a roll-off and the energy decreases at a continuously increasing rate. At $x/c = 2$, spectra of the NV in the vortex core show a similar plateau in the range of frequencies below 10. A spike in the spectra was observed at f^* of about 10. The amplitude of this spike was found to increase as the vortex center location is approached. The appearance of this

dominant frequency in the spectra was in agreement with the observations of [2, 7, 103] who suggested that the spike is associated with an instability in the vortex core.

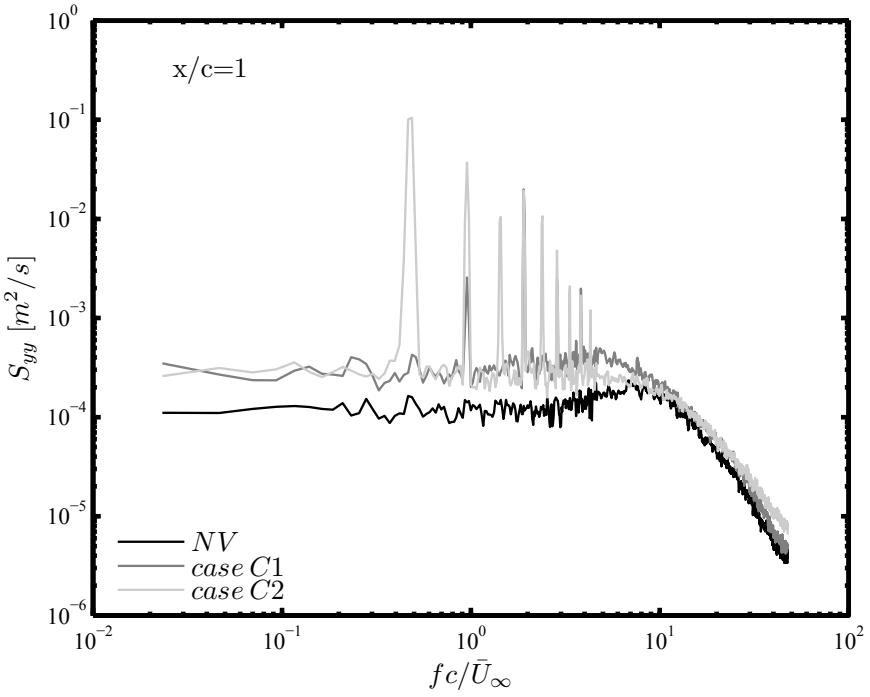

(a)

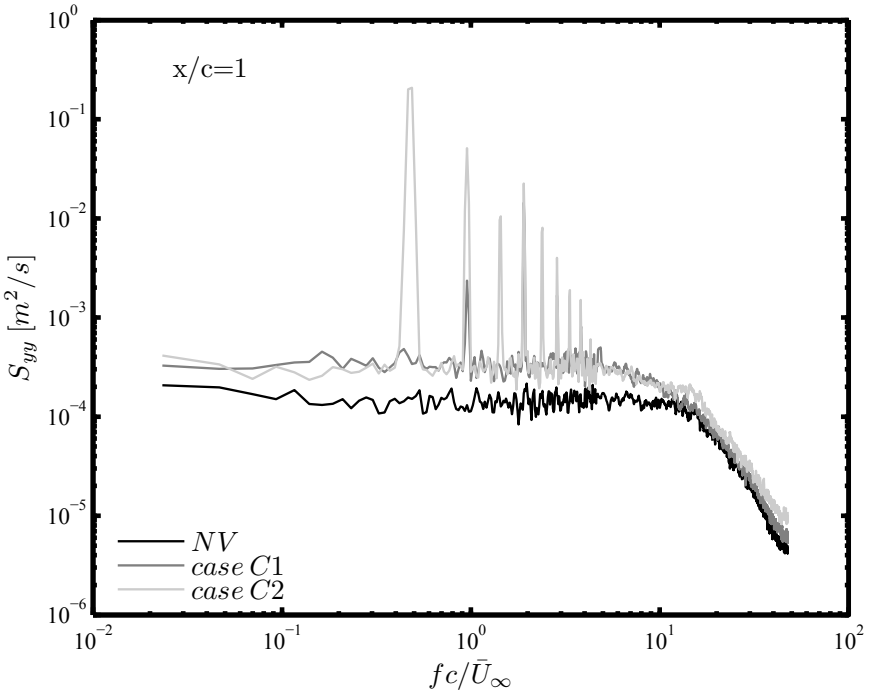

(b)

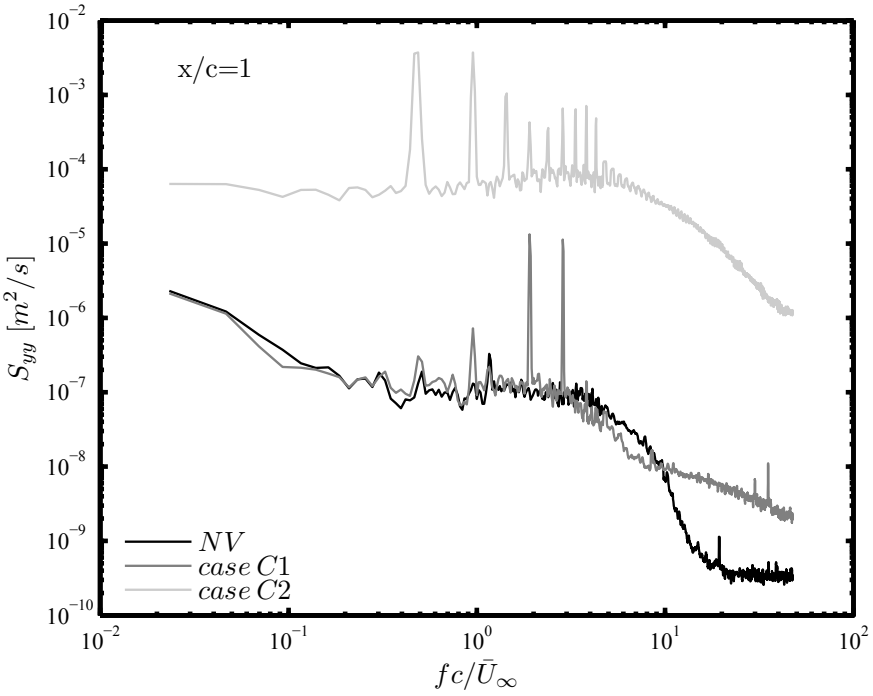

(c)

Figure 2.13 Frequency spectra of the spanwise velocity at $x/c = 1$. (a) inside the core region, (b) at the vortex center and (c) outside the vortex region.

At frequencies beyond 10, the spectra show a much steeper roll-off slope than those observed at $x/c = 1$ and a much lower energy level of the small scale turbulence within the vortex core in agreement with the findings of [37]. Conversely, the energy level associated with the low frequency fluctuations was found to increase with increased downstream distance which supports the findings of [2, 37, 57]. These authors suggest that this may be due to the wandering amplitude that increases with downstream distance. With control, $S_{yy}(f)$ spectra of case C1 and C2, show dominant sharp peaks at the actuation frequencies and their higher harmonics. At the vortex center, the maximum energy level at the actuation frequency of case C2 is nearly two decades higher than that of the NV in the plateau region. The peak in the spectra of case C1 appeared at a much higher frequency with an energy level that was at least one decade lower than that of case C2. The spike in the spectra of the NV, which was observed at f^* of about 10, was shown to disappear under the effect of control of both C1 and C2 cases. Additionally, with the control of case C2, the turbulent energy associated with actuation persisted at longer radii away from the vortex core (Figure 2.13c and Figure 2.14c) in agreement with the Reynolds stress contour plots shown in Figure 2.11 and Figure 2.12 suggesting that the SJ penetrated further distances into the vortex structure due to its longer stroke length, λ. It would

be surmised that vortex meandering is affected by the actuation. However, these effects cannot be inferred from the measured spectra since the contribution to the total energy

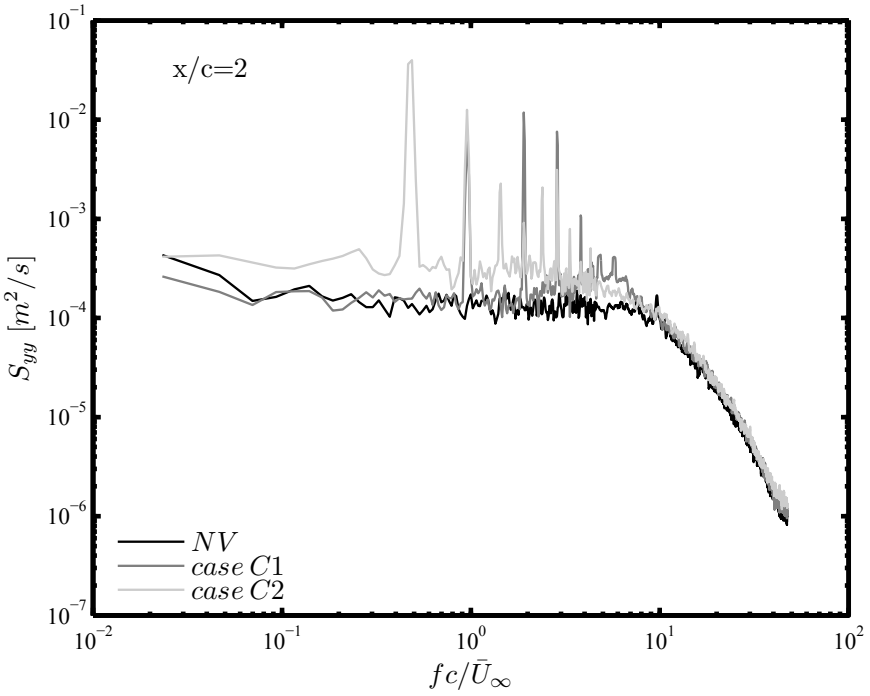

(a)

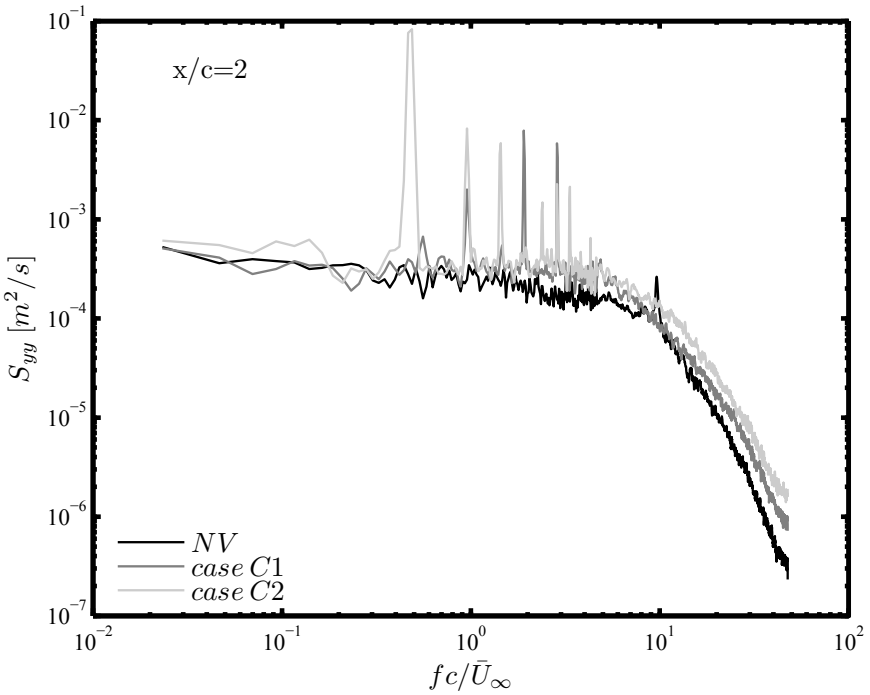

(b)

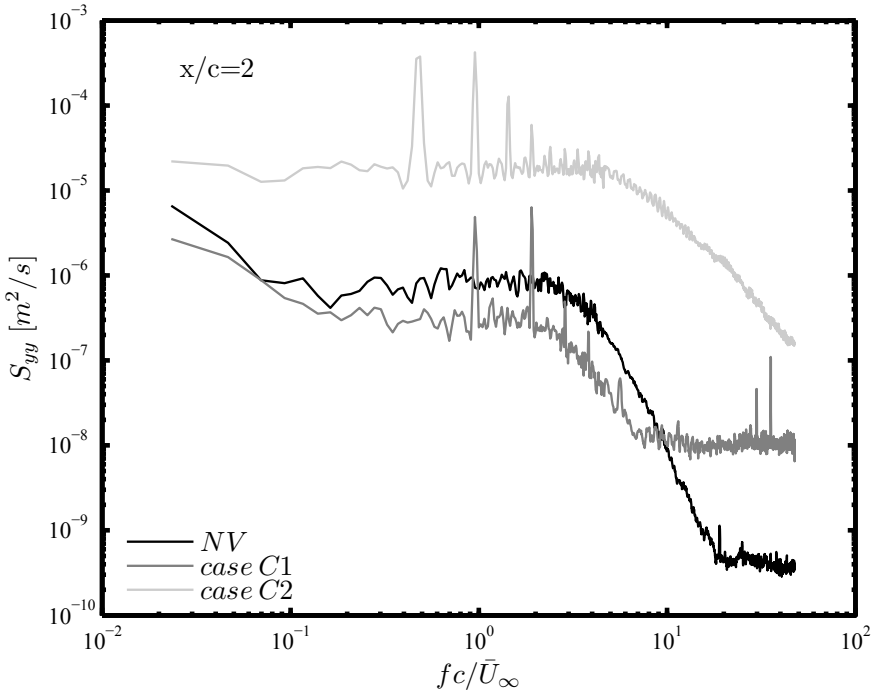

(c)

Figure 2.14 Frequency spectra of the spanwise velocity at $x/c = 2$. (a) inside the core region, (b) at the vortex center and (c) outside the vortex region.

is largely due to the actuation. More specifically, in Figure 2.13c and Figure 2.14c, the contribution of actuation to the total energy is mainly due to the coherent component of the SJ structures as described in [25, 105]. Interestingly, it can be seen in Figure 2.13b and Figure 2.14b that the contribution of actuation to the total energy was reduced by at least one decade allowing for a more diffused vortex as the latter travelled from $x/c = 1$ to $x/c = 2$. This decreasing trend is expected to continue downstream as reported in [59]. At larger downstream distances, as the turbulence associated with actuation decreases, the contribution to the total energy becomes mainly due to vortex wandering. However, such a frequency cannot be identified with a reasonable accuracy. The wandering frequencies reported in previous studies were generally qualitative and were mostly within a range of frequencies below f^* of 1 [2, 34, 37]. To further assess the contribution of SJA to the total turbulence in the vortex core, the profiles of the normalized turbulent kinetic energy, $k/\bar{U}_0^2$, across the vortex centers of the NV, case C1 and case C2 were high-pass filtered at different threshold levels as shown in Figure 2.15a, Figure 2.15b and Figure 2.15c at $x/c = 1$ and in Figure 2.16a, Figure 2.16b and Figure 2.16c at $x/c = 2$. The normalized turbulent kinetic energy, $k/\bar{U}_0^2$, was evaluated as:

$$\frac{k}{\bar{U}_0^2} = \frac{1}{2}\left(R_{uu} + R_{vv} + R_{ww}\right) \tag{2.8}$$

Filtering $k/\bar{U}_0^2$ up to a dimensionless cut-off frequency, $f^*{}_{cut} = f_{cut}c/U_\infty$, of about 1 would be expected to eliminate most of the energy associated with wandering and coherent wake structures but leaves intact the energy of the smaller turbulence scales. However, the profiles of $k/\bar{U}_0^2$ across the vortex center of the NV show little effect with high-pass filtering at both $x/c = 1$ and $x/c = 2$. Contrastingly, with actuation, the profiles of $k/\bar{U}_0^2$ appeared to be largely affected by high-pass filtering with the effect being more pronounced for case C2 particularly at the cut-off frequencies 0.47 and 0.95 which correspond to the actuation frequencies of case C1 and case C2, respectively. Furthermore, the peak values of the filtered $k/\bar{U}_0^2$ were measured to be 2 times and 5 times smaller than that of the unfiltered profiles of case C1 and case C2, respectively, suggesting that most of the energy contained in the vortex core is introduced by the SJA.

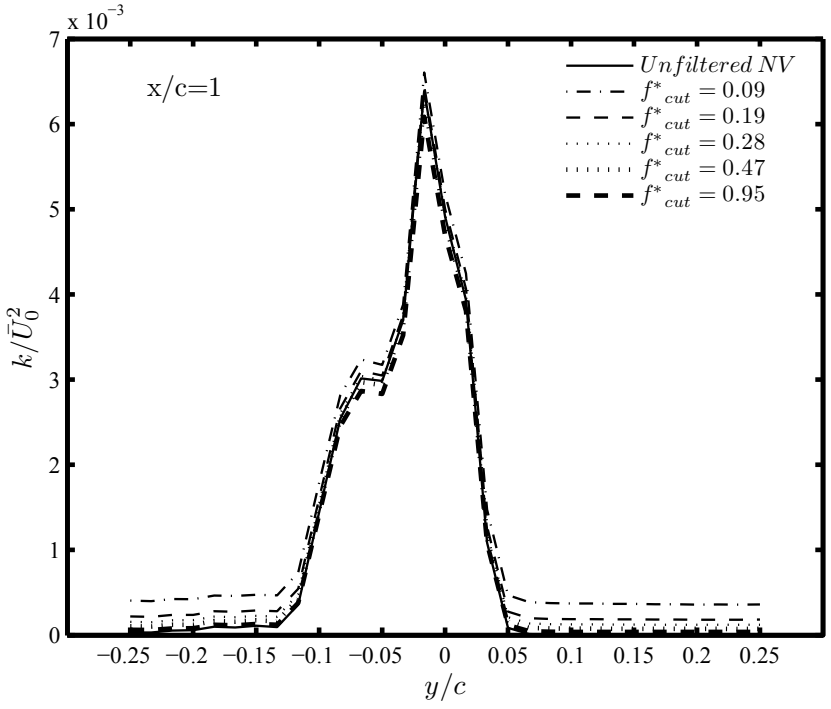

(a)

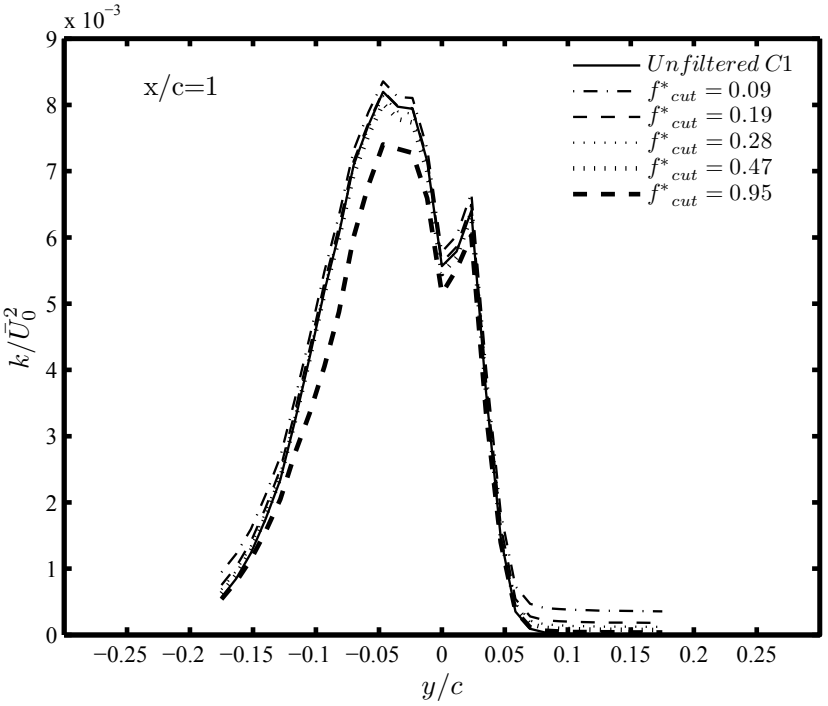

(b)

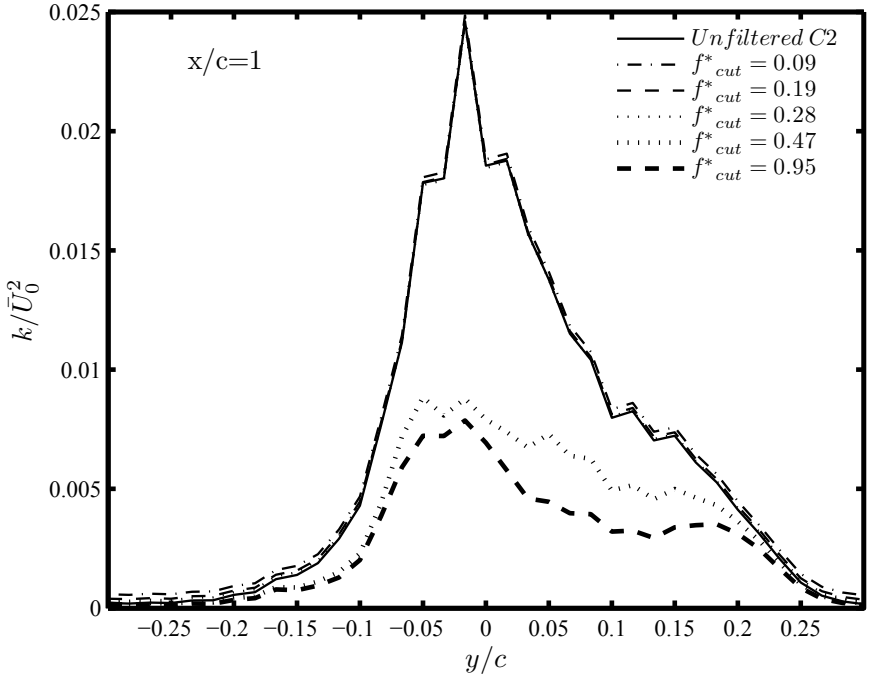

(c)

Figure 2.15 Distributions of the filtered $k/\bar{U}_0^2$ across the vortex center at $x/c = 1$. (a): NV, (b): C1 and (c) C2.

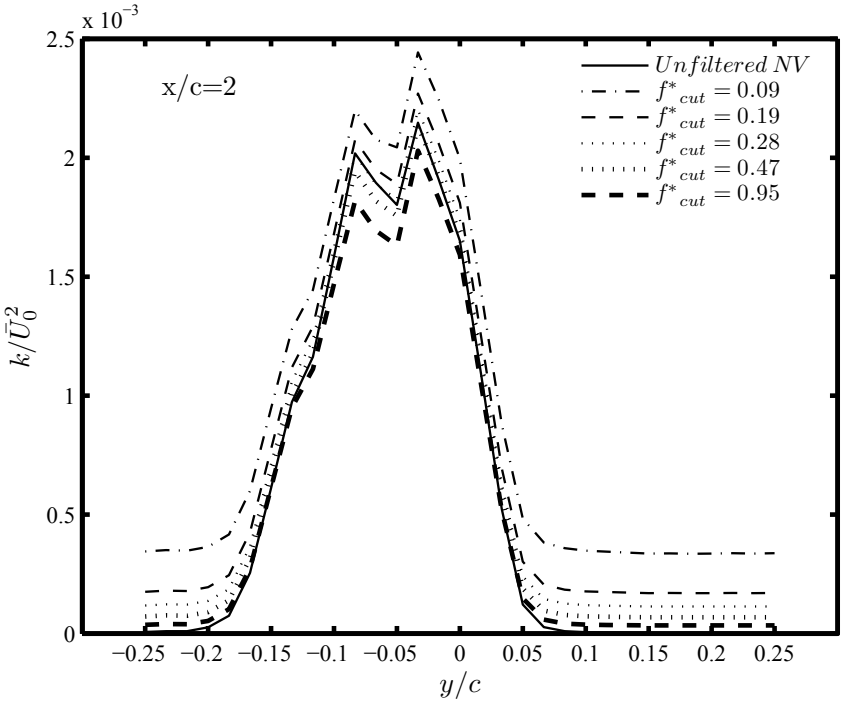
x 10^−3
x/c=2
Unfiltered NV
f*cut = 0.09
f*cut = 0.19
f*cut = 0.28
f*cut = 0.47
f*cut = 0.95
k/Ū0^2
y/c

(a)

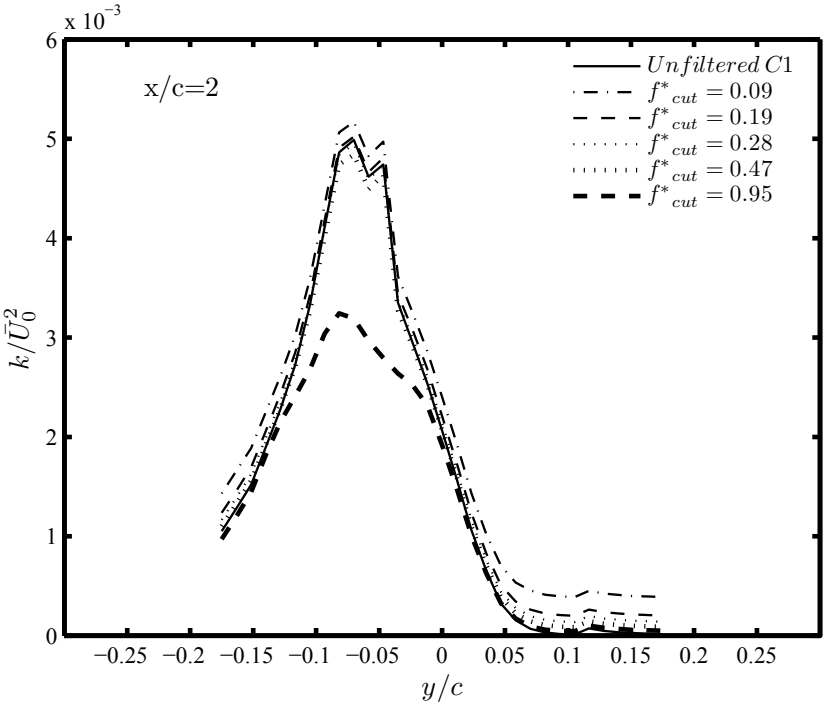
x 10^−3
x/c=2
Unfiltered C1
f*cut = 0.09
f*cut = 0.19
f*cut = 0.28
f*cut = 0.47
f*cut = 0.95
k/Ū0^2
y/c

(b)

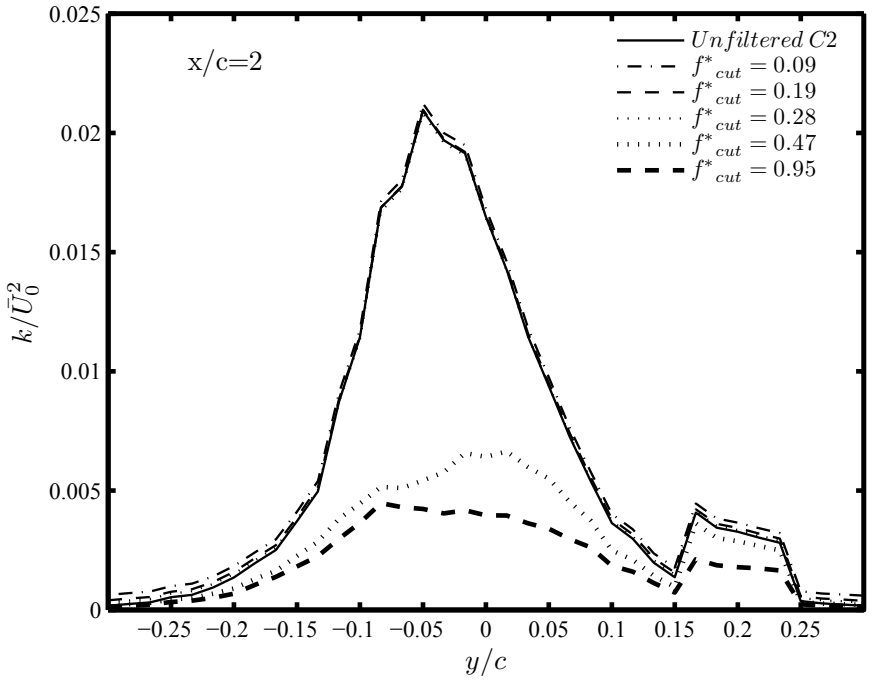

(c)

Figure 2.16 Distributions of the filtered $k/\bar{U}_0^2$ across the vortex center at $x/c = 2$. (a): NV, (b): C1 and (c) C2.

Discussion on the effectiveness of the synthetic jet actuation

It has been shown in the previous sections that the selection of the control parameters, $F^+ = 0.213$ and $C_\mu = 0.04$, was the most effective in altering the velocity field within the vortex flow and in weakening its strength measured by the magnitudes of $\bar{U}_\theta$, $\bar{\xi}_x$ and $\bar{\Gamma}_c$. In order to gain more insight into the mechanism of the apparent weakening of the wing tip vortex, contour plots of the turbulent kinetic energy of the NV, C1 and C2 cases were plotted and shown in Figure 2.17. In Figure 2.17a, the larger values of $k/\bar{U}_0^2$ for the NV were concentrated in the wake shear layer with a peak value of 3.2×10^{-4} when the vortex is at $x/c = 1$. Near the vortex core region, contours of $k/\bar{U}_0^2$ showed a relatively smaller concentration of turbulence with a maximum value of about 1.1×10^{-4}. As the vortex evolved to $x/c = 2$, the turbulent kinetic energy in the shear layer seemed to be drawn into the vortex core and then spread outwardly to cover a relatively larger area of the vortex region. Also, as the wake broadened, a considerable decrease of the values of $k/\bar{U}_0^2$ in the shear layer was observed with a peak of 3.8×10^{-5} (Figure 2.17b). However, due to the high viscous effect in the vortex core, the maximum value of $k/\bar{U}_0^2$ decreased to a value of 4.9×10^{-5}. In the C1 case and at $x/c = 1$, the large concentration of

turbulent kinetic energy was seen in the shear layer as in the case of NV but with the peak value of $k/\bar{U}_0^2$ twice as high as that of NV. The increase in turbulence in the shear layer was the result of unsteadiness of the shear layer as it was entrained by the SJ at the higher actuation frequency used in Case 1. Turbulence levels near the vortex core seemed to increase under C1 actuation as well, where $k/\bar{U}_0^2$ reached a maximum value of 4.8×10^{-4}. As for the NV flow at $x/c = 2$, the concentration of high turbulent kinetic energy in the shear layer was drawn into the vortex core region resulting in a decrease of the peak values of $k/\bar{U}_0^2$ to 5.1×10^{-5} and to 1.1×10^{-4} in the shear layer and the vortex core region, respectively. With control configuration C2 and at $x/c = 1$, a higher value of $k/\bar{U}_0^2$ appeared to be located near the wing tip surrounded by an elliptic-shaped region of high turbulent kinetic energy concentration (Figure 2.17e). The peak value of $k/\bar{U}_0^2$ in the shear layer was measured to be 2.8×10^{-4} which is of the same order of magnitude as the NV case, and nearly half that of the C1 case. As opposed to case C1, the higher C_μ and the lower actuation frequency of case C2 could not induce as much unsteadiness in the shear layer as shown in Figure 2.11 and Figure 2.12. In the vortex core region, the peak value of $k/\bar{U}_0^2$ was measured to be 5.4×10^{-4} which is five times higher than that of the NV case and nearly 13% higher than that of the C1 case. The concentration of turbulence in the C2 case at $x/c = 2$, was mainly located in the vortex core region (Figure 2.17f) where the peak value of $k/\bar{U}_0^2$ was measured to be 3.2×10^{-4}. It is clearly seen in Figure 2.17f that the high turbulent region was spread over a larger radial area as compared to the C1 case which clearly indicated a higher diffusion of the tip vortex. As suggested in the previous section, the larger turbulence region was triggered by the low actuation frequency of case C2, which allowed the SJ to travel larger distances during each blowing cycle, and injected high turbulence counter-rotating vortex structures, especially with higher C_μ, into the wing tip vortex core. Note that the SJA at higher F^+ values, even with a higher C_μ, would not achieve as much of an impact on the wing tip vortex as that at lower F^+ values. In fact as seen in Figure 2.4, actuation with $C_\mu = 0.04$ but $F^+ = 0.71$, had less improved spanwise distribution of $C_p/C_{p_{nv}}$ compared to the C2 case particularly close to the wing tip. This may indicate that the SJ stroke length, λ, was reduced with increased frequency, thus the vortices emanating from the SJ remained closer to the slot exit and did not penetrate well enough into the vortex core. The effect of frequency was clearly more pronounced at $x/c = 1$ where much of the turbulence generated by the SJ in case C1 was confined within a small region close to the wing tip. However, the turbulence induced by the SJ in case C2 appeared to act on a much larger area around the wing tip.

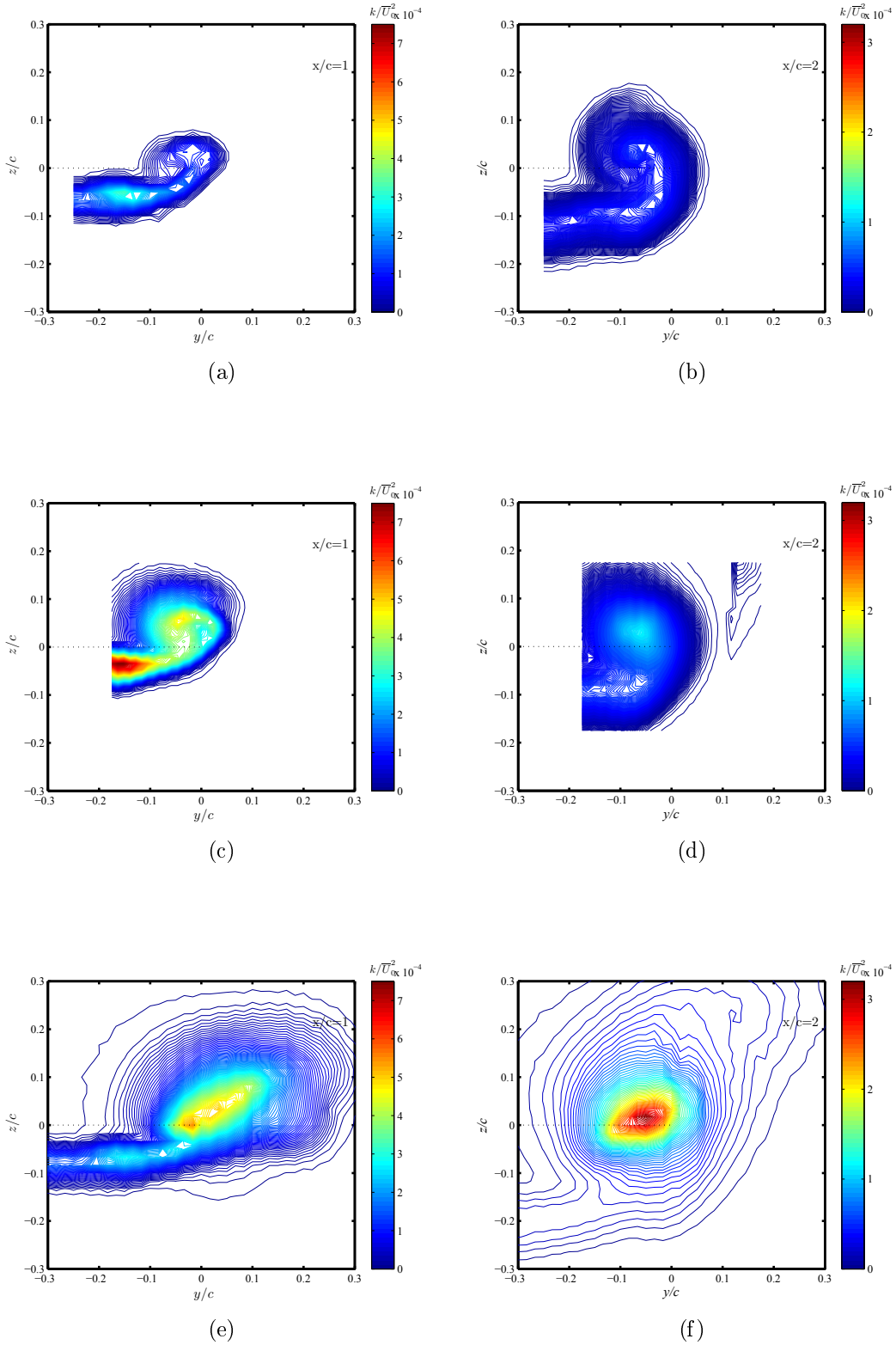

Figure 2.17 Contours of the TKE at $x/c = 1$ and $x/c = 2$ locations. (a) and (b): NV, (c) and (d): C1, (e) and (f): C2.

The effect of control on the vortex core flow behavior can be demonstrated from a close examination of the radial distribution of the circulation, $\bar{\Gamma}(r)$, when the wing tip vortex was actuated with the control configurations C1 and C2. Plots of $\bar{\Gamma}(r)$ normalized by the vortex core circulation, $\bar{\Gamma}_c$, against $\log(r/r_c)$ in Figure 2.18a and 2.18b at $x/c = 1$ and $x/c = 2$, respectively, along with the empirical curve-fit relationships suggested by [58] and [91] that describe the inner-core region and the region where $\bar{\Gamma}(r)$ distribution is logarithmic and are given as:

$$\frac{\bar{\Gamma}(r)}{\bar{\Gamma}_c} = A\left(\frac{r}{r_c}\right)^2 \quad \text{for} \quad \frac{r}{r_c} < 0.4 \tag{2.9}$$

$$\frac{\bar{\Gamma}(r)}{\bar{\Gamma}_c} = B\log\left(\frac{r}{r_c}\right) + C \quad \text{for} \quad 0.5 < \frac{r}{r_c} < 1.4 \tag{2.10}$$

where the constants A, B and C are 1.626, 0.833 and 0.982 at $x/c = 1$, respectively, and 1.716, 0.906 and 0.990 at $x/c = 2$, respectively. A reasonable self-similar behavior of the normalized radial circulation was clearly observed in the inner core and the buffer regions for all the cases investigated at both $x/c = 1$ and $x/c = 2$ locations. The universal behavior of the inner vortex indicated that the distribution of circulation within the vortex core, for the natural vortex and the actuated vortex whether with configuration C1 or C2, had a $\bar{\Gamma}(r)/\bar{\Gamma}_c \propto r^2$ behavior for $r/r_c < 0.4$ at both downstream locations. For $0.5 < r/r_c < 1.4$, and at $x/c = 1$, $\bar{\Gamma}$ varied logarithmically for the NV flow, however a slight departure from the logarithmic fit was observed for both C1 and C2 cases with the departure being more pronounced for the latter which indicates that the actuation affected the vortex structure during its early formation. At $x/c = 2$. However, the radial distribution of $\bar{\Gamma}(r)/\bar{\Gamma}_c$ depicted a self-similar behavior and showed a good agreement with the logarithmic fit for all the cases studied. For $r/r_c > 1.4$ and at both downstream locations, $\bar{\Gamma}(r)/\bar{\Gamma}_c$ was found to completely depart from the logarithmic fit. The departure was more pronounced in the C1 and C2 cases which might be attributed to the effect of actuation on the vorticity concentrated in the wake shear layer. The capability of SJs in controlling wing tip vortex flows was qualitatively underlined by comparing pressure coefficient distributions of different controlled configurations of $C_\mu = 0.04$ against normalized spanwise pressure coefficients collected by Montoya et al. [85] for a wing equipped with a winglet at a chord Reynolds number, $Re_c = 11.68 \times 10^6$. It was clearly shown in Figure 2.4 that the decrease in pressure on the suction side of the wing with actuation (F^+ of 0.71 and C_μ of 0.004) clearly outperformed the winglet's configuration by as much as 26% near the wing tip and by about 5% along the wing span $y/(b/2) < 0.8$. When the SJ was operated

at $F^+ = 0.213$, a larger reduction in the suction side pressure than that of the winglet configuration can still be achieved with relatively small C_μ values.

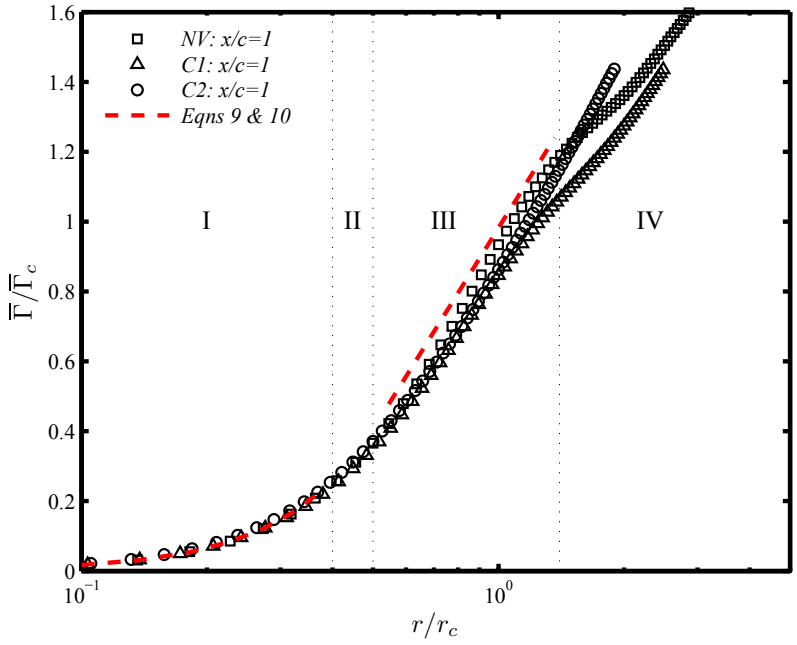

(a)

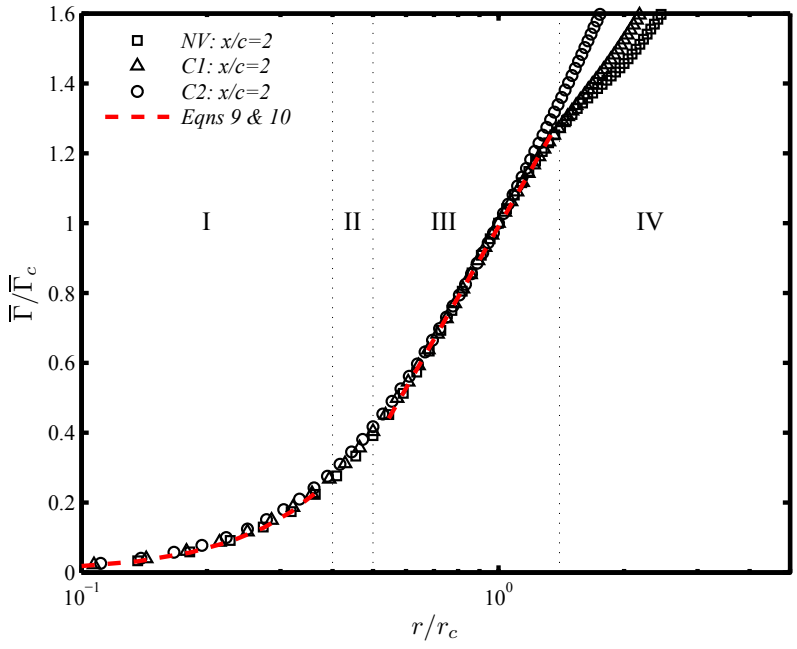

(b)

Figure 2.18 Behavior of inner-region circulation. I: inner-core, II: buffer region, III: logarithmic region, IV: outer region. (a) at $x/c = 1$ and (b) at $x/c = 2$.

2.2.5 Conclusions

In this work, an experimental investigation on the effectiveness of SJA to control a wing tip vortex in the near wake of a rectangular NACA 0012 wing was conducted. The wing was placed at an angle of attack of 5 degrees in a low turbulence wind tunnel flow, at chord Reynolds number, $Re_c = 8 \times 10^4$, and spanning the tunnel half width. The SJ emanated from a thin, trapezoidal slot with a curved exit placed at the wing tip in the chordwise direction. First, a parametric study on the effects of the actuation frequency, F^+, and momentum coefficient, C_μ, on the pressure spanwise distribution on the suction surface of the wing was performed. The pressure measurements for F^+ ranging between 0.0213 and 1.42 and C_μ ranging from 0.0021 to 0.04 showed that the most efficient frequencies in improving the pressure distribution on the suction surface of the wing resulted when F^+ was in the range of frequencies between the long-wave Crow's instability and shorter-wave Widnall instability. In this range of actuation frequencies, further improvement was achieved when C_μ was increased. Second, hot-wire measurements were performed at two downstream cross-flow planes namely, $x/c = 1$ and $x/c = 2$. The measurements were carried out for the natural vortex and for two SJ configurations, namely, a "least efficient" configuration with $F^+ = 0.71$ and $C_\mu = 0.004$ and a "most efficient" configuration with $F^+ = 0.213$ and $C_\mu = 0.04$. When the flow was actuated with a lower frequency and higher C_μ (longer λ), the measurements in the wake at $x/c = 1$ showed that the actuation had a significant impact on the wing tip vortex. More specifically, the wing tip vortex was stretched into an ellipsoid shape with increased size. Because a vortex core radius could not be defined in the traditional sense, an effective radius was defined as half the distance separating the positions where the changes in the tangential velocity, $\bar{U}_\theta$, were not significant. It was found that the control achieved a 30% broadening of vortex core radius, r_c. Furthermore, the wing tip vortex strength decreased compared to the natural vortex at the same streamwise location; the actuation achieved a 23% reduction in the axial velocity deficit, $\bar{U}_x$, and a 50% average decrease in the peak tangential velocity, $\bar{U}_\theta$. Also, the axial vorticity values near the core were found to be largely reduced and hence, a reduction of 11% in the wing tip vortex strength, $\bar{\Gamma}_c$. Further downstream, at $x/c = 2$, the wing tip vortex regained its traditional shape but with a reduced strength. The results suggested that the low frequency of the "most efficient" control configuration allowed the SJ to travel larger distances into the wing tip vortex core bringing high turbulence structures with it. This resulted in increased turbulent mixing in the vortex core and subsequently decreased vortex strength.

2.2.6 Acknowledgments

This work was supported by the Directorate of Technical Airworthiness and Engineering Support (DTAES) office of the Royal Canadian Air Force.

2.2.7 Nomenclature

Greek symbol	Units	Description
$\bar{\Gamma}$	m^2/s	Circulation
$\bar{\Gamma}_c$	m^2/s	Vortex core circulation
δ	deg	Wing dihedral
ρ_∞	kg/m^3	Freestream air density
ρ_j	kg/m^3	Synthetic jet air density
$\bar{\xi}_x$	s^{-1}	Streamwise vorticity
λ_L	m	Wavelength of the Crow's instability
λ_S	m	Wavelength of the Widnall's instability
λ	m	Synthetic jet stroke length

Symbol	Units	Description
A_j	m^2	Synthetic jet slot area
A_w	m^2	Half-wing planform area
$b/2$	m	Wing half span
c	m	Wing chord
C_μ	-	Synthetic jet momentum coefficient
C_p	-	Pressure coefficient
$C_{p_{nv}}$	-	Pressure coefficient of the natural flow
F^+	-	Non-dimensionalized actuation frequency
f_a	Hz	Synthetic jet actuation frequency
f_λ	Hz	Frequency of the corresponding instability
f	Hz	Frequency
f_{cut}	Hz	High-pass filter cut-off frequency
f^*	-	Non-dimensionalized frequency
f^*_{cut}	-	Non-dimensionalized high-pass filter cut-off frequency
k	m^2/s^2	Turbulent kinetic energy
L_j	m	Synthetic jet slot length
$\vec{v}_j$	m/s	Synthetic jet exit velocity field
$\bar{U}_\infty$	m/s	Wind tunnel freestream velocity
$\bar{U}_0$	m/s	Local freestream velocity
$\bar{U}_x$	m/s	Mean axial velocity
$\bar{U}_y$	m/s	Mean spanwise velocity
$\bar{U}_z$	m/s	Mean transverse velocity
$\bar{U}_\theta$	m/s	Circumferential velocity
$\bar{V}_j$	m/s	Synthetic jet space time-averaged velocity scale
$\bar{uu}$	m^2/s^2	Streamwise Reynolds stress
$\bar{vv}$	m^2/s^2	Spanwise Reynolds stress
$\bar{ww}$	m^2/s^2	Transverse Reynolds stress
Re	-	Reynolds number
R_{uu}	-	Normalized streamwise Reynolds stress
R_{vv}	-	Normalized spanwise Reynolds stress
R_{ww}	-	Normalized transverse Reynolds stress
S_{xx}	m^2/s	Frequency spectra of $\bar{U}_x$
S_{yy}	m^2/s	Frequency spectra of $\bar{U}_y$
S_{zz}	m^2/s	Frequency spectra of $\bar{U}_z$
T	s	Actuation period
r	m	Radial distance from mean vortex center
r_c	m	Vortex core radius
r_{NV}	m	Vortex core radius of the natural vortex
r_{C1}	m	Vortex core radius of case C1
r_{C2}	m	Vortex core radius of case C2
(x, y, z)	m	Streamwise direction from wing tip quarter-chord reference location

CHAPTER 3

Effect of active flow control on the development of a wing tip vortex in the mid-wake region

3.1 Avant-propos

Auteurs et affiliations:

1. Marouen DGHIM: Étudiant au doctorat[†]
2. Mohsen FERCHICHI: Professeur titulaire[*]
3. Hachimi FELLOUAH: Professeur agrégé[†]

[†]Université de Sherbrooke, Faculté de génie, Département de génie mécanique.
[*]Collège Militaire Royal du Canada, Faculté de génie, Département de génie mécanique et aérospatial.

Date d'acceptation: 12 Mai 2018.

État de l'acceptation: version finale publiée.

Revue: Experimental Thermal and Fluid Science.

Titre en français:

Dynamique d'un tourbillon de bout d'aile dans la région du sillage intermédiaire sous l'effet du contrôle fluidique actif.

Contribution au document:

Cet article contribue à la thèse en évaluant l'effet du contrôle actif par jet synthétique sur l'atténuation et la dissipation de tourbillon de bout d'aile dans la région de sillage intermédiaire et en tenant compte du phénomène d'errance des tourbillons.

Résumé en français:

Le développement d'un tourbillon de bout d'aile sous l'effet du contrôle par jet synthétique (JS) a été examiné pour une aile rectangulaire à bout carré ayant un profil aérodynamique NACA 0012 en utilisant l'anémométrie à fils chauds à un nombre de Reynolds $Re_c = 8 \times 10^4$. Trois configurations de contrôle ont été considérées pour une étude comparative, à savoir le cas C1 avec un coefficient de moment $C_\mu = 0.004$ et une fréquence d'activation $F^+ = 0.96$, cas C2 avec $C_\mu = 0.04$ et $F^+ = 0.96$ et cas C3 avec $C_\mu = 0.04$ et $F^+ = 0.29$. Dans le cas C3, le vortex a été étiré en une forme ellipsoïdale avec une diminution de près de 60% de la vitesse circonférentielle de crête et de la vorticité axiale du noyau. Le rayon du noyau du tourbillon s'est élargi, ce qui suggère que la configuration de contrôle de la fréquence la plus basse a permis au jet synthétique de parcourir de plus grandes distances dans le vortex, amenant des structures turbulentes dans son noyau. Cela a entraîné un mélange accru et par la suite un vortex plus diffus. Les mesures du développement du vortex dans la région du sillage proche et intermédiare (jusqu'à $x/c = 5$) ont montré que la vitesse circonférentielle était largement réduite sous l'effet de l'actionnement de SJ. Le mélange turbulent amélioré dans la région interne du vortex a entraîné une diffusion accélérée vers l'extérieur de son noyau même dans des configurations de contrôle non optimales.

3.2 Mid-Wake Wing Tip Vortex Dynamics with Active Flow Control

The development of a wing tip vortex under the effect of synthetic jet (SJ) actuation was examined for a rectangular, square-tipped wing having a NACA 0012 airfoil using hot-wire anemometry at a chord Reynolds number $Re_c = 8 \times 10^4$. Three control configurations were considered for a comparative study, namely case C1 with momentum coefficient $C_\mu = 0.004$ and an actuation frequency $F^+ = 0.96$, case C2 with $C_\mu = 0.04$ and $F^+ = 0.96$ and case C3 with $C_\mu = 0.04$ and $F^+ = 0.29$. Under case C3, the vortex was stretched into an ellipsoid shape with a nearly 60% decrease in the peak circumferential velocity and the core axial vorticity. The vortex core radius largely broadened suggesting that the lower frequency control configuration allowed the synthetic jet to travel larger distances into the vortex bringing turbulent structures within its core. This resulted in an increased mixing and subsequently a more diffuse vortex. Measurements of the vortex development in the near and mid-wake regions (up to $x/c = 5$) showed that the circumferential velocity was largely reduced under the effect of the SJ actuation. The enhanced turbulent mixing at the inner region of the vortex resulted in an accelerated outward diffusion of its core even under non-optimal control configurations.

3.2.1 Introduction

Wing tip vorticies, also known as trailing vorticies, are an ineluctable byproduct of finite span lifting wings. These vortices remain a major concern for the aviation industry because of their hazardous effects on flight safety. For airplanes, the long-lasting nature of the trailing vortices in their wake causes congestion on airport runways due to the space and time required for these vortices to dissipate. Nowadays, most airports require minimum distances between landing aircraft dependent on the weights of the leading and following aircraft [107]. With continuously increasing number and frequency of commercial flights, there is a strong desire amongst aircraft manufacturers to reduce air-traffic congestion. In addition to the wake turbulence, induced drag due to these vortices accounts for up to 40% of the aircraft drag during cruise [73]. Therefore, there is a significant incentive for the aviation industry to reduce the effects of the trailing vortices of an aircraft using flow control technologies. Over the past few decades, considerable effort has been devoted to understand the structure and development of wingtip vortices in the near and far fields and to design effective control strategies capable of alleviating their effects [29]. In fact, since the 70's, many airplane wings have been retrofitted with passive devices, such as winglets, wing end-plates, etc., because of their simple implementation and their minimal

performance penalty [17]. However, these devices are only designed for cruise configuration. Recently, there has been considerable interest in active flow control because it can be adapted to changing flow conditions as it is the case for typical flight envelopes. Active flow control seems to provide an effective control authority over trailing vortices which generally involves blowing and/or suction in the vicinity of the wing tip [40, 50, 57, 59, 79] and the use of articulated surfaces such as oscillating flaps, spoliers and winglets [30, 53, 71, 81]. The former includes expelling a mass of fluid from various locations in the vicinity of the wing tip, which is usually provided by an engine bleed that may result in a reduction of the engine efficiency. This reduction however is generally detrimental during take-off and cruise, as engines are usually idled during approach. The second control authority involves perturbing the inherent long and short-wave cooperative instabilities of the wing tip vortex, namely Crow [31] and Widnall [117] instabilities. The potential of exciting the vortex at particular frequencies requires the design of control devices capable of introducing frequency-dependent perturbations into the vortex core to hasten its dissipation. It has been suggested in the literature that this challenge may be circumvented through the implementation of zero-net mass flux devices, such as synthetic jets (SJ), capable of adding momentum, turbulence and vorticity to the flow at frequencies that can be tuned to the inherent instabilities of the wing tip vortex. Heyes et al. [57] studied the effect of steady and pulsed blowing on the structure and position of a wing tip vortex. With steady blowing, the vortex was found to move upward and outboard and became more diffuse. The vortex diffusion was mainly attributed to the increased turbulence production due to the increased velocity deficit close to the trailing edge [26]. With pulsed spanwise jets, the authors showed that when exciting the vortex at frequencies close to those of the vortex inherent instabilities, the position of the vortex center changed resulting in an increased meandering amplitude, with the effect of the actuation frequencies in the range of those of the vortex instabilities being more pronounced. They were also able to achieve a remarkable increase in the vortex core radius which was accompanied with a decrease in the peak circumferential velocity and an increase in the core axial velocity deficit close the trailing edge. Margaris and Gursul [79] conducted a PIV investigation on the effect of SJ actuation on a wing tip vortex using a wing equipped with several blowing slots placed at different positions in the wing tip proximity. They found that the rate of reduction in the circumferential velocity was comparable to that obtained with steady blowing. However no conclusions were drawn on the choice of the actuation parameters. Also, the authors found that the SJ actuation resulted in high meandering amplitudes with the vortex circulation remaining relatively constant. Conversely, the steady blowing was found to increase the circulation levels of the vortex. Greenblatt [50] studied the effect of a separated shear

layer on a wing tip vortex by deflecting an outboard flap near the tip. By creating a separated shear layer that was controllable with SJ actuation, he showed that the axial velocity deficit was reversed to an axial surplus due to the increase in transverse velocity. A substantial increase in the core axial vorticity and an associated overshoot in circulation were both reported with actuation. The SJ actuation resulted in only small changes in the overall aerodynamic loads. In a more recent study, Dghim et al. [40] used a curved nozzle SJ blowing in the spanwise direction in order to diffuse a wing tip vortex. Using hot-wire anemometry, they reported that the selection of a low actuation frequency, in the range of the wing tip vortex natural instabilities, led to a more diffuse vortex with a reduced circumferential velocity. In their study, only two control configurations were tested, namely $C_\mu = 0.004$, $F^+ = 0.71$ and $C_\mu = 0.040$, $F^+ = 0.213$, where C_μ and F^+ denote the momentum coefficient and the non-dimensionalized actuation frequency, respectively, with a particular focus on the near wake region (up to $x/c = 2$). However, no conclusions were drawn on the effect of the SJ actuation at larger downstream distances. Therefore, the purpose of this study is to experimentally explore the self-similar behavior and the mid-wake development of a wing tip vortex under the effect of SJ actuation. In particular, a parametric study was conducted at $x/c \sim 3$ using various control configurations, namely case C1 where $C_\mu = 0.004$ and $F^+ = 0.96$, case C2 where $C_\mu = 0.040$ and $F^+ = 0.96$ and case C3 where $C_\mu = 0.040$ and $F^+ = 0.29$, to examine the effect of the SJ actuation on the self-similar behavior of a wing tip vortex. Furthermore, under the control case C1, measurements were extended to cover six transverse planes (up to $x/c \sim 5$) in order to study the persistence of the SJ actuation in the mid-wake region with a particular focus on the vortex structure and diffusion.

3.2.2 Experimental Facilities and Instrumentation

Experiments were carried out in a blow-down, low-speed wind tunnel located in the Department of Mechanical and Aerospace Engineering at the Royal Military College of Canada, as described in [40]. A brief summary of the experimental apparatus is provided in this section. The wind tunnel has a cross-sectional area of 0.41×0.41 m^2 and the flow in the empty wind tunnel is uniform to within $\pm 1\%$ with a turbulence level of less than 0.2%. A rectangular planform half-wing with a NACA 0012 airfoil section was used as a vortex generator. It had a chord c of 154.2 mm and a semi-span $b/2$ of 203.2 mm, corresponding to an aspect ratio of 2.7. The origin of the coordinate system was attached to the blunt wing tip at the quarter-chord location with x, y and z coordinates aligned respectively with the streamwise, spanwise and transverse directions of the wind tunnel reference frame, as sketched in Figure 3.1a. Provision was made for the supply of air from the SJ cavity to

the wing tip via a plenum chamber. This air passage spanned the entire half-span of the model and was in fluidic communication with a blowing slot placed at the plane surface of the wing tip, as illustrated in Figure 3.1b. The slot had a trapezoidal shape such that the velocity of the emanating SJ is non-uniform along the chord direction. Flow perturbations were generated by a speaker-type actuator (180 W electric power, 4 Ω electric impedance) mounted outside the test section and connected to the hollow plenum through a contraction nozzle. The speaker was powered by an electric sine wave voltage with a peak value of 16 V_{rms}. Instantaneous three components of the velocity vector field were measured using a custom-built miniature four-sensor hot-wire probe (Auspex scientific®, AVOP-4-100) consisting of two orthogonal X-wire array of sensors. The tungsten sensors had a diameter of 5 μm, a length of 0.9 mm and a nominal distance of about 1 mm. They were operated separately using a TSI IFA 300 multichannel constant temperature anemometer and the output signals were digitized using a 16 bit, 1 MHz A/D converter. The acquired data were sampled at 5 kHz and low-pass filtered at 2 kHz. At each measurement point, time-averaged statistics were evaluated from 15 s long records. The hot-wire probe was positioned in the flow by a two-dimensional motorized traversing system (model: Velmex BiSlide ®) having a resolution of 0.02 mm and automatically controlled by a computer. Each measurement plane consisted of a rectangular 81×81 grid points equally spaced in both y and z directions. The grid resolution, $\Delta y = \Delta z = 2.54$ mm, was carefully selected to ensure at least 10 measurement points within the vortex core. The strength of the SJ was quantified using the blowing momentum coefficient, C_μ, defined as [40]:

$$C_\mu = \frac{A_j}{A_w} \frac{\rho_j \bar{V}_j^2}{\rho_\infty \bar{U}_\infty^2} \tag{3.1}$$

where A_j is the slot area and A_w is the half-wing planform area. The time and spatial-averaged velocity scale, $\bar{V}_j$, was calculated based on the SJ exit velocity, $v_j(t)$, measured along the slot centerline using hot-wire anemometry. $\bar{V}_j$ was based only on the blowing phase of the actuation cycle, as follow [60]:

$$\bar{V}_j = \frac{2}{T} \frac{1}{A_j} \int_A \int_0^{\frac{T}{2}} \vec{v}_j \cdot d\vec{A}\, dt \tag{3.2}$$

The actuation frequency was non-dimensionalized as:

$$F^+ = \frac{f_a \cdot c}{\bar{U}_\infty} \tag{3.3}$$

where f_a is the actuation frequency, c is the chord length of the wing and $\bar{U}_\infty$ is the free stream velocity [51].

Considering these SJ actuation parameters, four configurations were investigated in the present study; (NV) natural vortex, (C1) $C_\mu = 0.004$ and $F^+ = 0.96$, (C2) $C_\mu = 0.040$ and $F^+ = 0.96$ and (C3) $C_\mu = 0.040$ and $F^+ = 0.29$, as summarized in Table 3.1. These cases were selected based on the preliminary study on the selection of actuation parameters reported in [40]. In their study, Dghim *et al.* [40] conducted a parametric study on the effect of the actuation parameters on the pressure distribution along the upper surface of the wing at the quarter-chord position. Although these measurements were not presented in this paper, the selection of control cases refers to the discussion of the parametric study detailed therein. In the same study, hot-wire measurements were conducted at only two transverse planes located at $x/c = 1$ and 2, and only two control configurations were considered. In this study however, measurements were extended to cover both near and mid-wake regions at particularly six transverse planes located at $x/c = 0.75$, 1, 2, 3, 4 and 5. Experiments were conducted at an angle of attack of 5 degrees and a free stream velocity, $\bar{U}_\infty$, of 8 m/s, corresponding to a Reynolds number $Re_c = 8 \times 10^4$. The estimated maximum uncertainties of the experimental measurements are 3% and 9% for velocity and vorticity, respectively [70].

Table 3.1 Experimental configurations

	F^+	C_μ
Natural Vortex case (NV)	-	-
Control case 1 (C1)	0.96	0.004
Control case 2 (C2)	0.96	0.040
Control case 3 (C3)	0.29	0.040

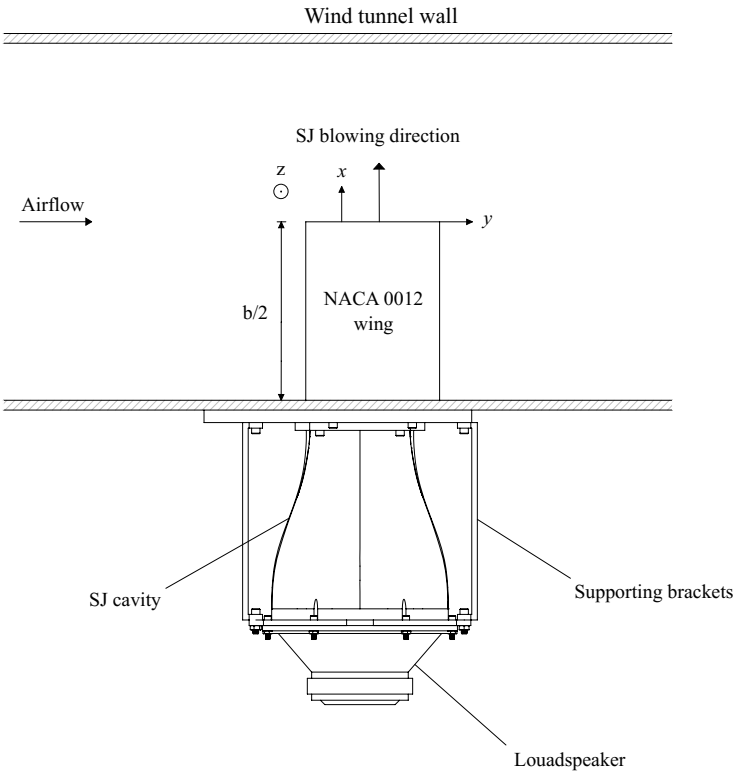

(a)

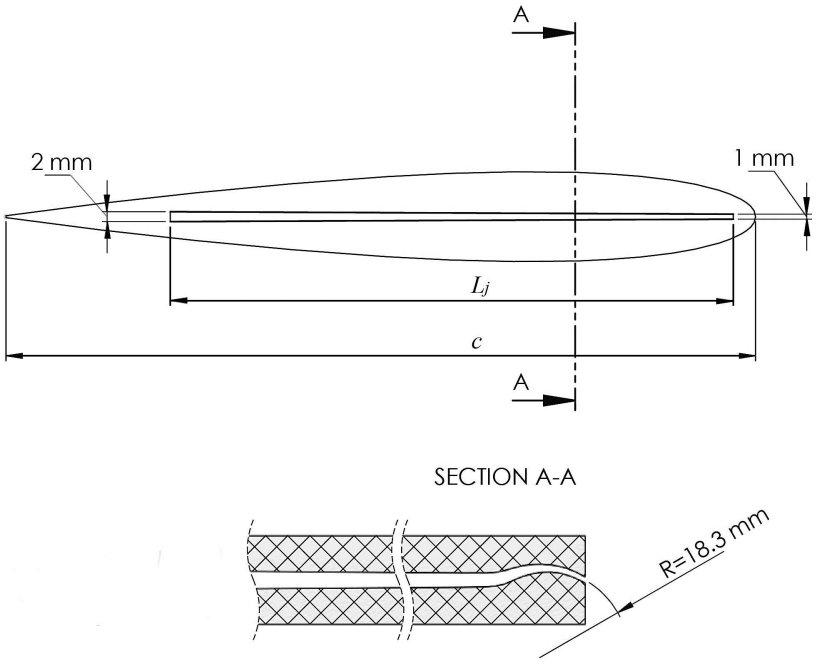

(b)

Figure 3.1 (a) Experimental setup, (b) Slot geometry [40].

3.2.3 Vortex meandering

It has been well-documented in the literature that tip vortices exhibit a broadband, low-frequency motion in their core which is referred to as vortex meandering. The latter is known to create artificially reduced circumferential velocity and increased vortex core radius [2, 12, 37, 57]. These effects were found to be more profound when turbulence or low-frequency forcing were applied to the vortex, as reported in [2, 12, 50, 57, 79]. Thus, an ultimate correction is believed to be necessary in order to isolate the effect of vortex meander from that of the active flow control on the mean flow structure. Devenport *et al.* [37] developed an iterative technique to correct single-point flow field measurements and remove the meandering effect in order to recover the true velocity field of the tip vortex. As such, the time-averaged circumferential velocity profile along the $y = 0$ axis is fitted with a series based on the Lamb-Oseen vortex, given as

$$\bar{U}_\theta(0, z) = \sum_{i=1}^{n} \frac{D_i}{z} \left[1 - \exp\left(\frac{-z}{c_i^2}\right)\right] \tag{3.4}$$

where D_i and c_i are the fitting coefficients of the measured profiles.
In this study, the mean circumferential velocity was calculated using the following expression:

$$\bar{U}_\theta = \left(\bar{U}_z - \bar{U}_{z_c}\right)\cos\theta - \left(\bar{U}_y - \bar{U}_{y_c}\right)\sin\theta \tag{3.5}$$

where $\bar{U}_{y_c}$ and $\bar{U}_{z_c}$ are the local spanwise and transverse velocities of the time-averaged vortex center, respectively. The circumferential velocity was evaluated using the radial, r, and angular, θ, coordinates of each of the raw measurement points centred around the mean vortex center position. The circumferential velocities were then plotted as a function of the radial distance from the vortex center. The scatter was then averaged at each of the radial intervals.
Over a long period of time, the vortex position relative to the measurement point can be described by a bi-normal joint probability density function (j.p.d.f) of the form

$$P(y, z) = \frac{1}{2\pi\sigma_y\sigma_z(1 - e^2)^{1/2}} \exp\left[\frac{1}{2(1 - e^2)}\left(\frac{z^2}{\sigma_z^2} + \frac{y^2}{\sigma_y^2} - \frac{2eyz}{\sigma_y\sigma_z}\right)\right] \tag{3.6}$$

where σ_y and σ_z are the r.m.s amplitudes of meandering in the spanwise and transverse directions, respectively, and e is the correlation coefficient. Initial guess values were determined using the 'rules of thumb' suggested by [37]. These parameters were iteratively updated until the estimated variances due to meandering of the corrected profiles at the vortex center reach comparable levels with the measured variances of the velocity fluc-

tuations in both y and z directions. Note that the Devenport's technique assumes that turbulence within the core is negligible compared to that induced by vortex meandering.

The radial profiles of the measured circumferential velocity, fitted by equation 12, are shown in Figure 3.2, along with the corresponding corrected profiles, for all the cases studied at $x/c = 3$. For the NV case, the effect of meandering on the peak value of the circumferential velocity was essentially negligible. Moreover, no effect on the vortex radius was observed at the selected downstream position $x/c = 3$. Similar effects were also observed closer to the wing trailing edge at $x/c = 1$ and further downstream at $x/c = 5$, as illustrated in Figure 3.3a and 3.3b. It is believed that the undistinguishable effect of vortex meandering on the corrected velocity field of the NV case is probably attributed to the higher turbulent fluctuations within the vortex core compared to the meandering-induced turbulence, as suggested in [12, 101]. With control and under case C1, the corrected peak circumferential velocity at $x/c = 3$ was found to be 5% higher than that of the measured profile. This slight increase was associated with nearly 8% decrease in vortex radius. For case C2, the peak value of the corrected circumferential velocity was found to increase by roughly 13% with respect to the NV case. In addition, the vortex radius was found to decrease by nearly 18% as a result of meandering correction. Amongst all the cases studied, case C3 exhibited the most significant impact of vortex meandering on the measured flow field. In fact, the peak value of the corrected circumferential velocity was 16% higher than that of the measured profile. The corrected vortex radius was measured to be 23% smaller than that of the measured profile. It is noteworthy that, despite the meandering correction of the measured velocity field, the peak value of the corrected circumferential velocity remained substantially lower than that of the NV case and the vortex appeared to be significantly diffuse. It was conjectured that the turbulence addition from the SJ actuation largely contributed to the diffusion of the tip vortex as a result of the increased turbulent mixing within its core.

The streamwise development of the independent meandering amplitudes, σ_y and σ_z, for all the cases studied is summarized in figure Figure 3.4. For case NV, the meandering amplitudes were found to slightly grow with increased streamwise distance, consistent with previous observations reported in [2, 12, 37, 57]. The meandering amplitudes of σ_y and σ_z were of the same order of magnitude at all downstream locations, indicating a non-preferred direction for the nearly isotropic meandering motion. With control, σ_y and σ_z of the case C1 were measured to be 5 and 4 times larger than those of the NV case, respectively. The meandering amplitudes were seen to rapidly decrease with increased downstream distance and appeared to reach a nearly asymptotic value at $\sim x/c = 5$. At this position, σ_y and σ_z were found to be 75 and 53% higher than those of the NV case,

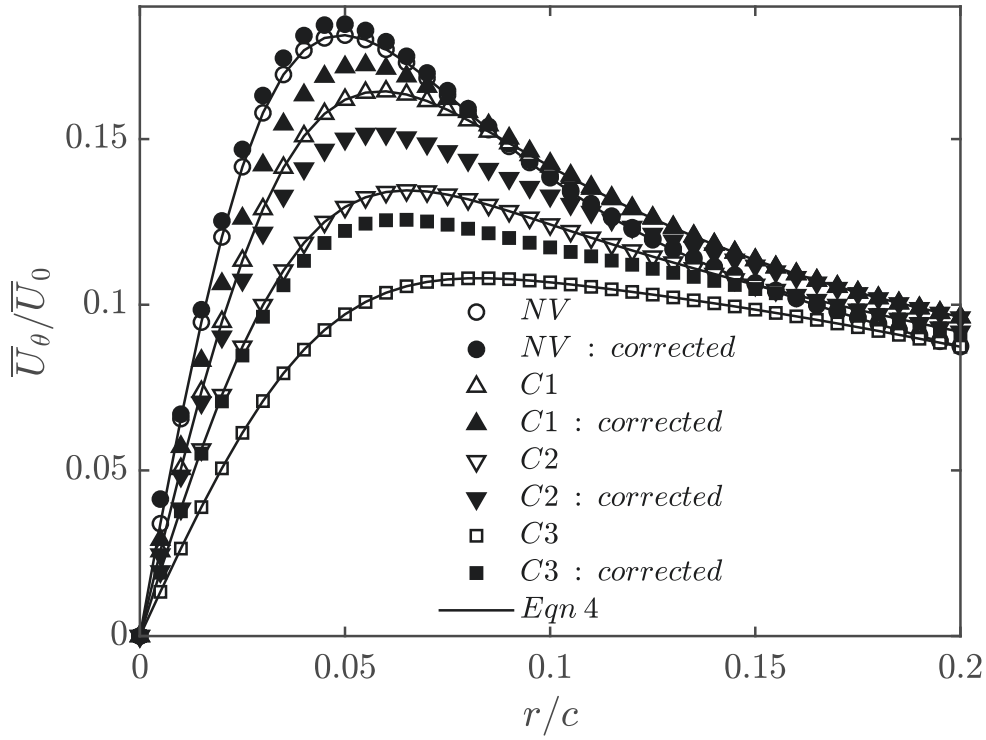

Figure 3.2 Circumferential velocity profiles of all the cases studied, fitted by equation (12) and corrected for vortex meandering, at $x/c = 3$.

respectively. Interestingly, at $x/c = 3$, the control cases C2 and C3 exhibited significantly larger meandering amplitudes compared to both NV and C1 cases, particularly in the z direction. In fact, σ_z was nearly 7 and 10 times higher than that of NV for both C2 and C3 cases, respectively. In retrospect, although the SJ actuation has shown to alter the structure of the corrected vortex flowfield, it is believed that the coherent part of the turbulence fluctuations injected by the SJs causes the vortex to meander with significantly larger amplitudes compared to the NV case. However, since the Devenport's correction assumes that all the measured turbulence within the core is essentially attributed to meandering, it is virtually impossible to separate the effects of both coherent and random components of the turbulence fluctuation on the measured turbulence within the vortex using a single-point measurement technique.

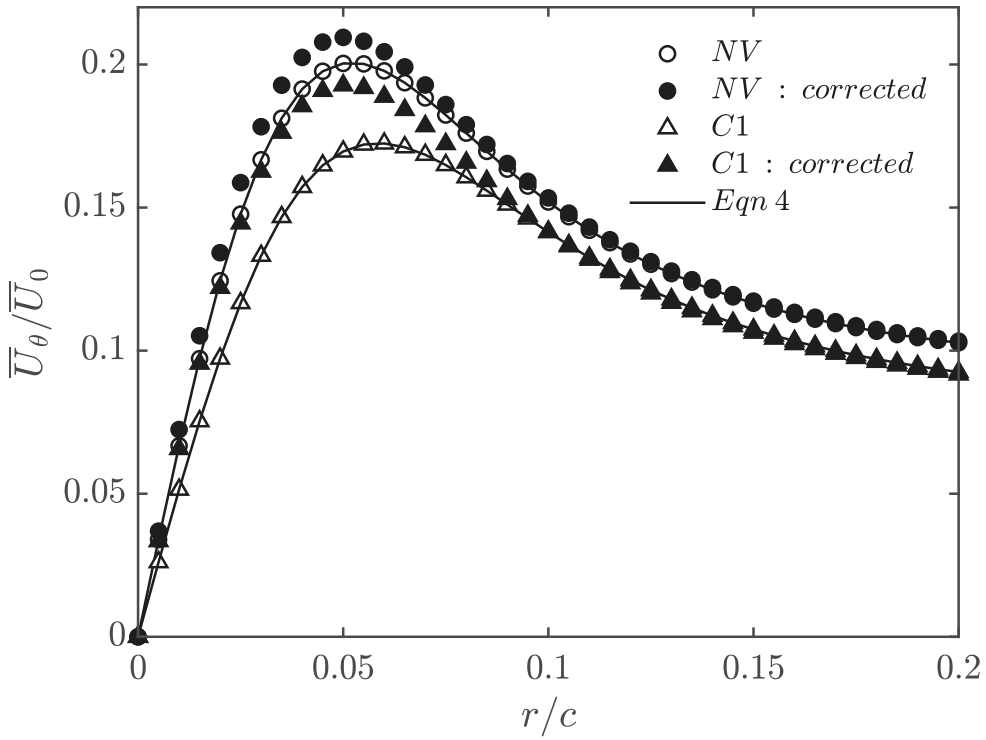

(a)

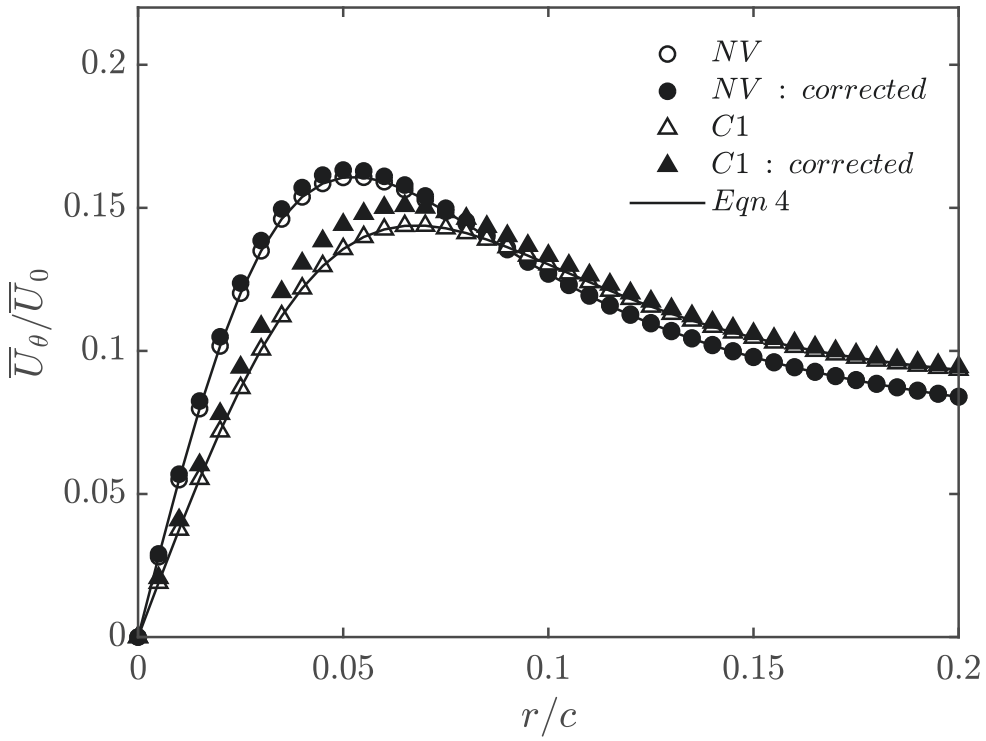

(b)

Figure 3.3 Circumferential velocity profiles of both NV and C1 cases, fitted by equation (12) and corrected for vortex meandering, at (a) $x/c = 1$ and (b) $x/c = 5$.

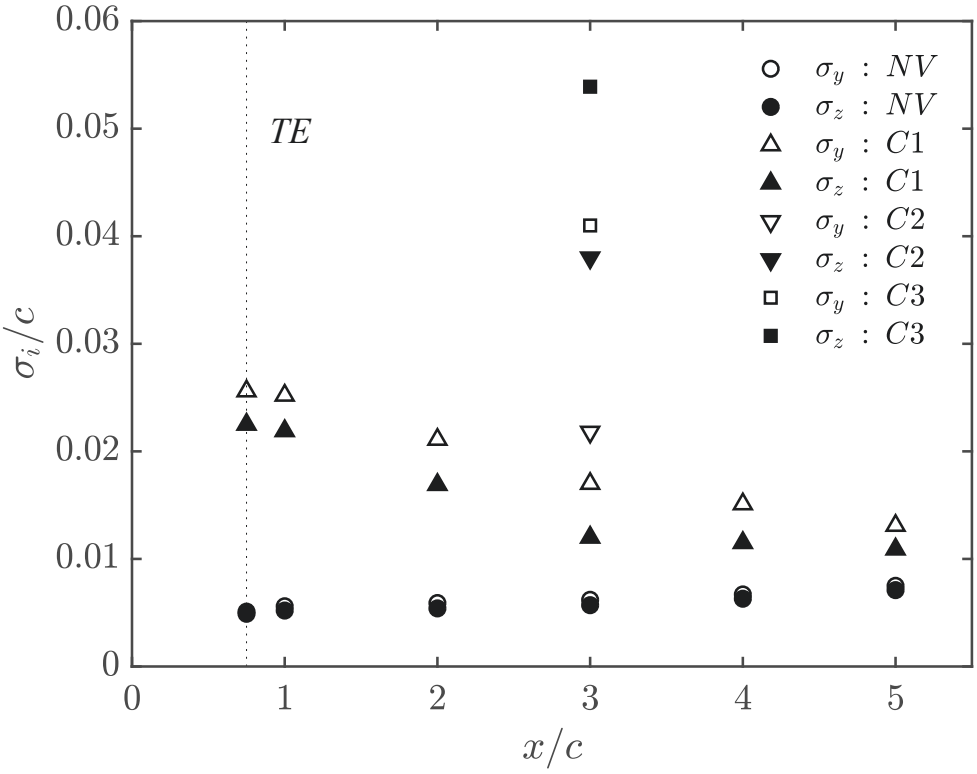

Figure 3.4 Streamwise development of the normalized meandering amplitudes, σ_y and σ_z, for all the cases studied.

3.2.4 Results and discussion

Effect of the SJ control parameters on the vortex characteristics

In order to assess the sensitivity of the wing tip vortex structure to the SJ control parameters, a parametric study of different control configurations was conducted at the downstream location $x/c = 3$. The configurations considered for this study are summarized in Table 3.1.

Time-averaged axial velocity deficit

Contour plots of the normalized axial velocity deficit, $(\bar{U}_0 - \bar{U}_x)/\bar{U}_0$, where $\bar{U}_0$ is the local free-stream velocity which was at worst 3% higher than the undisturbed free-stream $\bar{U}_\infty$, are shown in Figure 3.5a for the natural vortex (NV), Figure 3.5b for the control case C1, Figure 3.5c for the control case (C2), and Figure 3.5d for the control case (C3) at the measurement plane $x/c = 3$. The wing tip vortex was evidenced by a nearly axisymmetric region of strong velocity deficit with a peak of about 0.23 (Figure 3.5a). Outside the core region of the NV, velocity contours showed a curved region dominated by a velocity deficit of about 0.1. This region corresponds to wake shear layer being drawn and fully wrapped

around the main vortex core as a result of the strong pressure gradient. The position of the trailing edge of the wing was indicated with a horizontal dashed line. With control, the wake shear layer region of case C1 was slightly thickened and its maximum velocity deficit decreased by nearly 50% with respect to the NV case as illustrated in Figure 3.5b. Velocity contours of the C1 vortex exhibited a well-organized but a rather diffuse core region compared to NV with a maximum velocity deficit of about 0.18. The reduction in the core velocity deficit is the result of the outward diffusion of the vortex by the spanwise flow imparted from the SJ [40]. Figure 3.5c shows the contours of the vortex velocity deficit under the case C2 at $x/c = 3$. Nearly 45% decrease in the core maximum velocity deficit with respect to NV was achieved under the control case C2. Interestingly, velocity contours of the tip vortex under the control case C3 exhibited a different structure than those of NV, C1 and C2 cases. In that, the wake shear layer appeared to be broadened and more diffuse with the maximum wake velocity deficit being 35% lower than that of NV. Furthermore, the core region of the C3 vortex was found to be stretched in the spanwise direction to adopt a nearly elliptical shape. This is due to the subsequent interaction of the high C_μ SJ of case C3 with the tip vortex during its early rollup process. Note that the stretching of the vortex under control case C3 was accompanied by an outward broadening of the velocity deficit contours which indicates an increase in the vortex size. It is noteworthy that, although the vortex core under the control case C3 appeared larger and more diffuse than those of C1 and C2 cases, the resulting deficit was 26% lower than the NV, as illustrated in Figure 3.5d. Additionally, the time-averaged location of the maximum velocity deficit for the case C3 appeared to move further inboard towards the wing root.

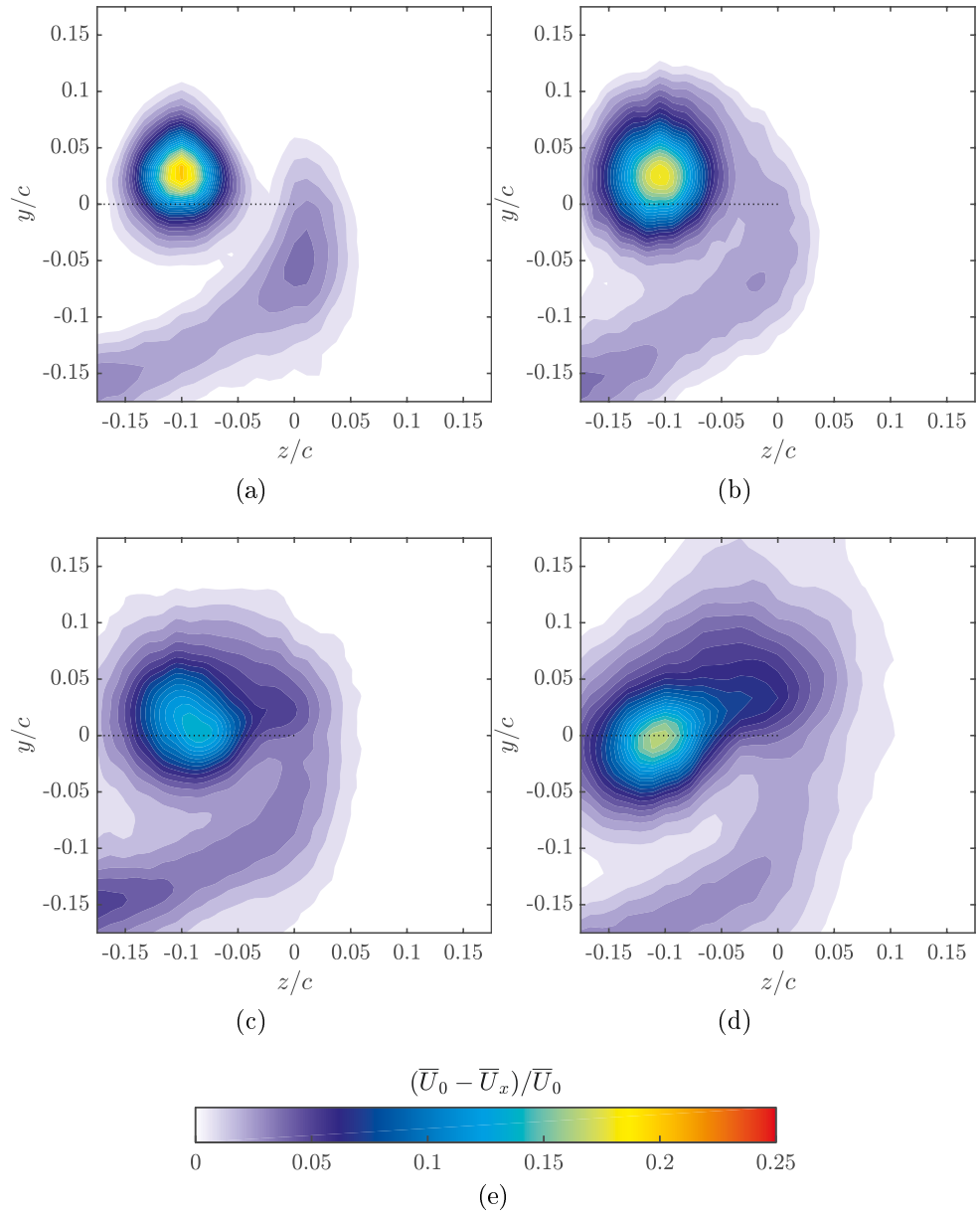

Figure 3.5 Uncorrected contours of the normalized axial velocity deficit at $x/c = 3$. (a): NV, (b): C1, (c): C2 and (d): C3.

Time-averaged circumferential velocity

The radial distributions of the normalized mean circumferential velocity, $\bar{U}_\theta/\bar{U}_0$ for NV, C1, C2 and C3 cases are shown in Figure 3.6 at the measuring plane $x/c = 3$. The vortex radius, r_c, was defined as the distance from the vortex center, which corresponds to the position of the maximum axial vorticity, and the radial location of the peak value of $\bar{U}_\theta$. The latter was denoted with vertical dashed lines placed at the vortex radii of all the cases investigated. The region between the time-averaged vortex center and radial location at which the peak value of $\bar{U}_\theta$ occurred is often refered to as the inner core region, and the outer region lies beyond the radial position of maximum $\bar{U}_\theta$. For NV, the radial profile of $\bar{U}_\theta/\bar{U}_0$ reached a peak value of nearly 0.185 corresponding to a normalized vortex radius, $r^*_{NV} = r_{NV}/c$ of about 0.05. With actuation of case C1, the gradient of $\bar{U}_\theta/\bar{U}_0$ within the core region showed a slight decrease with respect to NV causing the peak value of $\bar{U}_\theta$ to decrease to a value of about 0.172. The reduction of the magnitude of $\bar{U}_\theta$ in case C1 was accompanied with a 10% increase of the vortex radius with respect to NV. Under case C2, further increasing C_μ resulted in a significant decrease of the peak value of $\bar{U}_\theta$ by about 18 and 12% with respect to NV and case C1, respectively. Note that, although the high C_μ value of case C2 largely reduced the peak value of the circumferential velocity, only 9% increase of the normalized vortex radius, $r^*_{C2} = r_{C2}/c$, was found with respect to the low C_μ case. Under case C3, decreasing the actuation frequency, F^+, while keeping the high C_μ value of case C2 resulted in a significant deceleration of $\bar{U}_\theta$ inside the core region as well as the shear layer region. In fact, the peak value of the circumferential velocity was roughly 32%, 27% and 17% lower than those of NV, C1 and C2 cases, respectively. As opposed to case C2, reducing F^+ was found to further promote vortex diffusion by increasing its size to nearly twice that of NV. The larger effect of the low frequency actuation is in agreement with the findings of [40, 79]. It is also noteworthy that, despite the large radial diffusion of the tip vortex under case C3, the peak of the circumferential velocity was less identifiable than that of the other remaining cases. Furthermore, the distribution of the circumferential velocity in the outer region of the vortex seemed to level around a nearly asymptotic value in a similar manner of that reported in [40, 57]. It has been reported in [91] that the circumferential velocity profiles in the core of a wing tip vortex adopt a self-similar behavior, when $\bar{U}_\theta$ and r are normalized by the peak value, $\bar{U}_{\theta,m}$, and the vortex radius, r_c, respectively. For NV, this behavior was clearly depicted in Figure 3.7 where $\bar{U}_\theta/\bar{U}_{\theta,m}$ reached a peak value of 1 at the normalized radial position $\eta = r/r_c$ of 1, typical of a self-preserved vortex structure. This is attributed to the fact that, at $x/c = 3$, the rollup process may have been completed and the vortex core had reached an asymptotic state. The profile of $\bar{U}_\theta/\bar{U}_{\theta,m}$ was also described fairly well with

the curve fit proposed in [8] within the region $\eta < 1.2$. Outside the vortex core and for $\eta > 1.2$, the profile of $\bar{U}_\theta/\bar{U}_{\theta,m}$ for NV slightly departed from the curve fit of [8]. The slight upward departure from the theoretical model was observed in previous studies [4, 34, 114] and might be attributed to the gradual transition between the viscous core region and the outer region dominated by the rotational flow of the rolling vortex sheet [100]. For case C1, the actuation did not appear to alter the shape of the vortex core and the profile of $\bar{U}_\theta/\bar{U}_{\theta,m}$ showed a reasonable collapse with the theoretical fit. Outside the core region, the profile of $\bar{U}_\theta/\bar{U}_{\theta,m}$ was found to move further upward from the theoretical fit. As opposed to both NV and C1 cases, the increased C_μ of case C2, caused the profile of $\bar{U}_\theta/\bar{U}_{\theta,m}$ to slightly depart from the theoretical fit inside the core region, suggesting a non asymptotic behavior of the tip vortex. The low frequency actuation of case C3 resulted in a more pronounced departure of the profile of $\bar{U}_\theta/\bar{U}_{\theta,m}$ from the theoretical fit outside the core region, inferring an atypical vortex shape under the control case C3 requiring larger downstream distances to achieve a self-similar state.

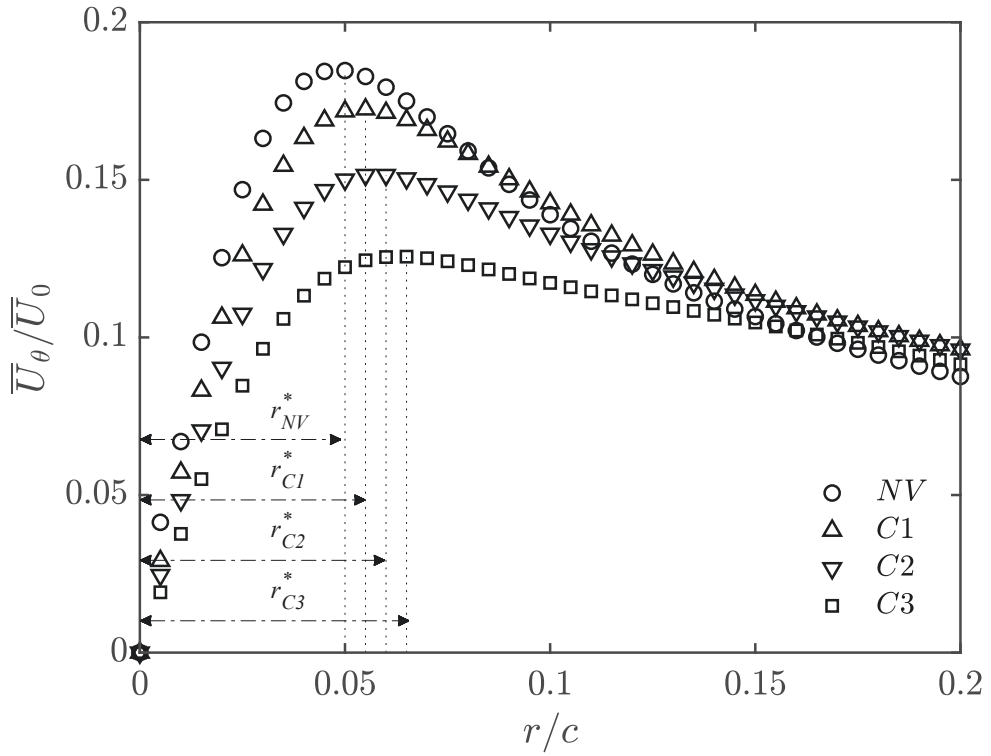

Figure 3.6 Corrected radial profiles of the normalized circumferential velocity at $x/c = 3$.

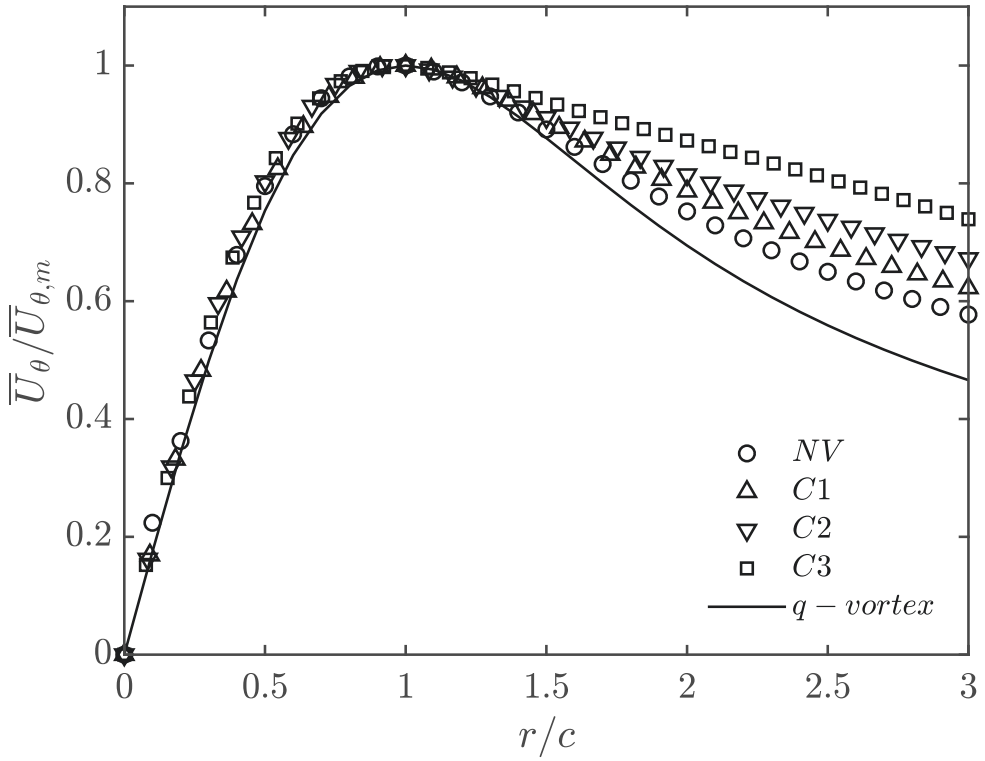

Figure 3.7 Corrected radial profiles of the normalized circumferential velocity in a self-similar coordinate system at $x/c = 3$.

Time-averaged axial vorticity

The mean axial vorticity, $\bar{\xi}_x$, was estimated using a second order central differencing scheme as

$$\bar{\xi}_x = \frac{\partial \bar{U}_z}{\partial y} - \frac{\partial \bar{U}_y}{\partial z} \approx \frac{\bar{U}_{z_{j,i+1}} - \bar{U}_{z_{j,i-1}}}{2\Delta y} - \frac{\bar{U}_{y_{j+1,i}} - \bar{U}_{y_{j-1,i}}}{2\Delta z} \tag{3.7}$$

where $i = 1, 2, ...m$, $j = 1, 2, ...n$, m and n were the number of measurement points, and $\Delta y = 2.54$ mm and $\Delta z = 2.54$ mm were the cross-stream spacing of the measurement grid.

Contours of the normalized mean axial vorticity, $\bar{\xi}_x\, c/\bar{U}_0$, at $x/c = 3$ are displayed in Figure 3.8a, 3.8b, 3.8c and 3.8d for NV, case C1, case C2 and case C3, respectively. In Figure 3.8a, the axial vorticity contours of NV clearly show two distinct regions in the flow field: the wake shear layer and the tip vortex. The former exhibited a spiral shape with relatively low vorticity levels, whereas the latter contained most of the vorticity within an area of a nearly circular shape with a radius of about $0.05c$. Outside the wake and the tip vortex regions, the vorticity was essentially zero. The peak value of the normalized

axial vorticity at the center of this region was about 13. Under control case C1, the region of high vorticity seemed to cover a much larger and more axisymmetric area compared to NV, as illustrated in Figure 3.8b. The apparent outward diffusion of the vortex was accompanied with a 22% decrease in the peak value of the axial vorticity. In case C2, the higher C_μ actuation led to a further decrease in the peak value of the axial vorticity of about 50%. As shown in Figure 3.8c, the vorticity contours close to the vortex core region of case C2 appeared to be slightly stretched in the spanwise direction. The control case C3 (Figure 3.8d) had the most significant impact on the vorticity compared to both C1 and C2 cases. More specifically, over 60% decrease in the peak value of the axial vorticity was achieved at the vortex center compared to NV along with a thickening of wake shear layer where the axial vorticity level was reduced by up to 45% with respect to NV. Furthermore, contours of the axial vorticity appeared to cover a larger area around the vortex center compared to case C2. A more pronounced spanwise stretching of the vortex was also seen for case C3 as a result of the stronger interaction with the low frequency jet emanating from the wing tip. Similar behavior was also observed at earlier wake ages, namely at $x/c = 1$ and 2, which their measurements were reported in a previous study published by the same authors [40]. It can be inferred from these measurements along with the data collected at $x/c = 3$ that the reduced vorticity levels and the increased vortex radii at multiple streamwise positions for both C1 and C3 cases can reasonably corroborate the conclusion of a diffuse vortex. Note that the time-averaged location of the vortex centers for cases C1 and C2 were drawn inboard towards the wing root.

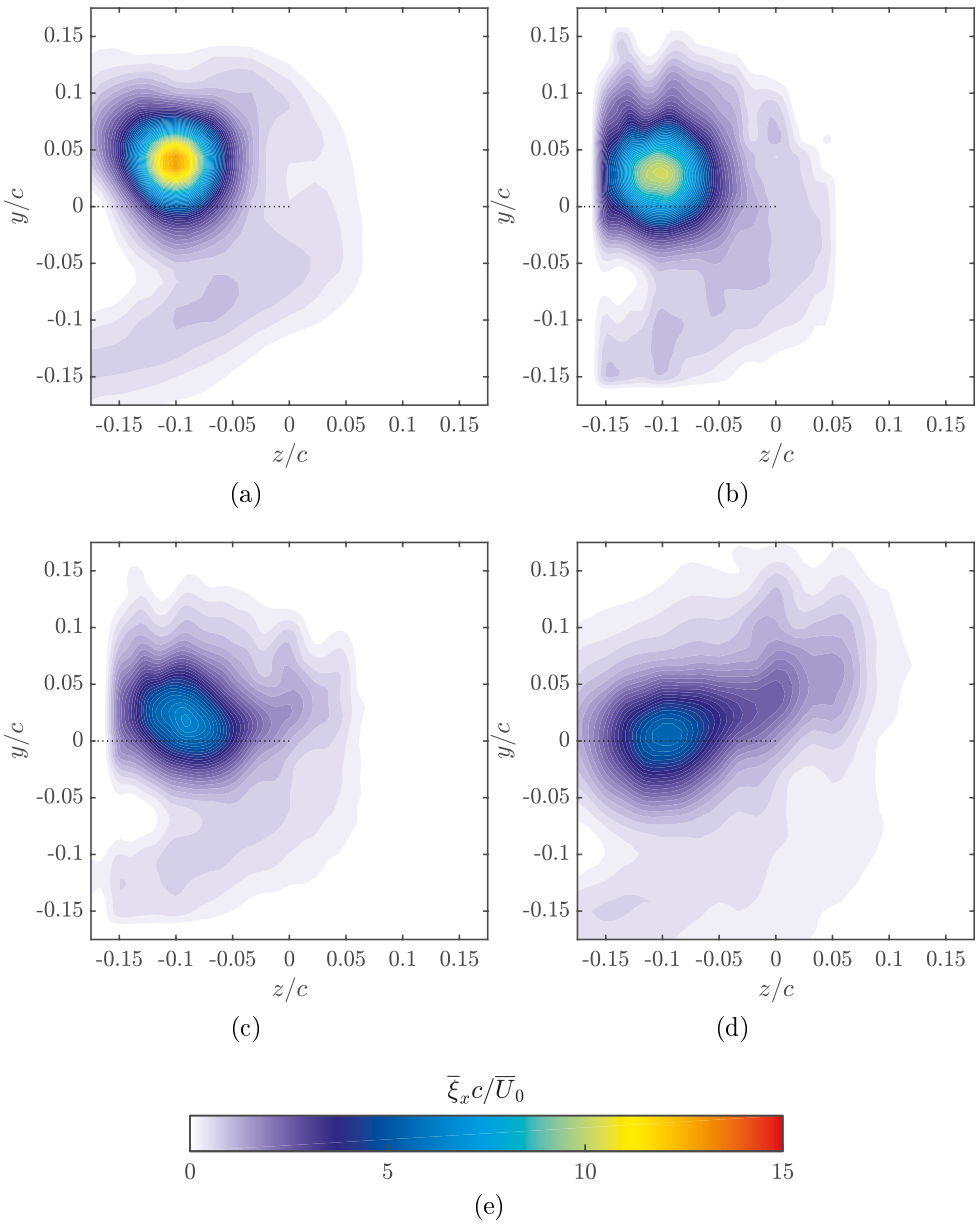

Figure 3.8 Uncorrected contours of the normalized axial vorticity at $x/c = 3$. (a): NV, (b): C1, (c): C2 and (d): C3.

Time-averaged circulation

The time-averaged circulation was estimated by integrating the interpolated values of $\bar{U}_\theta/\bar{U}_0$ over circular contours linearly spaced in the r/c direction:

$$\bar{\Gamma}(r) = \int_0^{2\pi} \bar{U}_\theta(r)\, r\, d\theta \tag{3.8}$$

In order to assess the effect of SJ actuation on the vortex strength, the radial distributions of the time-averaged circulation, $\bar{\Gamma}(r)$, of NV, C1, C2 and C3 cases were normalized by the vortex core circulation of NV, $\bar{\Gamma}_{c_{NV}}$, and were plotted against r/c at the downstream location $x/c = 3$, as illustrated in Figure 3.9. The vortex core circulation, $\bar{\Gamma}_c$, was defined using the following expression:

$$\bar{\Gamma}_c = r_c \int_0^{2\pi} \bar{U}_\theta(r_c)\, d\theta \tag{3.9}$$

where r_c is the vortex radius. For NV, it is believed that, at $x/c = 3$, the vortex was fully developed and its circulation would remain unchanged with increased downstream distances, as reported in [15, 47]. In Figure 3.9, the profile of the normalized circulation for NV showed an inflexion point in the inner core region at $r/c \sim 0.01$ beyond which the circulation increased monotonically with increased radial distances. Outside the core region, $r/c > r^*_{NV}$, the normalized circulation kept increasing with increased radial positions until reaching a second inflection point at $r/c \sim 0.06$ marking the extent of the rollup of the shear layer. Beyond this point, the rate of growth of the normalized circulation started to decrease as the vortex velocity field approached an irrotational state outside the core region [114]. With control, the gradient of the normalized circulation of case C1 within the core region was slightly lower than that of NV due to the decreased vorticity in this region. Note that the vortex core circulation at $r/c = r^*_{C1}$, $\bar{\Gamma}_{c_{C1}}$, was roughly 6% higher than $\bar{\Gamma}_{c_{NV}}$, which might indicate an increase of the wing bound circulation [50, 59]. Furthermore, as seen for NV, the circulation profile of case C1 exhibited an inflexion point outside the core region ($r/c > r^*_{C1}$), where the growth rate of the normalized circulation slightly decreased but remained noticeably higher than NV, indicative of the diffusion of vorticity towards larger radial distances. A similar behavior was also observed under case C2 with the radial values of circulation being noticeably lower than those of NV. In that, the gradient of the circulation profile within the core region was less steep in case C2 compared to both NV and case C1 and the vortex core circulation, $\bar{\Gamma}_{c_{C2}}$, was almost 8% higher than $\bar{\Gamma}_{c_{NV}}$. Under the control configuration C3, a noticeable reduction in circulation was observed at

all radial positions as compared to NV, C1 and C2 cases. This reduction in circulation may be attributed to the considerable diffusion of vorticity towards larger radial distances under the effect of the higher C_μ and the lower actuation frequency, F^+. Similar to the control cases C1 and C2, the vortex core circulation, $\bar{\Gamma}_{c_{C3}}$, increased by roughly 15% with respect to NV. Unlike the other cases, the circulation distribution of case C3 did not exhibit an inflexion point and was nearly linear inside and outside the core region as a result of the nearly flat circumferential velocity profile, as illustrated in Figure 3.6. This atypical behavior suggests that the SJ of case C3 had significantly affected the structure of the tip vortex resulting in an increased outward diffusion of the vorticity and a significant broadening of the vortex size compared to both C1 and C2 cases. It is interesting to note that, with the noticeably high growth rate of the circulation of case C3, it is expected that the velocity field outside the vortex core would remain rotational over large distances from the mean vortex center position before its reaches a nearly irrotational state.

The effect of the control on the vortex core structure of case C3 can be further demonstrated from the close examination of the radial distribution of the normalized circulation, $\bar{\Gamma}(r)/\bar{\Gamma}_c$, plotted against the similarity variable, $\log \eta$, as shown in Figure 3.10. Empirical

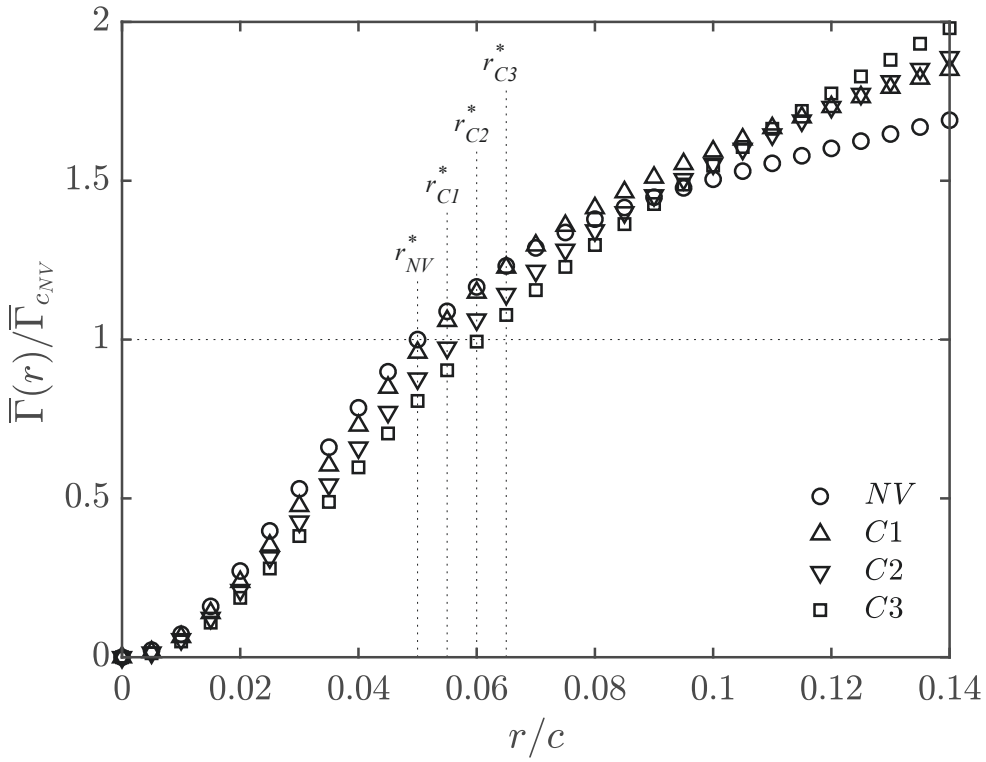

Figure 3.9 Corrected radial distribution of the normalized circulation at $x/c = 3$. $\bar{\Gamma}_c$ corresponds to the intersection of $\bar{\Gamma}(r)$ with the vertical lines indicating the normalized vortex radius of each case.

curve-fit relationships suggested by [58], which describe the circulation behavior within the inner-core and the logarithmic regions of the vortex, were fitted to the radial profiles of $\bar{\Gamma}(r)/\bar{\Gamma}_c$ of all the cases studied, such that:

$$\frac{\bar{\Gamma}(r)}{\bar{\Gamma}_c} = A\eta^2 \quad \text{for} \quad \eta < 0.4 \tag{3.10}$$

$$\frac{\bar{\Gamma}(r)}{\bar{\Gamma}_c} = 1 + B\log(\eta) \quad \text{for} \quad 0.5 < \eta < 1.4 \tag{3.11}$$

where the constants A and B are 1.83 and 0.93, respectively. A reasonable collapse between the radial profiles of $\bar{\Gamma}(r)/\bar{\Gamma}_c$ of NV, C1 and C2 cases, along with the curve-fits of equations 4.21 and 4.22, was clearly observed in Figure 3.10. Moreover, all the data of NV, C1 and C2 cases within $0 < \eta < 1.2$ collapsed together onto a sixth-order polynomial suggested by [15, 93] following the expression:

$$\frac{\bar{\Gamma}(r)}{\bar{\Gamma}_c} = a_0\eta^2 + a_1\eta^4 + a_2\eta^6 \tag{3.12}$$

where the constants a_0, a_1 and a_2 are 1.756, -1.044 and 0.263, respectively. Inside the inner core region, the circulation profiles of NV, C1 and C2 were $\propto \eta^2$ and exhibited a parabolic shape. This indicated that this region was mainly dominated by the viscous effect where the vortex core had an approximately rigid body rotation [58]. Unlike NV, C1 and C2 cases, the circulation profile of case C3 depicted a clear departure from the self-similar collapse and the curve-fits given by equations 4.21, 4.22 and 4.23. Interestingly, the departure from the universal behavior was more pronounced within the inner region suggesting that the vortex core has lost its self-similar behavior by the momentous SJ of case C3.

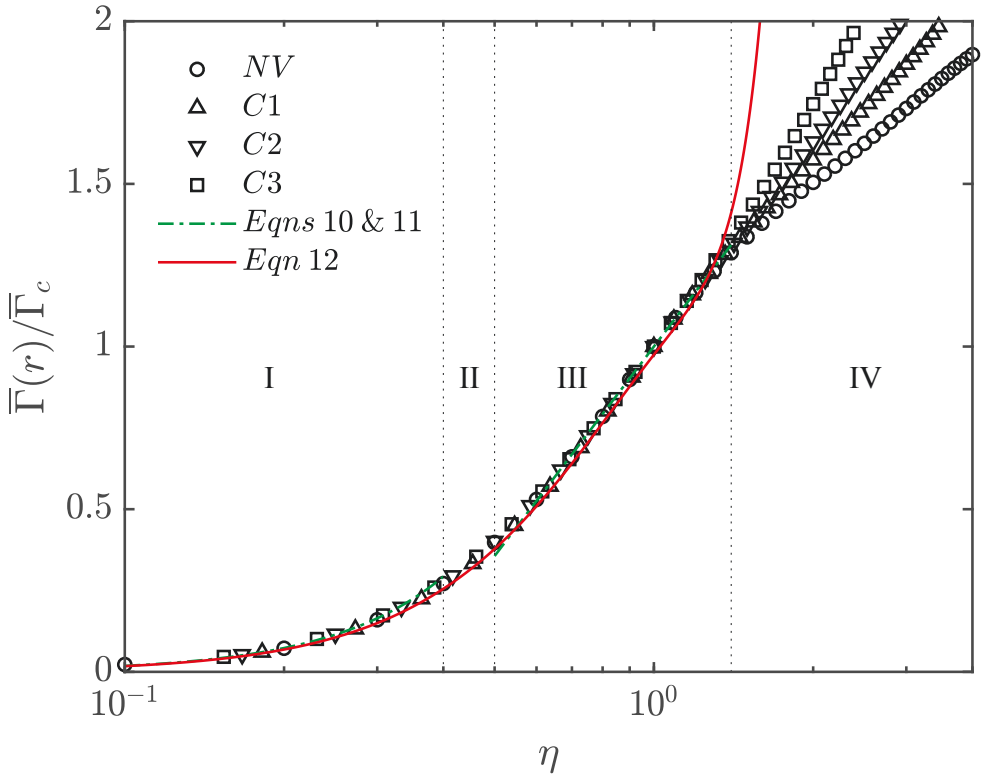

Figure 3.10 Corrected self-similar circulation profiles of the inner-region at $x/c = 3$: I: inner-core, II: buffer region, III: logarithmic region and IV: outer region.

Turbulent kinetic energy

In order to gain more insight into the mechanisms of the vortex weakening and diffusion under the effect of the SJ actuation, the normalized turbulent kinetic energy, $k/\bar{U}_0^2$, was evaluated using the following expression:

$$\frac{k}{\bar{U}_0^2} = \frac{1}{2}\left(R_{uu} + R_{vv} + R_{ww}\right) \tag{3.13}$$

where $R_{uu} = \overline{u'u'}/\bar{U}_0^2$, $R_{vv} = \overline{v'v'}/\bar{U}_0^2$ and $R_{ww} = \overline{w'w'}/\bar{U}_0^2$ are the normalized streamwise, spanwise, and transverse Reynolds stresses, respectively. u', v' and w' are the fluctuating velocities in the x, y and z directions, respectively, which include both coherent and turbulent components. Contour plots of the turbulent kinetic energy are plotted in Figure 3.11a for NV, Figure 3.11b for the control case C1, Figure 3.11c for the control case C2, and Figure 3.11d for the control case C3, at the measurement plane $x/c = 3$. In Figure 3.11a, contours of $k/\bar{U}_0^2$ near the vortex core region showed a small concentration of turbulence with a maximum value of about 2.7×10^{-3}. For case C1, a large concentration of turbulent kinetic energy was seen in the vortex core (Figure 3.11b) with a peak value of $k/\bar{U}_0^2$ twice

as high as that of NV. Under C2 control configuration, Figure 3.11c depicts a 15% increase in peak value of $k/\bar{U}_0^2$ in the core region as compared to the C2 case. Contours of $k/\bar{U}_0^2$ were seen to cover a larger area of the vortex core than those of NV and C1 cases. With control configuration C2, an ellipsoid-shaped region of significantly higher values of $k/\bar{U}_0^2$ appeared to be concentrated around the vortex core region. The peak value of $k/\bar{U}_0^2$ in the vortex core was measured to be 23.2×10^{-3}, which is approximately one order of magnitude, four times and three times higher than that of the NV, C1 and C2 cases, respectively. It can readily be inferred from Figure 3.11d that the high turbulent region in the vortex core of case C3 was spread over a larger radial area compared to both C1 and C2 cases. Although not shown here, the stretching of the contours of the turbulent kinetic energy, which predominantly occured in the spanwise direction, was also depicted at earlier wake ages, namely $x/c = 1$ and 2, which were reported in a previous study conducted by the same authors [40]. It can be conjectured from the measurements at multiple streamwise positions that the low actuation frequency of case C3, which allowed the SJ to largely penetrate the vortex during each blowing cycle, resulted in an increased meandering-induced turbulence within the vortex core. The latter along with the increased random turbulence introduced by the SJ led to an enhanced turbulent mixing within the core and therefore a significant vortex diffusion compared to the other control cases studied.

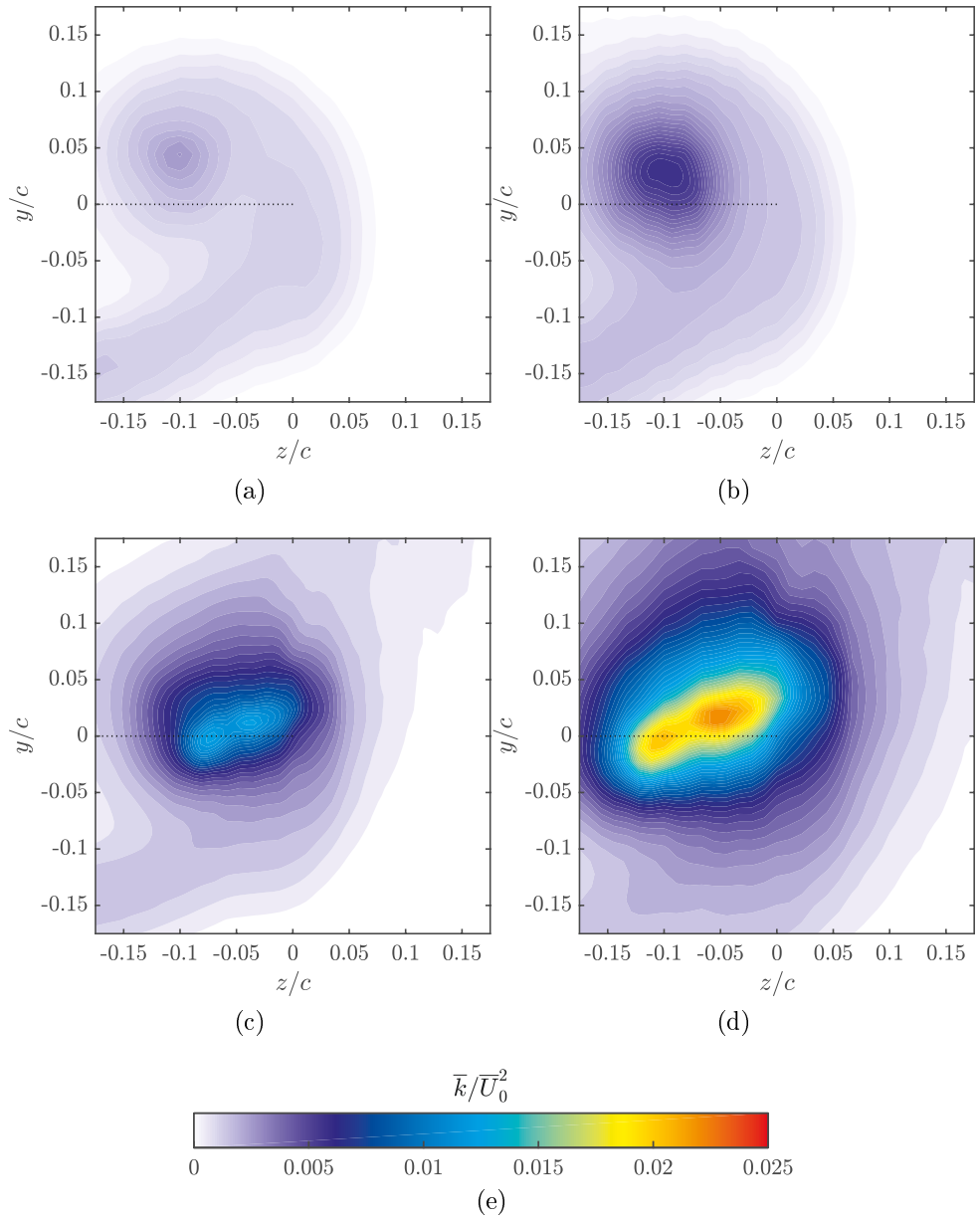

Figure 3.11 Uncorrected contours of the normalized turbulent kinetic energy at $x/c = 3$. (a): NV, (b): C1, (c): C2 and (d): C3.

Effect of SJ actuation on the streamwise development of a wing tip vortex

In the previous section, it has been demonstrated that the control case C3 had the most pronounced effect of the tip vortex amongst all tested configurations at the particular downstream position $x/c = 3$. Nonetheless, a judicious choice had to be taking when selecting the control parameters to be tested at larger downstream distances. As such, C_μ and F^+ of the SJ have to be tuned without significantly altering the structure of the vortex and therefore ensuring that the effect of the SJ actuation can still be measured at larger downstream distances. The close examination of the data of the different control cases measured at $x/c = 3$, around which the NV case attained an asymptotic state, revealed that, unlike case C3, the tip vortex under case C1 exhibited a self-similar behavior despite the measurable effect of the control on the mean flow and the turbulent statistics of case C1. In consequence, the "least-optimal" case C1 was considered for a more comprehensive hot-wire survey at the downstream positions $x/c = 0.75, 1, 2, 3, 4$ and 5.

Contour plots of the normalized axial velocity deficit, $(\bar{U}_0 - \bar{U}_x)/\bar{U}_0$, are shown in Figure 3.12a, 3.12c, 3.12e, 3.12g, 3.12i and 3.12k for NV and Figure 3.12b, 3.12d, 3.12f, 3.12h, 3.12j and 3.12l for case C1, at the measurement planes $x/c = 0.75, 1, 2, 3, 4$ and 5, respectively. Note that $x/c = 0.75$ is exactly aligned with the wing trailing edge. Velocity contours in the outer region of the NV case showed a curved region dominated by a velocity deficit ranging between 0.06 and 0.02. A nearly axisymmetric region of velocity contours was observed around the location where the maximum velocity deficit occurred. The latter decreased from 0.7 at $x/c = 0.75$ to a value of about 0.24 at $x/c = 5$. With control case C1, and at $x/c = 0.75$, the wake shear layer was found to be stretched in the spanwise direction and was slightly thinned in the transverse direction. The maximum velocity deficit in the wake increased by nearly 10% with respect to the NV case. As the vortex evolved downstream, the vortex rolled into a more axisymmetric shape with a rather weak velocity deficit at its core [38, 39], which was decreased by nearly 40% as the vortex evolved from $x/c = 0.75$ to $x/c = 5$.

Contours of the normalized axial vorticity, $\bar{\xi}_x\, c/\bar{U}_0$, are plotted in Figure 3.13a, 3.13c, 3.13e, 3.13g, 3.13i and 3.13k for NV and Figure 3.13b, 3.13d, 3.13f, 3.13h, 3.13j and 3.13l for case C1, at the measurement planes $x/c = 0.75, 1, 2, 3, 4$ and 5, respectively. Vorticity contours of NV at $x/c = 0.75$ clearly show the rollup of the shear layer into the tip vortex where vorticity reached higher levels than those in the outer region. As the vortex developed downstream, the rolling shear layer thickened and its vorticity levels decreased. Inside the core region, the peak value of the normalized vorticity decreased from a value of about 30 at $x/c = 0.75$ to a value of about 12 at $x/c = 5$ in agreement with [39].

Outside the wake and the tip vortex regions, the vorticity was essentially zero. With actuation and under case C1, vorticity contours appeared to be more diffuse than those of case NV and covered a larger area around the vortex core [38, 40]. At $x/c = 0.75$, the peak value of $\bar{\xi}_x\ c/\bar{U}_0$ decreased by nearly 15% compared to NV. As the vortex was convected downstream, its normalized core vorticity decreased substantially reaching a value of about 8.5 at $x/c = 5$.

The variation of the vortex core parameters $\bar{U}_{\theta,m}/\bar{U}_0$ and r_c/c with streamwise distance for NV and case C1 are shown in Figure 3.14 and Figure 3.15, respectively. For NV, peak values of the normalized $\bar{U}_\theta$ decreased monotonically with increased downstream distance before reaching a quasi-asymptotic value at $x/c \sim 3$. The streamwise changes in the values of the normalized vortex radius, r_c/c, were seen to slowly decrease from $x/c \sim 3$. As stated in the previous section, it is believed that around $x/c = 3$ the rollup process was complete and the vortex has nearly reached a self-similar state. With actuation of case C1, values of $\bar{U}_{\theta,m}/\bar{U}_0$ were significantly lower than those of NV at all downstream locations. The reduction of the peak circumferential velocity was accompanied with a broadening of the vortex core where its radius increased by roughly 28% at $x/c = 5$.

The streamwise development of the core circulations, $\bar{\Gamma}_c$ for NV and case C1 cases were plotted in Figure 3.16. The trailing edge of the wing (TE) was denoted with a vertical dashed line at the streamwise location $x/c = 0.75$. The core circulation was normalized with its respective local NV core circulation, $\bar{\Gamma}_{c_0}$. In the near field and at $x/c = 0.75$, the relatively high C_μ of case C1 caused the core circulation to significantly decrease as a result of the vortex stretching, in agreement with the results reported in [38, 57]. As the vortex evolved downstream and started to regain its original shape ($x/c > 2$), its core circulation started to gradually increase as the vorticity injected by the SJ was gradually drawn into the vortex core with the spiraling shear layer (Figure 3.13d, 3.13f, 3.13h, 3.13j).

The radial distributions of the normalized circulation, $\bar{\Gamma}(r)/\bar{\Gamma}_c$, for NV were plotted against the similarity variable, η, for different downstream positions, as illustrated in Figure 3.17a. The profiles of $\bar{\Gamma}(r)/\bar{\Gamma}_c$ depicted an excellent collapse with the curve-fits given by equations 4.21, 4.22 and 4.23 for $x/c > 2$. In the region $0.75 \leq x/c \leq 2$, the profiles of $\bar{\Gamma}(r)/\bar{\Gamma}_c$ exhibited a clear departure from the empirical curve-fits in the inner and outer region of the vortex, suggesting that the rollup process was incomplete and that the vortex had reached a self-similar state only for $x/c > 2$. These observations corroborate the results reported in §3.2.4. With control and for $x/c > 1$, circulation profiles in the inner region of the vortex collapsed with the curve-fits suggested by [15, 58, 93], as shown in Figure 3.17b. In both inner and logarithmic regions of the vortex, a discernible departure from the collapse

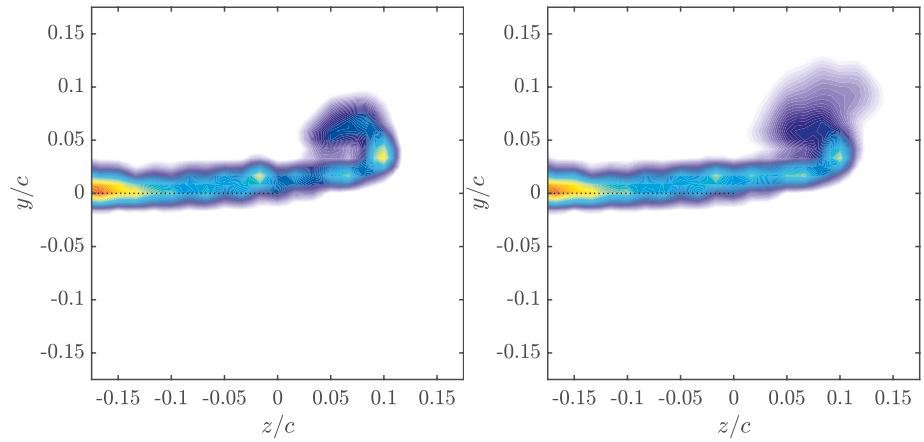

(a) $x/c = 0.75$ (b) $x/c = 0.75$

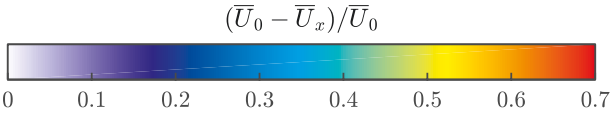

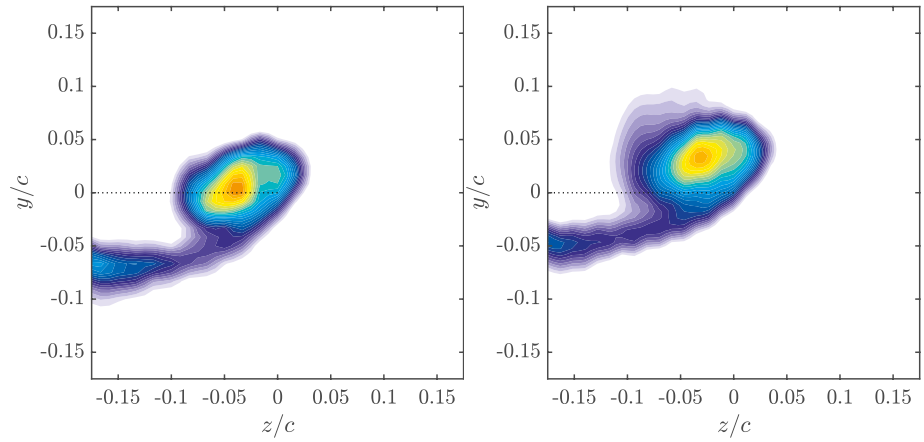

(c) $x/c = 1$ (d) $x/c = 1$

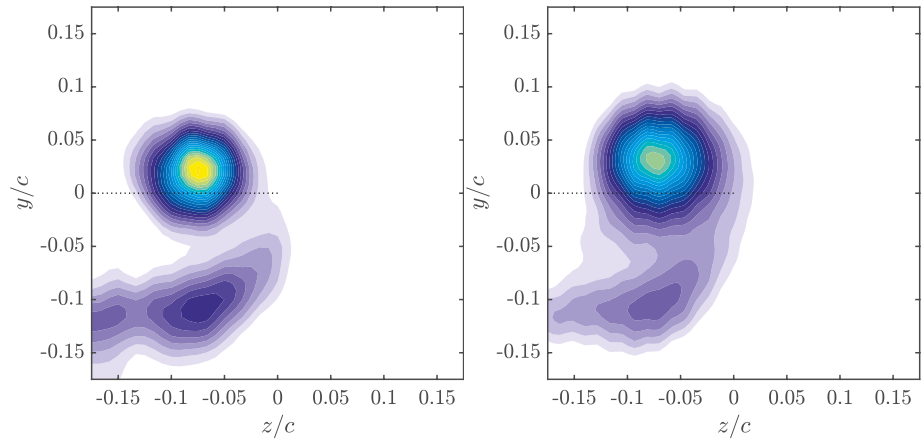

(e) $x/c = 2$ (f) $x/c = 2$

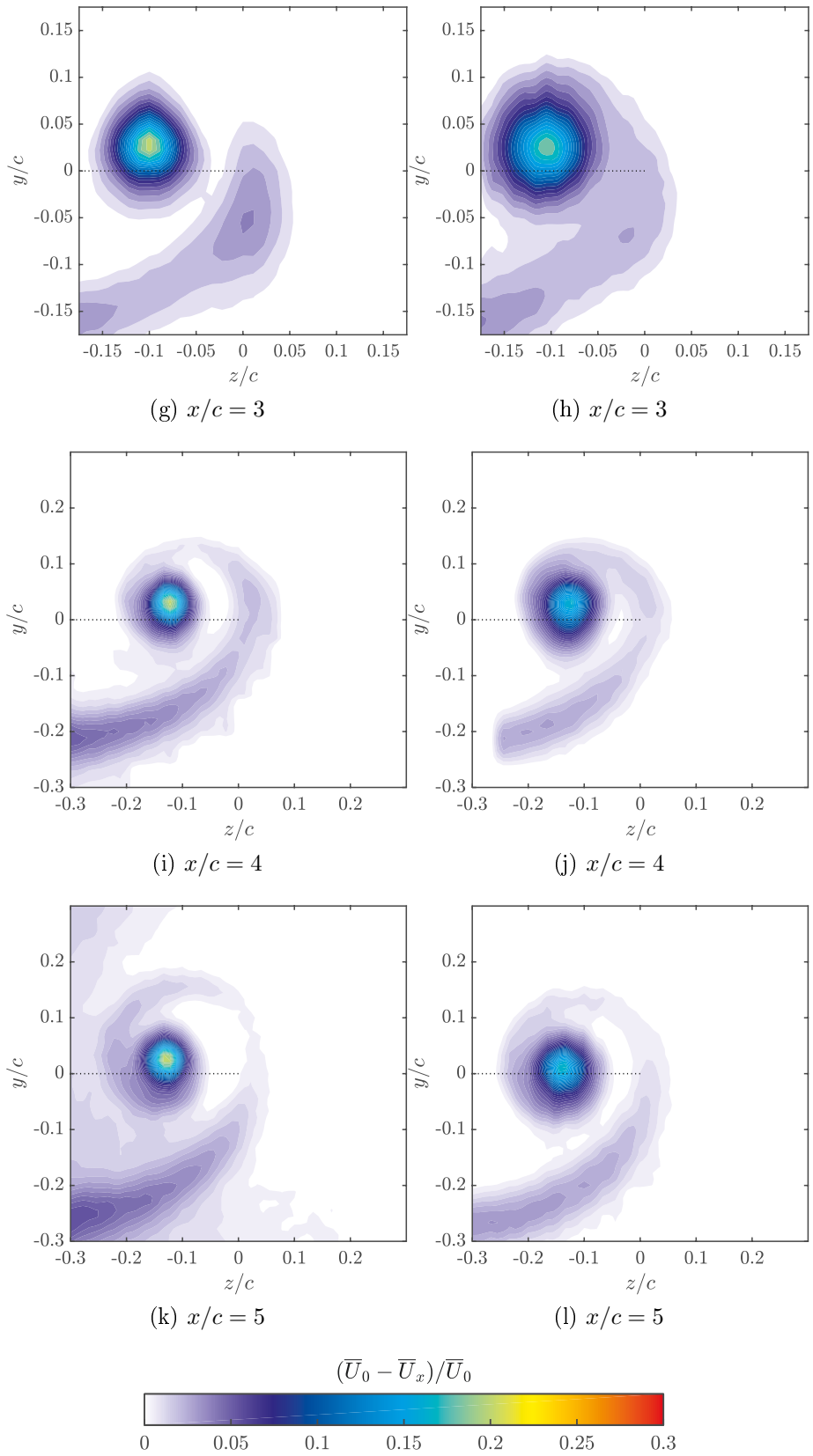

Figure 3.12 Uncorrected contours of the normalized axial velocity deficit. (a), (c), (e), (g), (i) and (k): NV, (b), (d), (f), (h), (j) and (l): C1.

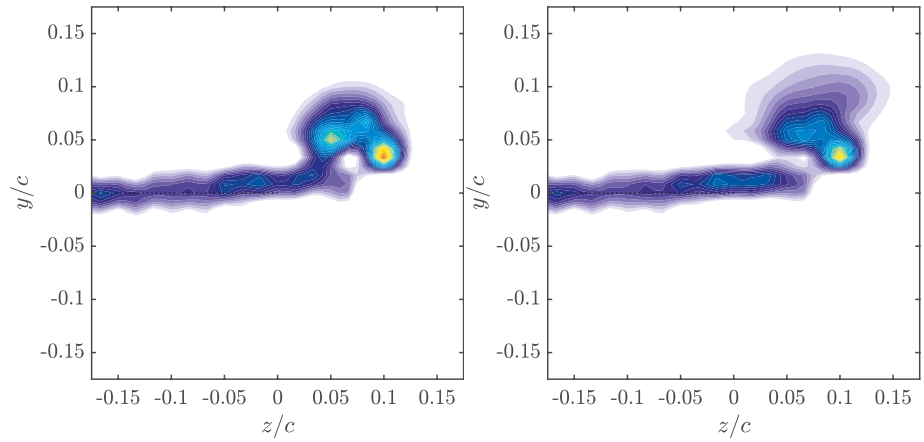

(a) $x/c = 0.75$ (b) $x/c = 0.75$

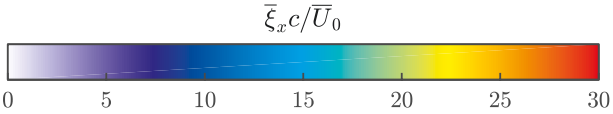

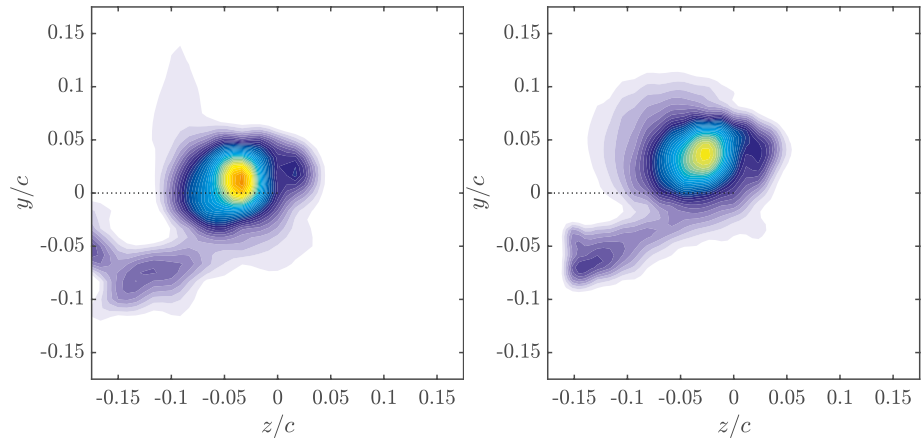

(c) $x/c = 1$ (d) $x/c = 1$

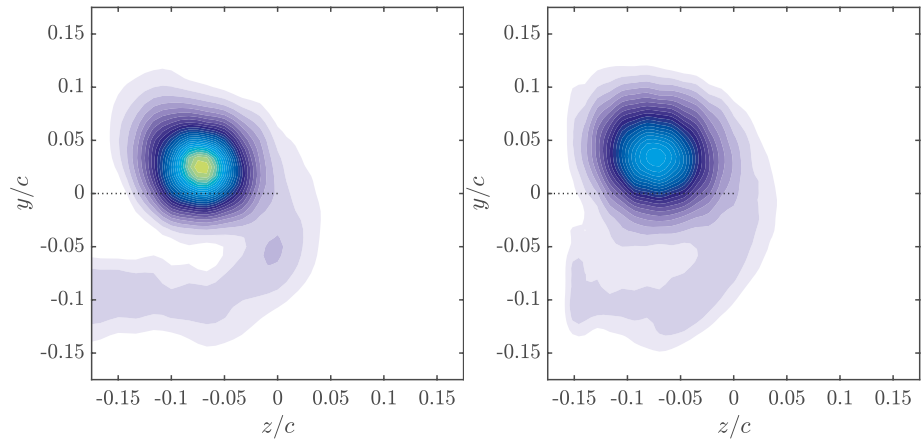

(e) $x/c = 2$ (f) $x/c = 2$

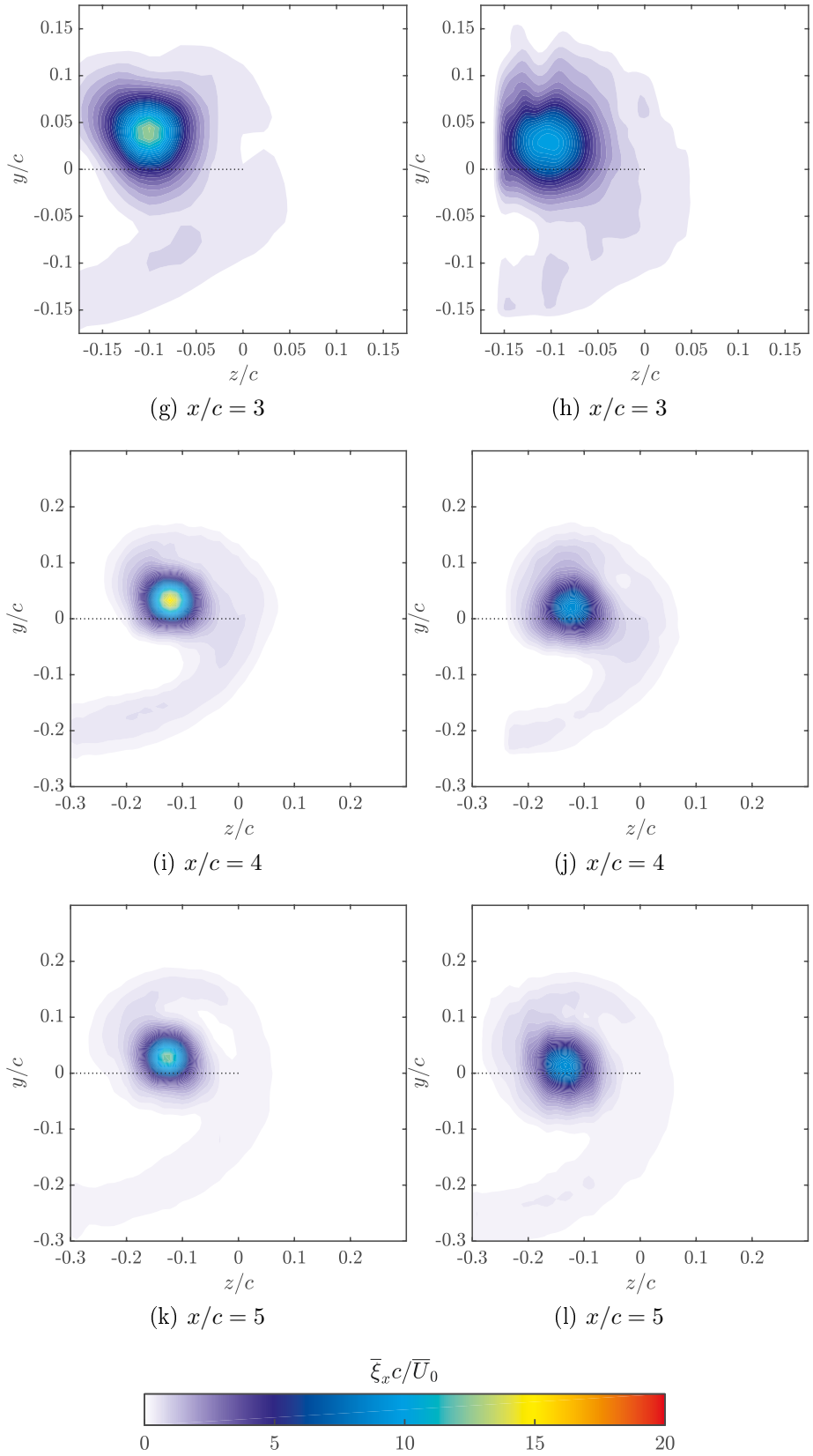

(g) $x/c = 3$ (h) $x/c = 3$

(i) $x/c = 4$ (j) $x/c = 4$

(k) $x/c = 5$ (l) $x/c = 5$

Figure 3.13 Uncorrected contours of the normalized axial vorticity. (a), (c), (e), (g), (i) and (k): NV, (b), (d), (f), (h), (j) and (l): C1.

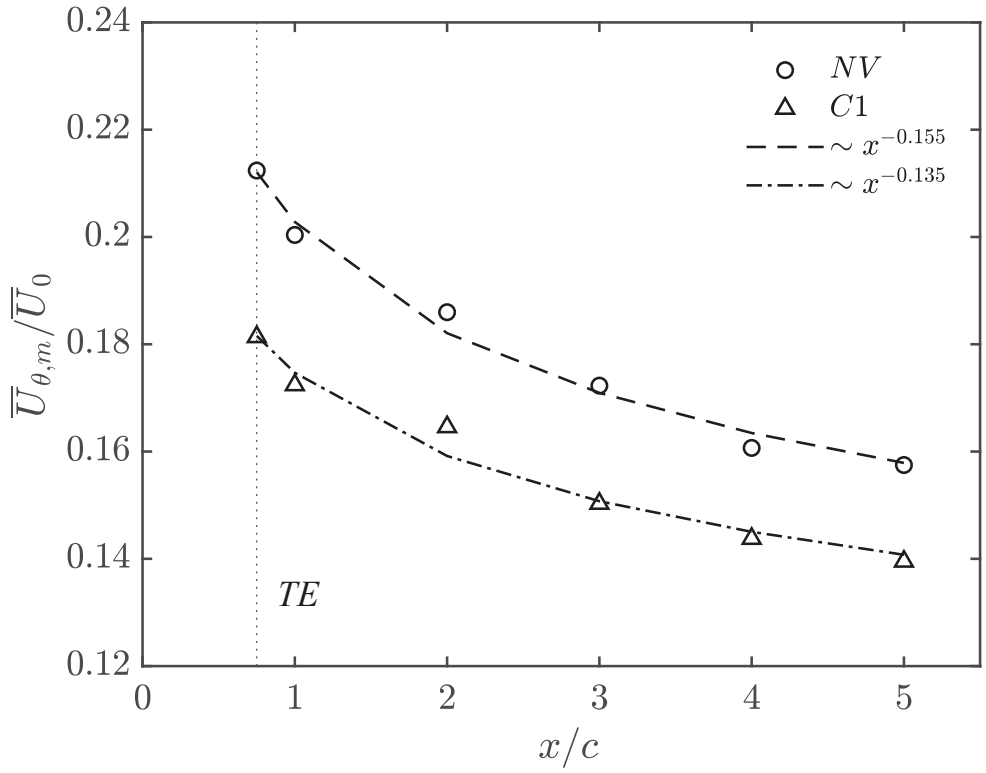

Figure 3.14 Streamwise development of the peak value of the corrected circumferential velocity.

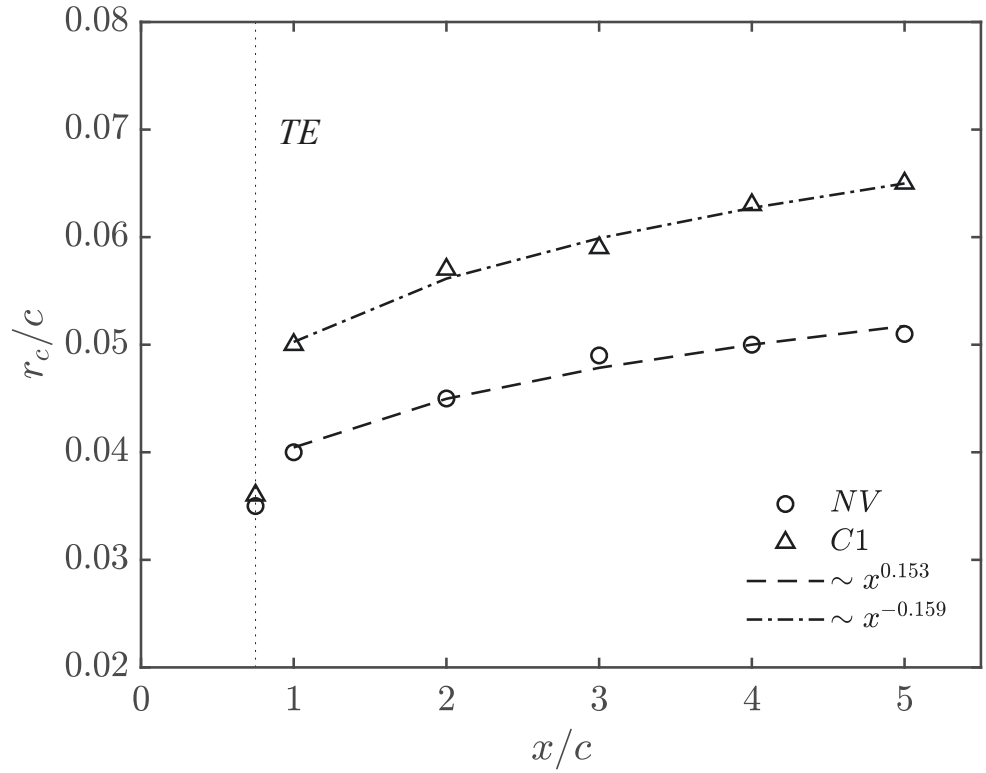

Figure 3.15 Streamwise development of the corrected vortex core radii.

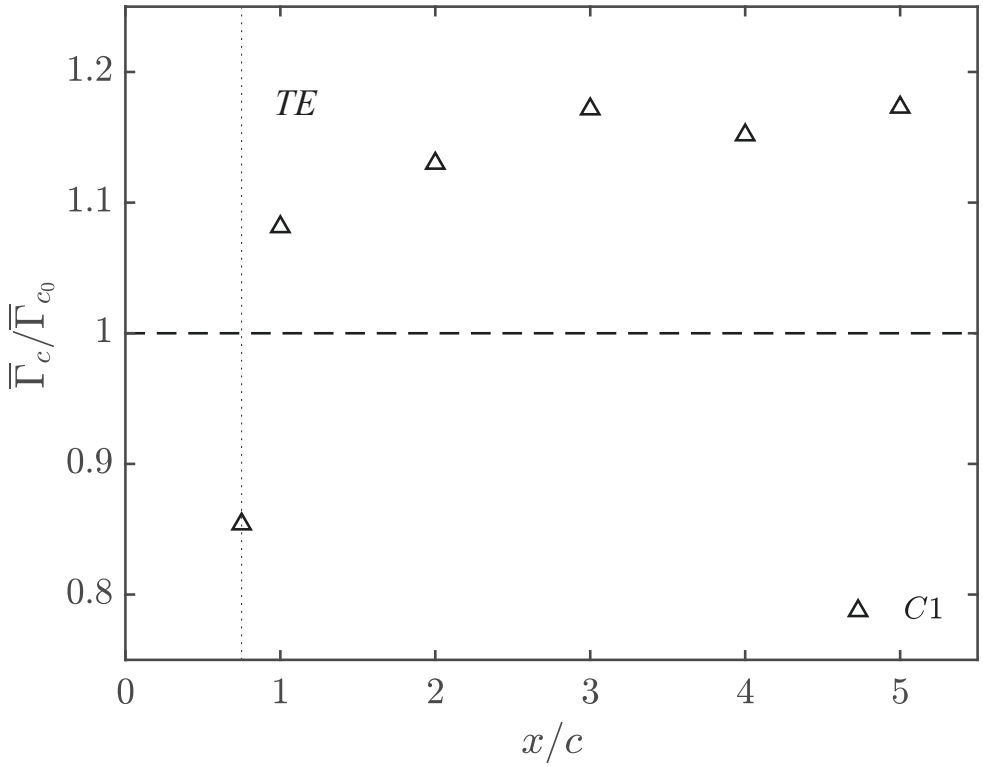

Figure 3.16 Streamwise development of the corrected vortex core circulations.

was only observed at $x/c = 0.75$. More interestingly, as opposed to NV, nearly no collapse between the circulation profiles was observed in the outer region of the controlled vortex. This suggests that, although the low C_μ and hight F^+ of case C1 clearly affected the outer region of the vortex during its formation, they led to a well-organized and an axisymmetric vortex core shape compared to that of NV, in agreement with the findings of [40]. Note that, at $x/c = 0.75$, the significant departure of the circulation profile in the outer region of the vortex for both NV and C1 cases is attributed to the weak vorticity of the shear layer, which would be still bounded to the wing surface at the trailing edge position.

In order to demonstrate the helical symmetry of the self-similar vortex of cases NV and C1, the radial profiles of the normalized circumferential velocity, $\bar{U}_\theta/\bar{U}_{\theta,m}$, and the normalized axial velocity, $(\bar{U}_x - \bar{U}_0)/\bar{U}_{\theta,m}$, were tested against the analytical model suggested in [113], as illustrated in Figure 3.18a and Figure 3.18b for the NV and C1 cases, respectively. This model suggests that, based on the Batchelor vortex model and some empirical observations, the circumferential and axial velocities of a helical vortex can be written as

$$\bar{U}_\theta(r) = \frac{\bar{\Gamma}}{2\pi r}\left[1 - \exp\left(\frac{-r^2}{\epsilon^2}\right)\right], \tag{3.14}$$

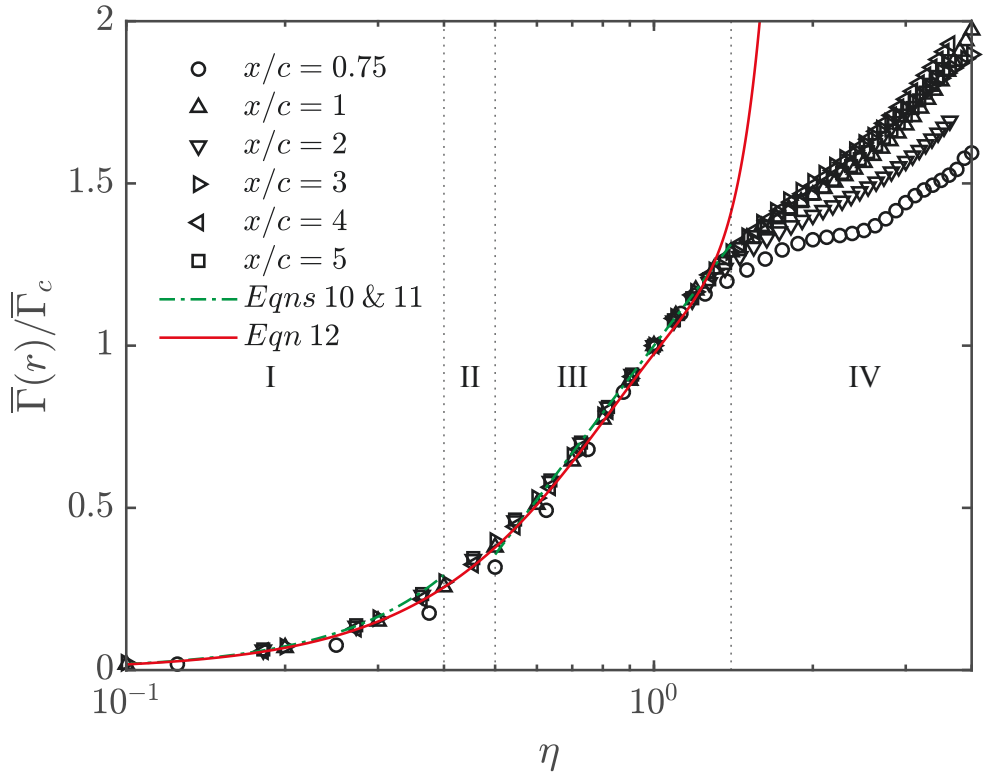

(a)

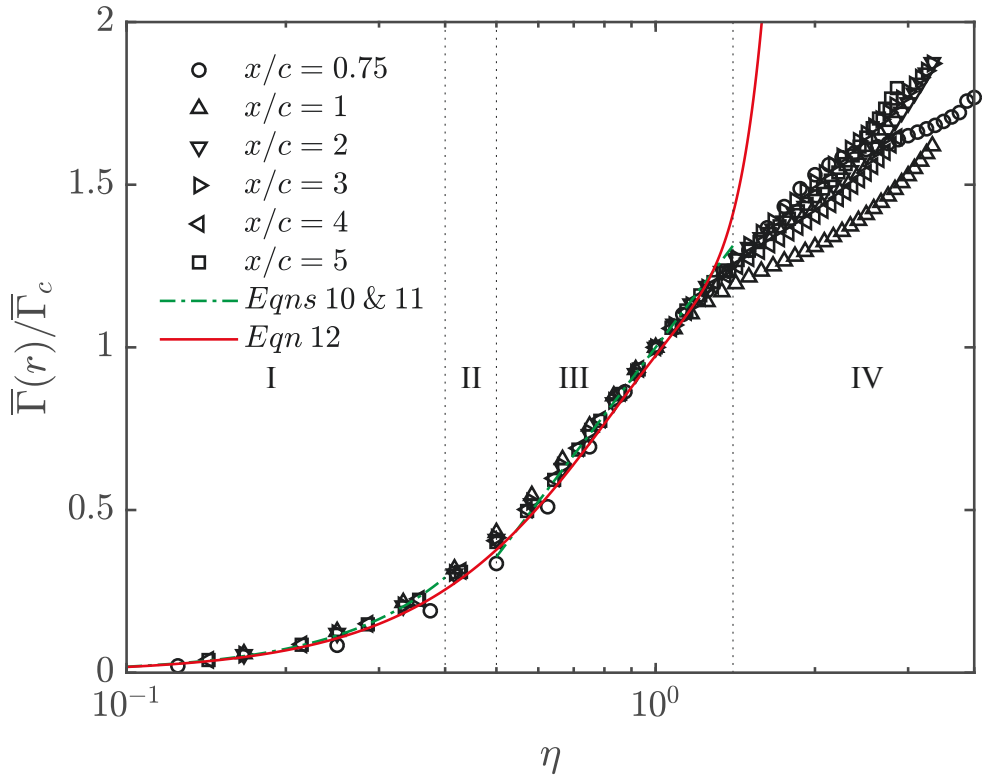

(b)

Figure 3.17 Corrected self-similar circulation profiles of the inner-region at different downstream positions: (a): NV and (b): C1. I: inner-core, II: buffer region, III: logarithmic region and IV: outer region.

$$\bar{U}_x(r) = \bar{U}_x(r=0) - \frac{\bar{\Gamma}}{2\pi l}\left[1 - \exp\left(\frac{-r^2}{\epsilon^2}\right)\right] \tag{3.15}$$

where l is the helical pitch of the vortex and ϵ is the effective size of the vortex core. These parameters can be directly computed from the experimental data. In particular, the helical pitch and the vortex core size were measured to be -0.07 and 0.046 for the NV case, and -0.095 and 0.065 for case C1, respectively. In this model, the axial and circumferential velocities are linearly related with the following condition

$$\bar{U}_x(r) = \bar{U}_x(r=0) - \frac{r}{l}\bar{U}_\theta(r) \tag{3.16}$$

Verification of the hypothesis of helical symmetry was conducted by comparing the measured profiles of the normalized circumferential and axial velocities at $x/c = 5$, where the vortex was shown to be self-similar, against 3.14 and 3.15, respectively. Figure 3.18a, 3.18b showed a reasonable collapse of the measured profiles of both NV and C1 cases with the analytical model particularly within the core region, suggesting that the vortex maintained its helical symmetry under the actuation of case C1.

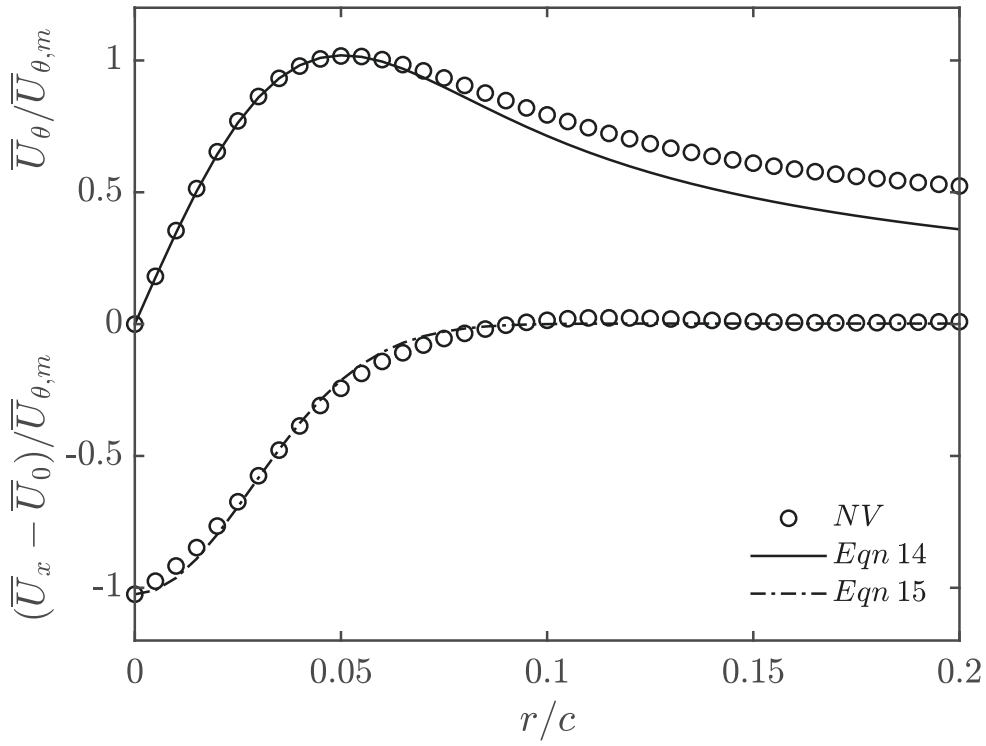

(a)

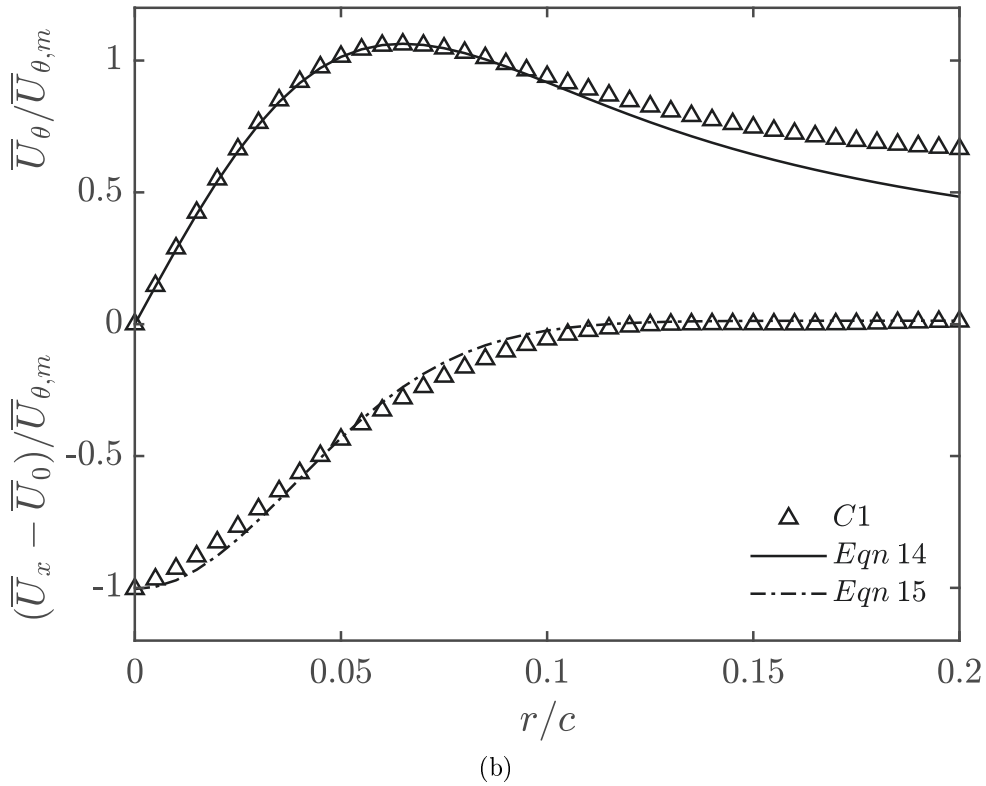

(b)

Figure 3.18 Testing of helical symmtery of the corrected (a) NV and (b) C1 cases at $x/c = 5$ against the analytical model suggested in [113].

Spectral analysis

The normalized frequency spectra, $S^*_{yy} = S_{yy}(f)/\bar{U}_\infty c$, of the spanwise velocity measured at the vortex centres of both NV and C1 cases are plotted in Figure 3.19 against the normalized frequency $f^* = fc/\bar{U}_\infty$. Although the general shapes of the frequency spectra $S_{xx}(f)$ and $S_{zz}(f)$ were similar to those of $S_{yy}(f)$, only frequency spectra $S_{yy}(f)$ were presented in this study since the contribution of the large scale motion to the total fluctuation energy happened to be the greatest in the spanwise direction. For clarity, spectra of both NV and C1 cases were shifted down by one, two, three and four decades for $x/c = 1$, 2, 3 and 5, respectively. For the NV, and in the range of frequencies $f^* < 10$, the spectra exhibited a plateau of high energy which increased in level with increased downstream distance. This systematic increase in the low frequency energy is consistent with the observations of [2, 11, 37, 40]. These authors suggested that this may be due to vortex meandering which its amplitude increases with inscreased downstream distance. At higher frequencies, $f^* > 10$, the spectra at the vortex center of NV followed a power law behavior with a decreasing exponent with increased downstream distance. The exponents of the power law were found to be -3 and -7 for $0.75 \leq x/c \leq 2$, and $x/c \geq 3$, respectively. The slopes of these asymptotic lines were in agreement with the findings of [11, 37]. It is noteworthy that the f^{*-7} decay in the high frequency range characterizes the dissipation range where the effect of the viscous forces dominates [46]. Furthermore, the energy level in this range of frequencies was found to decrease by nearly three decades with increased downstream distance. This suggested the relaminarization of the turbulent structures within the core region as a result of the high rotational motion which impeded radial motion and momentum exchange with the surrounding turbulent shear layer [7, 16, 37]. Note that a spike of energy in the frequency spectra of NV appeared at $x/c = 2$ at a frequency f^* of about 10. This spike persisted further downstream at $x/c = 3$, with a rather smaller amplitude, before it dissapeared at $x/c = 5$. This dominant frequency in the spectra is most likely associated with an instability in the vortex core as suggested by [2, 7, 40, 64, 103]. With actuation, the frequency spectra of case C1 exhibited dominant sharp peaks at the actuation frequency ($f^* \sim 0.96$) and its corresponding subharmonics. At these local peaks, the energy level was nearly one to two decades higher than that of NV in the low frequency region. As the vortex evolved downstream, the energy level of the actuation frequency peak increased by roughly one decade. This energy rise in the low frequency range may be attributed to the increased vortex meandering induced by the alternating blowing and suction cycles of SJ actuation. The spike in the spectra of the NV evidenced at f^* of about 10, disappeared under the effect of control case C1 for all downstream locations. For $f^* > 10$, the frequency spectra of case C1 exhibited a roll-off with slightly smaller

slopes compared to NV. The increase in the turbulent energy associated with the SJ was also observed in the frequency spectra measured at an offset point located outside the vortex region as illustrated in Figure 3.20. In this figure and at $x/c = 0.75$, the maximum energy was nearly three decades higher than that measured in the plateau region of NV. As opposed to Figure 3.19, the spectra of NV exhibited an inertial subrange with a -5/3 exponent, consistant with Kolmogorov turbulence decay laws [37]. Further downstream, the contribution of actuation to the total energy decreased by nearly two decades but remained one decade higher than that of NV in agreement with the observations reported in [40]. Furthermore, the harmonics of the actuation frequency were rapidly attenuated with increased downstream distance indicating a strong dissipation of the SJ structures and a reduction in the total turbulent kinetic energy. At $x/c = 5$, the spectral decay in case C1 was more prominent at frequencies slightly above the actuation frequency with a concomitant decrease in the energy level at high frequencies with respect to NV. Therefore, it was conjectured that, following the formation and penetration of the SJ structures into the vortex core, the energy was transferred from these large scale eddies into the mean flow and then cascaded down to smaller scales at which the turbulent dissipation ultimately dominated. The contribution of the actuation to the total energy is mainly attributed to the coherent component of the SJ structures as suggested in [25, 105].

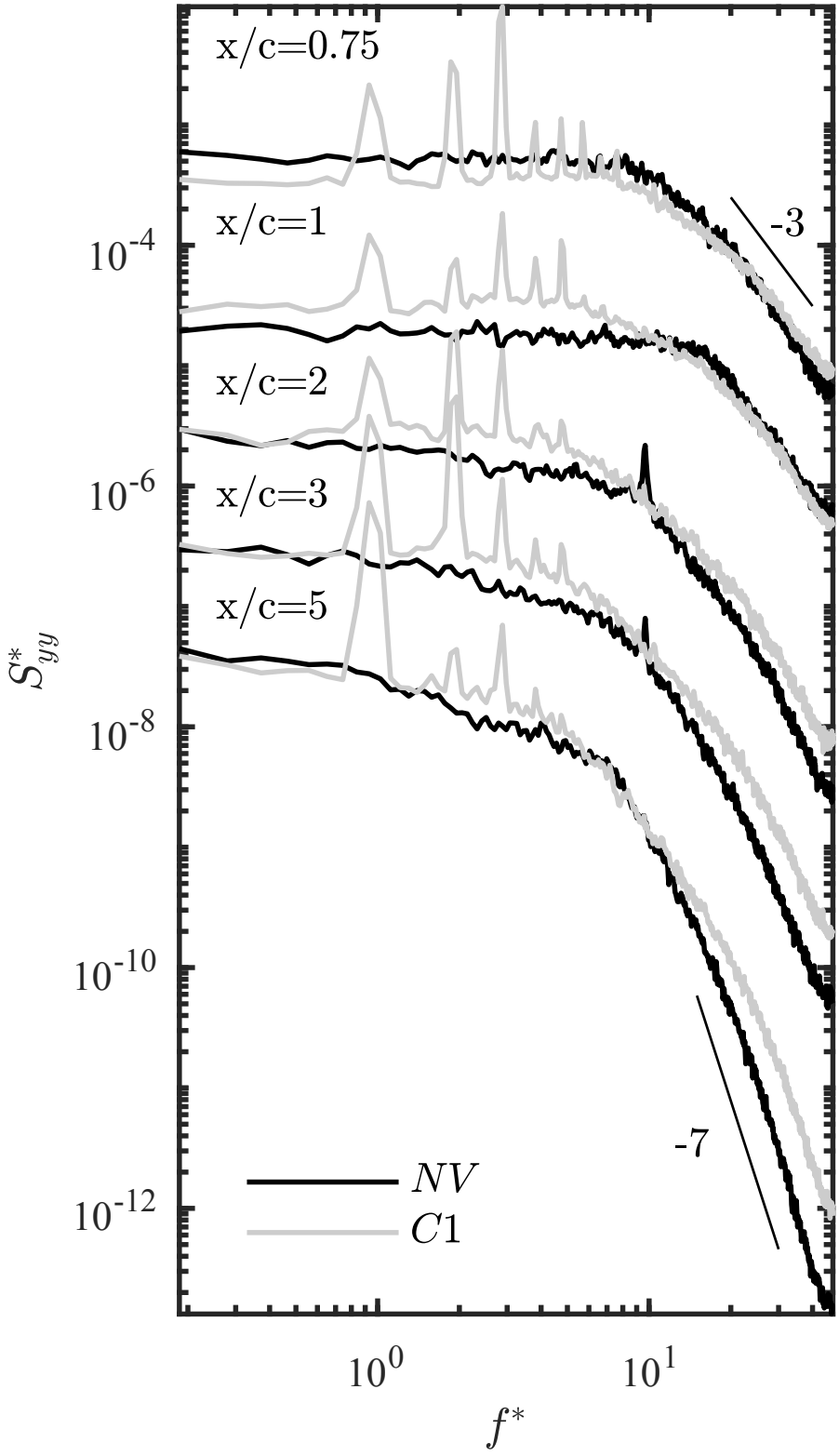

Figure 3.19 Frequency spectra of the spanwise velocity at the vortex center.

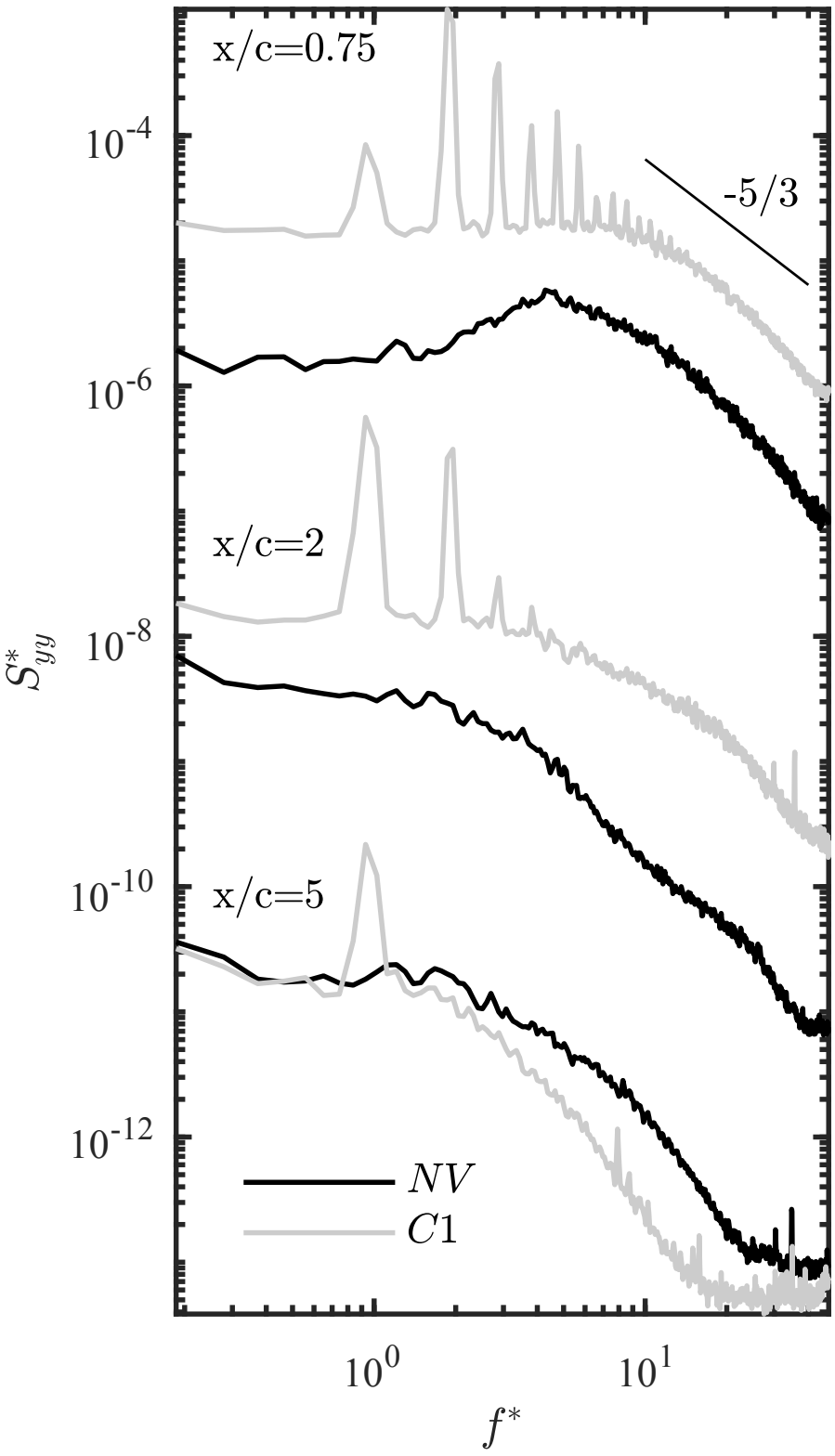

Figure 3.20 Frequency spectra of of the spanwise velocity outside the vortex region.

3.2.5 Conclusions

In this work, a comparative study on the effectiveness of SJ actuation parameters to control a wing tip vortex in the near and mid-wake of a rectangular wing with a NACA 0012 airfoil section was conducted. The actuation was achieved using a curved trapezoidal nozzle connected to a SJ cavity through a spanwise channel embedded inside the wing. Hot-wire measurements in the wake at $x/c = 3$ showed that the low frequency actuation of case C3, $F^+ = 0.29$ and the high momentum coefficient $C_\mu = 0.04$, had the most significant impact on the wing tip vortex. More specifically, the wing tip vortex was stretched into an ellipsoidal shape with more than 50% broadening of vortex core radius, r_c. The actuation of case C3 achieved a 35% reduction in the axial velocity deficit, $\bar{U}_x$ and a 40% average decrease in the peak circumferential velocity, $\bar{U}_\theta$. Additionally, the peak value of the normalized axial vorticity near the vortex core decreased by over 60% compared to the NV. The results suggested that the low frequency and the high momentum coefficient of the control configuration C3 allowed the SJ to travel larger distances into the wing tip vortex core bringing high turbulence structures with it. This resulted in increased turbulent mixing in the vortex core and subsequently a more diffuse vortex. Comprehensive hot-wire measurements of the vortex development at different downstream positions up to $x/c = 5$ showed that the circumferential velocity decreased monotonically under the effect of SJ actuation. The apparent outward diffusion of the vortex core translated to a nearly 35% increase of its radius at the farthest downstream locations. Frequency spectra, measured inside and outside the core region, showed a significant increase of the total energy in the range of low frequencies with SJ actuation. The dominant peak of the actuation frequency and its higher harmonics were found to persist with increased radial and downstream distances. This suggests that the turbulent mixing, the mechanism responsible for the vortex diffusion, was mainly triggered by the turbulence injection of the SJ actuation.

3.2.6 Acknowledgments

The authors would like to thank Prof. William Devenport at Virginia Polytechnic Institute for his valuable insights on the implementation of the meandering correction technique. This work was supported by the Directorate of Technical Airworthiness and Engineering Support (DTAES) office of the Royal Canadian Air Force and the Natural Sciences and Engineering Research Council (NSERC) of Canada.

3.2.7 Nomenclature

Symbol	Units	Description
A_j	m^2	Synthetic jet slot area
A_w	m^2	Half-wing planform area
$b/2$	m	Wing half span
c	m	Wing chord
C_μ	-	Synthetic jet momentum coefficient
F^+	-	Non-dimensionalized actuation frequency
f_a	Hz	Synthetic jet actuation frequency
f	Hz	Frequency
f^*	-	Non-dimensionalized frequency
k	m^2/s^2	Turbulent kinetic energy
L_j	m	Synthetic jet slot length
$\vec{v}_j$	m/s	Synthetic jet exit velocity field
$\bar{U}_\infty$	m/s	Wind tunnel freestream velocity
$\bar{U}_0$	m/s	Local freestream velocity
$\bar{U}_x$,$\bar{U}_y$,$\bar{U}_z$	m/s	Mean axial, spanwise and transverse velocities
$\bar{U}_\theta$	m/s	Circumferential velocity
$\bar{V}_j$	m/s	Synthetic jet space time-averaged velocity scale
$\overline{u'u'}$,$\overline{v'v'}$,$\overline{w'w'}$	m^2/s^2	Streamwise, spanwise and transverse Reynolds stresses
Re	-	Reynolds number
R_{uu},R_{vv},R_{ww}	-	Normalized streamwise, spanwise and transverse Reynolds stresses
S_{xx},S_{yy},S_{zz}	m^2/s	Frequency spectra of $\bar{U}_x$, $\bar{U}_y$ and $\bar{U}_z$
S^*_{xx},S^*_{yy},S^*_{zz}	-	Normalized Frequency spectra of $\bar{U}_x$, $\bar{U}_y$ and $\bar{U}_z$
T	s	Actuation period
r_c	m	Vortex core radius
r_{NV}	m	Vortex core radius of the natural vortex (NV)
r_{C1}	m	Vortex core radius of case C1
r_{C2}	m	Vortex core radius of case C2
r^*_{NV}	-	Normalized vortex core radius of NV
r^*_{C1}	-	Normalized vortex core radius of case C1
r^*_{C2}	-	Normalized vortex core radius of case C2
x, y, z	m	Streamwise, spanwise and transverse directions

Greek symbol	Units	Description
$\bar{\Gamma}$	m^2/s	Circulation
$\bar{\Gamma}_c$	m^2/s	Vortex core circulation
$\bar{\Gamma}_{c_{NV}}$	m^2/s	Vortex core circulation of NV
$\bar{\Gamma}_{c_{C1}}$	m^2/s	Vortex core circulation of case C1
$\bar{\Gamma}_{c_{C2}}$	m^2/s	Vortex core circulation of case C2
δ	deg	Wing dihedral
η	-	Normalized vortex core radius
ρ_∞	kg/m^3	Freestream air density
ρ_j	kg/m^3	Synthetic jet air density
$\bar{\xi}_x$	s^{-1}	Streamwise vorticity

CHAPTER 4

Effect of synthetic jet actuation on the meandering of a wing tip vortex

4.1 Avant-propos

Auteurs et affiliations:

1. Marouen DGHIM: Étudiant au doctorat[†]
2. Mohsen FERCHICHI: Professeur titulaire[*]
3. Hachimi FELLOUAH: Professeur agrégé[†]

[†]Université de Sherbrooke, Faculté de génie, Département de génie mécanique.
[*]Collège Militaire Royal du Canada, Faculté de génie, Département de génie mécanique et aérospatial.

État de l'acceptation: article en cours de préparation.

Revue: Journal of Fluid Mechanics.

Titre en français:

L'effet du contrôle actif sur l'errance d'un tourbillon de bout d'aile.

Contribution au document:

Cet article contribue à la thèse en quantifiant l'effet du phénomène d'errance sur la structure et le développement d'un tourbillon de bout d'aile et les mécanismes physiques causant sa dissipation.

Résumé en français:

Le développement d'un tourbillon de bout d'aile sous l'effet d'un contrôle par jet synthétique (JS) a été examiné pour une aile rectangulaire à extrémité carrée ayant un profil aérodynamique NACA 0012 à un nombre de Reynolds $Re_{c_w} = 2 \times 10^5$ en utilisant la technique de vélocimetrie par imagerie laser stéreoscopique. Cinq configurations de contrôle ont été considérées pour une étude comparative, à savoir le cas C1 avec coefficient de

quantité $C_\mu = 0.001$ et une fréquence d'activation $F^+ = 0.075$, le cas C2 avec $C_\mu = 0.001$ et $F^+ = 0.15$, le cas C3 avec $C_\mu = 0.001$ et $F^+ = 0.3$, le cas C4 avec $C_\mu = 0.001$ et $F^+ = 0.6$ et le cas C5 avec $C_\mu = 0.001$ et $F^+ = 1.2$. Dans le cas C3, le vortex a été étiré en une forme ellipsoïdale avec une diminution de près de 60% de la vitesse circonférentielle de crête et de la vorticité axiale du noyau. Le rayon du noyau du vortex s'est largement élargi, suggérant que la configuration de contrôle avec la fréquence la plus basse permettait au jet synthétique de parcourir de plus grandes distances dans le tourbillon, entraînant des structures turbulentes dans son noyau et un mélange accru et par conséquent un tourbillon plus diffus.

4.2 On the effect of active flow control on the meandering of a wing tip vortex

The development of a wing tip vortex under the effect of synthetic jet (SJ) actuation was examined for a rectangular, square-tipped wing having a NACA 0012 airfoil at a chord Reynolds number $Re_{c_w} = 2 \times 10^5$. Five control configurations were considered for a comparative study namely; case C1 with momentum coefficient $C_\mu = 0.001$ and an actuation frequency $F^+ = 0.075$, case C2 with $C_\mu = 0.001$ and $F^+ = 0.15$, case C3 with $C_\mu = 0.001$ and $F^+ = 0.3$, case C4 with $C_\mu = 0.001$ and $F^+ = 0.6$ and case C5 with $C_\mu = 0.001$ and $F^+ = 1.2$. Under case C3, the vortex was stretched into an ellipsoid shape with a nearly 60% decrease in the peak circumferential velocity and the core axial vorticity. The vortex core radius largely broadened suggesting that the lower frequency control configuration allowed the synthetic jet to travel larger distances into the vortex bringing turbulent structures within its core resulting in increased mixing and subsequently a more diffuse vortex.

4.2.1 Introduction

Tip vortices generated by a finite wing continue to be of a particular interest in aeronautical applications due to their significant contribution to the overall drag of the aircraft, and to their persistence in runways which poses a potential hazard and a flight safety concern in congested airports [107]. Over the past few decades, considerable effort has been devoted to understand the structure and development of wing tip vortices in the near and far fields, in order to design effective control strategies capable of alleviating their undesirable effects. It has been recognised in the literature that the dominant mechanisms in the natural decay of wing tip vortices are the inherent long and short-wave instabilities, namely Crow [31] and Widnall [117] instabilities. Perturbing the natural instabilities of a wing tip vortex may result in an early breakup and a rapid decay of the trailing vortices in the wake. In fact, Heyes and Smith [57] studied the effect of pulsed spanwise blowing, at frequencies closer to those of cooperative instabilities, on the structure of a wing tip vortex. They were able to achieve a remarkable increase in the core radius which was accompanied with a decrease in the peak circumferential velocity and an increase in the core axial velocity deficit close the trailing edge. In their study, they showed that the trajectory of the vortex could be altered by changing the angle of the jet with respect to the mid-plane of the wing. Margaris and Gursul [79] conducted a PIV investigation on the effect of synthetic jet (SJ) actuation on a tip vortex using a wing equipped with several blowing slot geometries placed at different positions at the tip. They found that the introduction of SJ actuation

led the tip vortex to diffuse by reducing its maximum tangential velocity. However, no conclusions were drawn on the choice of the actuation parameters and the SJ blowing locations. In a recent study, Greenblatt [50] used a different technique to control the wing tip vortex consisting of deflecting an outboard flap mounted on a wing semi-span and then, modifying the shear layer above the flap by means of SJ perturbations. He showed that a relatively small control momentum coefficient can produce large changes in the shear layer deflection and the flap pressure distribution with relatively small changes in the local aerodynamic loads. A substantial increase in the core axial vorticity and an associated overshoot in circulation were both reported with actuation. In a more recent study, Dghim *et al.* [40] used a curved nozzle SJ blowing in the spanwise direction in order to diffuse a wing tip vortex. They showed that the selection of an optimal actuation frequency, in the range of the wing tip natural instabilities, led to a more diffuse vortex with a reduced tangential velocity. In their study, only one tip geometry was tested and the Reynolds number was limited to 8×10^4 with a particular focus on the near wake region (using hot-wire anemometry and at x/c up to 2). It has been well-documented in the literature that tip vortices exhibit a broadband, low-frequency motion in their core which is referred to as vortex meandering or wandering. This movement is characterized by a side-by-side drift of the vortex core about an average location at frequencies much lower than those associated with turbulent motion [2, 27, 37, 57, 102]. Meandering in wind tunnel flows has been attributed to freestream background turbulence [5, 27, 37]. Gursul and Xie (1999) proposed that meandering is a by-product of the interaction of the vortex with secondary vortices. Jacquin *et al.* [64], Rokhsaz *et al.* [96] attributed vortex meandering to self-induced Biot-Savart induction from Kelvin-Helmhotlz vortices forming in the shear layer, but suggested that the vortex induces its own motion when its trajectory is mildly perturbed. Jacquin *et al.* [65] explained vortex meandering by the amplification of bending waves triggered by external freestream turbulence and linear cooperative instabilities. Similarly, Beninati and Marshall [11] found no evidence for vortex meandering but a bending wave resulting from the interaction of the vortex with freestream turbulence. In a more recent study, Edstrand *et al.* [42] conducted both POD and stability analysis on a wing tip vortex flow and suggested that the underlying mechanism of vortex meandering is mainly attributed to a self-induced instability originating in the vortex. Regardless of the source of vortex meandering, this phenomenon is known to influence the mean measured properties of the vortex and to obscure important flow features therein. In fact, Bailey and Tavoularis [2], Devenport *et al.* [37] reported that meander creates a smearing effect that causes the mean vortex to appear more diffused with a reduced peak azimuthal velocity and an increased artificial turbulent stresses at its core [2, 5, 12, 13, 37, 57]. These effects

were found to be more profound when turbulence or low-frequency forcing were applied to the vortex [2, 12, 50, 56, 79, 80]. Despite the appreciable complications that vortex meandering introduces to experimental studies, it has been shown that its effect can be removed from the measured velocity field generated by the vortex. In fact, Devenport *et al.* [37] developed an analytical technique to correct single-point flow field measurements and remove the meandering effect in order to recover the true velocity field of the tip vortex. Heyes and Smith [57] developed a more robust technique to correct for vortex meandering using particle image velocimetry (PIV) data. This method consists of re-aligning the vortex velocity fields such that the instantaneous vortex positions collocate with the mean vortex center position, directly removing the effect of meandering while retaining the true random fluctuations of the velocity field within the vortex core.

4.2.2 Experimental apparatus and instrumentation

Wind tunnel setup

The experiments were conducted in a closed-circuit, low-speed wind tunnel located in the Department of Mechanical Engineering at the Université de Sherbrooke (QC, Canada). The wind tunnel has a test section of 1.82×1.82 m^2 cross section. The mean streamwise velocity in the empty wind tunnel is uniform to within $\pm 3\%$ and a turbulence intensity of about 0.5%. The model used in the present study was a rectangular planform half-wing with a NACA 0012 airfoil section. The square-tipped half-wing had a chord $c_w = 0.3$ m and a semi-span $b/2 = 0.9$ m, corresponding to an aspect ratio $AR = 3$. The origin of the coordinate system was anchored to the wing tip at the quarter-chord location with X,Y and Z axes aligned respectively with the streamwise, spanwise and transverse directions of the wind tunnel reference frame. Moreover, the local Cartesian coordinate system, (x, y, z), was defined at each field of view (FOV) such that its origin moved along with the ensemble-averaged axis of the vortex (figure 4.1(a)). The half-wing was manufactured from Glass-Filled Nylon Powder using a high resolution 3D printer (Synergeering Group, LLC). It has a hollow rectangular chamber throughout the wingspan for the supply of airflow generated by the loudspeakers. The SJ cavity consisted of a contraction nozzle placed outside the wind tunnel where two loudspeakers (model: Visaton GF200) were attached. The loudspeakers were controlled by a function generator connected to a power amplifier (model: QSC PLX 2402). The blowing slot at the wingtip was in fluidic communication with the hollow plenum. The slot had a trapezoidal shape of 2 mm height close to the leading edge and 4 mm height near the trailing edge, as illustrated in figure 4.1(b). The total slot length, L_j, was about 0.23 m. The slots were designed such that the exit

velocities are non-uniform along the chord direction. The experiments were carried out at an angle of attack of 5 degrees and a chord Reynolds numbers, Re_{c_w}, of about 2×10^5.

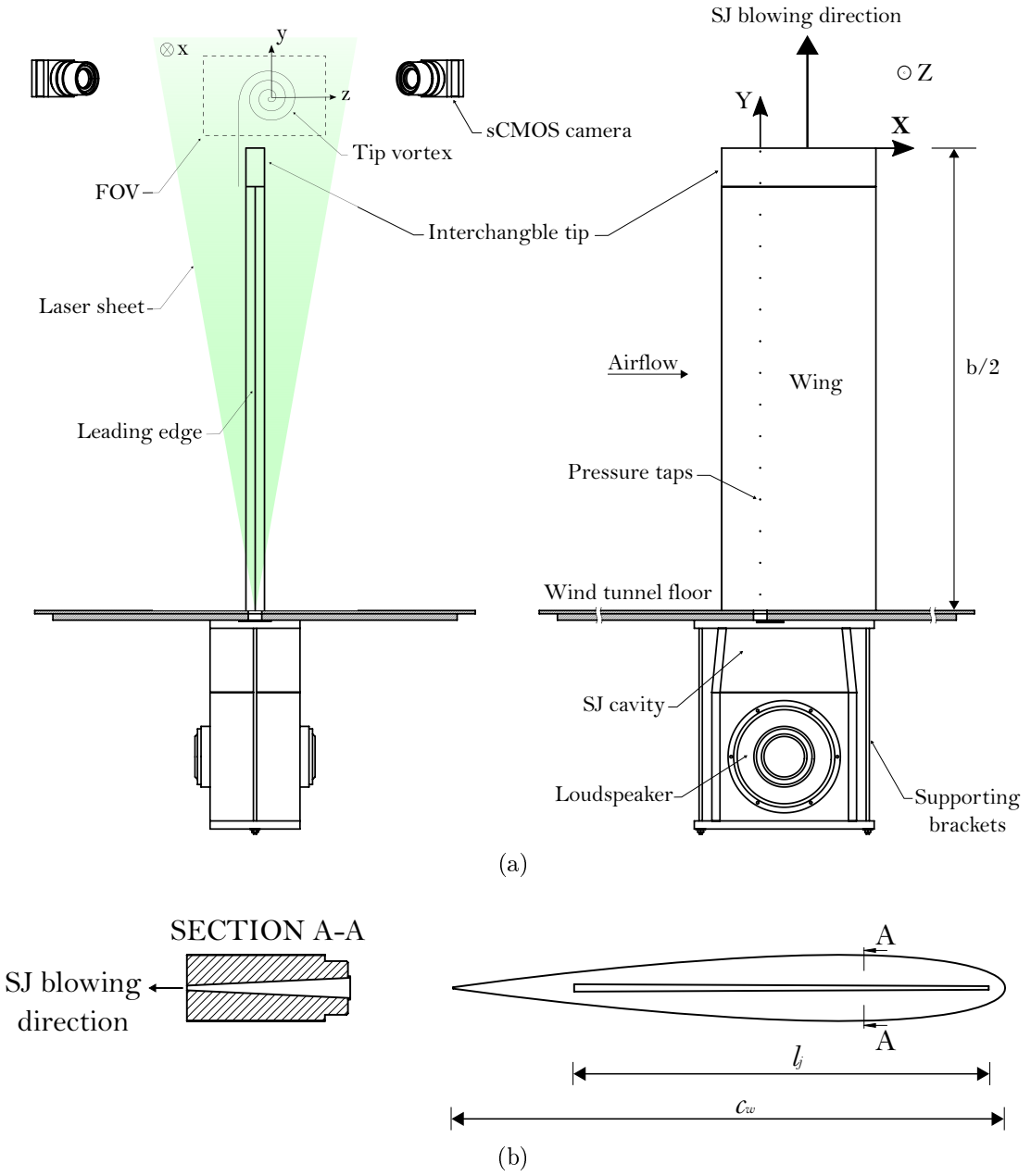

Figure 4.1 (a) Schematic of the experimental set-up and (b) SJ slot geometry.

Pressure measurement

Pressures on the suction side of the wing were measured using 15 taps equally spaced (62.6 mm) along the wing span at $c_w/4$ location. The pressure taps were connected to a Digital Sensor Array (DSA 3217/16px) Scanivalve® pressure transducers through flexible Tygon tubing. The DSA 3217 consists of 16 temperature-compensated piezo-resistive

pressure sensors with an A/D converter and a microprocessor, capable of measuring and digitizing both static and fluctuating surface pressures. A total number of 2^{15} scans were sampled at the maximum rate of 500 Hz/channel.

Stereoscopic PIV

The instantaneous three components of the velocity vector field were measured using stereoscopic Particle Image Velocimetry (SPIV). The system consisted of a Quantel Evergreen dual cavity Laser with a maximum pulse frequency of 15 Hz emitting visible green light at a wavelength of 532 nm. The maximum pulse energy of the Laser was about 200 mJ. A Laser light steering arm was used to deliver the Laser beam to the light-sheet optics which was mounted on an optical rotary table and a two-axes traversing system. This arrangement allowed 5 degrees of freedom for the Laser sheet covering much of the viewing area of the test section. The airflow was seeded with water-glycol-based fog particles generated by a thermal smoke generator (model: Pea Soup Rocket) that produces particles with a typical diameter of 1 μm. Recording of the particles image pairs was accomplished with two 16-bit double-frame sCMOS cameras having a 2560×2160 px^2 sensor resolution, equivalent to a sensor size of approximately 16.64×14.04 mm^2, and a pixel-pitch of 6.5 μm. The cameras were equipped with Nikon Nikkor fixed focal length of 200 mm adjusted to a numerical aperture of $f_{\#} = 11$. A total number of 2000 images were recorded in double-frame mode at a frequency of 15 Hz. The stereo calibration, self-calibration and analysis of the PIV datasets was performed using LaVision Davis 8.4®. The velocity vector fields were calculated at a final correlation window size of 32 px by 32 px with an overlap of 75%, resulting in a vector spacing of approximately 0.5 mm. The measurement uncertainty level for the velocity vectors was estimated to be within 2%.

Spectral measurement

The velocity fluctuations for spectra were measured using a custom-built miniature cross-wire probe (Auspex scientific, AHWX-100) with tungsten sensors having a diameter of 5 μm, a length of 0.9 mm and a nominal distance of about 1 mm. The two sensors were operated separately using a multichannel TSI IFA 300 constant temperature anemometer. The hot-wire signals were low-pass filtered at a cut-off frequency of 10 kHz (3 dB point) and were simultaneously digitized at a frequency of 20 kHz, using a 16 bit, 1 MHz analog-to-digital converter (National Instruments PCI-6230). To ensure a good statistical representation of the coherent structures of the flow, records of 2^{20} data points were collected at each measuring position. The hot-wire probe is positioned in the flow by a two-

dimensional motorized traversing system (model: Velmex BiSlide®) having a resolution of 0.02 mm and automatically controlled by a computer.

4.2.3 Synthetic jet actuation parameters

The characterization of the SJ actuator was performed using a fast-response four-hole pressure probe (model: TFI Cobra®) [86]. The custom-built pressure probe has the ability to simultaneously measure all three components of the velocity field. At each measurement point along the centerline of the SJ exit nozzle, velocity data were sampled at 2 kHz and 2^{15} data points were acquired covering a sufficient number of actuation cycles. the measurement uncertainty of the four-hole pressure probe was estimated to be within 3%.

The SJ momentum coefficient, C_μ, was estimated as

$$C_\mu = \frac{A_j}{A_w}\frac{\rho_j \bar{v}_j^2}{\rho_\infty \bar{u}_\infty^2} \tag{4.1}$$

where A_j is the slot area, A_w is the half-wing planform area and $\bar{u}_\infty$ is the free-stream velocity. The SJ time and spatial-averaged velocity scale, $\bar{v}_j$, measured along the slot centerline, was given by Holman *et al.* [60]

$$\bar{v}_j = \frac{2}{T}\frac{1}{A_j}\int_A \int_0^{\frac{T}{2}} \vec{v}_j \cdot d\vec{A}\, dt \tag{4.2}$$

The actuation frequency was non-dimensionalized as

$$F^+ = \frac{f_a \cdot c_w}{\bar{u}_\infty} \tag{4.3}$$

where f_a and c_w are the actuation frequency and wing chord, respectively. The characteristics of the SJ actuator, used in this study, were first investigated in the quiescent-flow condition before being applied to a tip vortex flow configuration. The SJ centerline velocities were measured as the actuator was operated at different supplying voltages, v_{rms}, ranging from 2.8 to 8.5V, and different actuation frequencies, F^+, ranging from 0.075 to 1.2. Figure 4.2 illustrates the contours of the momentum coefficient, C_μ, as a function of both actuation voltage and frequency. In this figure, it can be clearly depicted that the momentum coefficient, C_μ, increases with increased driving voltage. However, the bandwidth of the SJ flat frequency response was found to narrow down with increased v_{rms}. It was also observed that, for a given C_μ, the minimum required driving voltage was

reached for frequencies between 0.2 and 0.4. It is believed that the local minima in the contours of C_μ were achieved at the SJ Helmholtz resonance frequency, which is a function of the SJ cavity volume, slot area and more importantly the driving voltage [21, 24, 60]. This suggests that, for effective tip vortex control, it is recommended to operate the current SJ near its Helmholtz resonance frequency, i.e. $0.2 \lesssim F^+ \lesssim 0.4$. Considering the SJ design characteristics, few control cases were selected to further investigate the effect of the actuation frequency on the overall efficiency of the control process. In fact, six control configurations with a constant momentum coefficient, $C_\mu = 0.001$, and increasing actuation frequency, F^+, were tested in the present study, namely; C0: $F^+ = 0$ (natural vortex), C1: $F^+ = 0.075$, C2: $F^+ = 0.15$, C3: $F^+ = 0.3$, C4: $F^+ = 0.6$ and C5: $F^+ = 1.2$. Typical profiles of the maximum velocity measured along the centerline of the SJ slot exit, $\bar{v}_j$, normalized by the freestream velocity, $\bar{u}_\infty$, are shown in figure 4.3. For all the cases studied, a noticeable velocity gradient was observed as a result of the trapezoidal shape of the SJ exit slot. Furthermore, for a given momentum coefficient, $C_\mu = 0.001$, tuning the SJ at $F^+ = 0.3$ resulted in the highest peak jet velocity, $\bar{v}_j^{\max}$, along the centerline of the SJ slot using the lowest driving voltage, $v_{rms} = 2.8V$, amongst all the cases studied. This observation is corroborated by the spectra of the SJ exit velocity, $v_j(t)$, (normal to the SJ exit slot) measured at $X/l_j \sim 0.2$ for all the cases studied, as illustrated in figure 4.4. For clarity, spectra of the cases C2, C3, C4 and C5 were shifted down by one, two, three and four decades, respectively. The frequency spectra exhibited dominant sharp peaks at the corresponding actuation frequencies of the cases studied and their respective higher harmonics. It is noteworthy that the magnitude of the dominant peak in the frequency spectra of case C3 was 66, 24, 87 and 92% higher than those of the cases C1, C2, C4 and C5, respectively. Therefore, it would be surmised that the turbulent kinetic energy (TKE) generated by the SJ under the control case C3 is the largest.

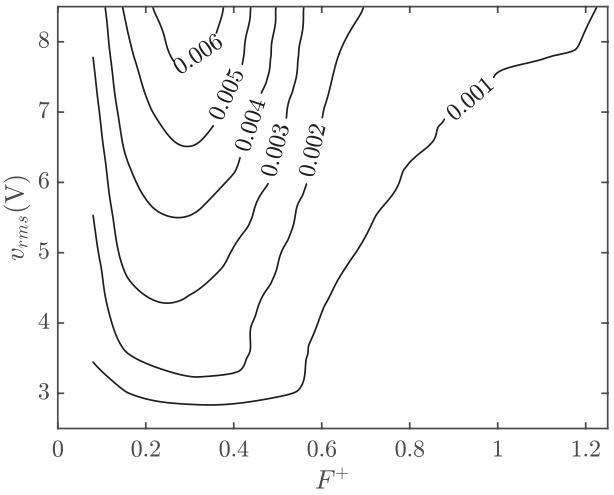

Figure 4.2 SJ characteristics map: momentum coefficient, $C\mu$, as a function of the driving voltage, v_{rms} and the actuation frequency,m F^+.

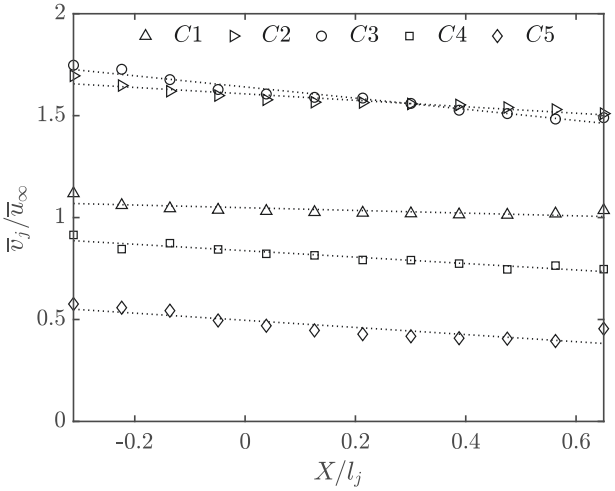

Figure 4.3 Profiles of the maximum exit velocities along the centerline of the SJ slot.

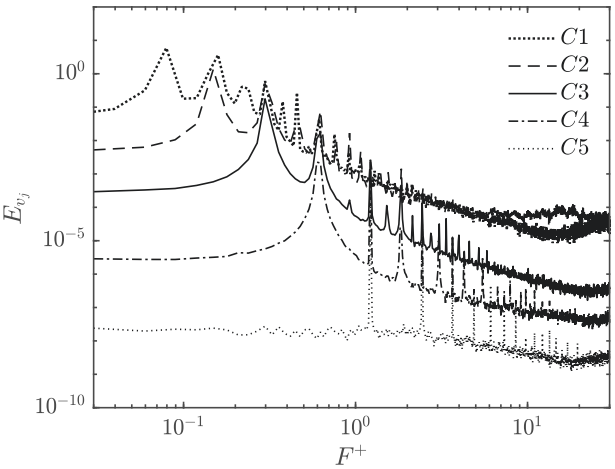

Figure 4.4 Spectra of the SJ exit velocity at the center of the slot.

4.2.4 Analysis techniques

Vortex center identification

In order to determine the location of the instantaneous vortices for each PIV snapshot, a precise and robust method is required. Various vortex identification schemes have been adopted in past studies namely, the swirling strength [12, 119], Q and λ_2 criteria [20, 63, 68], centroid of vorticity and normalized helicity [22, 33, 42, 57] and the geometric center [87, 88]. Comprehensive reviews of most common vortex identification techniques were reported in Chakraborty *et al.* [23], Cucitore *et al.* [32], McAlister [83], Ramasamy *et al.* [94], van der Wall and Richard [111]. Despite being largely used in the literature, the techniques listed above lack the sufficient accuracy in determining the physical location of the vortex center owing to their mathematical formulation which is mostly based on the divergence of the velocity field. To overcome this limitation, Graftieaux *et al.* [49] introduced a non-Galilean invariant approach which provides a robust and accurate way to identify the location of vortex centers in a flow. This method defines a scalar function Γ_1 as (bold indicates a vector quantity)

$$\Gamma_1(P) = \frac{1}{N} \sum_S \frac{(\boldsymbol{PM} \times \boldsymbol{u}_M) \cdot \hat{\boldsymbol{e}}_x}{|\boldsymbol{PM}||\boldsymbol{u}_M|}, \tag{4.4}$$

where $\boldsymbol{PM}$ is the vector from the center point P to a subregion point M in the region S, which could be of any arbitrary shape, that encloses the point P for an estimate of $\Gamma_1(P)$. $\boldsymbol{u}_M$ is the total velocity vector at point M and $\hat{\boldsymbol{e}}_x$ is the unit vector normal to the measurement plane. The vortex center corresponds then to the measurement point where the scalar function Γ_1 is maximum. The Γ_1 function was developed is such a way that the velocity fluctuations caused by large scale vortices are separated from those related to small scale turbulence [49].

Triple decomposition

In order to extract the coherent meandering motion of the trailing vortex, the triple decomposition of Reynolds and Hussain [95] was applied to the SPIV instantaneous flow fields. The instantaneous velocity vector $\boldsymbol{u}(\boldsymbol{x}, t_k)$ can be decomposed into a strictly spatial mean term $\bar{\boldsymbol{u}}(x)$, a coherent term $\tilde{\boldsymbol{u}}(\boldsymbol{x}, t_k)$ and a random term $\boldsymbol{u'}(\boldsymbol{x}, t_k)$, given by

$$\boldsymbol{u}(\boldsymbol{x}, t_k) = \bar{\boldsymbol{u}}(\boldsymbol{x}) + \tilde{\boldsymbol{u}}(\boldsymbol{x}, t_k) + \boldsymbol{u'}(\boldsymbol{x}, t_k). \tag{4.5}$$

If the vortex meandering is assumed to be the consequence of a coherent motion, a meandering-corrected flow field can be obtained by subtracting the coherent term from the each of the instantaneous velocity fields. In this study, the meandering correction was achieved following Edstrand *et al.* [42], where the instantaneous vortex centres, $\boldsymbol{x_c}(t_k)$, determined using Γ_1 method for each of the SPIV snapshot, were linearly translated and superimposed at the location of the mean vortex center. Consequently, the instantaneous velocity fields were systematically shifted by the same displacement vector and then interpolated into a common grid centred around the mean vortex position. This resulted in a meandering-corrected instantaneous velocity field, $\hat{\boldsymbol{u}}(\boldsymbol{x} - \boldsymbol{x_c}(t_k), t_k)$. The meandering-corrected mean flow field, $\bar{\hat{\boldsymbol{u}}}(x)$, was then obtained by time-averaging the meandering-corrected instantaneous velocity fields, as follows

$$\bar{\hat{\boldsymbol{u}}}(\boldsymbol{x}) = \frac{1}{N}\sum_{k=1}^{N} \hat{\boldsymbol{u}}(\boldsymbol{x} - \boldsymbol{x_c}(t_k), t_k). \tag{4.6}$$

The meandering-corrected velocity fluctuation, $\hat{\boldsymbol{u}}'$, was obtained by subtracting the mean meandering-corrected flow field from each of the "re-centred" snapshots such that

$$\boldsymbol{u}'(\boldsymbol{x}, t_k) = \hat{\boldsymbol{u}}(\boldsymbol{x} - \boldsymbol{x_c}(t_k), t_k) - \bar{\hat{\boldsymbol{u}}}(\boldsymbol{x}). \tag{4.7}$$

The coherent meandering flow field, $\tilde{\boldsymbol{u}}$, can be directly inferred from 4.5 and 4.6

$$\tilde{\boldsymbol{u}}(\boldsymbol{x}, t_k) = [\boldsymbol{u}(\boldsymbol{x}, t_k) - \bar{\boldsymbol{u}}(\boldsymbol{x})] - [\hat{\boldsymbol{u}}(\boldsymbol{x}, t_k) - \bar{\hat{\boldsymbol{u}}}(\boldsymbol{x})], \tag{4.8}$$

where the first right-hand term contains both the coherent meandering motion and the background turbulence, while the second right-hand term removes turbulence.

Proper Orthogonal Decomposition

In this study, the proper orthogonal decomposition (POD) was used in order to extract the most energetic features of the turbulence fluctuations within the trailing vortex. This technique was first introduced in the context of fluid mechanics by Lumley [78]. Further details on the mathematical implementation of the POD technique can be found in Berkooz *et al.* [14]. Owing to its computational efficiency, the so-called Snapshot POD (SPOD) approach outlined by Sirovich [104] has been adopted in the current study. It is also customary to use SPOD when the number of instantaneous snapshots, N, is largely smaller than the number of the velocity vectors, N_{zy} calculated in each snapshot [84]. Note

that, in this study, the SPOD analysis was performed on 2000 statistically independent snapshots, each of them encompassing about 10^5 vectors. In practice, the SPOD consists of decomposing the coherent vector field into a deterministic spatial functions $\boldsymbol{\Phi}^k(\boldsymbol{x})$ weighted by random time coefficients $a^k(t)$ such that

$$\tilde{\boldsymbol{u}}(\boldsymbol{x}, t_k) = \sum_{k=1}^{N} a^k(t)\boldsymbol{\Phi}^k(\boldsymbol{x}). \tag{4.9}$$

The coherent velocities $\tilde{w}$ and $\tilde{v}$ were first rearranged into two $N \times N_{zy}$ matrices of snapshots $\mathbf{S}_w$ and $\mathbf{S}_v$. The autocovariance matrix of the velocity fields is defined as

$$\mathbf{C} = \frac{1}{N}\left(\mathbf{S}_w\mathbf{S}_w^T + \mathbf{S}_v\mathbf{S}_v^T\right). \tag{4.10}$$

The corresponding eigenvalue problem is then formulated as

$$\mathbf{C}\boldsymbol{A}^k = \lambda^k\boldsymbol{A}^k, \tag{4.11}$$

where λ^k and $\boldsymbol{A}^k$ are the eigenvalues and eigenvectors of the autocovariance matrix $\mathbf{C}$, respectively. As $\mathbf{C}$ is symmetric and positive semi-definite, all the eigenvalues are real and non-negative and usually sorted in a descending order that relates to the decreasing TKE of the corresponding modes

$$\lambda^1 > \lambda^2 > ... > \lambda^N = 0. \tag{4.12}$$

The scalar modes $\phi_w^k(\boldsymbol{x})$ and $\phi_v^k(\boldsymbol{x})$, which respectively correspond to the coherent velocities $\tilde{w}$ and $\tilde{v}$, are obtained by the projections

$$\phi_w^k(\boldsymbol{x}) = \mathbf{S}_w^T\boldsymbol{A}^k, \tag{4.13}$$

$$\phi_v^k(\boldsymbol{x}) = \mathbf{S}_v^T\boldsymbol{A}^k. \tag{4.14}$$

The spanwise and transverse components of the scalar modes $\boldsymbol{\phi}^k(\boldsymbol{x})$ were subsequently normalized to form an orthonormal basis

$$\boldsymbol{\Phi}^k(\boldsymbol{x}) = \frac{\boldsymbol{\phi}^k(\boldsymbol{x})}{||\boldsymbol{\phi}^k(\boldsymbol{x})||}. \tag{4.15}$$

The time coefficients are then determined by projecting the coherent velocity field onto the scalar modes

$$a^k(t) = \mathbf{S}_w \boldsymbol{\Phi}_w^k(\boldsymbol{x}) + \mathbf{S}_v \boldsymbol{\Phi}_v^k(\boldsymbol{x}). \tag{4.16}$$

The main advantage of the POD approach is the ability to give the best approximation of the flow in an energetic sense. In that, the total TKE of the flow is given by the sum of the eigenvalues

$$\boldsymbol{E} = \sum_{k=1}^{N} \lambda^k. \tag{4.17}$$

A TKE percentage, based upon the scalar mode specific eigenvalue, can be determined to quantify the energy contribution of each mode to the total TKE

$$\boldsymbol{E}^k(\%) = \frac{\lambda^k}{\boldsymbol{E}} \tag{4.18}$$

4.2.5 Results and discussion

Effect of actuation frequency on the ensemble-averaged vortex characteristics

In order to asses the sensitivity of the tip vortex structure to the SJ actuation frequency, F^+, a comprehensive parametric study was conducted at the downstream location $X/c_w = 1.25$. The configurations considered in this study were those summarized in table 4.1. Contour plots of the normalized axial velocity deficit, $(\bar{u}_0 - \bar{u}_x)/\bar{u}_0$, where $\bar{u}_0$ is the local free-stream velocity which was at worst 3% higher than the undisturbed free-stream, $\bar{u}_\infty$, are shown in figure 4.5(a), 4.5(b),4.5(c), 4.5(d), 4.5(e) and 4.5(f), for the cases C0, C1, C2, C3, C4 and C5, respectively, at the measurement plane $X/c_w = 1.25$. For case C0 (figure 4.5(a)), the wing tip vortex was evidenced by a nearly axisymmetric region of strong velocity deficit with a peak of about 0.3. Outside the core region, velocity contours showed a curved region dominated by a velocity deficit of about 0.1. This region corresponds to the wake shear layer being drawn and fully wrapped around the main vortex core as a result of the strong velocity deficit. With control, the wake shear layer was found to be

stretched in the spanwise direction and was slightly thinned where its maximum velocity deficit slightly increased by up to 25% (in case C5) with respect to case C0, as illustrated in figure 4.5. More interestingly, velocity contours of the controlled cases exhibited a nearly elliptic and a rather diffuse core region compared to C0 with maximum velocity deficits at the core being 30, 38, 28, 8 and 4% lower than C0 for the cases C1, C2, C3, C4 and C5, respectively. Note that, as the actuation frequency increases, the extent of the vortex stretching was found to decrease and the contours of the velocity deficit appeared less elongated in the blowing direction. This suggests that the stroke length of the SJ penetrates less distances into the vortex core with increased actuation frequency [40].

Contours of the normalized mean axial vorticity, $\bar{\xi}_x \, c_w/\bar{u}_0$, at $X/c_w = 1.25$, are displayed in figure 4.6(a), 4.6(b), 4.6(c), 4.6(d), 4.6(e) and 4.6(f), for the cases C0, C1, C2, C3, C4 and C5, respectively. In figure 4.6(a), the axial vorticity contours of C0 clearly depicts two distinct regions: the wake shear layer with relatively low vorticity levels and vortex structure where most of the vorticity is contained. The latter shows a nearly circular shape with a radius of about $0.05c_w$ and peak value of 35. An apparent stretching of the vorticity contours, similar to that of the contours of the velocity deficit, was clearly observed in the controlled cases. The apparent outward diffusion of the vortex was also accompanied with a 32, 27, 40, 38 and 36% decrease in the peak value of the axial vorticity of the cases C1, C2, C3, C4 and C5, respectively, compared to C0. It can readily be inferred from figure 4.6 that, although the vorticity contours of case C2 appeared more stretched, the control case C3 had the most significant impact of the core vorticity amongst all control configurations. In that, contours of the axial vorticity in the vortex core of case C3 were found to be more diffuse, hence covering a larger area around the mean vortex center.

The effect of the SJ actuation frequency on the tip vortex can be further quantified by evaluating the radial profiles of the azimuthal velocity using the method detailed in Dghim *et al.* [38, 40]. In figure 4.7(a), the distributions of $\bar{v}/\bar{u}_0$ reached a peak value before slowly decreasing to a nearly asymptotic value. The region between the ensemble-averaged vortex

Table 4.1 Summary of the control configurations studied.

Case	C_μ	F^+	f_a(Hz)	v_{rms}(V)	$\bar{v}_j^{\max}$(m/s)
C0	-	-	-	-	-
C1	0.001	0.075	2.5	3.4	11.2
C2	0.001	0.15	5	3	16.9
C3	0.001	0.3	10	2.8	17.5
C4	0.001	0.6	20	4.2	9.1
C5	0.001	1.2	40	8.2	5.7

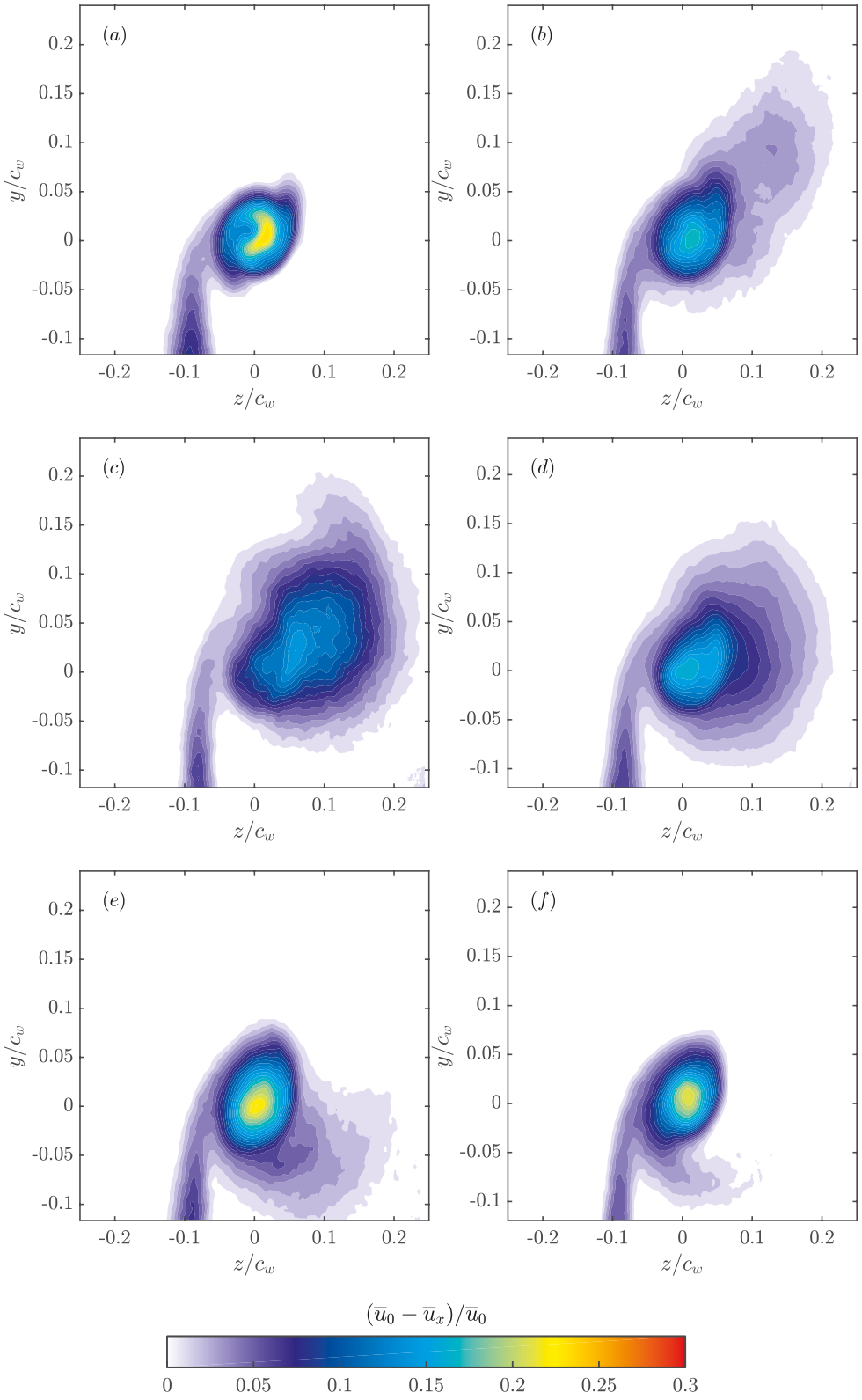

Figure 4.5 Contours of the normalized axial velocity deficit at $X/c_w = 1.25$. (a): C0, (b): C1, (c): C2, (d): C3, (e): C4 and (f): C5.

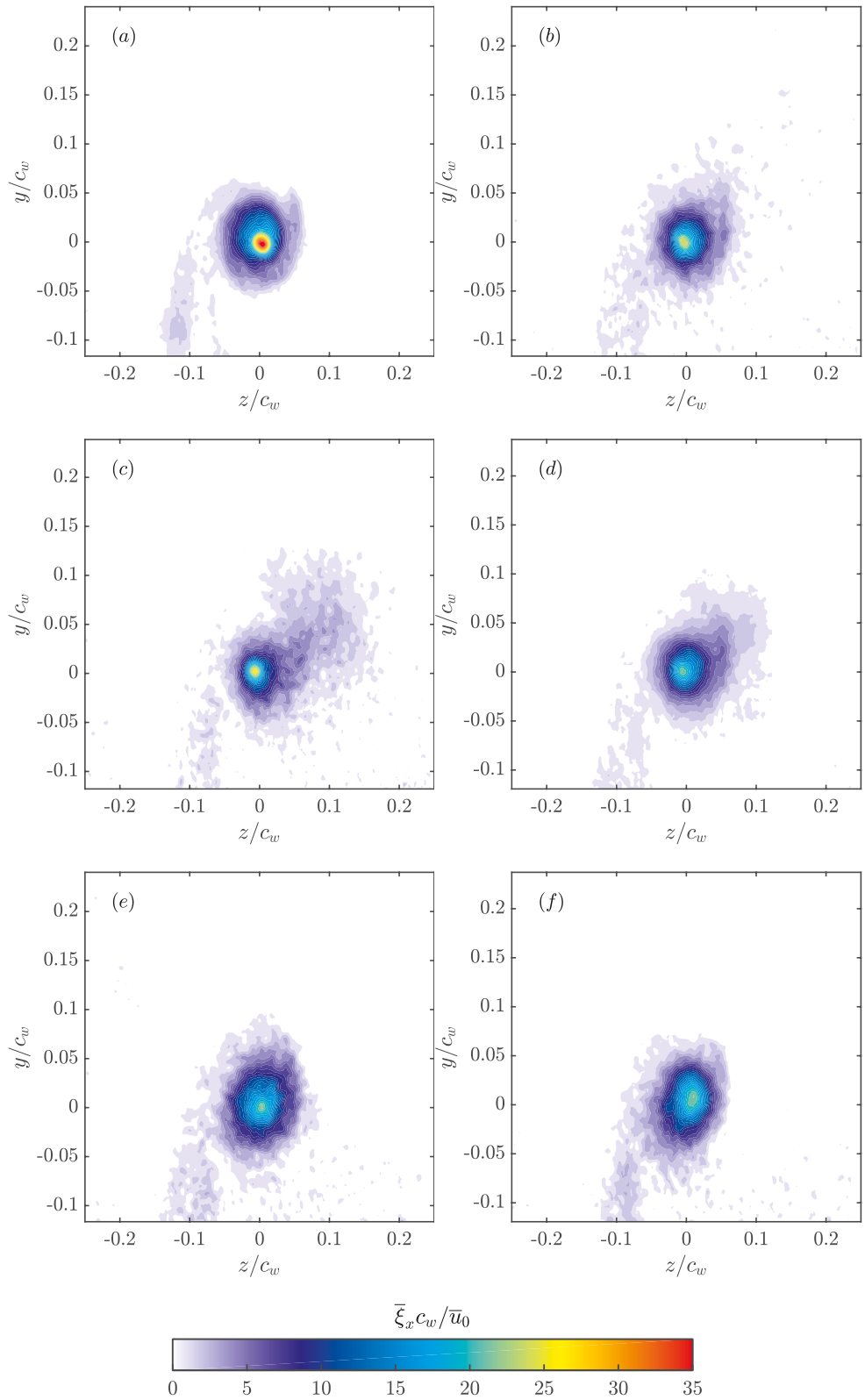

Figure 4.6 Contours of the normalized axial vorticity $X/c_w = 1.25$. (a): C0, (b): C1, (c): C2, (d): C3, (e): C4 and (f): C5.

location ($r/c_w = 0$) and the radial location at which the peak value of $\bar{v}/\bar{u}_0$ occurs is often referred to as the inner vortex region and the size of this region corresponds to the vortex radius, r^*. The outer vortex region, however, lies in the region where $r/c_w > r^*$. For case C0, the radial profile of $\bar{v}/\bar{u}_0$ reached a peak value of nearly 0.24 corresponding to a normalized vortex radius, $r_0^* = r_0/c$, of about 0.038. With actuation, the gradient of $\bar{v}/\bar{u}_0$ were seen to slightly decrease with increased actuation frequency, causing the peak value of $\bar{v}/\bar{u}_0$ to significantly drop to a value of about 0.17 under case C3, before slowly rising again. This increase in the core velocity gradient was also accompanied with a remarkable increase in the peak value of $\bar{v}/\bar{u}_0$ which reached a value of about 0.22 under the highest actuation frequency of case C5. This behavior was clearly illustrated in figure 4.7(b) which indicates that the control case C3 resulted in the lowest peak value of $\bar{v}/\bar{u}_0$ amongst all the cases studied, indicative of a significant vortex diffusion. Interestingly, however, the normalized vortex radius, r^* at $X/c_w = 1.25$, was found to be essentially unaffected by the actuation frequencies $F^+ < 0.4$, despite the 30% reduction in the peak azimuthal velocity of case C3. At higher control frequencies, the vortex radius was seen to marginally increase compared to cases C1, C2 and C3, reaching a nearly 10% increase in size with respect to C0, under the control case C5. The effectiveness of the low actuation frequency in promoting the vortex diffusion process is in close agreement with the findings of Dghim *et al.* [40], Margaris and Gursul [79].

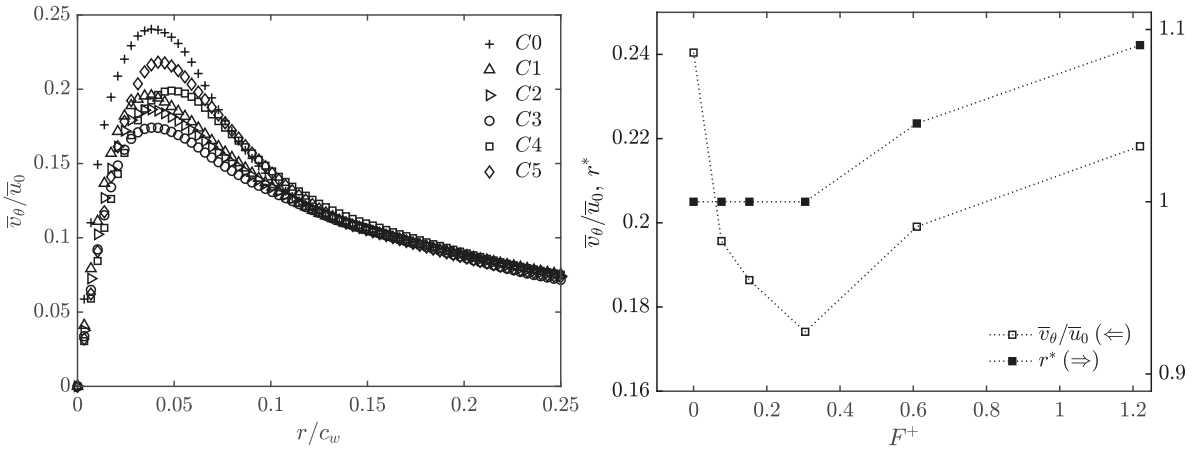

Figure 4.7 Effect of the actuation frequency on (a) the radial distributions of the ensemble-averaged azimuthal velocity, on (b) the peak azimuthal velocities and the normalized vortex radii. Values were evaluated at $X/c_w = 1.25$ for all the configurations studied.

Circulation was also used as a metric to assess the effect of the actuation frequency on the vortex strength. Figure 4.8(a) shows the radial distributions of the vortex circulation

evaluated at $X/c_w = 1.25$ for all control configurations. In this figure, profiles of the normalized circulation showed an inflection point in the inner core region at $r/c_w \sim 0.01$, beyond which the circulation increased monotonically with increased radial distance. Outside the core region, the circulation continued to increase with increased radial position until reaching a second inflection point at $r/c_w \sim 0.06$, marking the extent of the wake shear layer. In the inner vortex region, the actuation caused the circulation gradient to measurably decrease with respect to C0 with the effect being more pronounced under C3. In consequence, the vortex core circulation, γ, was expected to decrease, as illustrated in figure 4.8(b). In this figure, the vortex core circulations were normalized by that of the reference case C0, γ_0 and then plotted against the actuation frequency, F^+. Similar to the peak values of $\bar{v}/\bar{u}_0$ (figure 4.7(b)), the lowest vortex core circulation was achieved under the control case C3 where the actuation frequency corresponds to resonance frequency of the SJ actuator. Moreover, as the vortex radii of the control cases were unaffected, the reduction in their core circulations was mainly attributed to the decreased vorticity in this region (as seen in figure 4.6). Beyond the second inflexion point, the circulation profiles started to increase at a much lower rate than that in the inner core as the vortex flowfield approaches a nearly irrotational state outside the core region [38, 114]. In this region, the circulation profile of case C0 exhibited a marginally asymptotic state which might be attributed to the remnants of the vortex sheet spiral around the core region [112]. With control, the profiles of the normalized circulation exhibited higher values than those of C0, with the effect being more pronounced under case C3. This increase was clearly reflected in the values of the total circulation, as indicated in figure 4.8(b). It can be inferred from this figure that forcing the tip vortex at the SJ resonance frequency (case C3) caused the total circulation to increase by nearly 12% with respect to case C0, which might indicate an increase of the wing bound circulation [50, 59]. Although no information on aerodynamic forces can be inferred from this study, it would be reasonable to expect the lift to have increased as a result of the SJ actuation.

In order to gain more insight into the effect of the actuation frequency of the vortex diffusion, the normalized turbulent kinetic energy, $\bar{k}/\bar{u}_0^2$, was evaluated using the following expression

$$\frac{\bar{k}}{\bar{u}_0^2} = \frac{1}{2}\left(R_{uu} + R_{vv} + R_{ww}\right) \tag{4.19}$$

where $R_{uu} = \overline{u'u'}/\bar{U}_0^2$, $R_{vv} = \overline{v'v'}/\bar{u}_0^2$ and $R_{ww} = \overline{w'w'}/\bar{u}_0^2$ are the normalized streamwise, spanwise, and transverse Reynolds stresses, respectively. u', v' and w' are the fluctuating

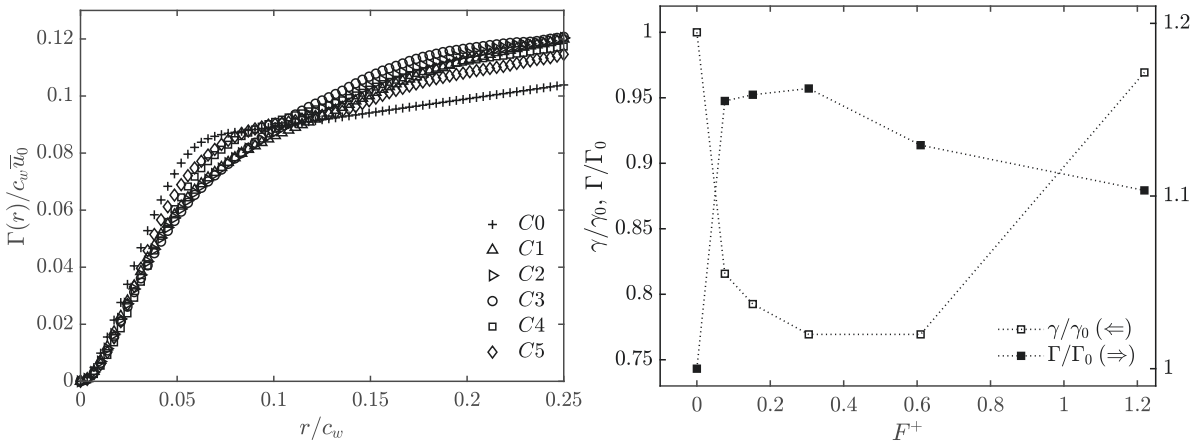

Figure 4.8 Effect of the actuation frequency on (a) the radial distributions of the normalized circulation, on (b) the normalized core circulations and the normalized total circulations. Values were evaluated at $X/c_w = 1.25$ for all the configurations studied.

velocities in the x, y and z directions, respectively, which contain both coherent and random components. Contour plots of the turbulent kinetic energy are plotted in figure 4.9(a), 4.9(b), 4.9(c), 4.9(d), 4.9(e) and 4.9(f), for the cases C0, C1, C2, C3, C4 and C5, respectively, at the measurement plane $X/c_w = 1.25$. For case C0, figure 4.9(a), showed a small region of TKE located near the ensemble-averaged vortex center position with a peak value of about 6×10^{-3}, while most of the TKE was mostly concentrated in the wake shear layer. With control, an elliptic-shaped region of high values of TKE appeared to be concentrated in the vortex core region. In particular, peak values of $\bar{k}/\bar{u}_0^2$ were measured to be 0.022, 0.027, 0.035, 0.014 and 0.011 for cases C1, C2, C3, C4 and C5, respectively. It is noteworthy that the region of high TKE appeared to be stretched in the spanwise direction, following the same behavior observed in both velocity (see figure 4.5) and vorticity contours (see figure 4.6). Furthermore, for all control cases, contours of high TKE levels were seen to cover a larger area within the vortex core with noticeably larger effect under control case C3. This observation suggests that the high TKE region in the vortex core were essentially triggered by the high unsteadiness contained in the counter-rotating structures injected into the vortex at a frequency analogous to the resonance frequency of the SJ actuator used in this study [40].

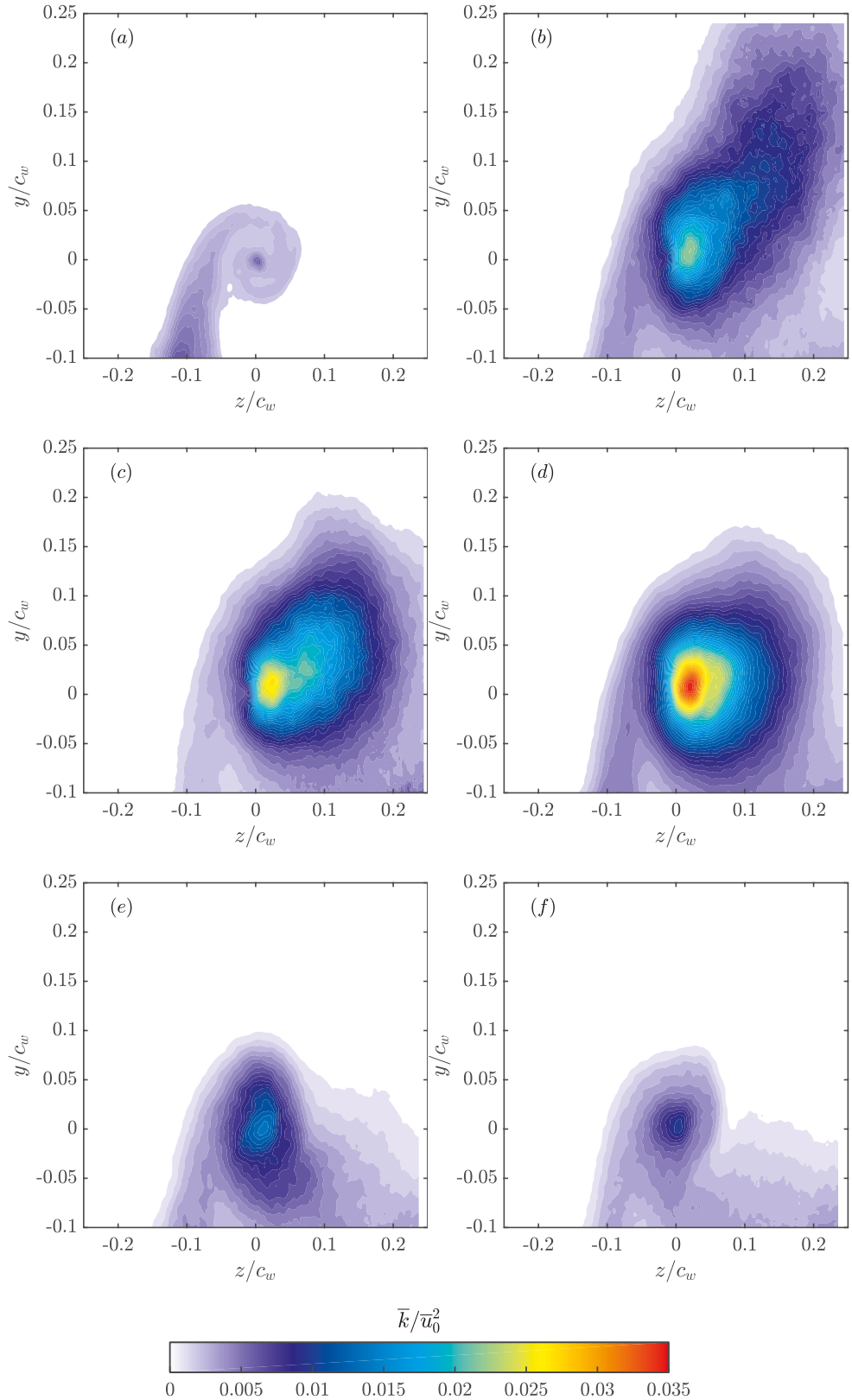

Figure 4.9 Contours of the normalized TKE at $X/c_w = 1.25$. (a),(c) and (e): C0, (b),(d) and (f): C3.

The streamwise development of the actuated vortex

It has been established in §4.2.5 that the control case C3 had the most pronounced effect on the tip vortex amongst all configurations studied. It is, therefore, of a particular interest to study the effect of SJ actuation under case C3 on the tip vortex in the near and mid-wake regions. In fact, a comprehensive SPIV survey has been conducted at the downstream positions $X/c_w = 1.25, 3.25, 6.25$ and 7.75. Contours of the normalized axial vorticity, $\bar{\xi}_x\, c/\bar{u}_0$, are plotted in figure 4.10(a), 4.10(c), 4.10(e) and 4.10(g) for case C0, and figure 4.10(b), 4.10(d), 4.10(f) and 4.10(h) for case C3, at the measurement planes $X/c_w = 1.25, 3.25, 6.25$ and 7.75, respectively. Figure 4.10(a) clearly depicts the the shear layer rollup of case C0 around the vortex core where vorticity reached higher levels than those of the outer region. As the vortex developed downstream, the wake shear layer were seen to thicken and its vorticity levels decreased by nearly 50% with increased downstream distance. Inside the core region, the peak value of the normalized vorticity decreased by roughly 35% as the vortex was convected from $X/c_w = 1.25$ to $X/c_w = 7.75$. Outside the wake and the tip vortex regions, the vorticity was essentially zero. With actuation and under case C3, vorticity contours appeared to be more diffuse than C0 and covered a larger area around the vortex core [38–40, 79]. At $X/c_w = 1.25$, the peak value of $\bar{\xi}_x\, c/\bar{u}_0$ decreased by nearly 40% compared to C0, in agreement with [38]. As the vortex travelled downstream, its core vorticity decreased substantially from a value of about 22 at $X/c_w = 1.25$ to a value of about 8.5 at $X/c_w = 7.75$.

Despite the fact that very crucial three-dimensional effects dominate the genesis of the vortex rollup and formation, it is of a particular interest to analyse its asymptotic behavior. It has been reported in Phillips [91] that the circumferential velocity profiles in the core of a wing tip vortex adopt a self-similar behavior, when $\bar{v}_\theta$ and r/c_w are normalized by the peak value, $\bar{v}_{\theta,m}$, and its corresponding radial location, r^*, respectively. The normalized radial positions were denoted with the self-similar variable, η, such that the profiles of the scaled azimuthal velocities can be educed from the following expression

$$\frac{\bar{v}_\theta}{\bar{v}_{\theta,m}} = \left(1 + \frac{1}{2\alpha}\right) \frac{1}{\eta} \left(1 - e^{-\alpha\eta^2}\right) \tag{4.20}$$

where α is defined by $e^\alpha = 1+2\alpha$, yielding to $\alpha \approx 1.256$. This behavior was clearly depicted in figure 4.11(a) for case C0, where $\bar{v}_\theta/\bar{v}_{\theta,m}$ reached a peak value of 1 at the normalized radial position η of 1. Inside the vortex core ($\eta < 1.2$), a slight departure from the theoretical fit was clearly observed at $X/c_w = 1.25$. For larger downstream distances, the profiles of the scaled azimuthal velocity were found to collapse fairly well with the curve fit

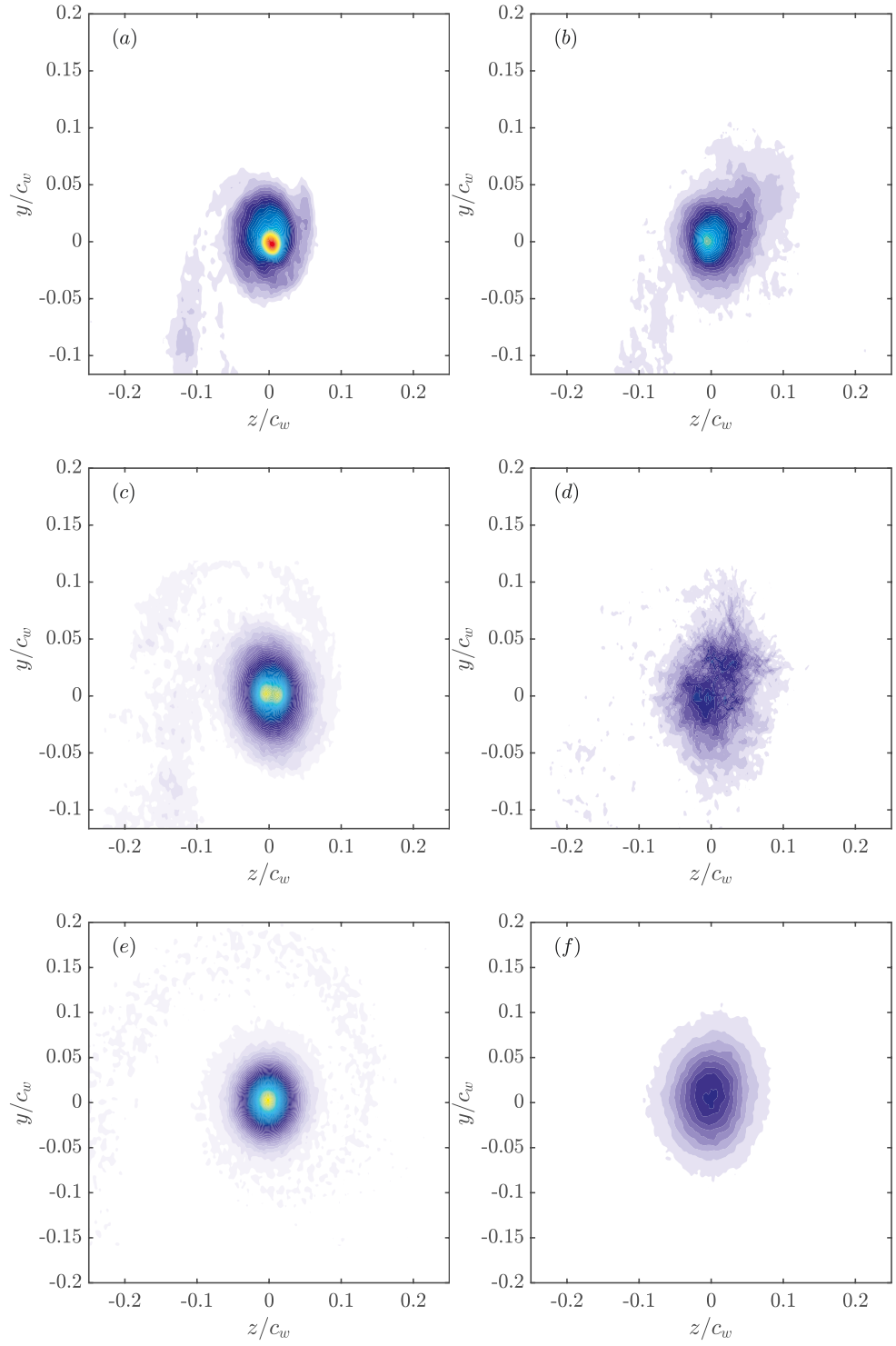
(a)
(b)
(c)
(d)
(e)
(f)
y/c_w
z/c_w
0.2
0.15
0.1
0.05
0
-0.05
-0.1
-0.15
-0.2

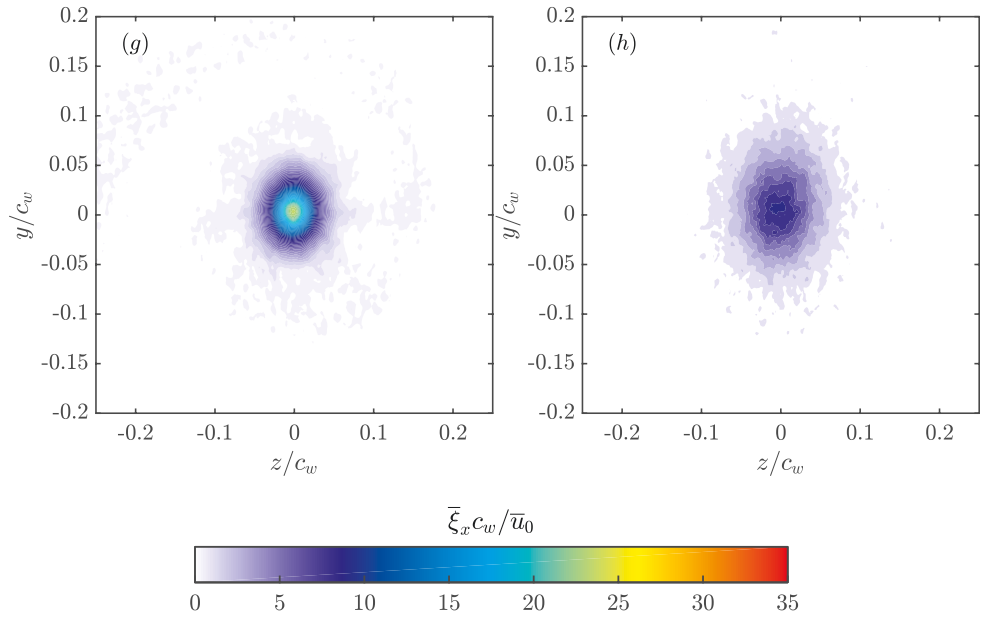

Figure 4.10 Contours of the normalized axial vorticity at $X/c_w = 1.25, 3.25, 6.25$ and 7.75. (a),(c),(e) and (g): C0, (b),(d),(f) and (h): C3.

proposed in Phillips [91], typical of a self-preserved vortex structure. It would be surmised that, at $x/c \sim 3$, the rollup process may have been completed and the vortex core had evolved asymptotically to reach a nearly axisymmetric distribution, in accordance with the results reported in Dghim *et al.* [38]. Outside the vortex core and for $\eta > 1.2$, the profiles of $\overline{v}_\theta/\overline{v}_{\theta,m}$ exhibited a measurable discrepancy from the vortex model. This slight upward departure from the theoretical model was observed in the previous studies of Bailey *et al.* [4], Del Pino *et al.* [35], Sousa and Pereira [106], Waldman and Breuer [114] and might be attributed to the large turbulence levels around the vortex core and the smoothing velocity gradients which might endow a higher spreading rate along the radial direction, as reported in Hoffmann and Joubert [58]. Saffman [100], however, suggested that the lack of collapse with the theoretical model is presumably caused by the gradual transition between the viscous core region and the outer region dominated by the non-irrotational flow of the rolling vortex sheet. Under case C3, figure 4.11(b) showed that the actuation did not appear to alter the structure of the vortex core as the profiles of $\overline{v}_\theta/\overline{v}_{\theta,m}$ exhibited a reasonable collapse with the theoretical fit at all downstream locations, suggesting an asymptotic state of the vortex core. Outside the core region, profiles of $\overline{v}_\theta/\overline{v}_{\theta,m}$ were found to move further upward from the theoretical fit, with the effect being more pronounced at $X/c_w = 1.25$. This atypical behavior suggests that the SJ of case C3 had significantly affected the region around the vortex core (rolling shear layer) where high turbulence mixing smears out velocity gradients of the rotational field, causing a slow deceleration of

the azimuthal velocity and, therefore, an increased outward diffusion of vorticity. As the vortex evolved further downstream, it started to gradually regain its axisymmetric shape as the shear layer continues to wrap around the now weakened vortex, resulting in a higher decrease of the azimuthal velocity in the outer region of the vortex.

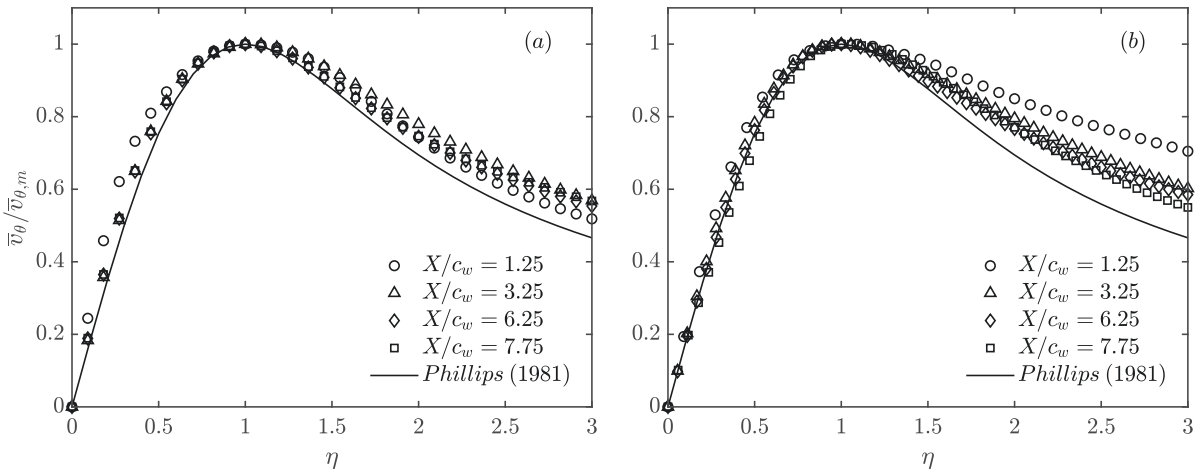

Figure 4.11 Radial profiles of the normalized azimuthal velocity in a self-similar coordinate system, at different downstream positions. (a) C0 and (b) C3.

The effect of control on the vortex core structure can be further demonstrated from the close examination of the radial distribution of the normalized circulation, Γ/γ, plotted with the similarity variable, $\log\eta$, for different downstream positions, as illustrated in figure 4.12(a) and 4.12(b), for cases C0 and C3, respectively. Empirical curve-fit relationships suggested by Hoffmann and Joubert [58], which describe the circulation behavior within the inner-core and the logarithmic regions of the vortex were fitted to the radial profiles of $\Gamma(\eta)/\gamma$ of all the case studied given by

$$\frac{\Gamma(\eta)}{\gamma} = A\eta^2 \quad \text{for} \quad \eta < 0.4 \tag{4.21}$$

$$\frac{\Gamma(\eta)}{\gamma} = 1 + B\log(\eta) \quad \text{for} \quad 0.5 < \eta < 1.4 \tag{4.22}$$

where the constants A and B are 1.83 and 0.93, respectively. In figure 4.12(a), a reasonable collapse between the radial profiles of $\Gamma(\eta)/\gamma$ of case C0 with the curve-fits of equations 4.21 and 4.22, was clearly observed for the downstream positions $X/c_w > 3$. In the region $X/c_w \leq 3$, the profile of $\Gamma(\eta)/\gamma$ exhibited a clear departure from the empirical curve-fits in the inner and outer region of the vortex, suggesting that the rollup process was incomplete

and that the vortex has yet to reached a self-similar state. These observations corroborate the results reported in figure 4.11(a). Moreover, for $0 < \eta < 1.2$, these profiles collapsed together onto a sixth-order polynomial suggested by [15, 93] following the expression

$$\frac{\Gamma(\eta)}{\gamma} = a_0\eta^2 + a_1\eta^4 + a_2\eta^6 \tag{4.23}$$

where the constants a_0, a_1 and a_2 are 1.756, -1.044 and 0.263, respectively. With control, circulation profiles in the inner region of the vortex depicted an excellent collapse with the curve-fits suggested by Birch *et al.* [15], Hoffmann and Joubert [58], Ramaprian and Zheng [93], as shown in figure 4.12(b). Inside the inner core region (I), the self-similar circulation profiles of case C0 and C3 were $\propto \eta^2$ and exhibited a parabolic shape. This indicated that this region was mainly dominated by the viscous effect where the vortex core had an approximately rigid body rotation [37, 58]. Note that, as opposed to case C0, no collapse between the circulation profiles was observed in the outer region (IV) of the controlled vortex. This suggests that, although the vortex core under the control case C3 regained a well-organized and axisymmetric structure while being convected downstream, the increase in circulation caused by the SJ momentum injection would require larger downstream distances before the outer region of the vortex can reach an asymptotic state [40].

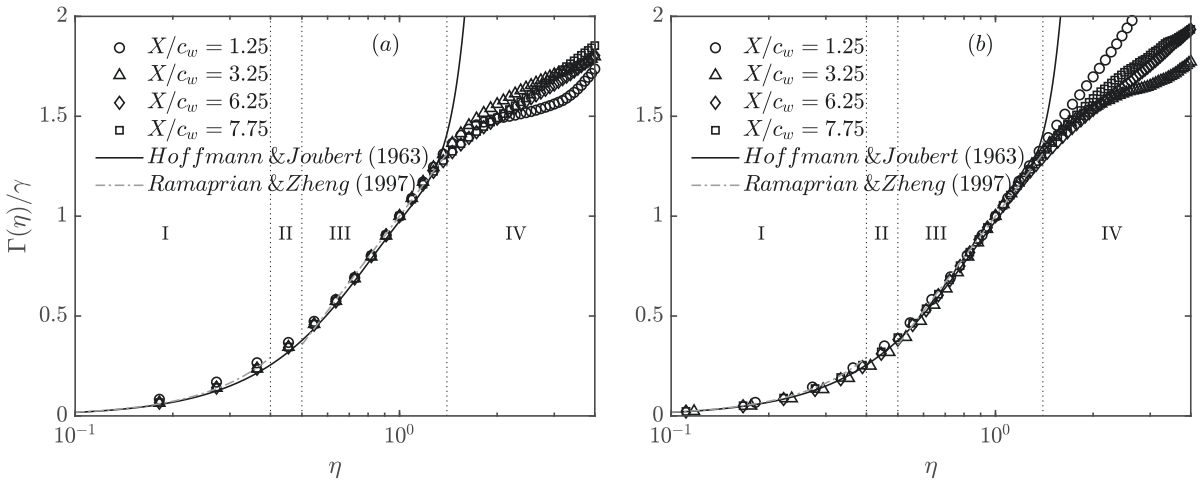

Figure 4.12 Self-similar circulation profiles of the inner-region at different downstream positions. (a) C0 and (b) C3. I: inner-core, II: buffer region, III: logarithmic region and IV: outer region.

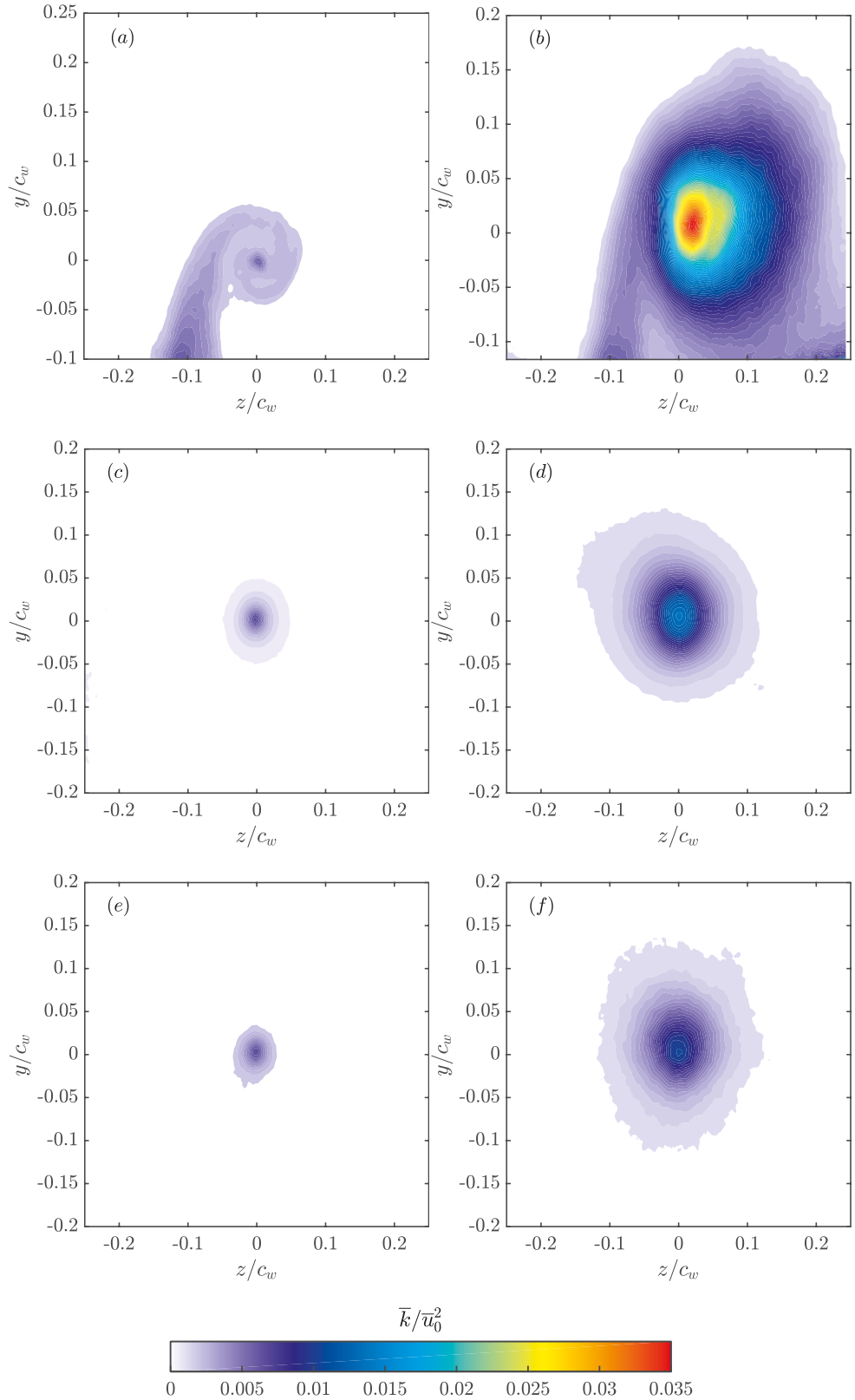

Figure 4.13 Contours of the normalized TKE at $X/c_w = 1.25, 6.25$ and 7.75. (a), (c), (e): C0 and (b), (d), (f): C3.

Effect of active flow control on vortex meander

Vortex meander can be clearly observed when examining the instantaneous positions of the vortex center. In practice, these positions were extracted from each individual SPIV velocity field by computing the Γ_1 function defined by Graftieaux *et al.* [49], as detailed in §4.2.4. The in-plane coordinates of the vortex center locations were then plotted with respect to the ensemble-averaged vortex position centred at $(z_w, y_w) = (0, 0)$, as indicated by the red cross plotted in figure 4.14. In figure 4.14(a), the scatter of the instantaneous vortex positions of case C0 at $X/c_w = 1.25$ exhibits an isotropic aperiodic motion around the mean vortex position with no particularly preferred direction. As the vortex evolved to $X/c_w = 6.25$, the displacement magnitude of the vortex center position, refereed to as meandering amplitude, was found to increase however the dispersion pattern was similar to that observed at $X/c_w = 1.25$. It is reasonable to assume that, within the experimental uncertainty of the present study, the vortex center positions may be fitted fairly well by a bi-normal joint probability distribution function (j.p.d.f) where the meandering amplitudes can be effectively represented by its corresponding standard deviations σ_z and σ_y in the z and y directions [2, 3, 37, 42]. In figure 4.15(a) and (c), the Gaussian j.p.d.f of case C0 showed concentric iso-contours of equal levels, covering larger radii with increased downstream distance. With control, figure 4.14(b) and (c) indicate a rather more stochastic motion of the instantaneous vortex centres about the mean vortex location. It is interesting to note that the scatter of the vortex positions displays an oblique angle canted at approximately 45 degrees with respect to the spanwise direction. At $X/c_w = 1.25$, the amplitude of meandering in the upper right quadrant, $(z, y) > 0$, was measured to be approximately three times larger than the amplitude in the other directions. The asymmetry in the scatter of the vortex center position appeared to be consistent with the stretching observed in the contours of the mean flow field (as described in §4.2.5), and is believed to be triggered by the SJ actuation which tends to push the vortex away from the wing tip. Moreover, the anisotropy of the meandering direction was corroborated by the elliptic-shaped j.p.d.f contours which portrayed slightly eccentric probability levels towards the preferred meandering direction. Further downstream, the helical nature of the rolling vortex forced the oblique angle of the meandering scatter to rotate around the mean vortex axis and as the vortex reached $X/c_w = 6.25$, the meandering direction was found to be predominately aligned with the spanwise direction (figure 4.14(d)). The scatter remains essentially anisotropic, however, the j.p.d.f iso-contours exhibited perfectly concentric ellipses with the major axes aligned with the spawise direction, as illustrated in figure 4.15(d). The streamwise development of the independent meandering amplitudes, σ_z and σ_y, was summarized in figure 4.16. For case C0, the meandering amplitudes were found to

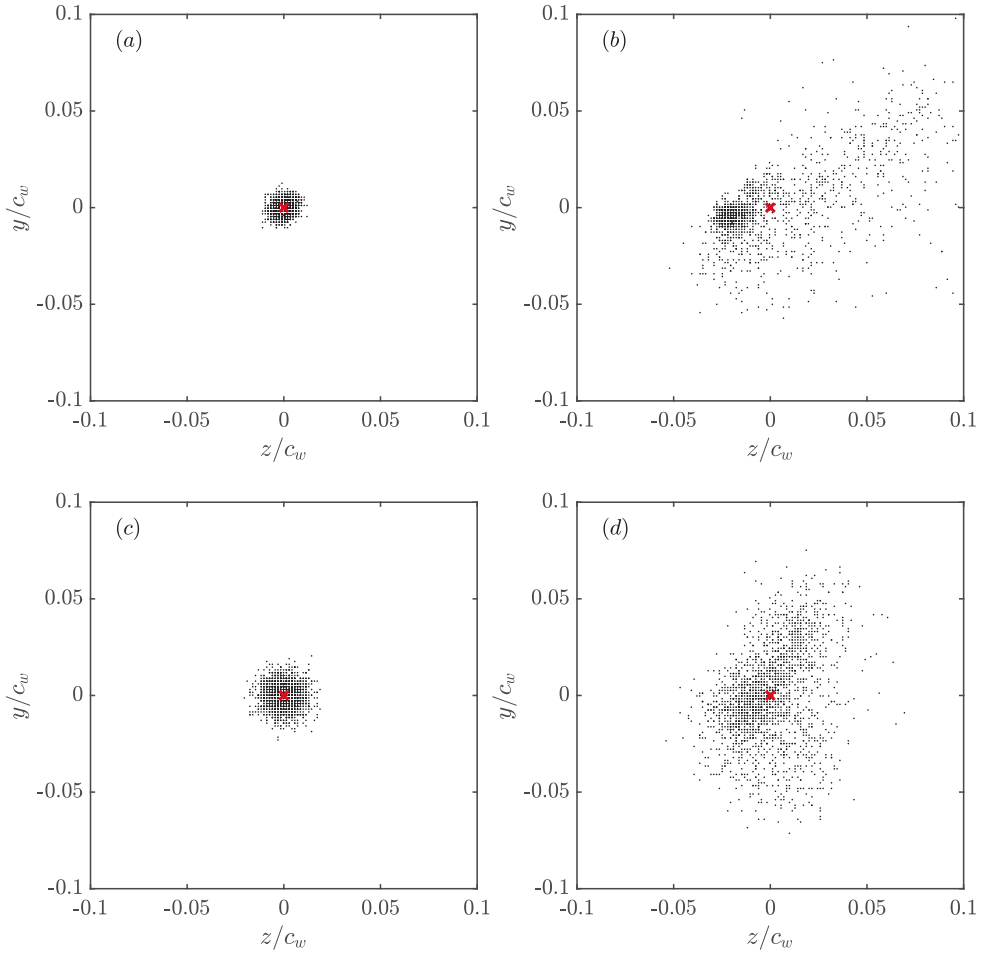

Figure 4.14 Scatter plots of the instantaneous vortex center positions at $X/c_w = 1.25$ and 6.25. (a), (c): C0 and (b), (d): C3.

grow with increased streamwise distance, consistent with previous observations reported in Bailey and Tavoularis [2], Beresh *et al.* [12], Devenport *et al.* [37], Heyes *et al.* [56]. More interestingly, at $X/c_w = 6.25$, the meandering amplitudes under the SJ actuation of case C3 were 8 and 5 times higher than those of C0 in z and y directions, respectively. The higher meandering amplitude in the z direction in consistent with the iso-contours of the j.p.d.f displayed in figure 4.15(b). As the vortex evolves downstrean, σ_z/c_w was seen to rapidly drop from a value of 0.03 at $X/c_w = 1.25$ to a value of 0.017 at $X/c_w = 6.25$ where it appeared to reach a nearly asymptotic value. In contrast, σ_z/c_w exhibited an opposite behavior as it increased from a value of a about 0.02 to an asymptotic value of about 0.025 at $X/c_w > 6$. The mirrored behaviors of the meandering amplitudes clearly substantiate the angular inversions observed in the skewed j.p.d.f iso-contours and caused by the helical structure of the rolling vortex. Despite reaching nearly asymptotic values for $X/c_w > 6$, σ_z/c_w and σ_y/c_w remained substantially larger than those evaluated for

case C0. As noted earlier, meandering is known to create artificially reduced azimuthal velocity and increased vortex core radius [2, 5, 12, 13, 37, 57]. In fact, [37] reported that the azimuthal velocity and the vortex radii were altered by nearly 15%, while [2] found velocity changes nearing 50% at high freestream turbulence levels. Insignificant meandering effects were, however, found in [12, 57]. Considering the significant meandering amplitudes reported in this study, an ultimate correction is believed to be necessary in order to isolate the effect of vortex meander from the effect of active flow control on both mean and turbulence flow fields. Profiles of the raw ensemble-averaged azimuthal velocities, $\bar{v}_\theta/\bar{u}_0$, and the corrected one, $\bar{\hat{v}}_\theta/\bar{u}_0$, were plotted in figure 4.17 for both C0 and C3 cases at the selected streamwise position $X/c_w = 6.25$. For the natural vortex, a nearly 5% increase in the peak value of the azimuthal velocity was achieved with wandering correction however no significant effect was observed on the vortex radius. It is believed that the undistinguishable effect of the meandering correction on the mean azimuthal velocity of case C0 is probably attributed to the higher turbulent fluctuations within the vortex core compared to the meandering-induced turbulence, as suggested in Beresh *et al.* [12], Shah *et al.* [101]. With control, the peak value of the corrected azimuthal velocity, $\bar{\hat{v}}_\theta/\bar{u}_0$, was measured to be 10% higher than that of $\bar{v}_\theta/\bar{u}_0$. This increase was associated with a nearly 20% decrease in the vortex radius.

The significant vortex diffusion caused by the increased meandering effect under the SJ actuation can be inferred by closely examining the contours of the normalized TKE for both raw and corrected flow fields. In figure 4.18(a), contours of the raw TKE, $\bar{k}/\bar{u}_0$, of case C0 exhibited a peak value of about 0.006 within the vortex core surrounded by low TKE levels in the core periphery and the wake shear layer. On the other hand, contours of the meandering-corrected TKE, $\bar{\hat{v}}_\theta/\bar{u}_0$, revealed a strikingly different behavior. In that, figure 4.18(b) showed a turbulence-free vortex core where TKE levels at the vortex center were measured to be zero. Outside the core region, turbulence was evidenced by a croissant-shaped lobe of lower TKE levels surrounding the vortex core. The existence of a laminar core at the center of the vortex surrounded by low turbulence levels near the core radius has previously been observed experimentally by Bandyopadhyay *et al.* [7], Beresh *et al.* [12], Devenport *et al.* [37], computationally by Ragab and Sreedhar [92] and has been further supported by the analytical studies of Cotel and Breidenthal [28], Jacquin and Pantano [66]. This behavior arises from the stabilizing Coriolis effects of the strong rotational motion inside the vortex core which tends to relaminarize the turbulent fluid crossing the periphery of the vortex. The existence of the turbulent region around the vortex core is mainly attributed to the strong shearing between the laminar core and the rolling turbulent wake. It is noteworthy that the meandering correction was found to

reduce the peak level of TKE around the vortex core by nearly 90% compared to the values measured at the vortex center of the raw case. Despite the higher TKE levels recorded for the actuated vortex, the core region exhibited virtually similar behavior to that observed in the raw flowfield of case C0. In fact, the peak value of $\bar{v}_\theta/\bar{u}_0$ at the vortex center was approximately 70% higher than that of the natural vortex and higher TKE levels were found to cover a larger area of the vortex core. With meandering correction, the artificial turbulence at the center of the vortex was essentially absent and the peak value of $\bar{\hat{v}}_\theta/\bar{u}_0$ near the vortex radius was nearly three times higher than that of case C0. Additionally, the size of the croissant-shaped annulus of turbulence around the core was noticeably larger and covered larger radial area. This suggests that more turbulent fluid is believed to be ingested into the vortex core under the effect of the SJ actuation causing higher turbulent mixing and therefore larger momentum transfer between the turbulent shear

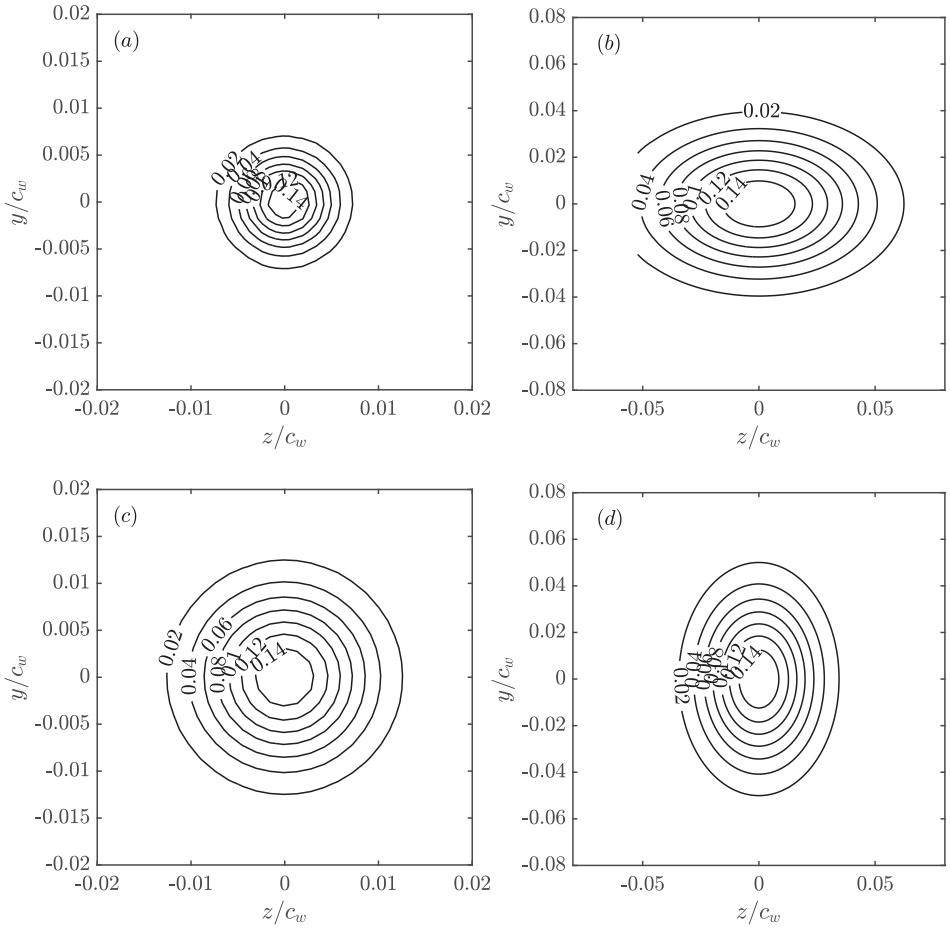

Figure 4.15 Contours of the Gaussian j.p.d.f. distribution of the instantenous vortex center positions evaluated at $X/c_w = 1.25$ and 6.25. (a), (c): C0 and (b), (d): C3.

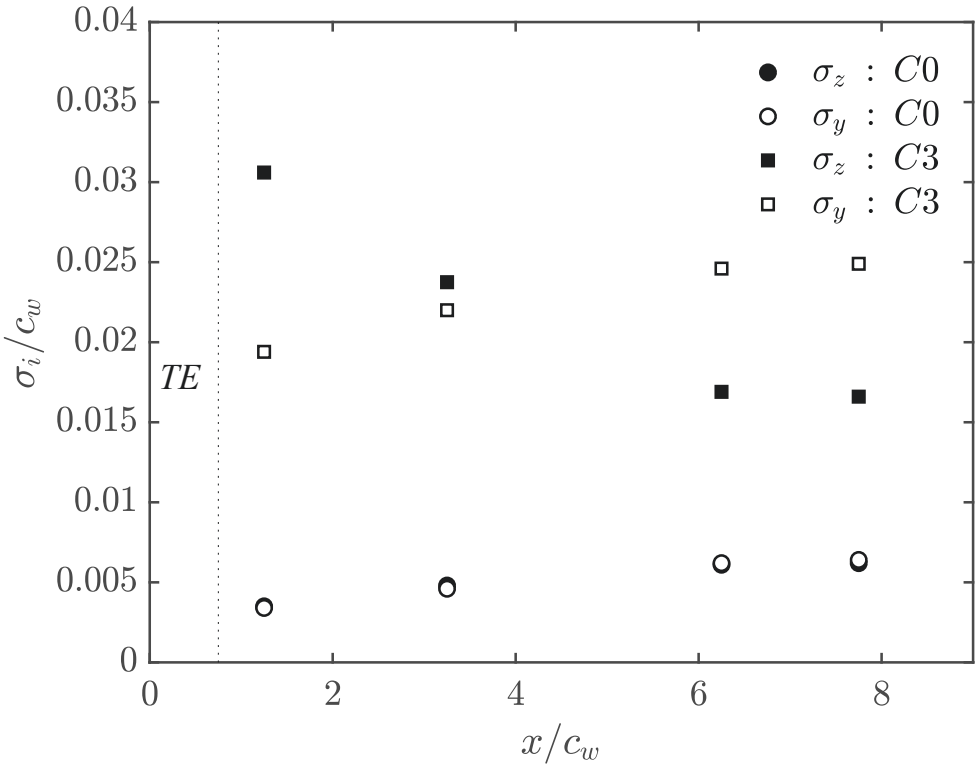

Figure 4.16 Vortex meandering amplitudes, σ_z and σ_y at different downstream positions.

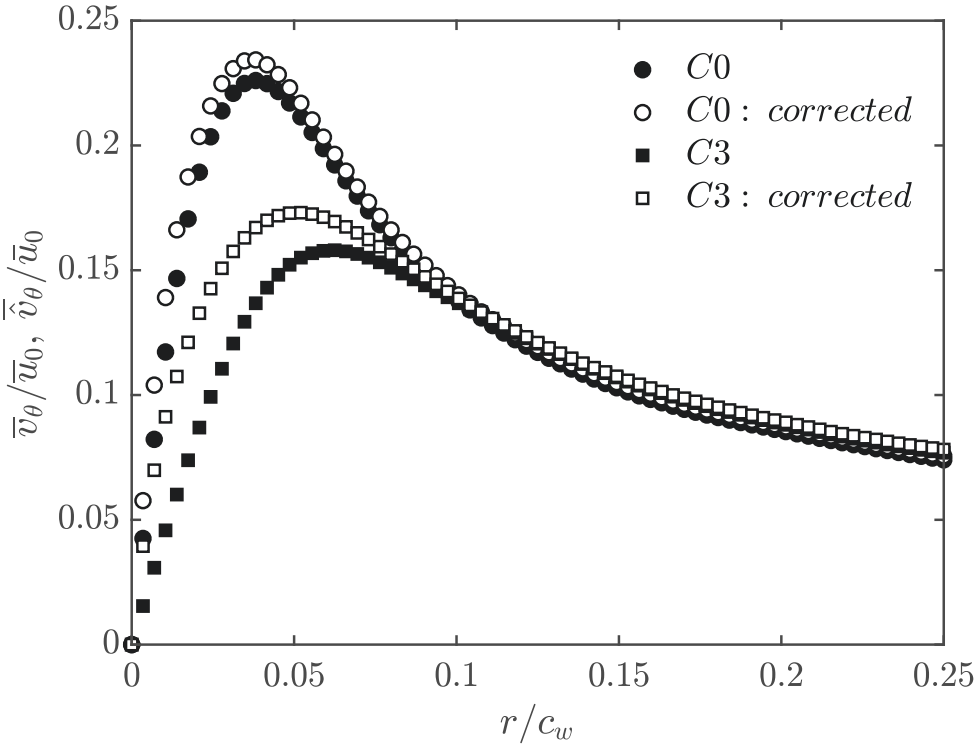

Figure 4.17 Profiles of the raw and meandering-corrected azimuthal velocities for cases C0 and C3 determined at $X/c_w = 6.25$.

layer and the vortex core. The latter plays a key role in smoothing the velocity gradient of the rotational field across the periphery of the vortex core which results in a decreased azimuthal velocity and an enhanced outward diffusion of vorticity [2]. Note that, despite the high level of turbulence injected by the SJ turbulent structures, a relaminarization process was observed at vortex core owing to the strong stabilizing nature of the rotating flow-field therein [2, 12].

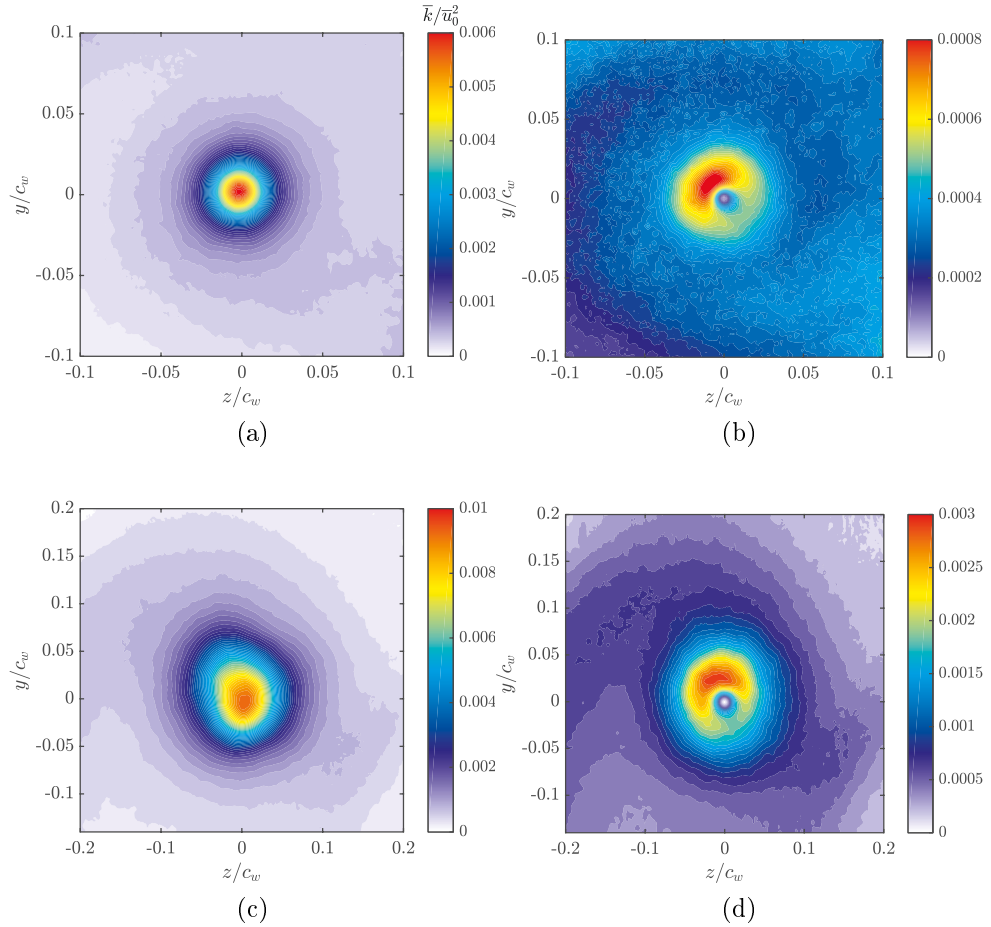

Figure 4.18 Contours of the normalized TKE at $X/c_w = 6.25$ evaluated using; (a) raw data of case C0, (c) raw data of case C3, (b) meandering-corrected data of case C0 and (d) meandering corrected data of case C3.

Modal analysis of the mechanism of vortex decay

In order to elucidate the most energetic flow features responsible for the vortex diffusion under the effect of SJ actuation, the snapshot proper orthogonal decomposition (SPOD), detailed in §4.2.4, was performed on the coherent component of the velocity field. The vorticity contours of the leading POD mode are shown in figure 4.19(a), (c) and (e) for case C0 and figure 4.19(b), (d) and (f) for case C3, at the measurement planes $X/c_w =$

1.25, 6.25 and 7.75, respectively. At $X/c_w = 1.25$, the first mode of case C0 showed spiralling vorticity contours which are believed to be associated with the coherent wake shear layer. Around the vortex center location, two opposite regions of relatively high vorticity were clearly observed. At further downstream distances, the two symmetrical vorticity regions of opposite signs were seen to grow into a nearly circular vortex dipole centred around the mean vortex center location, as illustrated in figure 4.19(c) and (e). This vortex dipole constitute the helical displacement of the vortex with an azimuthal wavenumber $m = 1$, in agreement with the observations of Del Pino *et al.* [34], Edstrand *et al.* [42], Roy and Leweke [98], Roy *et al.* [99]. The azimuthal symmetry of the vortex dipole is mainly associated with the global lateral displacement of the vortex where the decrease in one of the vortex doublet is compensated by an increase in the other, resulting in an overall helical displacement of the vortex core [45]. Although not shown here, the second POD mode exhibited a similar behavior to the first mode with the vortex dipoles being orthogonal to those of the first mode. It is believed that the first two modes are paired and orthogonally rotate together as the vortex evolves downstream; however, no conclusions on the direction of rotation can be drawn from figure 4.19 due to insufficient temporal resolution. The energies contained in the two leading modes were nearly similar but largely higher than the remaining POD modes, as indicated in the POD energy spectra of the first twenty modes shown in figure 4.20. It is possible to associate the two dominant modes with a Kelvin wave of azimuthal wavenumber $m = 1$. The lower energy modes consist of higher order azimuthal modes. The linear combination of the two dominant modes results in a relatively large fraction of the coherent TKE contained in the vortex core, as shown in figure 4.21. This portion of the energy is mainly used to displace the vortex which results in its meandering motion. In figure 4.21, the meandering energy increases with increased downstream distances, in a similar manner observed in the streamwise evolution of the meandering amplitudes (figure 4.16). With control, the azimuthal symmetry of the helical structure was found to be disrupted as the two vortex doublet exhibited different shapes and largely asymmetric vorticity levels. At $X/c_w = 1.25$, the positive vorticity contours (coloured in blue) were seen to be stretched at an oblique angle similar to that observed in the scatter of the instantaneous vortex positions. The size and vorticity levels associated with the vortex doublet were larger than those recorded in case C0, indicating an increased meandering amplitude of the controlled vortex. As the vortex evolved downstream, the helical mode was seem to rotated at an azimuthal angle homologous with the angular inversion of the preferred vortex meander, as displayed in figure 4.15(d). In figure 4.21, the streamwise growth of the meandering energy (associated with the dominant modes) corroborates results observed in figure 4.16 as in the case of

the controlled vortex, a substantially higher energy is required to displace the vortex with larger meandering amplitudes.

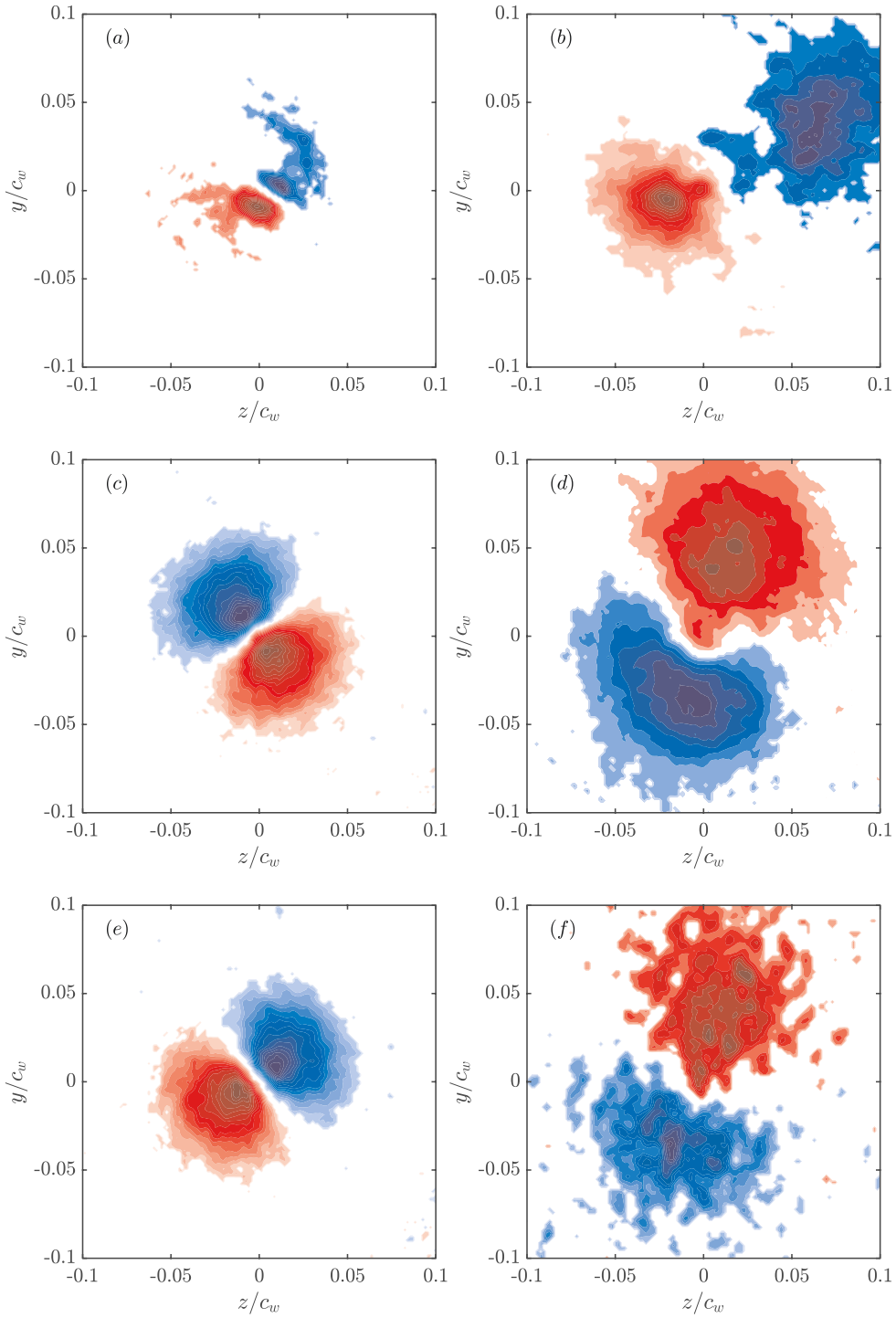

Figure 4.19 Axial vorticity contours of the leading POD mode evaluated at $X/c_w = 1.25, 6.25$ and 7.75. (a), (c), (e): C0 and (b), (d), (f): C3

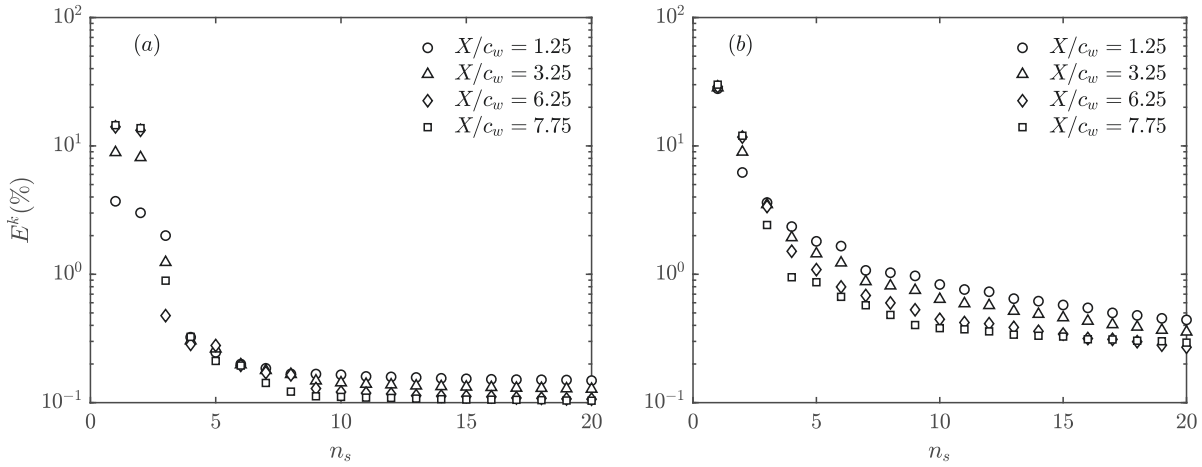

Figure 4.20 Energy spectra of the first twenty POD modes. (a) C0 and (b) C3.

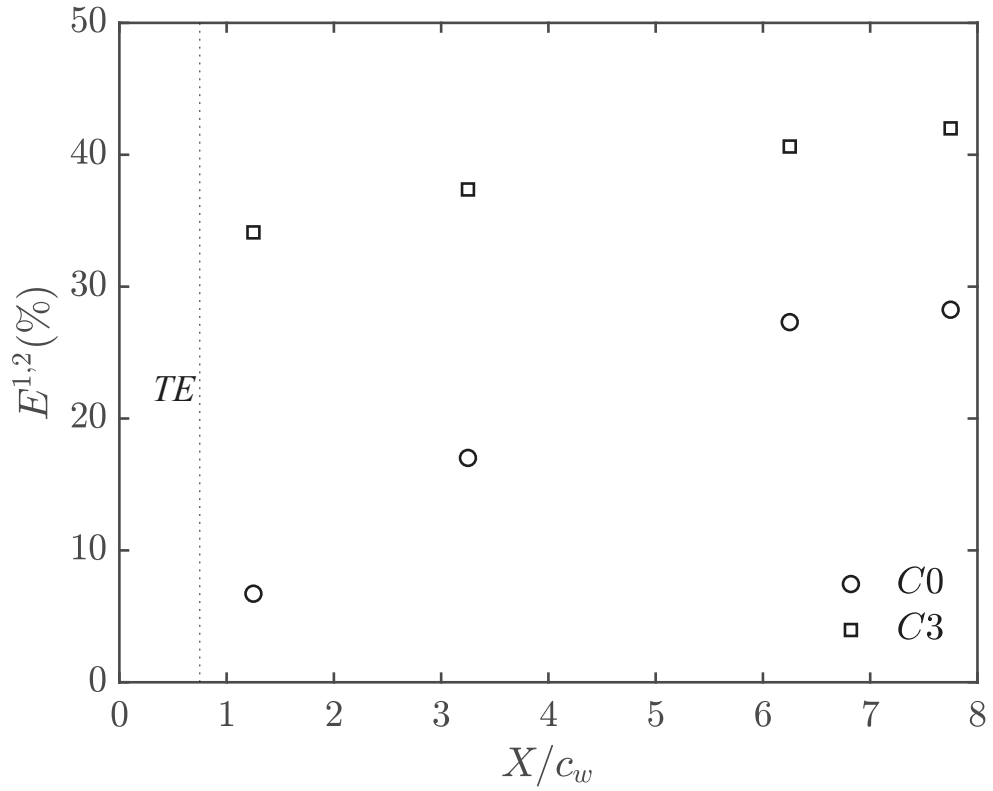

Figure 4.21 Energy content of the dominant helical mode (two first modes) as a function of streamwise distance.

4.2.6 Discussion on the mechanism of vortex diffusion: Enstrophy transport equation

A quantitative description of the physical mechanisms associated with the outward diffusion of the vortex core and the reduction of its strength can be obtained by examining the transport equation of the enstrophy, Ξ, defined as the trace of the time-averaged vorticity covariance, $\bar{\xi}_i\bar{\xi}_i$. Tennekes and Lumley [110] and Balint *et al.* [6] derived the transport equation of the mean enstrophy from the momentum equation as

$$\begin{aligned}\frac{\partial}{\partial t}\left(\frac{1}{2}\Xi\right) = &\underbrace{-\bar{u}_j\frac{\partial}{\partial x_j}\left(\frac{1}{2}\Xi\right)}_{C^\Xi} - \underbrace{\frac{\partial}{\partial x_j}\left(\bar{\xi}_i\overline{\xi_i' u_j'}\right)}_{T^\Xi} + \underbrace{\overline{u_j'\xi_i'}\frac{\partial\bar{\xi}_i}{\partial x_j}}_{P^\Xi} \\ &+ \underbrace{\bar{\xi}_i\overline{\xi_j' s_{ij}}}_{S^\Xi} + \underbrace{\nu\frac{\partial^2}{\partial x_j\partial x_j}\left(\frac{1}{2}\Xi\right)}_{\nu^\Xi} - \underbrace{\nu\frac{\partial\bar{\xi}_i}{\partial x_j}\frac{\partial\bar{\xi}_i}{\partial x_j}}_{\epsilon^\Xi}\end{aligned} \tag{4.24}$$

where $\bar{\xi}_i$ and ξ_i' are the components of the vorticity vector of the time-averaged and fluctuating fields respectively and are given by

$$\bar{\xi}_i = \epsilon_{ijk}\frac{\partial\bar{u}_k}{\partial x_j} \tag{4.25}$$

$$\xi_i' = \epsilon_{ijk}\frac{\partial u_k'}{\partial x_j} \tag{4.26}$$

where ϵ_{ijk} is the Levi-Civita symbol, and $\bar{u}_k$ and u_k' are the components of the time-averaged and the fluctuating velocity fields, respectively. Moreover, s_{ij} corresponds to the fluctuating strain rate.

Although not shown here, the spanwise and transverse components of the vorticity vector were found to be negligible compared to the axial component. Thus, the mean enstrophy can be reasonably approximated as only a function of the axial vorticity, $\Xi \approx \bar{\xi}_x\bar{\xi}_x$. Consequently, the different terms of the equation 4.24 can be written as

$$C^\Xi = -\bar{u}_z\frac{\partial}{\partial z}\left(\frac{1}{2}\Xi\right) - \bar{u}_y\frac{\partial}{\partial y}\left(\frac{1}{2}\Xi\right); \tag{4.27}$$

$$T^\Xi = -\frac{\partial}{\partial z}\left(\bar{\xi}_x\overline{\xi_x' u_z'}\right) - \frac{\partial}{\partial y}\left(\bar{\xi}_x\overline{\xi_x' u_y'}\right); \tag{4.28}$$

$$P^\Xi = \overline{u_z'\xi_x'}\frac{\partial\bar{\xi}_x}{\partial z} + \overline{u_y'\xi_x'}\frac{\partial\bar{\xi}_x}{\partial y}; \tag{4.29}$$

$$S^{\Xi} = \bar{\xi}_x \overline{\xi'_z s_{xz}} + \bar{\xi}_x \overline{\xi'_y s_{xy}}; \tag{4.30}$$

$$\nu^{\Xi} = \nu \left[\frac{\partial^2}{\partial z \partial z} \left(\frac{1}{2} \Xi \right) + \frac{\partial^2}{\partial y \partial y} \left(\frac{1}{2} \Xi \right) \right]; \tag{4.31}$$

and

$$\epsilon^{\Xi} = -\nu \left[\frac{\partial \bar{\xi}_x}{\partial z} \frac{\partial \bar{\xi}_x}{\partial z} + \frac{\partial \bar{\xi}_x}{\partial y} \frac{\partial \bar{\xi}_x}{\partial y} \right]. \tag{4.32}$$

where the term C^{Ξ} represents the advection of enstrophy by mean flow, T^{Ξ} is the transport of enstrophy by turbulent vorticity-velocity interactions, P^{Ξ} is the turbulence production term, S^{Ξ} corresponds to the production (or removal) of enstrophy caused by stretching (or squeezing) of fluctuating vorticity components by fluctuating strain rate, while ν^{Ξ} and ϵ^{Ξ} represent viscous diffusion and dissipation of enstrophy respectively. Radial distributions of the dominant terms in the mean enstrophy transport equation are illustrated in figure 4.22(a) and (c) for case C0 and figure 4.22(b) and (d) for case C3, at the measurement planes $X/c_w = 1.25$ and 6.25, respectively. Figure 4.22(a) shows that the dominant term in the transport equation is the turbulent transport, T^{Ξ}, which mainly contributed to the generation of the mean enstrophy within the vortex core of case C0. The transport of the mean enstrophy, which is generated over the wing tip and then convected further downstream, was found to trigger other production terms within the core region. In fact, the fluctuating strain rate stretched the transported vorticity resulting in a further production of enstrophy (P^{Ξ}). It can be inferred from figure 4.22(a) that T^{Ξ}, S^{Ξ}, P^{Ξ} and ν^{Ξ} were balanced by the advection due to the mean flow, C^{Ξ}, and the viscous dissipation, ϵ^{Ξ}. Note that, outside the core region, all the terms asymptotically approach zero where the flow is nearly irrotational. Further downstream and at $X/c_w = 6.25$, the significant reduction in the peak value of the transported enstrophy in the vortex core was accompanied with a noticeable decrease in the peak values of both stretching and production terms. The latter, however, were nearly of the same order of magnitude which can be attributed to the self-similar state of the vorticity field at $X/c_w = 6.25$ and therefore, the mechanism of turbulent production is only limited to the vorticity stretching by fluctuating strain rate. With control and at $X/c_w = 1.25$, the peak value of the turbulent transport term, T^{Ξ}, nearly doubled with respect to case C0. This significant increase in the turbulent transport may be attributed to the increase in the velocity and vorticity fluctuations caused by the turbulence injection from the SJ. The same mechanism along with the vorticity stretching and the increased fluctuating strain rate caused the turbulent production term, P^{Ξ}, to also increase by roughly two times compared to case C0. It is noteworthy that the radial position of the peak values of these terms were seen to move further away from the vortex center indicating an increased outward transport of enstrophy under the effect of

the SJ actuation. When the vortex was convected to $X/c_w = 6.25$, all the terms were seen to significantly decrease, as illustrated in figure 4.22(d). In this figure, the contribution of the vorticity stretching appeared to be the dominant term in the transport equation at the vortex center location. In the contrary, the turbulent production term appeared to be of the same level of magnitude of the dissipation terms indicating that the vortex has reached an equilibrium state.

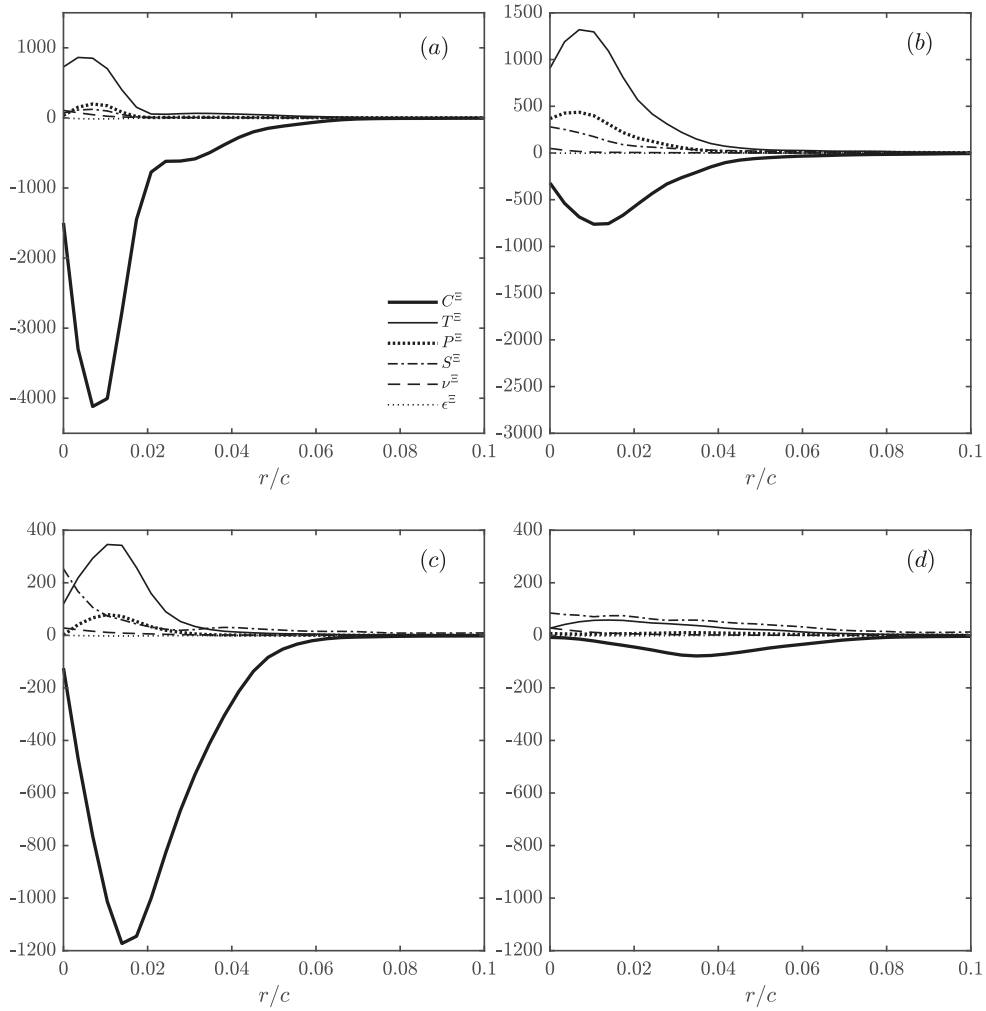

Figure 4.22 Radial distribution of the different terms of the mean enstrophy transport equation at $X/c_w = 1.25$ and 6.25. (a), (c): C0 and (b), (d): C3. All terms are normalized by $(\bar{u}_\infty/c_w)^3$

4.2.7 Conclusions

In this study, Stereoscopic PIV experiments have been conducted to document the development of a wing tip vortex under the effect of synthetic jet (SJ) actuation for a rectangular, square-tipped wing having a NACA 0012 airfoil at a chord Reynolds number

$Re_{c_w} = 2 \times 10^5$. A total number of five control configurations were considered for a comparative study namely; case C1 with momentum coefficient $C_\mu = 0.001$ and an actuation frequency $F^+ = 0.075$, case C2 with $C_\mu = 0.001$ and $F^+ = 0.15$, case C3 with $C_\mu = 0.001$ and $F^+ = 0.3$, case C4 with $C_\mu = 0.001$ and $F^+ = 0.6$ and case C5 with $C_\mu = 0.001$ and $F^+ = 1.2$. Amongst all the cases studied, case C3 was shown to have the most pronounced effect on the structure of the wing tip vortex in the near wake region at $X/c_w = 1.25$. In fact, under case C3, the vortex was stretched into an ellipsoid shape with a nearly 60% decrease in the peak circumferential velocity and the core axial vorticity. The vortex core radius largely broadened suggesting that the lower frequency control configuration allowed the synthetic jet to travel larger distances into the vortex bringing turbulent structures within its core resulting in increased mixing and subsequently a more diffuse vortex. Consequently, a comprehensive SPIV survey has been conducted at the downstream positions $X/c_w = 1.25, 3.25, 6.25$ and 7.75 covering both near and mid-wake vortex regions. Further insights into the contribution of synthetic jet actuation on the vortex meandering has been provided using proper orthogonal decomposition (POD). The meandering coherent motion was extracted via a triple decomposition of the meandering-corrected raw velocity field at different streamwise positions. An in-depth characterization of the physical mechanisms associated with the vortex diffusion was provided by quantifying the different terms of the transport equation of the streamwise enstrophy. The dominant terms responsible for the destruction of enstrophy in the budget equation were shown to be attributed to increased vorticity stretching and fluctuating strain rate as a result of the fluidic actuation.

4.2.8 Acknowledgements

This work was supported by the Natural Sciences and Engineering Research Council (NSERC) of Canada and the Directorate of Technical Airworthiness and Engineering Support (DTAES) office of the Royal Canadian Air Force.

CHAPTER 5
CONCLUSION GÉNÉRALE

Deux études expérimentales sur l'efficacité de l'actionnement d'un jet synthétique pour contrôler un tourbillon de bout d'aile dans le sillage d'une aile rectangulaire NACA 0012 a été menées. L'aile était placée à un angle d'attaque de 5 degrés dans un flux de soufflerie à faible turbulence, à un nombre de Reynolds basé sur la corde, $Re_c = 8 \times 10^4$ et 2×10^5, et enjambant la demi-largeur du tunnel. Le SJ émanait d'une mince fente trapézoïdale avec une sortie courbée placée à l'extrémité de l'aile dans le sens de la corde. Dans un premier temps, une étude paramétrique sur les effets de la fréquence d'actionnement, F^+, et le coefficient de quantité de mouvement, C_μ, sur la distribution de la pression sur la surface d'aspiration de l'aile a été menée. Les mesures de pression pour F^+ comprises entre 0.0213 et 1.42 et C_μ comprises entre 0.0021 et 0.04 ont montré que les fréquences les plus efficaces pour améliorer la distribution de pression sur la surface d'aspiration de l'aile résultaient lorsque F^+ était dans la gamme de fréquences entre les instabilités de Crow à grande longueur d'onde et les instabilités de Widnall à courte longueur d'onde. Dans cette plage de fréquences d'activation, une amélioration supplémentaire a été obtenue lorsque C_μ est augmenté.

Dans le deuxième chapitre, les mesures à fils chaud ont été effectuées dans deux plans d'écoulement transversal en aval, à savoir, $x/c = 1$ et $x/c = 2$. Les mesures ont été effectuées pour le tourbillon naturel et pour deux configurations SJ, à savoir, une configuration "moins efficace" avec $F^+ = 0.71$ et $C_\mu = 0.004$ et une configuration "plus efficace" avec $F^+ = 0.213$ et $C_\mu = 0.04$. Lorsque le flux a été actionné avec une fréquence plus faible et un C_μ (plus long λ)plus élevé, les mesures dans le sillage à $x/c = 1$ ont montré que le contrôle avait un impact significatif sur le tourbillon de bout d'aile. Plus spécifiquement, le tourbillon a été étiré en une forme ellipsoïdale avec une taille accrue. Comme le rayon du noyau de tourbillon ne pouvait pas être défini dans le sens traditionnel, un rayon effectif était défini comme la moitié de la distance séparant les positions où les changements dans la vitesse tangentielle, $\bar{U}_\theta$, n'étaient pas significatifs. Il a été constaté que le contrôle a permis d'obtenir un élargissement de 30% du rayon du noyau de tourbillon, r_c. En outre, la résistance du tourbillon de l'extrémité de l'aile a diminué par rapport au tourbillon naturel dans le même emplacement dans le sens de l'écoulement; l'actionnement a engendré une réduction de 23% du déficit de la vitesse axiale, $\bar{U}_x$, et une diminution moyenne de 50% de la vitesse tangentielle maximale, $\bar{U}_\theta$. De plus, les valeurs de la vorticité axiale à

proximité du cœur sont largement réduites et, par conséquent, une réduction de 11% de la force de tourbillon de bout d'aile, $\bar{\Gamma}_c$. Plus en aval, à $x/c = 2$, le tourbillon de bout d'aile a retrouvé sa forme traditionnelle, mais avec une circulation réduite. Les résultats ont suggéré que la basse fréquence de la configuration de contrôle «la plus efficace» permettait au SJ de parcourir de plus grandes distances dans le noyau du tourbillon de bout d'aile, ce qui apportait des structures à forte turbulence. Cela a entraîné une augmentation du mélange turbulent dans le noyau de tourbillon et par la suite, une diminution de la circulation de tourbillon.

Dans le troisième chapitre, afin d'identifier l'effet de l'actionnement de jet synthétique dans la région du milieu du sillage, une étude comparative sur l'efficacité des paramètres d'actionnement SJ pour contrôler un tourbillon de bout d'aile dans le sillage proche et moyen a été menée. Les mesures à fil chaud dans le sillage à $x/c = 3$ ont montré que l'activation à basse fréquence du cas C3 ($F^+ = 0.29$) et le coefficient élevé de quantité de mouvement $C_\mu = 0.04$, avaient l'impact le plus significatif sur le tourbillon de bout d'aile. Plus spécifiquement, le tourbillon a été étiré en une forme ellipsoïdale avec plus de 50% d'élargissement du rayon du noyau du tourbillon, r_c. L'actionnement du cas C3 a permis une réduction de 35% du déficit de la vitesse axiale, $\bar{U}_x$ et une diminution moyenne de 40% de la vitesse circonférentielle de crête, $\bar{U}_\theta$. De plus, la valeur maximale de la vorticité axiale normalisée près du noyau tourbillon a diminué de plus de 60% par rapport au cas naturel (NV). Les résultats suggèrent que la basse fréquence et le coefficient de quantité de mouvement élevé de la configuration de contrôle C3, ont permis au SJ de parcourir de plus grandes distances dans le noyau du tourbillon de l'extrémité de l'aile, ce qui a entraîné des structures turbulentes. Cela a entraîné une augmentation du mélange turbulent dans le noyau du tourbillon et, par la suite, un tourbillon plus diffus. Des mesures complètes à fil chaud du développement de tourbillon à différentes positions en aval jusqu'à $x/c = 5$ ont montré que la vitesse circonférentielle diminuait de façon monotone sous l'effet de l'actionnement de SJ. La diffusion vers l'extérieur du noyau du tourbillon s'est traduite par une augmentation de près de 35% de son rayon aux endroits les plus en aval. Les spectres de fréquence, mesurés à l'intérieur et à l'extérieur de la région centrale, ont montré une augmentation significative de l'énergie totale dans la plage des basses fréquences avec un actionnement SJ. Le sommet dominant de la fréquence d'activation et ses harmoniques supérieurs ont persisté à des distances radiales élevées. Ceci suggère que le mélange turbulent, le mécanisme responsable de la diffusion du tourbillon, a été principalement déclenché par l'injection de turbulence de l'actionnement SJ.

Dans le chapitre quatre, des mesures PIV stéréoscopiques ont également été menées pour documenter le développement d'un tourbillon de bout d'aile sous l'effet d'un actionnement

par jet synthétique pour une aile rectangulaire à bout carré ayant un profil aérodynamique NACA 0012 à un nombre de Reynolds basé sur la corde, $Re_{c_w} = 2 \times 10^5$. Cinq configurations de contrôle ont été considérées pour une étude comparative à savoir; cas C1 avec coefficient de quantité $C_\mu = 0.001$ et une fréquence d'activation $F^+ = 0.075$, cas C2 avec $C_\mu = 0.001$ et $F^+ = 0.15$, cas C3 avec $C_\mu = 0.001$ et $F^+ = 0.3$, cas C4 avec $C_\mu = 0.001$ et $F^+ = 0.6$ et cas C5 avec $C_\mu = 0.001$ et $F^+ = 1.2$. Parmi tous les cas étudiés, il a été démontré que le cas C3 avait l'effet le plus prononcé sur la structure du tourbillon de l'extrémité de l'aile dans la région proche du sillage à $X/c_w = 1.25$. En fait, dans le cas C3, le tourbillon a été étiré en une forme ellipsoïdale avec une diminution de près de 60% de la vitesse circonférentielle maximale et de la vorticité axiale du noyau. Le rayon du noyau du tourbillon s'est élargi, suggérant que la configuration de contrôle à basse fréquence permettait au JS de parcourir de plus grandes distances dans le tourbillon, entraînant des structures turbulentes dans son noyau et un mélange accru et par conséquent un tourbillon plus diffus. Par conséquent, une étude exhaustive SPIV a été menée aux positions en aval $X/c_w = 1.25, 3.25, 6.25$ et 7.75 couvrant à la fois les régions de proximité et de mi-sillage. De plus amples informations sur la contribution de l'actionnement de jet synthétique sur l'errance des tourbillons ont été fournies en utilisant une décomposition orthogonale aux valeurs propres (POD). Le mouvement cohérent sinueux a été extrait par une triple décomposition du champ de vitesse dépourvu du mouvement d'errance à différentes positions en aval de l'aile. Une caractérisation approfondie des mécanismes physiques associés à la diffusion des tourbillons a été fournie en quantifiant les différents termes de l'équation de transport de l'enstrophie. On a montré que les termes dominants responsables de la destruction de l'enstrophie dans l'équation de transport étaient attribuables à l'allongement de la vorticité et à la fluctuation du taux de cisaillement résultant de l'actionnement fluidique.

CHAPTER 6

GENERAL CONCLUSION

An experimental investigation on the effectiveness of synthetic jet actuation to control a wing tip vortex in the near wake of a rectangular NACA 0012 wing was conducted. The wing was placed at an angle of attack of 5 degrees in a low turbulence wind tunnel flow, at chord Reynolds number, $Re_c = 8 \times 10^4$, and spanning the tunnel half width. The SJ emanated from a thin, trapezoidal slot with a curved exit placed at the wing tip in the chordwise direction. First, a parametric study on the effects of the actuation frequency, F^+, and momentum coefficient, C_μ, on the pressure spanwise distribution on the suction surface of the wing was performed. The pressure measurements for F^+ ranging between 0.0213 to 1.42 and C_μ ranging from 0.0021 and 0.04 showed that the most efficient frequencies in improving the pressure distribution on the suction surface of the wing resulted when F^+ was in the range of frequencies between the long-wave Crow's instability and shorter-wave Widnall instability. In this range of actuation frequencies, further improvement was achieved when C_μ was increased.

In the second chapter, hotwire measurements were performed at two downstream cross-flow planes namely, $x/c = 1$ and $x/c = 2$. The measurements were carried out for the natural vortex and for two SJ configurations, namely, a "least efficient" configuration with $F^+ = 0.71$ and $C_\mu = 0.004$ and a "most efficient" configuration with $F^+ = 0.213$ and $C_\mu = 0.04$. When the flow was actuated with a lower frequency and higher C_μ (longer λ), the measurements in the wake at $x/c = 1$ showed that the actuation had a significant impact on the wing tip vortex. More specifically, the wing tip vortex was stretched into an ellipsoid shape with increased size. Because a vortex core radius could not be defined in the traditional sense, an effective radius was defined as half the distance separating the positions where the changes in the tangential velocity, $\bar{U}_\theta$, were not significant. It was found that the control achieved a 30% broadening of vortex core radius, r_c. Furthermore, the wing tip vortex strength decreased compared to the natural vortex at the same streamwise location; the actuation achieved a 23% reduction in the axial velocity deficit, $\bar{U}_x$, and a 50% average decrease in the peak tangential velocity, $\bar{U}_\theta$, Also, the axial vorticity values near the core were found to be largely reduced and hence, a reduction of 11% in the wing tip vortex strength, $\bar{\Gamma}_c$. Further downstream, at $x/c = 2$, the wing tip vortex regained its traditional shape but with a reduced strength. The results suggested that the low frequency of the "most efficient" control configuration allowed the SJ to travel

larger distances into the wing tip vortex core bringing high turbulence structures with it. This resulted in increased turbulent mixing in the vortex core and subsequently decreased vortex strength.

In the third chapter, in order to identify the effect of synthetic jet actuation in the mid-wake region, a comparative study on the effectiveness of SJ actuation parameters to control a wing tip vortex in the near and mid-wake. Hotwire measurements in the wake at $x/c = 3$ showed that the low frequency actuation of case C3, $F^+ = 0.29$ and the high momentum coefficient $C_\mu = 0.04$, had the most significant impact on the wing tip vortex. More specifically, the wing tip vortex was stretched into an ellipsoidal shape with more than 50% broadening of vortex core radius, r_c. The actuation of case C3 achieved a 35% reduction in the axial velocity deficit, $\bar{U}_x$ and a 40% average decrease in the peak circumferential velocity, $\bar{U}_\theta$. Additionally, the peak value of the normalized axial vorticity near the vortex core decreased by over 60% compared to the NV. The results suggested that the low frequency and the high momentum coefficient of the control configuration C3 allowed the SJ to travel larger distances into the wing tip vortex core bringing high turbulence structures with it. This resulted in increased turbulent mixing in the vortex core and subsequently a more diffuse vortex. Comprehensive hotwire measurements of the vortex development at different downstream positions up to $x/c = 5$ showed that the circumferential velocity decreased monotonically under the effect of SJ actuation. The apparent outward diffusion of the vortex core translated to a nearly 35% increase of its radius at the farthest downstream locations. Frequency spectra, measured inside and outside the core region, showed a significant increase of the total energy in the range of low frequencies with SJ actuation. The dominant peak of the actuation frequency and its higher harmonics were found to persist with increased radial and downstream distances. This suggests that the turbulent mixing, the mechanism responsible of the vortex diffusion, was mainly triggered by the turbulence injection of the SJ actuation.

In the four chapter, stereoscopic PIV experiments have also been conducted to document the development of a wing tip vortex under the effect of synthetic jet (SJ) actuation for a rectangular, square-tipped wing having a NACA 0012 airfoil at a chord Reynolds number $Re_{c_w} = 2 \times 10^5$. A total number of five control configurations were considered for a comparative study namely; case C1 with momentum coefficient $C_\mu = 0.001$ and an actuation frequency $F^+ = 0.075$, case C2 with $C_\mu = 0.001$ and $F^+ = 0.15$, case C3 with $C_\mu = 0.001$ and $F^+ = 0.3$, case C4 with $C_\mu = 0.001$ and $F^+ = 0.6$ and case C5 with $C_\mu = 0.001$ and $F^+ = 1.2$. Amongst all the cases studied, case C3 was shown to have the most pronounced effect on the structure of the wing tip vortex in the near wake region at $X/c_w = 1.25$. In fact, under case C3, the vortex was stretched into an ellipsoid shape with a nearly 60%

decrease in the peak circumferential velocity and the core axial vorticity. The vortex core radius largely broadened suggesting that the lower frequency control configuration allowed the synthetic jet to travel larger distances into the vortex bringing turbulent structures within its core resulting in increased mixing and subsequently a more diffuse vortex. Consequently, a comprehensive SPIV survey has been conducted at the downstream positions $X/c_w = 1.25, 3.25, 6.25$ and 7.75 covering both near and mid-wake vortex regions. Further insights into the contribution of synthetic jet actuation on the vortex meandering has been provided using proper orthogonal decomposition (POD). The meandering coherent motion was extracted via a triple decomposition of the meandering-corrected raw velocity field at different streamwise positions. An in-depth characterization of the physical mechanisms associated with the vortex diffusion was provided by quantifying the different terms of the transport equation of the streamwise enstrophy. The dominant terms responsible of the destruction of enstrophy in the budget equation were shown to be attributed to increased vorticity stretching and fluctuating strain rate as a result of the fluidic actuation.

APPENDIX A

Hot-wire measurement technique: Wittmer's method

The miniature four-sensor hot-wire probe Auspex Corp.® AVOP-4-100 was used for the velocity measurement of the three dimensional flow-field of a wing tip vortex. Multiple sensor hot-wire probes provide desirable advantages for measuring low to moderate turbulent flows away from walls. In fact, Devenport et al. [36] showed that the four-sensor hot-wire probe, usually associated with streamwise vorticity measurements, is capable of simultaneous three-components velocity measurements from a relatively compact measurement volume and is well-suited to wake measurements because of its weak axial velocity gradients. Although cross-wire probes are relatively easy to operate, they produce large uncertainties in the complete Reynolds stress tensor field due to non-simultaneousness of the three velocity components. Moreover, Devenport et al. [36] indicated that triple-wire probe was found to be very sensitive to gradient errors commonly found in vortex flows and that axial velocity are contaminated (up to 10%) by streamwise vorticity. Therefore, four-sensor hot-wire probes, consisting of two orthogonal X-wire arrays, appeared to overcome the gradients problems stated above. The probe is calibrated separately for velocity and angle response.

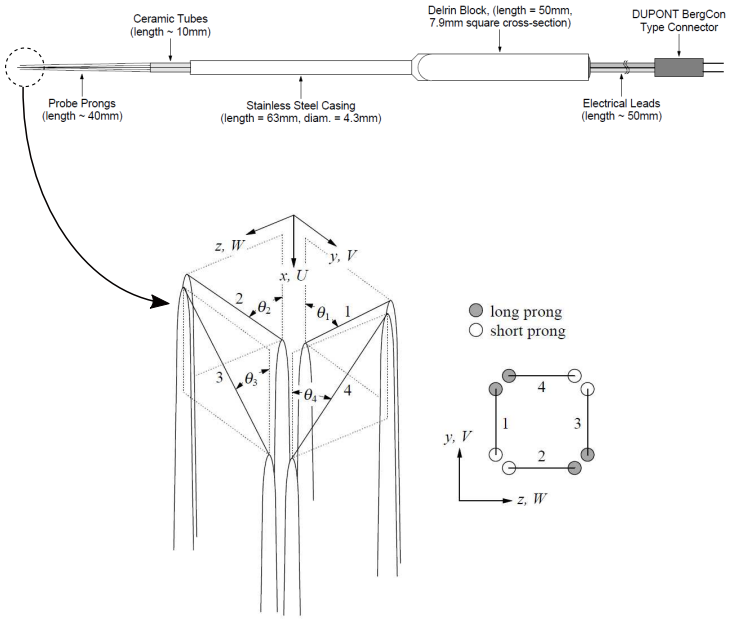

Figure A.1 Sketch of the four-sensor probe.

Velocity calibrations were performed in the wind tunnel before and after each measurement run. In order to perform the velocity calibration, the four-sensor probe was positioned within 20 mm of the TSI ® air velocity transducer. The anemometer output voltage, E_{a_i}, and the velocity measured by the air velocity transducer were recorded over $\sim 30s$ at 17 different free-stream velocities. The bridge output voltage, E_{b_i}, was determined from E_{a_i} for each sensor as $E_{b_i} = E_{a_i}/G_i - E_{off_i}$, where G_i is the channel conditioning gain and E_{off_i} is the offset. The relationship between E_{b_i} and U_{eff_i} was determined using the King's law

$$E_{b_i}^2 = A_i + B_i U_{eff_i}^{n_i}, \tag{A.1}$$

where A_i, B_i and n_i are the calibration constants. A representative set of calibration curves for the four sensors is illustrated in Figure A.2. To calibrate the angle response, a method

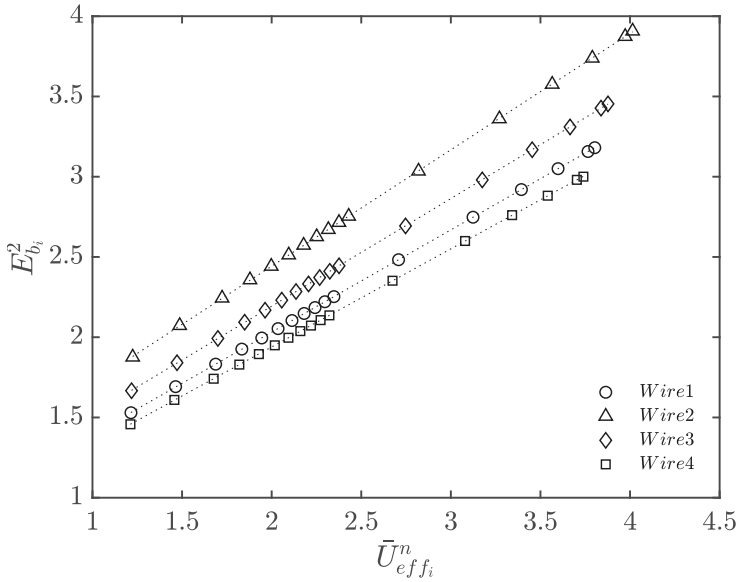

Figure A.2 Typical velocity calibration curves for the four sensors. Solid lines indicate the King's law curve fit.

developed by Wittmer et al. [118] similar to that of Mathioudakis and Breugelmans [82] was used. In this adaptation of their method, the four-sensor probe is placed in the potential core of a uniform jet (calibrator) of known flow direction and a velocity equal to wind tunnel freestream velocity. The cooling velocities are then measured as the probe is pitched and yawed over all likely angle combinations; usually $\pm 45°$ in increment of $5°$ or less. According to Jorgenson [69], the velocity estimates, U_e, V_e, W_e, can be determined by writing the effective cooling velocity of each sensor in terms of: the velocity component it experiences U_i, V_i, W_i, the effective sensor angle, θ_{eff_i}, and the pitch sensitivity, h_i, such that:

$$U_{eff1}^2 = (U_1 \sin\theta_{eff_1} + V_1 \cos\theta_{eff_1})^2 + (h_1 W_1)^2, \tag{A.2}$$

$$U_{eff2}^2 = (U_2 \sin\theta_{eff_2} + W_2 \cos\theta_{eff_2})^2 + (h_2 V_2)^2, \tag{A.3}$$

$$U_{eff3}^2 = (U_3 \sin\theta_{eff_3} + V_3 \cos\theta_{eff_3})^2 + (h_3 W_3)^2, \tag{A.4}$$

$$U_{eff4}^2 = (U_4 \sin\theta_{eff_4} + W_4 \cos\theta_{eff_4})^2 + (h_4 V_4)^2. \tag{A.5}$$

This set of equations were linearised and inverted to give explicit equations for the velocity component estimates:

$$Ve = \frac{C_1\sqrt{C_3}U_{eff_3} - C_3\sqrt{C_1}U_{eff_1}}{C_1 D_3 - C_3 D_1}, \tag{A.6}$$

$$We = \frac{C_2\sqrt{C_4}U_{eff_4} - C_4\sqrt{C_2}U_{eff_2}}{C_2 D_4 - C_4 D_2}, \tag{A.7}$$

$$Ue = \frac{1}{2}\left(\frac{U_{eff_1}}{\sqrt{C1}} - \frac{D_1}{C_1}V_e + \frac{U_{eff_2}}{\sqrt{C_2}} - \frac{D_2}{C_2}W_e\right), \tag{A.8}$$

where $C_i = \sin^2\theta_{eff_i}$ and $D_i = \sin\theta_{eff_i}\cos\theta_{eff_i}$. At each pitch and yaw combination in the angle calibration, velocity component estimates are compared with the actual velocity component, U, V, W, inferred from the known flow angles. The error fractions, $(V - V_e)/Q_e$, $(W - W_e)/Q_e$ and $(Q - Q_e)/Q_e$ were then determined where $Q_e = \sqrt{U_e^2 + V_e^2 + W_e^2}$ and $Q = \sqrt{U^2 + V^2 + W^2}$. By interpolating the calibration data, these fractions are then tabulated as functions of V_e/Q_e and W_e/Q_e. The tables are then used to correct instantaneous estimates of V_e, W_e and Q_e (and therefore U_e) obtained during a measurement.

LIST OF REFERENCES

[1] Arora, P., Hossain, A., Edi, P., Jaafar, A., Younis, T. S. and Saleem, M. (2005). Drag reduction in aircraft model using elliptical winglet. *Journal of the Institution of Engineers*, volume 66, number 4.

[2] Bailey, S. and Tavoularis, S. (2008). Measurements of the velocity field of a wing-tip vortex, wandering in grid turbulence. *Journal of Fluid Mechanics*, volume 601, pp. 281–315.

[3] Bailey, S. C., Estejab, B., Robert, M. and Tavoularis, S. (2011). Long-wavelength vortex motion induced by free-stream turbulence. In *TSFP DIGITAL LIBRARY ONLINE*, Begel House Inc.

[4] Bailey, S. C., Tavoularis, S. and Lee, B. H. (2006). Effects of free-stream turbulence on wing-tip vortex formation and near field. *Journal of aircraft*, volume 43, number 5, pp. 1282–1291.

[5] Baker, G., Barker, S., Bofah, K. and Saffman, P. (1974). Laser anemometer measurements of trailing vortices in water. *Journal of Fluid Mechanics*, volume 65, number 2, pp. 325–336.

[6] Balint, J.-L., Vukoslavcevic, P. and Wallace, J. (1990). The transport of enstrophy in a turbulent boundary layer. *Near-Wall Turbulence*, pp. 932–950.

[7] Bandyopadhyay, P. R., Ash, R. L. and Stead, D. J. (1991). Organized nature of a turbulent trailing vortex. *AIAA journal*, volume 29, number 10, pp. 1627–1633.

[8] Batchelor, G. K. (1964). Axial flow in trailing line vortices. *Journal of Fluid Mechanics*, volume 20, number 4, pp. 645–658.

[9] Bearman, P., Heyes, A., Lear, C. and Smith, D. (2006). Natural and forced evolution of a counter rotating vortex pair. *Experiments in Fluids*, volume 40, number 1, pp. 98–105.

[10] Bearman, P., Heyes, A., Lear, C. and Smith, D. (2007). Evolution of a forced counter rotating vortex pair for two selected forcing frequencies. *Experiments in Fluids*, volume 43, number 4, pp. 501–507.

[11] Beninati, M. and Marshall, J. (2005). An experimental study of the effect of free-stream turbulence on a trailing vortex. *Experiments in Fluids*, volume 38, number 2, pp. 244–257.

[12] Beresh, S. J., Henfling, J. F. and Spillers, R. W. (2010). Meander of a fin trailing vortex and the origin of its turbulence. *Experiments in Fluids*, volume 49, number 3, pp. 599–611.

[13] Beresh, S. J., Wagner, J. L. and Pruett, B. O. (2012). Particle image velocimetry of a three-dimensional supersonic cavity flow. *AIAA Paper*, volume 30, p. 2012.

[14] Berkooz, G., Holmes, P. and Lumley, J. L. (1993). The proper orthogonal decomposition in the analysis of turbulent flows. *Annual review of fluid mechanics*, volume 25, number 1, pp. 539–575.

[15] Birch, D., Lee, T., Mokhtarian, F. and Kafyeke, F. (2004). Structure and induced drag of a tip vortex. *Journal of Aircraft*, volume 41, number 5, pp. 1138–1145.

[16] Bradshaw, P. (1969). The analogy between streamline curvature and buoyancy in turbulent shear flow. *Journal of Fluid Mechanics*, volume 36, number 1, pp. 177–191.

[17] Breitsamter, C. (2011). Wake vortex characteristics of transport aircraft. *Progress in Aerospace Sciences*, volume 47, number 2, pp. 89–134.

[18] Breitsamter, C. and Allen, A. (2009). Transport aircraft wake influenced by oscillating winglet flaps. *Journal of Aircraft*, volume 46, number 1, pp. 175–188.

[19] Brion, V.and Sipp, D. and Jacquin, L. (2007). Optimal amplification of the crow instability. *Physics of Fluids*, volume 19, number 11, 111703.

[20] Bulathsinghala, D., Jackson, R., Wang, Z. and Gursul, I. (2017). Afterbody vortices of axisymmetric cylinders with a slanted base. *Experiments in Fluids*, volume 58, number 5, p. 60.

[21] Cattafesta III, L. N. and Sheplak, M. (2011). Actuators for active flow control. *Annual Review of Fluid Mechanics*, volume 43, pp. 247–272.

[22] Cerretelli, C. and Williamson, C. (2003). The physical mechanism for vortex merging. *Journal of Fluid Mechanics*, volume 475, pp. 41–77.

[23] Chakraborty, P., Balachandar, S. and Adrian, R. J. (2005). On the relationships between local vortex identification schemes. *Journal of fluid mechanics*, volume 535, pp. 189–214.

[24] Chaudhari, M., Verma, G., Puranik, B. and Agrawal, A. (2009). Frequency response of a synthetic jet cavity. *Experimental thermal and fluid science*, volume 33, number 3, pp. 439–448.

[25] Chiekh, M. B., Ferchichi, M. and Béra, J.-C. (2012). Aerodynamic flow vectoring of a wake using asymmetric synthetic jet actuation. *Experiments in fluids*, volume 53, number 6, pp. 1797–1813.

[26] Chow, J. S., Zilliac, G. G. and Bradshaw, P. (1997). Mean and turbulence measurements in the near field of a wingtip vortex. *AIAA Journal*, volume 35, number 10, pp. 1561–1567.

[27] Corsiglia, V., Schwind, R. and Chigier, N. (1973). Rapid scanning, three-dimensional hot-wire anemometer surveys of wing-tip vortices. *Journal of Aircraft*, volume 10, number 12, pp. 752–757.

[28] Cotel, A. J. and Breidenthal, R. E. (1999). Turbulence inside a vortex. *Physics of Fluids*, volume 11, number 10, pp. 3026–3029.

[29] Crouch, J. (2005). Airplane trailing vortices and their control. *Comptes Rendus Physique*, volume 6, number 4-5, pp. 487–499.

[30] Crouch, J., Miller, G. and Spalart, P. (2001). Active-control system for breakup of airplane trailing vortices. *AIAA Journal*, volume 39, number 12, pp. 2374–2381.

[31] Crow, S. (1970). Stability theory for a pair of trailing vortices. *AIAA Journal*, volume 8, number 12, pp. 2172–2179.

[32] Cucitore, R., Quadrio, M. and Baron, A. (1999). On the effectiveness and limitations of local criteria for the identification of a vortex. *European Journal of Mechanics-B/Fluids*, volume 18, number 2, pp. 261–282.

[33] Degani, D., Seginer, A. and Levy, Y. (1990). Graphical visualization of vortical flows by means of helicity. *AIAA journal*, volume 28, number 8, pp. 1347–1352.

[34] Del Pino, C., Lopez-Alonso, J., Parras, L. and Fernandez-Feria, R. (2011). Dynamics of the wing-tip vortex in the near field of a naca 0012 aerofoil. *The Aeronautical Journal*, volume 115, number 1166, pp. 229–239.

[35] Del Pino, C., Parras, L., Felli, M. and Fernandez-Feria, R. (2011). Structure of trailing vortices: Comparison between particle image velocimetry measurements and theoretical models. *Physics of Fluids*, volume 23, number 1, p. 013602.

[36] Devenport, W. J., Glegg, S. A. and Sharma, G. (1992). *Turbulence measurements in trailing vortices for BWI noise prediction* (Technical report). Virginia Polytechnic Institute and State University.

[37] Devenport, W. J., Rife, M. C., Liapis, S. I. and Follin, G. J. (1996). The structure and development of a wing-tip vortex. *Journal of Fluid Mechanics*, volume 312, pp. 67–106.

[38] Dghim, M., Ferchichi, M. and Fellouah, H. (2017). Stereoscopic piv investigation of the effect of synthetic jet actuation on a wing tip vortex. In *35th AIAA Applied Aerodynamics Conference*. p. 3038.

[39] Dghim, M., Ferchichi, M., Graveline, S. and BenChiekh, M. (2014). Control of wing tip vortex structure using fluidic actuation. In *7th AIAA Flow Control Conference*. Number AIAA 2014-2792.

[40] Dghim, M., Ferchichi, M., Perez, R. E. and BenChiekh, M. (2016). Near wake development of a wing tip vortex under the effect of synthetic jet actuation. *Aerospace Science and Technology*, volume 54, pp. 88–107.

[41] Duraisamy, K. and Baeder, J. D. (2003). Control of tip vortex structure using steady and oscillatory blowing. In *21st Applied Aerodynamics Conference*. Number AIAA 2003-3407.

[42] Edstrand, A. M., Davis, T. B., Schmid, P. J., Taira, K. and Cattafesta, L. N. (2016). On the mechanism of trailing vortex wandering. *Journal of Fluid Mechanics*, volume 801.

[43] Fabre, D., Cossu, C. and Jacquin, L. (2000). Spatio-temporal development of the long and short-wave vortex-pair instabilities. *Physics of Fluids*, volume 12, number 5, pp. 1247–1250.

[44] Fabre, D., Jacquin, L. and Loof, A. (2002). Optimal perturbations in a four-vortex aircraft wake in counter-rotating configuration. *Journal of Fluid Mechanics*, volume 451, pp. 319–328.

[45] Fabre, D., Sipp, D. and Jacquin, L. (2006). Kelvin waves and the singular modes of the lamb–oseen vortex. *Journal of Fluid Mechanics*, volume 551, pp. 235–274.

[46] Fellouah, H., Ball, C. and Pollard, A. (2009). Reynolds number effects within the development region of a turbulent round free jet. *International Journal of Heat and Mass Transfer*, volume 52, number 17, pp. 3943–3954.

[47] Gerontakos, P. and Lee, T. (2006). Near-field tip vortex behind a swept wing model. *Experiments in Fluids*, volume 40, number 1, pp. 141–155.

[48] Gerz, T., Holzäpfel, F. and Darracq, D. (2002). Commercial aircraft wake vortices. *Progress in Aerospace Sciences*, volume 38, number 3, pp. 181–208.

[49] Graftieaux, L., Michard, M. and Grosjean, N. (2001). Combining piv, pod and vortex identification algorithms for the study of unsteady turbulent swirling flows. *Measurement Science and technology*, volume 12, number 9, p. 1422.

[50] Greenblatt, D. (2012). Aiaa journal. *Fluidic Control of a Wing Tip Vortex*, volume 50, number 2, pp. 375–386.

[51] Greenblatt, D. and Wygnanski, I. J. (2000). The control of flow separation by periodic excitation. *Progress in Aerospace Sciences*, volume 36, number 7, pp. 487–545.

[52] Guerrero, J. E., Maestro, D. and Bottaro, A. (2012). Biomimetic spiroid winglets for lift and drag control. *Comptes Rendus Mecanique*, volume 340, number 1, pp. 67–80.

[53] Guha, T. and Kumar, R. (2017). Characteristics of a wingtip vortex from an oscillating winglet. *Experiments in Fluids*, volume 58, number 1, p. 8.

[54] Gupta, M. (2011). *Investigation of Active Control of Aircraft Wing Tip Vortices and Wake Turbulence*. Ph.D. thesis, Auburn University.

[55] Hasebe, H., Naka, Y. and Fukagata, K. (2011). An attempt for suppression of wing-tip vortex using plasma actuators. *Journal of Fluid Science and Technology*, volume 6, number 6, pp. 976–988.

[56] Heyes, A., Jones, R. and Smith, D. (2004). Wandering of wing-tip vortices. In *Proceedings of 12th international symposium on the applications of laser techniques to fluid mechanics. Lisbon, Portugal*.

[57] Heyes, A. and Smith, D. (2004). Spatial perturbation of a wing-tip vortex using pulsed span-wise jets. *Experiments in Fluids*, volume 37, number 1, pp. 120–127.

[58] Hoffmann, E. R. and Joubert, P. N. (1963). Turbulent line vortices. *Journal of Fluid Mechanics*, volume 16, number 3, pp. 395–411.

[59] Holloway, A. G. and Richardson, S. (2007). Development of a trailing vortex formed with spanwise tip jets. *Journal of Aircraft*, volume 44, number 3, pp. 845–857.

[60] Holman, R., Utturkar, Y., Mittal, R., Smith, B. L. and Cattafesta, L. (2005). Formation criterion for synthetic jets. *AIAA Journal*, volume 43, number 10, pp. 2110–2116.

[61] Holzäpfel, F., Dengler, K., Gerz, T. and Schwarz, C. (2011). Prediction of dynamic pairwise wake vortex separations for approach and landing. In *3rd AIAA Atmospheric Space Environments Conference*.

[62] Holzäpfel, F., Stephan, A., Körner, S. and Misaka, T. (2014). Wake vortex evolution during approach and landing with and without plate lines. In *52nd Aerospace Sciences Meeting*.

[63] Hunt, J. C., Wray, A. A. and Moin, P. (1988). Eddies, streams, and convergence zones in turbulent flows. In *Proceedings of the Summer Program*, Center of Turbulence Research.

[64] Jacquin, L., Fabre, D., Geffroy, P. and Coustols, E. (2001). The properties of a transport aircraft wake in the extended near field-an experimental study. In *39th Aerospace Sciences Meeting and Exhibit*. p. 1038.

[65] Jacquin, L., Fabre, D., Sipp, D., Theofilis, V. and Vollmers, H. (2003). Instability and unsteadiness of aircraft wake vortices. *Aerospace Science and technology*, volume 7, number 8, pp. 577–593.

[66] Jacquin, L. and Pantano, C. (2002). On the persistence of trailing vortices. *Journal of Fluid Mechanics*, volume 471, pp. 159–168.

[67] Jansen, P., Perez, R. and Martins, J. (2010). Aerostructural optimization of nonplanar lifting surfaces. *Journal of Aircraft*, volume 47, number 5, pp. 1490–1503.

[68] Jeong, J. and Hussain, F. (1995). On the identification of a vortex. *Journal of fluid mechanics*, volume 285, pp. 69–94.

[69] Jorgensen, F. (1971). *Directional sensitivity of wire and fiber-film probes* (Technical report). DISA Information.

[70] Jorgensen, F. E. (2002). *How to Measure Turbulence with Hot-Wire Anemometers, a Practical Guide*. Dantec Dynamics, Denmark.

[71] Kauertz, S. and Neuwerth, G. (2006). Excitation of instabilities in the wake of an airfoil by means of active winglets. this article was presented at the german aerospace congress 2005. *Aerospace science and technology*, volume 10, number 7, pp. 551–562.

[72] Klar, J. U. and Breitsamter, C. (2014). Unsteady aerodynamic loads on a high-agility aircraft due to wake vortex encounter. *Journal of Aircraft*, volume 51, number 5, pp. 1511–1521.

[73] Kroo, I. (2001). Drag due to lift: concepts for prediction and reduction. *Annual Review of Fluid Mechanics*, volume 33, number 1, pp. 587–617.

[74] Lee, T. and Gerontakos, P. (2006). Effect of winglet dihedral on a tip vortex. *Journal of Aircraft*, volume 43, number 1, pp. 117–124.

[75] Lee, T. and Pereira, J. (2013). Modification of static-wing tip vortex via a slender half-delta wing. *Journal of Fluids and Structures*, volume 43, pp. 1–14.

[76] Lee, T. and Su, Y. (2012). Wingtip vortex control via the use of a reverse half-delta wing. *Experiments in Fluids*, volume 52, number 6, pp. 1593–1609.

[77] Luber, W. (2009). Wake penetration effects on dynamic loads and structural design of military and civil aircraft. In *Proceedings of the International Forum on Aeroelasticity and Structural Dynamics*. Number IFASD-2009-001.

[78] Lumley, J. L. (1967). The structure of inhomogeneous turbulent flows. *Atmospheric turbulence and radio wave propagation*.

[79] Margaris, P. and Gursul, I. (2006). Wing tip vortex control using synthetic jets. *Aeronautical Journal*, volume 110, number 1112, pp. 673–681.

[80] Margaris, P. and Gursul, I. (2010). Vortex topology of wing tip blowing. *Aerospace Science and Technology*, volume 14, number 3, pp. 143–160.

[81] Matalanis, C. G. and Eaton, J. K. (2007). Wake vortex alleviation using rapidly actuated segmented gurney flaps. *AIAA Journal*, volume 45, number 8, pp. 1874–1884.

[82] Mathioudakis, K. and Breugelmans, F. (1985). Use of triple hot wires to measure unsteady flows with large direction changes. *Journal of Physics E: Scientific Instruments*, volume 18, number 5, p. 414.

[83] McAlister, K. W. (2004). Rotor wake development during the first revolution. *Journal of the American Helicopter Society*, volume 49, number 4, pp. 371–390.

[84] Mohammed-Taifour, A. and Weiss, J. (2016). Unsteadiness in a large turbulent separation bubble. *Journal of Fluid Mechanics*, volume 799, pp. 383–412.

[85] Montoya, L., Fiechner, S. G. and Jacobs, P. F. (1978). *Effect of an Alternate Winglet on the Pressure and Spanwise Load Distributions of a First-Generation Jet Transport Wing* (Technical Memorandum TM-78786). NASA.

[86] Mousley, S. W. P. and Vino, G. (2004). The development and use of dynamic pressure probes with extended cones of acceptance (eca). *Development*, volume 13, p. 17.

[87] Mula, S. M., Stephenson, J. H., Tinney, C. E. and Sirohi, J. (2013). Dynamical characteristics of the tip vortex from a four-bladed rotor in hover. *Experiments in fluids*, volume 54, number 10, p. 1600.

[88] Mula, S. M. and Tinney, C. E. (2015). A study of the turbulence within a spiralling vortex filament using proper orthogonal decomposition. *Journal of Fluid Mechanics*, volume 769, pp. 570–589.

[89] Nelson, R. (2006). Trailing vortex wake encounters at altitude - a potential flight safety issue? In *AIAA Atmospheric Flight Mechanics Conference and Exhibit*. Number AIAA-2006-6268.

[90] Ortega, J. M., Bristol, R. L. and Savas, . (2003). Experimental study of the instability of unequal-strength counter-rotating vortex pairs. *Journal of Fluid Mechanics*, volume 474, pp. 35–84.

[91] Phillips, W. (1981). The turbulent trailing vortex during roll-up. *Journal of Fluid Mechanics*, volume 105, pp. 451–467.

[92] Ragab, S. and Sreedhar, M. (1995). Numerical simulation of vortices with axial velocity deficits. *Physics of fluids*, volume 7, number 3, pp. 549–558.

[93] Ramaprian, B. R. and Zheng, Y. (1997). Measurements in rollup region of the tip vortex from a rectangular wing. *AIAA Journal*, volume 35, number 12, pp. 1837–1843.

[94] Ramasamy, M., Johnson, B., Huismann, T. and Leishman, J. G. (2009). Digital particle image velocimetry measurements of tip vortex characteristics using an improved aperiodicity correction. *Journal of the American Helicopter Society*, volume 54, number 1, pp. 12004–12004.

[95] Reynolds, W. and Hussain, A. (1972). The mechanics of an organized wave in turbulent shear flow. part 3. theoretical models and comparisons with experiments. *Journal of Fluid Mechanics*, volume 54, number 2, pp. 263–288.

[96] Rokhsaz, K., Foster, S. R. and Miller, L. S. (2000). Exploratory study of aircraft wake vortex filaments in a water tunnel. *Journal of aircraft*, volume 37, number 6, pp. 1022–1027.

[97] Rossow, V. J. (1999). Lift-generated vortex wakes of subsonic transport aircraft. *Progress in Aerospace Sciences*, volume 35, number 6, pp. 507–660.

[98] Roy, C. and Leweke, T. (2008). Experiments on vortex meandering. In *FAR-Wake Technical Report AST4-CT-2005-012238, CNRS-IRPHE, also presented in international workshop on fundamental issues related to aircraft trailing wakes*. pp. 27–29.

[99] Roy, C., Leweke, T., Thompson, M. C. and Hourigan, K. (2011). Experiments on the elliptic instability in vortex pairs with axial core flow. *Journal of Fluid Mechanics*, volume 677, pp. 383–416.

[100] Saffman, P. G. (1992). *Vortex dynamics*. Cambridge University Press.

[101] Shah, P., Atsavapranee, P., Hsu, T., Wei, T. and McHugh, J. (1999). Turbulent transport in the core of a trailing half-delta-wing vortex. *Journal of Fluid Mechanics*, volume 387, pp. 151–175.

[102] Shekarriz, A., Fu, T. C., Katz, J. and Huang, T. T. (1993). Near-field behavior of a tip vortex. *AIAA journal*, volume 31, number 1.

[103] Singh, P. I. and Uberoi, M. S. (1976). Experiments on vortex stability. *Physics of Fluids (1958-1988)*, volume 19, number 12, pp. 1858–1863.

[104] Sirovich, L. (1987). Turbulence and the dynamics of coherent structures. i. coherent structures. *Quarterly of applied mathematics*, volume 45, number 3, pp. 561–571.

[105] Smith, B. L. and Glezer, A. (1998). The formation and evolution of synthetic jets. *Physics of Fluids (1994-present)*, volume 10, number 9, pp. 2281–2297.

[106] Sousa, J. and Pereira, J. (2000). Rollup region of a turbulent trailing vortex issued from a blade with flow separation. *Experimental thermal and fluid science*, volume 20, number 3, pp. 150–161.

[107] Spalart, P. (1998). Airplane trailing vortices. *Annual Review of Fluid Mechanics*, volume 30, number 1, pp. 107–138.

[108] Spillman, J. (1978). The use of wing tip sails to reduce vortex drag. *Aeronautical Journal*, pp. 387–395.

[109] Strzelczyk, P. and Gil, P. (2016). Properties of velocity field in the vicinity of synthetic jet generator. In *Journal of Physics: Conference Series*, IOP Publishing. Volume 760. p. 012029.

[110] Tennekes, H. and Lumley, J. L. (1972). *A first course in turbulence*. MIT press.

[111] van der Wall, B. G. and Richard, H. (2006). Analysis methodology for 3C-PIV data of rotary wing vortices. *Experiments in Fluids*, volume 40, number 5, pp. 798–812.

[112] Van Jaarsveld, J., Holten, A., Elsenaar, A., Trieling, R. and Van Heijst, G. (2011). An experimental study of the effect of external turbulence on the decay of a single vortex and a vortex pair. *Journal of Fluid Mechanics*, volume 670, pp. 214–239.

[113] Velte, C. M., Hansen, M. O. and Okulov, V. L. (2009). Helical structure of longitudinal vortices embedded in turbulent wall-bounded flow. *Journal of Fluid Mechanics*, volume 619, pp. 167–177.

[114] Waldman, R. M. and Breuer, K. S. (2012). Accurate measurement of streamwise vortices using dual-plane piv. *Experiments in Fluids*, volume 53, number 5, pp. 1487–1500.

[115] WarThunderWiki (2012). Wing tip vortices. `https://vignette.wikia.nocookie.net/warthunder/images/f/f6/Wingtip_vortices.png/revision/latest?cb=20121227140326&format=original` (page consulted on 27 December 2012).

[116] Whitcomb, R. (1976). *A design approach and selected wind tunnel results at high subsonic speeds for wing-tip mounted winglets* (Technical Note NASA TN D-8260.). NASA.

[117] Widnall, S., Bliss, D. and Zalay, A. (1971). Theoretical and experimental study of the stability of a vortex pair. In *Aircraft Wake Turbulence and its Detection*. Springer US, pp. 305–338.

[118] Wittmer, K., Devenport, W. and Zsoldos, J. (1998). A four-sensor hot-wire probe system for three-component velocity measurement. *Experiments in fluids*, volume 24, number 5-6, pp. 416–423.

[119] Zhou, J., Adrian, R. J., Balachandar, S. and Kendall, T. (1999). Mechanisms for generating coherent packets of hairpin vortices in channel flow. *Journal of fluid mechanics*, volume 387, pp. 353–396.

[120] Zimmer, H. (1983). *Aerodynamic Optimization of Wings at subsonic Speeds and the Influence of Wingtip Design* (Technical Memorandum TM-88534). NASA.